Durham E-Theses

Conductor Architecture and Self-Field of Superconducting Strands

RIDGEON, FRANCIS,JEROME

How to cite:

Use policy

Conductor Architecture and Self-Field

of Superconducting Strands

Francis Jerome Ridgeon

A thesis submitted in partial

fulfilment of the requirements for the

degree of *Doctor of Philosophy*

Department of Physics,

Durham University

2019

Abstract

Conductor Architecture and Self-Field of Superconducting Strands

Francis Jerome Ridgeon

Three standard reference material Nb-Ti strands, manufactured for the ITER poloidal field magnets, were extensively characterised using both transport and magnetisation techniques, with a focus on the behaviour of the material in a magnetic field. To quantify the effect of magnetic self-field, the field generated by current flow, the critical current density was measured as a function of the applied magnetic field, temperature, current polarity, and geometry.

A high capacity probe was designed and commissioned for the transport measurements. The characterisation in different measurement geometries was possible with custom-built sample holders (i.e., barrels). As the titanium alloy Ti-6Al-4V used in the standard ITER VAMAS barrel is superconducting at 4.22 K, an alternative titanium alloy (Ti-6Al-2Sn-4Zr-2Mo-0.2Si) was identified that is not superconducting at 4.22 K and used to manufacture the barrels.

The transport measurements at low applied magnetic-fields resulted in high current densities, and the effect of self-field being large. To investigate the self-field both finite element analysis (FEA) and semi-analytic methods were employed. The *H*-formulation of Maxwell's equations was implemented using Comsol Multiphysics, a commercial FEA software. The model input for the superconductors properties were defined using a number of experimental $J_C(B)$ relationships. The architecture of the strand was approximated with different degrees of complexity. The FEA models considered the cross-section of the strand as circular, annular, and as three nested cylinders (i.e., tubes-within-tubes). The probability distribution of the magnetic field components in the superconducting domain was calculated and analysed. The changes in the field distribution due to the geometry of the measurement barrels and the current orientation, (resulting in opposite Lorentz force orientation), were used to quantify the magnitude and orientation of the self-field. A semi-analytic method was used to derive a the magnetic field distribution data from the FEA and the experimental data. The resultant piecewise $J_C(B)$ calculated for the Nb-Ti strand, can be considered a universal $J_C(B)$ relationship.

Publications

Conference Papers:

I.   F. J. Ridgeon, M. J. Raine, M. Lakrimi, A. Thomas, T. Boutboul, and D. P. Hampshire, "Self-field Effects on $J_C(B,T)$ Measurements of Nb-Ti Strands in High Magnetic Fields," *IEEE Trans. Appl. Supercond.* vol. 28, (4), 6353170, 2018.

II.   F. J. Ridgeon, M. J. Raine, D. P. Halliday, M. Lakrimi, A. Thomas, and D. P. Hampshire, "Superconducting Properties of Titanium Alloys (Ti-64 and Ti-6242) for Critical Current Barrels," *IEEE Trans. Appl. Supercond.*, vol. 27, (4) 4201205, 2017.

Table of Contents

List of Variables

Symbol	Description	Unit
$\boldsymbol{A}$	Magnetic vector potential	V.s.m^{-1}
a_0	Inter flux line spacing	m
A_θ	θ component of the vector potential	
A_{Eng}	Area of strands cross-section	m^2
A_{fr}	Area of the filamentary region of strands cross-section	m^2
A_{sc}	Superconducting area of strands cross-section	m^2
b	Reduced field: $b = B/B_{C2}$	-
$\mathrm{d}\mathbf{B}$	Magnetic field of a current element	
$\mathrm{d}\boldsymbol{S}$	Current element vector	
$\mathbf{B}$	Magnetic flux density	T
B_{App}	Applied magnetic field	T
B_{C}	Thermodynamic critical magnetic field (Type-I) ($=\mu_0 H_{\mathrm{C}}$)	T
B_{C1}	Lower critical magnetic field (Type-II) ($=\mu_0 H_{\mathrm{C1}}$)	T
B_{C2}	Upper critical magnetic field ($=\mu_0 H_{\mathrm{C2}}$)	T
$B_{c2}(0)$	Upper critical field T=0 K	T
$B_{\mathrm{C2}}^*(T)$	Upper critical field as a function of T	T
$B_{\mathrm{C2M}}^*(\epsilon)$	Maximum value of the upper critical field	T
B_{C3}	Surface upper critical field	T
B_{Net}	Net magnetic field	T
$\bar{B}$	Average of the distribution of the magnitude of the magnetic field	T
B_{SF}	Magnetic self-field	T
C_0	Scaling parameter	A·T^{-1}
CnC	Copper to non-copper ratio	
d_{s}	Strand diameter	m
d_{eff}	Effective filament dimeter	m
d_{f}	Filament diameter	m
e	Electron charge	C
$\boldsymbol{E}$	Electric field	V·m^{-1}
E_{A}	activation energy	
f_{skin}	Frequency skin thickness	
f	Helmholtz free energy density	

Symbol	Description	Unit
f_n	Normal state free energy density	
f_tr	Transposition factor	
Δf	Amplifier inverse time-constant	s^{-1}
$F_\mathrm{P(v)}$	Volume pinning Force	N
F_Pmax	Maximum pinning force	
F_L	Lorentz Force	N
$\mathbf{H}$	Magnetic field strength	$\mathrm{A \cdot m}^{-1}$
h	Planck Constant	$\mathrm{J \cdot s}$
$\hbar$	Reduced Planck constant (Dirac constant)	$\mathrm{J \cdot s}$
I	Current	A
I_C	Critical current	A
I_C^E	Critical current density: E-field criterion	A
I_C^P	Critical current density: power criterion	A
I_C^{Off}	Critical current density: Offset criterion	A
I_C^ρ	Critical current density: resistivity criterion	A
I_m	Measured critical current at the temperature T_m	A
$\boldsymbol{J}$	Current density	$\mathrm{A \cdot m}^{-2}$
J_C	Critical current density	$\mathrm{A \cdot m}^{-2}$
J_C0	Maximum critical current density ($\boldsymbol{B} = 0\,T$)	$\mathrm{A \cdot m}^{-2}$
$J_\mathrm{C}^\mathrm{Eng}$	Critical current density: Engineering	$\mathrm{A \cdot m}^{-2}$
J_C^fr	Critical current density: Filamentary region	$\mathrm{A \cdot m}^{-2}$
J_C^sc	Critical current density : Superconductor	$\mathrm{A \cdot m}^{-2}$
J_S	Supercurrent density	$\mathrm{A \cdot m}^{-2}$
$\boldsymbol{J}_\mathrm{Tr}$	Transport current density	$\mathrm{A \cdot m}^{-2}$
k	Self-field correction term	$\mathrm{T \cdot kA}^{-1}$
k_B	Boltzmann constant	$\mathrm{J \cdot K}^{-1}$
l_MPZ	Length: minimum propagation zone	m
m_e	Free electron mass	kg
$\mathbf{M}$	Magnetisation	$\mathrm{A \cdot m}^{-1}$
M	Nuclear mass	kg
N	Filament number	-
n_s	Number density of superconducting pairs	

Symbol	Description	Unit
$n(B,T)$	Index of transition (power law exponent)	-
n_d	Turn density	m^{-1}
p	Pinning force fitting parameter	-
q	Pinning force fitting parameter	-
R	Resistance	Ω
R_i	Inner radius of the filament region of the strand	m
R_0	Outer radius of the filament region of the strand	m
R_{of}	Radius to the outermost filament	m
R_Min	Minor radius of a helix/ ring	m
R_Maj	Major radius of a helix/ ring	m
S_T	Separation of turns	m
T	Absolute temperature	K
T_C	Critical temperature	K
T_C0	Critical temperature at **B** = 0	K
T_F	Fermi temperature	K
T_m	Measured temperature of liquid helium bath.	K
u	Dependent variable	
t	$t = T/T_C$, Reduced temperature	-
V	Interaction constant	
V_rms	Voltage: root-mean-squared	V
z_n	z-position of turn *n*	m
α_a	Lorentz force correction term	T·A^{-1}
α_{in}	Inward Lorentz force correction term	T·A^{-1}
α_{out}	Outward Lorentz force correction term	T·A^{-1}
Δ_BCS	BCS energy gap	
Δf	Inverse time-constant of the amplifier	Hz
ΔM	Magnetisation hysteresis loop width	A·m^{-1}
κ	Ginzburg-Landau Parameter	
μ_0	Permeability of free space	T·m·A^{-1}
μ_r	Relative permeability	
ϕ_0	Flux quantum	T·m^2
χ	Susceptibility	-

Symbol	Description	Unit
ξ_{GL}	Coherence length	
θ	Phase of the order parameter	
θ_{D}	Debye temperature	K
Ψ	Ginzburg-Landau order parameter	
ω_{D}	Debye frequency	Hz
ρ	Charge density	$C \cdot m^{-3}$
ρ	Resistivity	Ωm
ρ_N	Normal state resistivity	Ωm
ρ_{SC}	Superconducting state resistivity	Ωm
ϵ_0	Vacuum permittivity	$F \cdot m^{-1}$
ϵ	Tensile state	-
Ω_{C}	Conductor conductivity	$S \cdot m^{-1}$
Ω_{N}	Insulating air	$S \cdot m^{-1}$
δ	Skin depth	m
λ_L	London Penetration depth	m
λ_{SC}	Fraction of the superconductor	--
σ_{H}	Hoop stress	
σ_b	Bundle conductivity	
σ_{SC}	Superconductor electrical conductivity	
λ_{SC}	Superconductor volume fraction	
σ_{m}	Matrix electrical conductivity	

Declaration and Statement of Copyright

I confirm that no part of the material offered in this thesis has previously been submitted by me for a degree in this or any other university. If the material has been generated through joint work, my independent contribution has been clearly indicated. In all other instances, material from the work of others has been acknowledged and quotations and paraphrases suitably indicated.

Francis Jerome Ridgeon

September 2019

Acknowledgement

Quotations

Rather than put these quotes with a specific chapter, I thought I could report them all here. These quotes amused, and at times inspired me to continue.

''If we wish to boast of our achievements,

let us not point to the unerring pursuit of truth by a

logically faultless thinking machine, but to the more

astonishing way in which truth can be caused

to emerge from the toils of error and stupidity.''

Sir Alfred Brian Pippard

"A man of genius makes no mistakes.

His errors are volitional and are the portals of discovery."

James Joyce

"The easiest way to solve a problem is to deny it exists."

Isaac Asimov

"Remember that all models are wrong;

the practical question is how wrong do

they have to be to not be useful"

Dr George E.P. Box

"Ah, there's nothing more exciting than science.

You get all the fun of sitting still, being quiet,

writing down numbers, paying attention…

Science has it all."

Principal W. Seymour Skinner

I dedicate this thesis to my friend, Dr Thomas Frawley, who had been a constant throughout my time here in Durham and sadly passed away as I was writing up. I threatened him that I did not want to have a dedication…

He helped me throughout the PhD. Not with the scientific content rather with the things I should have known about. His passion and interest were varied. He saw the world differently.

We walked aimlessly around the city of Durham, fording streams, and looking at nature and wildlife. We discussed problems, nothing was too trivial or sacrosanct. He had faith in my ability and thought that I should stick at the PhD as it as an amazing opportunity, that opens many a door.

Tom was intelligent, a skilled python user, and a good friend.

CHAPTER 1

1.   Introduction

Superconducting materials can be used to generate very large magnetic fields and offer advantages over normal conductors if they are in the superconducting state. Superconducting technologies can be characterised by their magnetic field strength at which they operate. Low magnetic field applications include magnetic resonance imaging (MRI), transmission cables, transformers and fault current limiters [1]. Medium magnetic fields are used in: ultra-light rotating machines; superconducting air-travel [2]; power applications in compact generators for wind turbines, and for energy storage in flywheel technologies [3]. High magnetic fields are used to bend high-energy beams in particle accelerators [4], investigating hydrogen properties in nuclear magnetic resonance (NMR).

To use a superconducting material in the superconducting state, it is necessary to characterise its behaviour and quantify its critical surface. The critical surface is a three-dimensional space, formed by the applied magnetic field B_{App}, temperature T, and transport current density J_{Tr}. Points above the surface are in the normal region, and below superconducting. For a fixed B_{App} and T, as the current density J is increased, at the critical current density value, J_{C}, the critical surface is crossed and the material becomes normal and resistive. The most important aspect for engineers designing superconducting systems is understanding the J_{C} behaviour [5]. A precise value of J_{C} enables improved confidence in operational parameters. It can be assumed that the properties of the superconducting strand are specific to the strand and intrinsic. Before winding a magnet system, short sample lengths of the superconducting strands are characterised. The strand properties are characterised using magnetisation and or transport measurements of the critical current density [6]. For both measurement types, a magnetic field is applied to the sample. A basic difference between transport and magnetisation measurements is the use of a transport current, which modifies the field penetrating the sample. Transport measurements of critical current density are dependent upon the current flow between the voltage contacts. The transport current is increased, while the voltage is measured, and a voltage-current characteristic is obtained. The central concept to this thesis is that there is an uncertainty in the value of magnetic field the strand is characterised, due to the magnetic field generated by current flow in a conductor when performing transport measurements.

The magnetic field generated by the current flow is referred to as the self-field, B_{SF}. The magnetic field dependence of the critical current density $J_C(B)$ measured using transport current is complicated due to the fact there is typically both an applied magnetic field and a distribution of self-field within the strand.

It has been argued that the magnitude of the self-field is small compared with the applied magnetic field [7] and that broadly it can be ignored [8]. Standardisation of the transport measurement method has enabled the self-field to be disregarded in comparisons of measurements of strands by different institutes [9]. An effort to further standardise test and evaluation methods for superconductors, minimising geometric effects, is ongoing [10]. When the self-field is considered, the equations for calculating the effect of self-field produce 'good results' that enable comparisons between measurement methodologies and strands of different diameters. The self-field correction used when reporting transport data can be prescribed, institutional, chosen for its simplicity, or historic. Relative to the precision of the transport measurement, with an instrumental uncertainty of ~0.1 %, interlaboratory differences of 3.5 % [11], the uncertainty due to the effect of self-field is of significant importance. In this thesis using experimental data, the literature self-field corrections are applied, compared, and reviewed.

The critical current density of three low-temperature niobium-titanium (Nb-Ti) superconducting strands was characterised as a function of magnetic field and temperature in this work. The experimental results presented in this thesis highlight differences in the measured J_C of an individual strand, dependent on the measurement geometry and orientation of the resultant Lorentz force due to current. The results highlight that the measurement geometry and technique result in an uncertainty in the value of the net field B_{Net}. Using finite element analysis (FEA) methods, the magnetic field distribution is calculated in the transport measurement experimental geometry. Distributions in the magnetic field were used to characterise and identify the relevant spatial dependence of the magnetic field to analyse the experimental data. With the Nb-Ti strand measured in four configurations (two geometries, and with the current direction relative to the applied magnetic field parallel and anti-parallel), $J_C(B_{\mathrm{App}})$ is compared with $J_C(B_{\mathrm{Net}})$, where the effect of self-field has been considered. Although the four data sets did not converge to a single $J_C(B)$ relationship, which defines the success of the self-field calculations, several important results were produced. Using results from the FEA, a linearised analytic model, and experimental data the four experimental data sets were described by a critical current density relationship for the strand that accounts for the effect of self-field. The problem of self-field correction is still open [12].

While the external field dependence of Nb-Ti can be described by empirical fits and parametrisation from experimentally determined material properties, the results from this thesis highlight how the high precision results have low accuracy. Although each strand is designed and optimised for use at its operational magnetic field, It is necessary to extend the applicability of Nb-Ti $J_C(B,T)$ fit to a wider range of field [13].

Nb-Ti is the dominant commercial superconductor with a 98% share of the market [14]. For fusion energy to be realised, more energy needs to be generated by the plasma, than used in the control of the reaction. The Nb-Ti strand characterised in this thesis was manufactured for the ITER poloidal magnetic field (PF) coil and is the type that is used to form a cable in conduit conductors (CICC). The CICC is a bundle of Nb_3Sn, Nb_3Al or Nb-Ti cabled together [15]. The ITER reactor uses a superconducting magnet system [16] and it is expected to produce more energy than it consumes. In work by Mitchell [17], the Head of the ITER Magnets Division, the difference between the measured critical current using conventional methods and the behaviour of cables, consisting of 1200 individual strands, is problematic. Samples quench at currents lower than expected from the performance of individual strands investigated. The use of short sample test to verify conductors and joint performance is valid if the results are interpreted accounting for the effect of self-field. As the strands are twisted during the manufacturing of the cable, during operation current flow along the strand moving in and out of the highest magnetic field region. Experimental measurements of the critical current over an extended range of magnetic fields enables the impacts of self-field to be interpreted and analysed, despite the conductor not designed to operate at those magnetic fields.

The structure of the thesis is shown in Figure 1.1, with arrows indicate the connections between chapters. Chapter 2 outlines the theories of superconductivity. Chapter 3 describes both the properties of Nb-Ti strand investigated, the design of the probe and barrel, and methodology for transport measurements. Chapter 4 is a study of the superconducting properties of the titanium alloys used to manufacture the measurement barrels used in this thesis. Chapter 5 presents the analytic calculations used to verify the results of the finite element analysis calculations. Chapter 6 presents the data and analysis of the experimental critical current density measurements, the FEA model, and finally the semi-analytic method used to derive a universal critical current relationship. Chapter 7, outlines and the main results from the thesis and possible extensions. The appendix provides additional information about the strand, probe, details of implementing the FEA methods, and outputs from the FEA calculation.
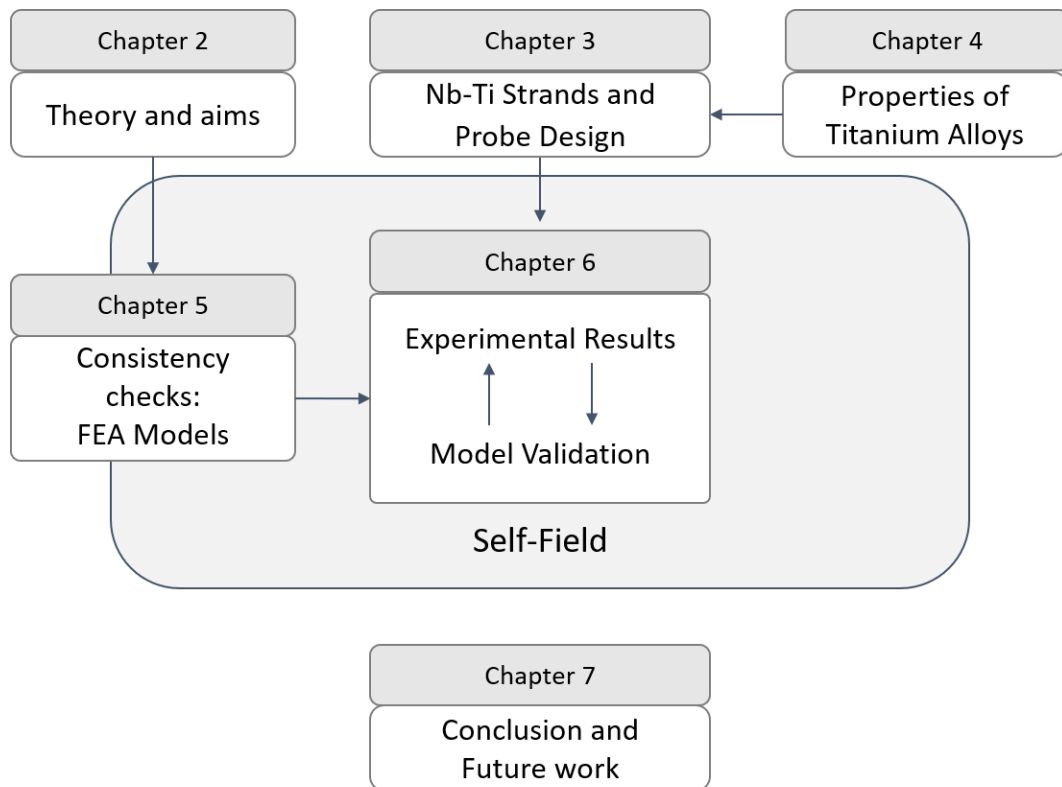
Figure 1.1 : Outline and structure of the thesis. The arrows indicate interrelated chapters.

References for chapter 1:

[1]   W. Paul, M. Chen, M. Lakner, J. Rhyner, D. Braun, and W. Lanz, "Fault current limiter based on high temperature superconductors - different concepts, test results, simulations, applications," *Physica C: Superconductivity and its Applications,* Article; Proceedings Paper vol. 354, no. 1-4, pp. 27-33, May 2001.

[2]   S. H. Kiruba *et al.*, "High power density superconducting rotating machines—development status and technology roadmap," *Superconductor Science and Technology,* vol. 30, no. 12, p. 123002, 2017.

[3]   W. Hassenzahl, "Will superconducting magnetic energy storage be used on electric utility systems?," *IEEE Transactions on Magnetics,* vol. 11, no. 2, pp. 482-488, 1975.

[4]   CERN. (2013, 21/05/2018). *The superconducting magnet of the big european bubble chamber (BEBC)* Available: http://cds.cern.ch/record/850617/files/

[5]   W. B. Sampson, "Procedures for measuring the electrical properties of superconductors for accelerator magnets," presented at the ICFA Workshop on Superconducting Magnets and Cryogenics, Brookhaven National Laboratory, 1986.

[6]   M. S. Lubell, "Empirical scaling formulas for critical current and critical field for commercial NbTi," *IEEE Transactions on Magnetics,* vol. 19, pp. 754-757, 1983.

[7]   P. Sunwong, J. S. Higgins, Y. Tsui, M. J. Raine, and D. P. Hampshire, "The critical current density of grain boundary channels in polycrystalline HTS and LTS superconductors in magnetic fields," *Superconductor Science and Technology,* vol. 26, p. 095006, 2013, Art. no. 095006.

[8]   M. Nannini *et al.*, "Characterization of industrial NbTi strands at variable field for JT-60SA toroidal field coils," *Fusion Engineering and Design,* vol. 84, no. 7, pp. 1404-1407, 2009/06/01/ 2009.

[9]   I. Pong *et al.*, "Worldwide Benchmarking of ITER Internal Tin Nb$_3$Sn and NbTi Strands Test Facilities," *IEEE Transactions on Applied Superconductivity,* Article; Proceedings Paper vol. 22, no. 3, p. 4802606, Jun 2012, Art. no. 4802606.

[10]   K. Osamura, "Standardization of Test Methods for Practical Superconducting Wires," *IEEE/CSC and ESAS European Superconductivity News Forum,* vol. 33, pp. 1-11, 2015.

[11]   A. Godeke *et al.*, "Interlaboratory Comparisons of NbTi Critical Current Measurements," *IEEE Transactions on Applied Superconductivity,* vol. 19, no. 3, pp. 2633-2636, 2009.

[12]   P. Fabbricatore and R. Musenich, B. Seeber, Ed. *Critical current measurements of superconducting cables by the transformer method* (Handbook of Applied Superconductivity). Bristol, UK: IOP Publishing Ltd, 1998.

[13]   P. Gislon, L. Muzzi, S. Chiarelli, A. Di Zenobio, M. V. Ricci, and M. Spadoni, "Electrical characterization of the NbTi strand for the ENEA stability SEx-up experiment," *IEEE Transactions on Applied Superconductivity,* vol. 13, no. 2, pp. 1429-1432, 2003, Art. no. 1211867.

[14]   P. J. Lee and D. C. Larbalestier, "Niobium-Titanium Superconducting Wires: Nanostructures by Extrusion and Wire Drawing," *Wire Journal International,* vol. 36, no. 2, pp. 61-66, 2003.

[15]   E. Salpietro, "Status of the ITER magnets," *Superconductor Science and Technology,* vol. 19, no. 3, p. S84, 2006.

[16]   M. Sborchia *et al.*, "Overview of ITER Magnet System and European Contribution," *IEEE/NPSS 24th Symposium on Fusion Engineering,* pp. 1-8, 2011.

[17]   N. Mitchell, "Steady state analysis of non-uniform current distributions in cable-in-conduit conductors and comparison with experimental data," *Cryogenics,* vol. 40, no. 2, pp. 99-116, 2/1/ 2000.

CHAPTER 2

2.   Critical Aspects of Superconductivity

This chapter outlines the phenomena and theories of superconductivity. The critical properties and the critical state model are described. The final section of this chapter outlines the effects of self-field and its relevance to magnet-system design and performance evaluation.

2.1.   Introduction

The liquefaction of helium (T = 4.2 K) in 1908, enabled measurements at lower temperatures than the previous cryogen hydrogen (T =20.3 K). In 1911 Onnes discovered that the direct current electrical resistance of mercury (Hg) wire drops to zero when its temperature is below 4.1 K shown in Figure 2.1 (a) [1]. Onnes received the Nobel Prize in 1913 for his investigations of the properties of matter at low temperatures. By 1914, Onnes had suggested the possibility of using superconductors for generating magnetic fields, a commercial application for this new state of matter [2].

Two properties define the superconducting state; the first is the ability to carry a dc electrical current without ohmic losses, observed by Onnes. The second property is the complete expulsion of magnetic flux from the bulk of the superconductor [3]. A magnetic field enters the bulk's interior up to a distance characterised by the penetration depth. The interior of the superconducting bulk is screened from external fields by surface currents and the electric field in the interior is zero. The penetration of the magnetic field was described by Meissner and Ochensfeld and is known as the Meissner effect [3].

Superconductors are characterised by their critical temperature, T_C critical current density, J_C, and an upper critical field, B_C or B_{C2} depending on superconductor type, above which the superconducting state cannot be retained. The volume below the surface shown in Figure 2.1 (b) corresponds to the superconducting materials niobium-titanium (Nb-Ti) and niobium-tin (Nb_3Sn), being in their superconducting state.

(a)   (b)
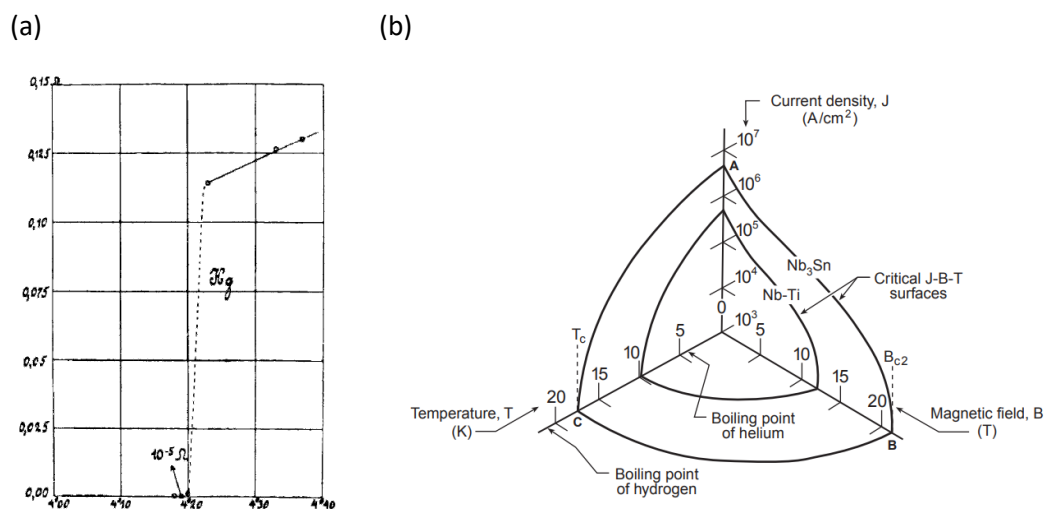
Figure 2.1 : (a) The resistivity versus temperature of mercury obtained by Onnes. Figure from Ref. [1]. (b) 3D critical *J-B-T* surface of two commercial Nb-based low T_C superconductors. Figure from Ref. [4].

2.2.   Superconductivity

Before the various theories of superconductivity are introduced, the discovery of the two types of superconductivity is outlined. The different theories of superconductivity progressively explained more of the phenomena associated with low-temperature superconductivity.

2.2.1. Type-I and Type-II Superconductors

In the presence of an applied magnetic field, two types of superconductors can be distinguished, generally referred to as type-I and type-II. In very low applied magnetic fields both types of superconductor are perfectly diamagnetic; a supercurrent flows without dissipation and generates a magnetic field that opposes and cancels the applied field in the interior of the sample. For a type-I superconductor [shown in Figure 2.2 (blue line)], the magnetic flux is perfectly shielded from the interior up to the thermodynamic critical field B_C at which the superconducting state is destroyed. The critical field B_C can be approximated by a quadratic temperature dependence [5].

For a type-II superconductor [shown in Figure 2.2 (red line)], above the lower critical field H_{C1}, fluxons penetrate the bulk. Details of fluxons will be outlined in section 2.2.2. When fluxons penetrate the bulk, this is called the mixed or Shubnikov phase. As the magnetic field applied to the bulk increases, the number of fluxon increases, at a point where the fluxons overlap completely at the second critical field H_{C2} the superconducting state is destroyed within the bulk and is restricted to the boundary.
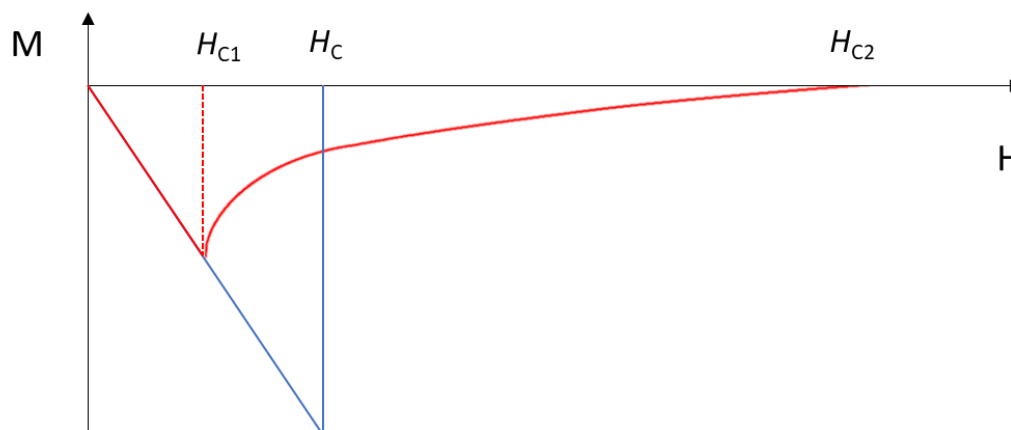
Figure 2.2 : Schematic magnetisation curves for Type-I (blue) below H_C the superconductor is in the Meissner state, above H_C it is a normal conductor. Type-II (red line) superconductors below H_{C1} the superconductor is in the Meissner state, above H_{C1} fluxons penetrate the superconductor, and is in the mixed, or Shubnikov state, at H_{C2} the superconducting state is destroyed.

The magnetic flux density **B** (T = N·A^{-1}·m^{-1}) is related to the magnetic field intensity **H** (A·m^{-1}) and magnetisation **M** (A·m^{-1}), through the susceptibility χ

$$\mathbf{B} = \mu_0 \mathbf{H} = \mu_0(\mathbf{H} + \mathbf{M}) = \mu_0(1 + \chi)\mathbf{H} \tag{2.1}$$

Where $1 + \chi$ is the relative permeability [μ_r (T·m·A^{-1})] of the material and holds for a linear relationship [6]. In the Meissner state, χ = -1. For type-II superconductors above H_{C1}, the magnitude of the magnetisation reduced as applied field increases.

The different types of superconductivity can be understood in terms of the surface energy associated with the boundary between the normal conductor and superconductor (NS) regions. The NS boundary energy can be either positive or negative depending on the dominant length scale. For positive NS boundaries, the boundary is stable. For negative NS boundary, interfaces are energetically favourable, as a result the superconductor split into as many domains as possible. The magnetic field penetrates the superconductor as fluxons, which will be outlined in section 2.2.2.

2.2.2. Fluxons

Abrikosov described the way magnetic field penetrates the bulk, maximising the surface area results in a region of normal material inside the bulk, a tube referred to as a fluxon. The fluxon has a non-superconducting normal core around which supercurrents circulate, shown in Figure 2.3. The magnetic field decays as the distance from the core increases and reduces over a length characterised by the London penetration depth. The radius (r) of the core is given by the coherence length (ξ).
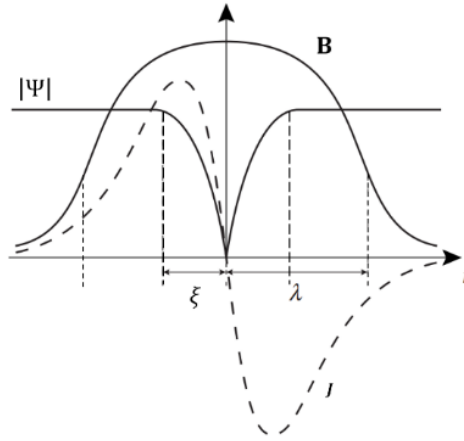
Figure 2.3 : The structure of an isolated fluxon, with supercurrents encircling the fluxon. The radial dependence of the order parameter $|\Psi|$ (length scales of the coherence length ξ) and magnetic field $\boldsymbol{B}$ (length scales of the penetration depth λ) and current density J.

For $r < \xi$ the order parameter Ψ is strongly suppressed. At the centre of the fluxon, the amplitude of the order parameter is zero. The integral of the magnetic flux over the volume gives the magnitude ϕ_0, the flux quantum. As the magnitude of the applied magnetic field is increased, the number of fluxons penetrating the sample increases.

2.2.3. London Equations

The London theory [7] (1935) is *phenomenological* and can explain the vanishing electrical resistivity, the Meissner effect, and distinguishes between a superconductor and a perfect conductor. Due to the screening currents inside the superconductor bulk, the magnetic field inside decays.

The characteristic decay length is the London penetration depth, λ_L,

$$\lambda_L \equiv \sqrt{\frac{m_{\mathrm{e}}}{\mu_0 e^2 n_{\mathrm{s}}}},$$

(2.2)

where m_{e} and e are the free electron mass and charge, μ_0 is the permeability of free space and n_{s} is the number density of superconducting pairs (assumed constant). The penetration depth is the characteristic distance that the applied magnetic field penetrates the superconductor and can be calculated from the lower critical field. In the two-fluid model of Gorter and Casimir, the number density of superconducting pairs is assumed to increase from zero at the critical temperature to the total electron density at T = 0 K [8].

2.2.4. Ginzburg-Landau Theory

The Ginzburg-Landau (G-L) theory (1950) [9] is *phenomenological* and uses Landau's theory of phase transitions. G-L theory is a macroscopic thermodynamic theory written in terms of an order parameter. Due to the symmetry of the order parameter, a great deal of the phenomenology can be accounted for without a full quantum mechanical description. The complex order parameter is defined:

$$\Psi = |\Psi| exp(-i\theta). \tag{2.3}$$

The phase is notated by θ. The modulus squared of the wavefunction $|\Psi|^2$ gives the density of superelectron pairs $n_s = |\Psi|^2$. The Helmholtz free energy density is expressed as a function of the order parameter near the transition between the normal and superconducting states. The Helmholtz free energy density takes the form

$$f = f_n + \alpha|\Psi|^2 + \frac{\beta}{2}|\Psi|^4 + \frac{1}{4m_e}|(-i\hbar\boldsymbol{\nabla} - 2e\boldsymbol{A})\Psi|^2 + \left(\frac{|\mathbf{B}|^2}{2\mu_0} - \frac{|\mu_0\mathbf{H}_0|^2}{2\mu_0}\right). \tag{2.4}$$

Where f_n is the normal state free energy density, $\hbar$ the reduced Planck constant, $\boldsymbol{A}$ the magnetic vector potential, and α and β are Taylor expansion parameters. The final term is the energy density of the magnetic induction field [10]. Minimising Eq. (2.4) with respect to the applied magnetic field, gives two coupled differential equations for the supercurrent density J_s, and the order parameter.

$$0 = \frac{1}{4m_e}|(-i\hbar\boldsymbol{\nabla} - 2e\boldsymbol{A})\Psi|^2 + (\alpha+\beta|\Psi|^2)\Psi \tag{2.5}$$

$$J_s = \frac{ie\hbar}{2m_e}(\Psi^*\boldsymbol{\nabla}\Psi - \Psi\boldsymbol{\nabla}\Psi^*) - \frac{2e^2}{m_e}\boldsymbol{A}\Psi^*\Psi \tag{2.6}$$

By minimising Eq. (2.4) with respect to the order parameter, in the absence of a magnetic field, a first-order ordinary differential equation is derived. Solving the ordinary differential equation, the coherence length, the spatial extent of the electron pair wavefunction (specific to $T < T_C$) is given by,

$$\xi_{GL} \equiv \sqrt{\frac{\hbar^2}{4m_e|\alpha|}} \tag{2.7}$$

where α is a coefficient in the non-trivial solution to G-L equation, with the simplification of no superconducting currents.

The ratio of the penetration depth and coherence length

$$\kappa \equiv \frac{\lambda_L}{\xi_{GL}},$$ (2.8)

is known as the Ginzburg-Landau parameter. The values of λ_L and ξ_{GL} are temperature dependent. κ is temperature-independent in G-L model, in the regions near T_C. The Ginzburg Landau parameter κ defines the type of superconductor. Superconductors with a value of $\kappa \leq 1/\sqrt{2}$ are "type-I", $\kappa > 1/\sqrt{2}$ are "type-II" superconductors. The value of κ varies from 0.03 for aluminium, to 60 for Nb-Ti, 94 for YBCO and 139 for Bi-2223[11]. From G-L theory, the thermodynamic critical field can be defined for a type-I superconductor:

$$H_C{}^2 = \frac{|\alpha|^2}{\mu_0 \beta}.$$ (2.9)

For type-II superconductors, due to the mixed state, the order parameter exhibits a second-order phase transition. From G-L theory an upper critical field is defined:

$$B_{C2} = \frac{\Phi_0}{2\pi\xi^2}.$$ (2.10)

where Φ_0 is the flux quantum, $\phi_0 = h/2e$ = 2.07 x 10^{-15} T·m^2.

2.2.5. Bardeen-Cooper-Schrieffer Theory

In 1957 Bardeen, Cooper, and Schrieffer (BCS) [5] provided a *microscopic* explanation of low-temperature superconductivity, jointly receiving the Nobel Prize in 1972. Understanding the mechanical or vibrational qualities of the crystal was an important step. The experimental evidence of the isotope effect, $M^\alpha T_C = constant$ [12], demonstrated that T_C was affected by the isotopic mass. Fröhlich proposed that the electron-phonon coupling is the origin of the attractive interaction between normal electrons near the Fermi surface[13]. For superconductivity, a net attractive interaction between electrons is necessary, the electrons within $\hbar\omega_D$ (where ω_D is the Debye frequency) of the Fermi surface, and the electrons feel a mutual attraction. Cooper in 1956 [14] showed that binding occurs in the presence of an attractive potential, no matter how weak. The electrons at the Fermi surface attract nearby lattice ions, through mutual Coulomb interaction, and this results in a local deformation of the crystal lattice. The lattice responds slower than the electrons

travel, as the Fermi temperature (T_F) is greater than the Debye temperature (θ_D). The accumulation of positive charge has the result of attracting negatively charged electrons towards it. The attractive force is mediated by the lattice distortion. The electrons pair off into integer-spin quasiparticles. The electrons act as a Cooper pair, typically pairing with opposite momentum and spins, resulting in a boson with zero spin. The integer-spin quasiparticles form a bosonic fluid, which can undergo a Bose-Einstein type condensation into a collective superfluid ground state.

The binding energy introduces an energy gap (Δ_{BCS}) between paired and unpaired states. At finite T, the critical temperature T_C is related to the excitation gap defined by a universal value,

$$\Delta_{BCS}(T = 0) = 1.764 k_B T_C \tag{2.11}$$

where k_B is the Boltzmann constant.

The critical temperature in BCS theory (for the weak coupling limit) is given by,

$$k_B T_C = 1.14 \hbar \omega_D \, exp(-1/N(0)V) = 2\Delta(0)/3.52 \tag{2.12}$$

where ω_D is the Debye frequency, $N(0)$ the density of states at the Fermi surface, and V the interaction constant.

The Nobel Prize in 2003 was awarded to Abrikosov, Ginzburg, and Leggett for showing that the macroscopic G-L theory can be derived from microscopic BCS theory at temperatures near the phase transition T_C. The combined theory is referred to as GLAG. The free parameters of Ginzburg-Landau theory can be equated to microscopic parameters.

2.2.6. High-Temperature Superconductivity

High-temperature superconductors (HTS) are unconventional, and their behaviour cannot be explained using BCS theory. The first HTS - lanthanum-barium-copper-oxide - was discovered in 1986 by Bednorz and Muller [15]. Several copper-oxide multilayer systems, the cuprates, have been found with high transition temperatures [16]. The two most widely commercialised superconductors are the first generation HTS bismuth-strontium-calcium-copper oxide (BSCCO, or $Ba_xLa_{5-x}Cu_5O_y$) and second-generation HTS yttrium-barium-copper-oxide (YBCO, or $YBa_2Cu_3O_{7-\delta}$).

Understanding the properties of the cuprates may be investigated by changing the hole concentration and mapping out the different phases. Under and over doping results in antiferromagnetic insulators and metal respectively. Between these phases, the cuprates become 'strange metals' with nonconventional Fermi surfaces [17]. In a range of hole concentrations and temperatures the cuprates superconduct. Quantum oscillations have been used to understand changes in Fermi surfaces to identify mechanisms for superconductivity [18]. The carriers (electrons or holes) within these copper oxide planes thought to be paired by a non-phonon mediated pairing mechanism. The precise mechanism of high-temperature superconductivity is still not known. Physicists have been "stumbling around in the dark for 30 years" trying to understand cuprates [18].

Another class of high-temperature superconductors are the iron-based layered superconductors, the pnictides and chalcogenides [19]. An important discovery in 2001 was of the intermediate temperature superconductor magnesium diboride (MgB_2) [20]. In 2015 metallic hydrogen sulphide set the record for highest T_C, with an onset temperature of 203.5 K [21]. Metallic hydrogen superconducts due to the light hydrogen atom, strong covalent bonds, and strong electron-phonon interaction.

2.3.   Critical Current Density

The critical current density is of interest as it is the most important superconducting parameter for magnet manufacturing. A confusing aspect of the word *critical* is that it is not a unique physical state when describing the current density in type-II superconductors. To understand the critical current density, the behaviour of fluxons with transport currents needs to be understood. The experimental data is analysed and further information about the strand derived, the methods used are outlined.

2.3.1. Microstructure

In engineering superconducting materials, impurities are useful and result in fluxon-defect interaction, which immobilises fluxons resulting in zero resistance. Stable unpinned fluxon-lattice configurations do not support a resistance-less transport current [22]. In a defect-free ellipsoidal isotropic superconductor, an ordered hexagonal lattice of fluxons is formed to maximise the separation between fluxons, a lower energy configuration than a random array [22]. The fluxons arrange due to repulsive interaction, between the magnetic field $\boldsymbol{B}$ of one vortex and the current density $\boldsymbol{J}$ present at the position of this field and arising from the other vortex. Imperfections such as defects, inclusions, voids, grain boundaries, are engineered by several methods including cold working and heat treatment. The critical current density depends on the type, size, and distribution of pinning centres. Fluxons interact with pinning centres, impeding fluxon movement, because the pinning centres

properties are different from the superconductor bulk. Flux lines are trapped in potential wells, due to the free energy difference between the matrix and its defects, and the flux profile does not relax homogenously throughout the interior. The type of interaction between fluxons and the pinning sites are dependent on the penetration depth, and flux-line spacing relative to the size and spacing of the pinning centres. The inter-flux-line spacing is the distance to the nearest neighbour in the hexagonal lattice, $a_0 = 1.07\sqrt{\phi_0/\mathbf{B}}$. If both the size and spacing of the pinning centres are greater than the penetration depth, the magnetic field can reach an equilibrium. When the size and spacing are less than the penetration depth, the magnetic field will assume an average value. If the system is closer to the critical temperature, the pinning forces become weaker. During magnetisation measurements, the fluxons sweep in and out of the bulk of the sample during each cycle around the hysteresis loop [23].

2.3.2. Lorentz Force

A finite supercurrent within the bulk imparts a Lorentz force, F_{L} from the fluxons onto the pinning sites [24]. The equation to describe the force is like the Lorentz force of electrodynamics and can be defined either as

$$F_{\mathrm{L}} = \begin{cases} \boldsymbol{J} \times \boldsymbol{\phi}_0 & \text{force per unit length} \\ \boldsymbol{J} \times \boldsymbol{B} & \text{force per unit volume} \end{cases} \tag{2.13}$$

where $\boldsymbol{J}$ is the spatially averaged supercurrent density, $\boldsymbol{\phi}_0$ is a vector of magnitude ϕ_0 in the direction of the flux line and $\boldsymbol{B}$ is the flux density due to the number of flux lines per unit area ($n\phi_0$) [24]. The force is perpendicular to both the current and the applied magnetic field shown in Figure 2.4 (a). The flux lines interact with the defects, in the critical state model, outlined in Section (2.4) the Lorentz force acts in opposition to the pinning force.

Flux pinning exerts an attractive volume pinning force. The critical current density can be derived by equating the Lorentz force to the maximum pinning force F_{P}. The required force to extract a fluxon from a defect can be used to calculate the volume flux pinning force, where the force is defined [25]:

$$\boldsymbol{F}_{\mathrm{P}}(B) = -\boldsymbol{J}_{\mathrm{C}}(B) \times \mathbf{B}. \tag{2.14}$$

It was observed that Nb-Ti data obtained at different temperatures and strains, can be mapped onto a single universal curve, by plotting the ratio of the pinning force to the maximum value i.e., $F_{\mathrm{P}}/F_{\mathrm{Pmax}}$ against the reduced field $b = B/B_{\mathrm{C2}}(T)$ [26].

(a)   (b)
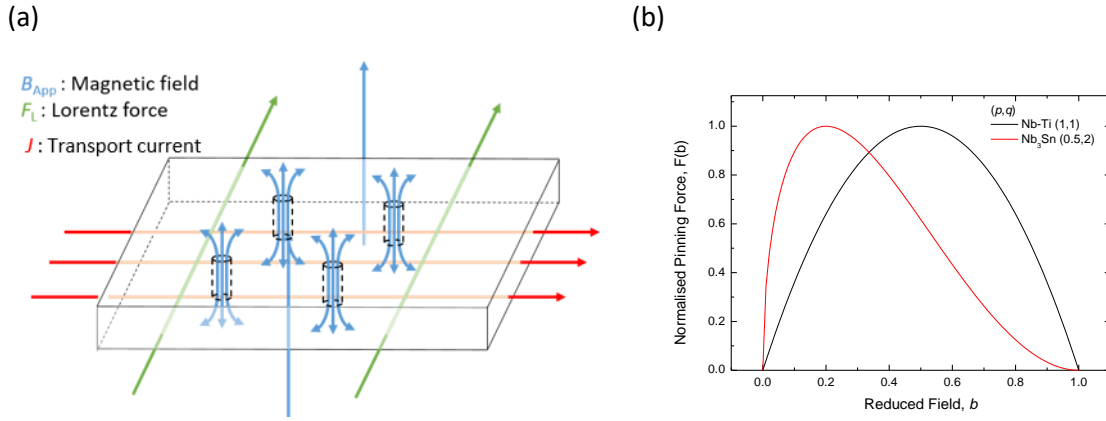
Figure 2.4 : (a) Representation of a fluxon lattice in a type-II superconductor. Transport current (red arrows), magnetic field (blue arrows), and Lorentz force acting on the fluxon array (green arrows). (b) The reduced field dependence of the volume pinning force for Nb_3Sn and Nb-Ti conductors with a peak in the pinning force at different reduced field values.

The magnetic field and temperature dependence of the volume flux pinning can be described by a unified scaling law of the form

$$F_P = Cf(b) \propto b^p(1-b)^q, \qquad (2.15)$$

where C is a constant, and $f(b)$ the field dependence of the volume pinning force. The p and q are fitting parameters, and b the reduced field. Measurements of $J_C(B_{App}, T)$ enable the interpretation of the pinning mechanisms. The values of the exponents p and q values are particular to the pinning centres with different interaction types and geometries [27]. The parameter p is related to the pinned length of flux lines per unit volume. The parameter q is related to the field dependence of the superconducting order parameter. Nb-Ti typically has p and q values of 1 [28], which indicates volume pinning is the dominant mechanism and the flux line lattice is plastic. Nb_3Sn typically has values of p = 0.5 and $q = 2$ [28] which indicate pinning is due to the elastic flux line lattice. The reduced field dependence of two Nb-based conductors is shown in Figure 2.4 (b).

2.3.3. Flux Flow

For current densities above the critical current density, pinning cannot counteract the Lorentz force, fluxons move and the material enters the flux flow regime [29]. Fluxons in constant motion generate an E-field and dissipate this energy as heat. The relationship between external current and fluxon velocity has a viscous drag term, giving the flux flow resistivity. The electric field current density (E-J) characteristics of the flux flow region are approximately linear ($\rho \propto b$) where b is the normalised critical field [30].

When there is no pinning, the fluxon velocity can be calculated from the applied current. For materials with pinning sites, the effects of pinning and the topology of the pinning sites need to be considered. For some conductors, the pinning sites are localised (e.g., defects), whereas for other conductors the pinning sites stretch across the entire sample (e.g., grain boundaries). Most technological superconductors used in large scale applications are polycrystalline, and the grain boundary structures strongly affect flux distribution in superconductors and limit J_C [31]. The grain boundaries provide channels for flux flow, a lower resistivity path. The flux flow mechanism is important in both low-temperature superconductors (LTS) and HTS materials [32].

2.3.4. Flux Creep

Flux creep is the thermally activated motion of groups of flux lines over the energy barriers arising from pinning. When energy (thermal, electrical, or magnetic) is supplied, there is a statistical probability that the fluxon will overcome the pinning force and will move through the superconductor under the influence of the Lorentz force. The fluxons hop into adjacent wells. Transport current modifies the effective depth of the barriers. To a first approximation, the Anderson-Kim model assumes that the barrier height reduces linearly with current. Flux creep driven by thermal energy can be described by Boltzmann law, with creep rate proportional to $\exp{(-\Delta E_A / k_B T)}$. The probability is dependent on the activation energy E_A relative to the product of the Boltzmann constant k_B and temperature T. With thermally activated depinning, although the barrier height is constant, as the temperature increases, fluxons are more energetic there is an increased probability of crossing the barrier.

2.3.5. Quantification of the Critical Current

The determination of the critical current density is dependent upon the criterion used to define it [33]. With a continuous E-J transition, it is necessary to define a criterion above which the superconductor is said to have stopped superconducting. The criterion selected is dependent on the measurement technique, and the intended use of the results. The numerical value of the criteria is dependent on the dominant dissipative regime, typically the thermally activated flux creep [34]. The most practical and useful technique for quantifying critical current densities are transport measurements [4].

The different critical current criteria are summarised schematically in Figure 2.5. The electric field (I_C^E) criterion, is the standard used in the reference laboratory and is used in this work. The E-field criterion is defined at a value above the baseline noise. The resistivity criterion, (I_C^ρ) is most commonly used in magnet engineering experiments [4]. The critical current is defined by the intersections of the sloped line from the origin to the intersection of the E-I curve. The slope is given by the resistivity criterion
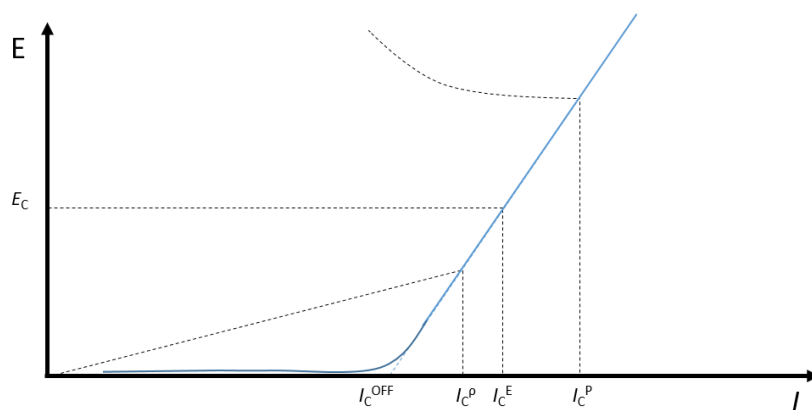
Figure 2.5 : Schematic of a typical E-I plot for a type-II superconductor, with the various criteria used to determine the critical current (I_C I_C) compared. The dashed horizontal line is the electric field criterion E_C used in this work.

and is specific to magnet applications; values of 10^{-14} to 10^{-15} Ωm are typically used. At high-applied magnetic fields, the resistivity criterion is limited by the sensitivity of the measurement of voltage. The offset criterion, (I_C^{OFF}) takes a tangent to the ($V - I$), curve at an E-field criterion. The intersection with zero volts gives I_C. As the material becomes ohmic, I_C tends to zero. The offset criteria were reported in several papers [35]. Another less commonly used criterion is the power criterion (I_C^P), (the product of current and voltage). The typical power criterion used is 10^4 W·m^{-3}. The power criterion is used because of its applicability to heat removal.

A non-criterion-based definition of the critical current ($I_{C,surfB}$) was presented in recent work [36]. The criterion is not a fixed value, but stated for each experimental measurement, at the threshold of dissipation. The author claims that at the point of dissipation in their experiment, the current distribution becomes uniform [36]. The difficulty in using a minimum detectable voltage is that the sensitivity of the experimental equipment will affect the value.

2.3.5.1.　Strand Areas

For the chosen criterion, a strand can have a well-defined critical *current* determined experimentally. However, to calculate the critical current *density*, the measured critical current and the relevant cross-sectional area (perpendicular to the current direction) are required. For an engineering parameterisation, the strands total cross-section (A_{Eng}) is used, the superconductor and the matrix. The superconducting critical current density, J_C^{sc} considers the current flow in just the filaments, resulting in the highest values of J_C. The uncertainty in the measurement of the strand diameter (d_s) can be due to the variation along its length, uncertainty in the strands circularity, and user error.

Parametrisation	Notation	Area [×10^{-7} m^2]
Engineering	J_C^{Eng}, A_{Eng}	4.254 ±0.003
Superconductor	J_C^{sc}, A_{sc}	1.596 ± 0.003

Table 2.1 : Summary of the criteria, notation, and areas for calculating current density. Typical values for a Nb-Ti ITER PF type 1 conductor.

For this work, the diameter of the strand was measured at five points along its length, and ten angles around the circumference of the strands. With the 50 data points, an average value was calculated, and the measurement uncertainty of 1 µm. To calculate the area of the superconducting filaments, in addition to d_s, the copper to non-copper (CnC) ratio is required:

$$A_{\text{sc}} = \left(\frac{\pi d_s^2}{4} \frac{1}{CnC} \right),$$
(2.16)

Table 2.1 summarises the criteria, notation and the values used in this work. The details of the CnC ratios are outlined in section 3.2.1. The uncertainty in the CnC value is ± 0.005. Further details of the strand and measurement procedure are outlined in A.1.

2.3.5.2.   Scaling Laws

Scaling laws are useful for engineering applications, and can be used to understand the underlying properties [37]. From a limited experimental data set, the performance of a strand can be determined. If the scaling law parametrises the experimental results, it is possible to calculate critical current densities at temperatures and values of applied magnetic fields outside of the measured range. An issue with scaling laws is that they may have limited applicability; the conductor may be superconducting when the extrapolation of the parameterisation suggests that it is not [38].

2.3.5.3.   *E-J* Relation and Index of Transition

The $E\text{-}J$, or equivalently the voltage-current ($V\text{-}I$), curves of real materials are described by several empirical equations. Most commonly, $E\text{-}J$ can be described by a power-law dependence, relating the electric field to the current density [39]:

$$E = \text{E}_\text{C} \left| \left(\frac{J}{J_\text{C}(B,T)} \right)^{n(B,T)} \right|.$$
(2.17)
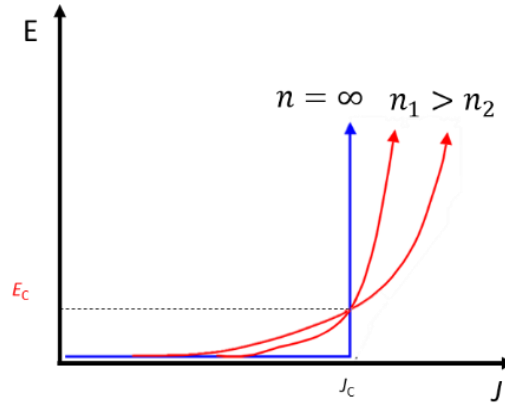
Figure 2.6 : Schematic of the *E-J* characteristic of a high-current superconductor as a function of the index of transition (*n*). A larger *n* value increases the gradient.

The index of transition $n(B, T)$ describes the sharpness of the transition. The n-value is an indication of the pinning strength, with higher values usually indicating better pinning and the homogeneity of the strand. The n-value characterises the entire conducting path and includes the stabilising materials. To define the n-value from experimental data, the gradient of the E-J transition is calculated

$$n = \frac{\partial(\log \mathrm{E})}{\partial(\log J)},$$
(2.18)

between two values of *E*-field, typically 10 or 100 µVm⁻¹. A schematic of E-J transitions with different n-values and identical J_C values are shown in Figure 2.6. Experimentally n-values are greater than 20 for HTS and can exceed 50 for LTS [40]. The low n-values in HTS is often attributed to thermally activated flux creep [41]. In a transition, if the heat transfer to the cryogen bath is lower than the heat generated, the increase in temperature can result in a higher n-value and a reduction in J_C [42]. The limits of the power-law are $1 \leq n \leq \infty$. The limit $n \rightarrow 1$, corresponds to the linear Ohm's law, and $n \rightarrow \infty$ corresponds to Bean's critical state model (section 2.4.1). For the infinite n-value, the electric field is multivalued for a single value of J [43].

The relationship between the n-value and I_C has been parameterised [44] using a modified power law of the form:

$$n - 1 = r(I_C)^s.$$
(2.19)

The parameters r and s are fitting parameters, and in principle are a function of temperature and strain [44]. The relationship is empirical, and the I_C is not uniquely correlated with the n-value.

2.4.   Critical State Models

Several phenomenological models, known as critical state models (CSM), describe the gradient of the magnetic flux density within a sample and how it changes with the applied magnetic field or current. The central idea is that the pinning force *exactly* matches the Lorentz force. The critical current density is always at its maximum possible value or zero.

2.4.1. Bean's Model

The original CSM is Bean's model [45, 46]. The first assumption in Bean's model is that the electric field E is parallel to the current density J. The second assumption is that the current density J take the values $\pm J_C$ or zero (where J_C is field and temperature-*independent*). Bean's model predicts an infinitely sharp E-J transition. Below the critical value, the electric field generated by the superconductor is zero until J_C where it becomes infinite. Although Bean's model assumed J_C is independent of B, it is used to analyse magnetisation measurement data, and is a reasonable approximation and description of the hysteresis. Type-II superconductors with flux pinning exhibit irreversible behaviour, with upper and lower magnetization plateaus. The Bean's model is applicable if the superconducting materials are homogenous [47].

When a magnetic field is applied to a superconducting sample in the mixed state, the field penetrates and shielding currents flow. The lossless current flowing induces a magnetic moment, shielding the bulk from the applied magnetic field. Considering the system on the macroscopic scale, the spatial gradient of the field is limited by J_C, following Ampère's law, the gradient in the magnetic field in the bulk is of magnitude $\mu_0 J_C$. Magnetic flux penetrates the superconductor until the local value equals the critical value. Reducing the applied magnetic field results in a change at the material surface, the average magnetic field inside the superconducting bulk is higher than the external applied magnetic field. The magnetic flux is trapped inside the superconductor bulk, even at B_{App}= 0 T. Flux shielding occurs when the average field is less than B_{App}; trapping is when the average field exceeds B_{App}. The magnetisation determines the difference between the applied magnetic field and the average internal magnetic field.

A schematic of the field profile, due to the field ramping for an infinite slab geometry is shown in Figure 2.7 (a) Above the lower critical field $\pm H_{C1}$, flux penetrates the sample (i- v). When the field is reduced (vi-ix), opposite surface currents flow and a characteristic 'M' shape in the magnetic field profile occurs, with shielding currents of equal magnitude flowing in opposite directions. For fields (x-xi) there is a trapped remnant magnetic field.
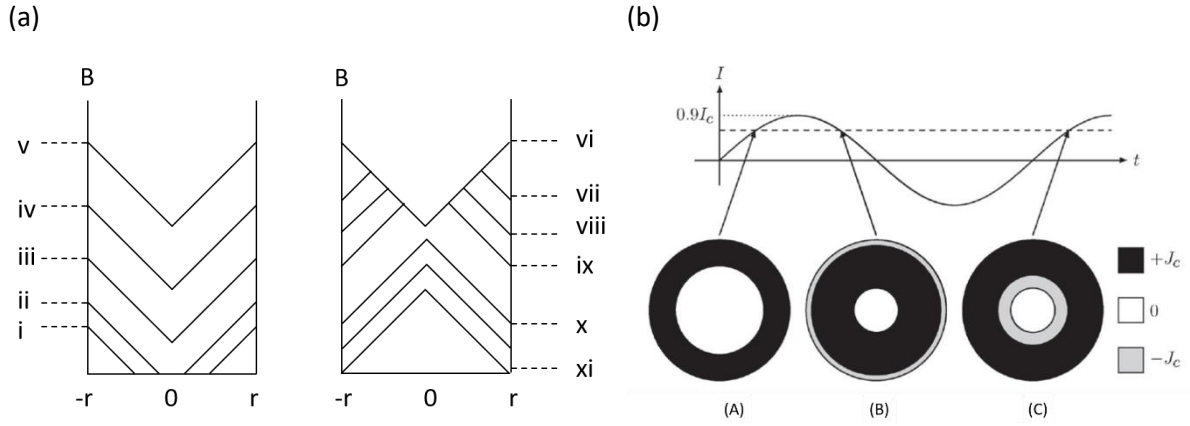
Figure 2.7 : Schematic of the profiles of the magnetic field inside an infinite superconductor for the Bean model (a) Infinite slab geometry: the applied magnetic field is increased from i-v and the field decreases from vi-xi. After the field is cycled, fluxons are trapped inside the superconductor. (b) Circular infinite wire with sinusoidal transport current in zero applied magnetic field. The current distribution at $I = 0.6I_C$ (A) initial ramp-up (B) ramp down, and (C) second ramp. Figure adapted from Fig. 3 in Ref. [48].

The differences in the current density for a virgin sample, and when a transport current has been imposed, for $B_{\mathrm{App}} = 0$ T, is shown in Figure 2.7 (b). The circular conductor is assumed to be infinite in the z-direction. Considering more than one period of a sinusoidal transport current results in current distribution with both $\pm J_C$ inside the circular conductors. The distribution (A,B,C) shown in Figure 2.7 (b) are for a current value $I = 0.6\ I_C$. For (A) the current flow is in one direction (+) and flows in the outer ring of the conductor at J_C. At time (B) the current direction is reversed, and current ($-J_C$) flows in the outer skin. At the time (C) the magnitude of the transport current is identical to time (A) the current profile is different with a larger part of the cross-section having a current flowing at J_C due to the magnetic history. At time (C) Some current flowing at J_C in the interior. As the current density is varied to a maximum value of less than J_C, the current does not penetrate fully into the cross-section. For this geometry, $\boldsymbol{B} = 0$ where $\boldsymbol{J} = 0$.

2.4.2. Magnetisation Measurements

The magnetic moment of a superconductor is proportional to its critical current density and is determined by sample geometry and magnetisation history [49]. Assuming that the magnetic field is fully penetrated and J_C is constant through the entire sample volume, the magnetic field inside the conductor, relative to the applied field gives the sample's magnetisation.

The magnetisation is given by the volume integral,

$$\boldsymbol{M} = \frac{1}{2V} \int_V (\boldsymbol{r} \times \boldsymbol{J})dV. \tag{2.20}$$

The magnetisation per unit volume of a stand under a transverse applied magnetic field can be measured by cycling the field, up to a value of several tesla, and back down again. The change in magnetisation or magnetisation width ΔM, is the difference between the upper and lower plateau, which are a result of the forward and reverse sweep branches [50]. For a strand coiled helically, with the long axis perpendicular to the magnetic field, the magnetisation critical current is given by the width of the magnetisation loop:

$$I_{\mathrm{C}} = J_{\mathrm{C}}^{\mathrm{M}} A_{\mathrm{SC}} = \frac{3\pi \Delta M}{2\lambda d_f},$$ (2.21)

where d_f is the filament diameter [50]. The volume of superconductor in the stand is derived from the copper to non-copper ratio $\lambda = [CnC + 1]^{-1}$. The copper to non-copper ratio will be defined in section 3.2.3. Analysing the data using ΔM is the standard [51]. The background magnetisation, due to the Nickel plating, has not been removed in the data, which is typical for these sorts of measurements [52].

The $J_{\mathrm{C}}(B)$ of a strand is typically interpolated, with magnetisation measurements providing low-field ($B_{\mathrm{App}} > 100$ mT) high-current region [51, 53], and transport measurements providing the high-field, low-current region data [54]. At very small B_{App} the superconducting filaments are perfectly diamagnetic (in the Meissner state), and the CSM cannot be used [55]. It is not typical to measure J_{C} at high B_{App} using magnetisation measurements due to the systematic errors associated with magnetic field inhomogeneities [51].

2.5.   Self-Field

An issue when measuring the critical current density of Nb-Ti strands is that a spatially variant self-field (B_{SF}) is generated by the current as it flows through the superconductor [56]. As the superconducting strand critical current density is magnetic field dependent, the uncertainty in the magnetic field is problematic. The net magnetic field ($\boldsymbol{B}_{\mathrm{Net}}$) is the vectorial sum of the applied field ($\boldsymbol{B}_{\mathrm{App}}$) and the self-field ($\boldsymbol{B}_{\mathrm{SF}}$):

$$\boldsymbol{B}_{\mathrm{Net}} = \boldsymbol{B}_{\mathrm{App}} + \boldsymbol{B}_{\mathrm{SF}}.$$ (2.22)

The experimentalist can control $\boldsymbol{B}_{\text{App}}$which is *ideally* homogeneous, but in practice it is not. As $\boldsymbol{B}_{\text{SF}}$ is inhomogeneous in the strand, the multi-valued $\boldsymbol{B}_{\text{Net}}$ results in non-uniform current densities [57]. Correcting data to account for the effect of self-field is useful in quality control and purchase specifications, and when comparing short sample data with magnet performance [58]. Extrapolation of critical current density data without a self-field correction can result in large errors [59].

Due to the $\boldsymbol{B}_{\text{App}}$ transport measurements are performed at, and the currents used, the effect of $\boldsymbol{B}_{\text{SF}}$ is typically neglected due to its magnitude [54, 60, 61]. When the effect of self-field is considered it is usually taken as the peak value in $\boldsymbol{B}_{\text{Net}}$ distribution. If the data is not corrected for the effect of self-field correction, larger strands will appear to carry proportionately lower current. In chapter 6, using experimental data and the peak in $\boldsymbol{B}_{\text{Net}}$, the applicability of using the peak in $\boldsymbol{B}_{\text{Net}}$ to account for the effect of self-field is discussed. With the extensive measurements of $J_C(\boldsymbol{B}_{\text{App}})$in chapter 6 the effect of self-field is highlighted, at low $\boldsymbol{B}_{\text{App}}$. Using results from the FEA calculations - the magnetic field distribution statistics - and numerical model it was possible to account for the effect of $\boldsymbol{B}_{\text{SF}}$.

2.5.1. The Origin of Self-Field

The Biot-Savart law, established in the 1820s, is the central equation that relates the current to the magnetic field and can be written

$$d\mathbf{B} = \frac{\mu_0 I}{4\pi}\frac{(\text{d}\mathbf{S} \times \hat{\boldsymbol{r}})}{r^2} = \frac{\mu_0 I}{4\pi r^2}\sin\theta\ \text{dl}\ \widehat{\boldsymbol{\theta}}, \tag{2.23}$$

where $d\mathbf{B}$ is the magnetic field of a current element, $\text{d}\mathbf{S}$ an element of length in the direction of current flow I. The distance from the current element to the point the magnetic field is calculated at point (*P*) is r and the unit vector, $\hat{\boldsymbol{r}}$ points from $\text{d}\mathbf{S}$ to *P* is shown schematically in Figure 2.8. The second form of Eq. (2.23) is the magnitude of the magnetic field. The angle θ is between the current element and the unit vector. The unit vector $\widehat{\boldsymbol{\theta}}$ is the angular direction. The Biot-Savart law is fundamental, and the relationship gives several analytic solutions for steady-state magnetic phenomena that are textbook exercises [62].

2.5.2. Correction Factor

Two methods to correct the experimental data, for the effect of self-field using shown schematically in Figure 2.9. The first method fixes the value of J_C, whereas in the second method, the value of the magnetic field is fixed. For a fixed experimental J_C the self-field correction factor $\Delta\boldsymbol{B}$, that
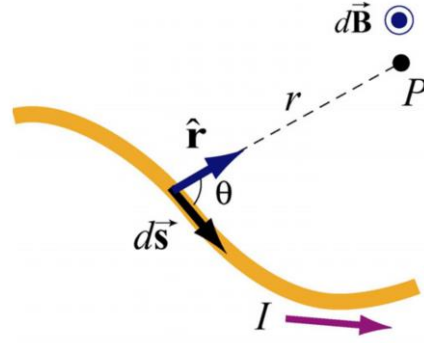
Figure 2.8 : Schematic of the Biot-Savart Law. At point P at distance r the magnetic field element $d\mathbf{B}$ due to the current-carrying element I d$\mathbf{S}$.
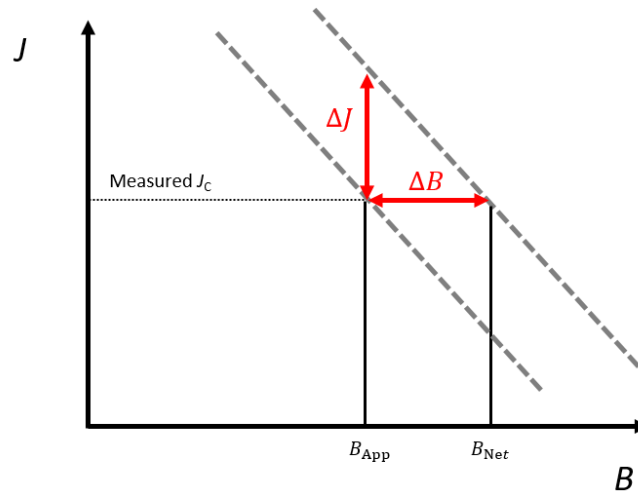
Figure 2.9 : Schematic comparing two methods of self-field correction. An increase in the magnetic field ($\Delta \mathbf{B}$) an increase in the current density ($\Delta \mathbf{J}$). The two dashed lines indicate the functional form of $J_C(\mathbf{B})$. Figure is modified from Ref. [63]

characterises the spatially varying self-field, is added vectorially to $\mathbf{B}_{\text{App}}$. For a fixed B, the functional form of $J_C(\mathbf{B}_{\text{Net}}) \equiv J_C(\mathbf{B}_{\text{App}})$ are assumed similar, and a correction factor $\Delta \mathbf{J}$ is added to the measured J_C. Both methods "seem to be valid" [63]. In this thesis, both methods are considered. $\mathbf{B}_{\text{SF}}$ is calculated and added to the applied field, Eq. (2.22), and the J_C is evaluated at a fixed value of $\mathbf{B}$.

2.5.3. Measuring Magnetic Fields

It is possible to use a Hall sensor (HS) array to measure $\mathbf{B}_{\text{Net}}$. From Eq. (2.22), it is possible to quantify $\mathbf{B}_{\text{SF}}$ at the point of the Hall probe. Early work in the literature used a hall sensor array, and the magnetic field gradient over the cross-section was confirmed with variations in the V-I measurements [64]. However, the accuracy of the method is low, with a 3% error in self-field measurement [65]. Even though the magnetic field can be measured, how this characterises the spatially varying self-field is unclear. In this thesis, the distribution of the magnetic field inside the volume of the strand was used to quantify the self-field correction.
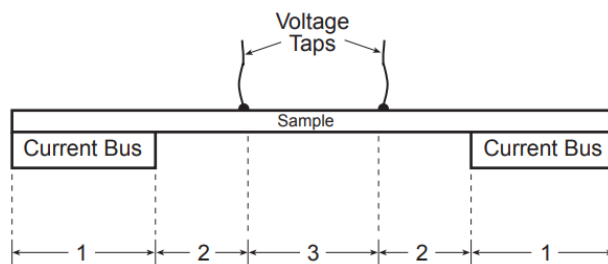
Figure 2.10 : Schematic of Voltage taps. Length 2 is the separation between the current supply and the voltage tap is defined by the strand being measured. Length 3 is the voltage tape length. Figure from Ref. [4].

2.5.4. Current transfer lengths

When current enters a multifilamentary superconductor it transfers through the normal material, and voltages can be generated. The current transfer length is shown schematically in Figure 2.10. A minimum separation length between the current contact and voltage tap is necessary to ensure that current fully transfers to the filaments before the voltage tap. Depending on the geometry it is easy to increase the contact length and separate voltage and current contacts, resulting in negligible current transfer voltages. A simplified analytic formula suggests the transfer length of about seven strand diameter is needed for Nb-Ti[66]. As the central 500 mm of the ~1.6 m length of strand is measured the transfer length is sufficiently long for any effects to be minimised. Experimental measurements of Nb-Ti in the literature [67] suggests that current transfer lengths were immeasurably small.

2.5.5. Geometric Effects

There are two length scales to consider when investigating the effects of geometry on the self-field: those due to measurement and those due to differences of the superconductor being measured. The focus of this thesis is the effects of coil measurement geometry, with the same strand measured in different orientations. The conductors investigated in this thesis are commercial Nb-Ti strands with identical structure and manufactured with identical processes. The properties of the Nb-Ti strand characterised are detailed in Chapter 3.

2.5.5.1.   Measurement Geometry

The effect of measurement geometry on the measured critical current, at low E-fields, is shown in Figure 2.11. The different I_C are measurable for long and short straight conductors, hairpins, and coils. At higher E-fields the effects of geometry on I_C are smaller. A difference of 83 A between the short sample and coil for the E-field criterion 0.1 $\mu V \cdot cm^{-1}$ (10 $\mu V \cdot m^{-1}$) is calculated from Figure 2.11.
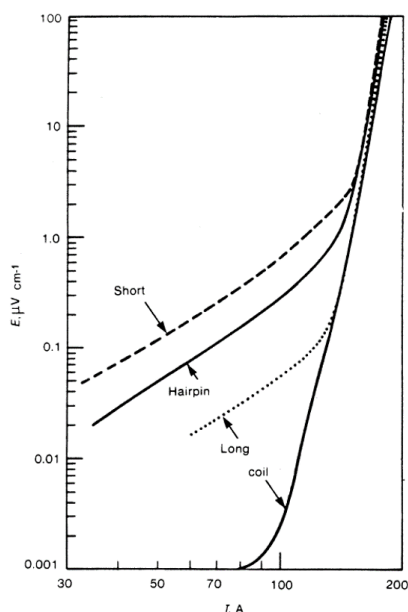
Figure 2.11 : E-I experimental data quantifying the effect of measurement geometry. Figure modified from Ref. [68].

Long lengths of commercial Nb-Ti strands are usually measured using the coil geometry, to increase the volume measured and the electrical signal [69]. A coil shape is an ideal configuration since it allows a long strand length to be tested in a confined space of a high-field solenoid magnet [70]. The length of the strand measured on coils makes it possible to have long contact lengths. The pitch of the helical sample holders ensures that the sample is in a homogenous part of the solenoidal magnet [69]. The measurements made in this thesis are coiled samples, on the ITER VAMAS barrel, which will be described in detail in section 3.4.1.

Because the strand is wound in a coil, the current flow in the strand generates a magnetic field in the centre of the coil. In the literature, it is assumed that the sample measured in a coil can be considered as infinitely straight, with effects due to measurement as a small percentage (1~2 %) correction [71].

For the hairpin geometry and straight wire geometry, the magnetic field is zero at the centre of the strand and increases linearly with radius. Due to the limited length of the perpendicular magnetic field, current redistribution reduces the achievable voltage resolution, in short straight, or hairpin samples.

2.5.5.2.   Conductor Geometry

For self-field characterisation, the architecture of a multifilamentary strand needs to be understood. Work by Stenvall found that the self-field generated depends on the structure and number of filaments and their position [72]. The resultant self-field field distribution depends upon the level that

the heterogeneities are modelled. The geometric complexity of the model considered is limited by computational resources.

Self-field measurement of HTS J_C i.e., without an applied magnetic field *are* used for quality control. The shape and dimensions of the sample affect the self-field [57, 73]. Flattening a YBCO tape increases the aspect ratio resulting in a different self-field distribution and therefore measured J_C[57]. It has been suggested that the reduced critical current density of YBCO with increasing thickness may be a result of the self-field [57].

2.5.6. Importance of Self-field

Achieving stable, efficient, high magnetic fields using superconductors is the technological and economic driver for material development. Magnetic self-field corrections are important when transport currents are high, for example when conductors operate at 1.9 K. As the current carrying capacity increases, the resultant self-field increases. Self-field measurements can be used to investigate fundamental aspects of superconductivity, in addition to understanding magnetic systems.

2.5.6.1. Performance Evaluation

The performance of the magnet system is calculated from short sample strand characterisation. Accurate short sample measurements are key to cable development and accurate analysis of coil and magnet performance [74]. Self-field corrections facilitate comparison of data between short-sample predictions and magnet performance [75]. The critical current and n-value of a cable are influenced by the self-field of the cable, which can be understood by comparing the electrical characterisation of the cable with the strands it is made from [42]. Comparisons of strand and cable performance highlight how using the local peak magnetic field results in a discrepancy, of 7-12 % depending on the direction of B_{App}. The paper also found degradation due to mechanical processing results in a local reduction of I_C [60].

2.5.6.2. Strand Performance

The behaviour of the short strands measured in the laboratory is different from the strand's behaviour in the wound magnet. Strands are characterised in a well-defined magnetic field profile. When characterising the strand in the lab, the transport current is ramped at a constant rate, whereas when the magnet is energised, each strand experiences a dynamic magnetic environment.

When the strands are cabled, the individual strands are in different magnetic field environments. The self-field from both the strand of interest and the other strands and the external field needs to be

considered. The comparison of the cables performance with the strand's measurement is complex due to the heterogeneities of the environment the strand is in within the cable. A major source of the heterogeneity is the gradient in the magnetic self-field which is significant in cable cross-section [61]. Self-field losses are generated in strands, depending on the twist direction of strands, the self-field losses are influenced. [76].

Using the coupled thermal-hydraulic electromagnetic model (THELMA) code, transient events are modelled for the cable in conduit conductors (CICC) [77]. Sudden quenches in the Nb-Ti joint samples are understood by considering the local effects. In CICC cables carrying large transport currents, the magnetic self-field gives rise to a large magnetic field gradient on the cable cross-section, resulting in larger gradient in J_C. The field gradients can cause instability and this affects quench behaviour [78]. The simulations of the quench are in *qualitative* agreement with experimental data [79].

Self-field instabilities are due to a sudden redistribution of transport current, and an uneven distribution [56]. Dynamic self-field instabilities have been studied extensively [80-82]. By comparing the V-I measurements, constant B_{App} and varied current, with V-H measurements constant current and B_{App} ramped from 0 T to the quench of the sample, it was demonstrated that the premature quenches are due to self-field instabilities [80]. The self-field instabilities are defined at different B_{App} at high field in the stable region, strands are measured and the current reaches its intrinsic critical current, and an intermediated field, where currents quench below their intrinsic critical current, and a low field region, where the strand quenches above a certain current.

2.5.6.3.   Importance of Self-field on magnet design

The self-field variation across the CICC, at operating at 40 kA and test currents up to 100 kA, can be more than ± 1 T [83]. The conductors' performance may appear better relative to the strand than expected, concealing non-uniform degradation [83]. For cabled strands, the current non-uniformity and redistribution between strands can result in E-fields above E_C at currents below the critical current density [84, 85]. Due to the non-uniform current distribution, the stability margin is reduced.

2.6.   Conclusions

The theories of superconductivity have explained the experimentally measured phenomena. The understanding of the properties of low-temperature superconductors has enabled the conductors to be commercialised. It is necessary to understand the microstructure and its effects on the critical currents possible in a conductor. The most important parameter in this thesis - and in the design of superconducting magnet systems - the critical current density, has been carefully defined. Characterising the E-J transition and the effects of measurements decisions were discussed. Understanding Bean's critical state model is necessary to evaluate the critical current in magnetisation measurements.

Quantification of the critical current density involves understanding how current flow in the sample generates a magnetic field. As the critical current density is a function of the magnetic field it is necessary to account for the effect of self-field. Using Maxwell's equations, it is possible to calculate the distribution of the magnetic field. Methods of applying the correction are discussed. The effect of geometry, and how to directly measure the magnetic field were discussed. The importance of self-field, both for characterising materials and for understanding superconductivity properties was presented. This thesis research aims to experimentally measure the effect of self-field and define relationships that address the experimental uncertainty.

References for chapter 2:

[1]   H. K. Onnes, "The resistance of pure mercury at helium temperatures," *Commun. Phys. Lab. Univ. Leiden,* vol. 12, p. 120, // 1911.

[2]   D. van Delft and P. Kes, "The discovery of superconductivity," *Physics Today,* Article vol. 63, no. 9, pp. 38-43, Sep 2010.

[3]   W. Meissner and R. Ochsenfeld, "Ein neuer Effekt bei Eintritt der Supraleitfähigkeit," *Naturwissenschaften,* vol. 21, pp. 787-788, 1933.

[4]   J. W. Ekin, *Experimental Techniques for Low-Temperature Measurements*. New York: Oxford University Press, 2007.

[5]   J. Bardeen, L. N. Cooper, and J. R. Schrieffer, "Theory of Superconductivity," *Physical Review,* vol. 108, no. 5, pp. 1175-1204, 1957.

[6]   S. Blundell, *Magnetism in Condensed Matter* (Oxford Master Series in Condensed Matter Physics). Oxford Oxford University Press, 2001, p. 256.

[7]   F. London and H. London, "The electromagnetic equations of the supraconductor," *Proceedings of the Royal Society A,* vol. A149, pp. 71-88, 1935.

[8]   C. J. Gorter, "Chapter I The Two Fluid Model for Superconductors and Helium II," in *Progress in Low Temperature Physics*, vol. 1, C. J. Gorter, Ed.: Elsevier, 1955, pp. 1-16.

[9]   V. L. Ginzburg and L. D. Landau, "On the Theory of Superconductivity," *Zhurnal Eksperimentalnoj i Teoreticheskoj Fiziki,* vol. 20, pp. 1064-1082, 1950.

[10]   D. R. Tilley and J. Tilley, "Ginzburg-Landau Theory," in *Superfluidity and Superconductivity*3rd ed. Bristol: IOP publishing Ltd., 1990, pp. 296-302.

[11]   D. P. Hampshire, "A barrier to increasing the critical current density of bulk untextured polycrystalline superconductors in high magnetic fields," *Physica C: Superconductivity and its Applications,* vol. 296, pp. 153-166, 1998.

[12]   E. Maxwell, "Isotope effect in the superconductivity of mercury," *Physical Review,* vol. 78, no. 4, p. 477, 1950.

[13]   H. Fröhlich, "Theory of the Superconducting State. I. The Ground State at the Absolute Zero of Temperature," *Physical Review,* vol. 79, no. 5, pp. 845-856, 1950.

[14]   L. N. Cooper, "Bound electron pairs in a degenerate Fermi gas," *Physical Review,* vol. 104, no. 4, pp. 1189 -1190, 1956.

[15]   J. G. Bednorz and K. A. Muller, "Possible High-T_c Superconductivity in the Ba-La-Cu-O System," *Zeitschrift Fur Physik B-Condensed Matter,* vol. 64, no. 2, pp. 189-193, 1986.

[16]   A. Yamamoto, N. Takeshita, C. Terakura, and Y. Tokura, "High pressure effects revisited for the cuprate superconductor family with highest critical temperature," *Nature Communications,* Article vol. 6, p. 8990, 12/01/online 2015.

[17]   N. E. Hussey, H. Gordon-Moys, J. Kokalj, and R. H. McKenzie, "Generic strange-metal behaviour of overdoped cuprates," *Journal of Physics: Conference Series,* vol. 449, p. 012004, 2013/07/17 2013.

[18]   E. Gibney, "Surprise graphene discovery could unlock secrets of superconductivity," (in eng), *Nature,* vol. 555, no. 7695, pp. 151-152, Mar 8 2018.

[19]   R. M. Norman, "High-temperature superconductivity in the iron pnictides," *Physics,* vol. 1, p. 21, 2008.

[20]   J. Nagamatsu, N. Nakagawa, T. Muranaka, Y. Zenitani, and J. Akimitsu, "Superconductivity at 39 K in magnesium diboride," *Nature,* vol. 410, pp. 63-64, 2001.

[21]   A. P. Drozdov, M. I. Eremets, I. A. Troyan, V. Ksenofontov, and S. I. Shylin, "Conventional superconductivity at 203 kelvin at high pressures in the sulfur hydride system," *Nature,* Letter vol. 525, no. 7567, pp. 73-76, 2015.

[22]   A. A. Abrikosov, "On the magnetic properties of superconductors of the second group," *Soviet Physics JETP,* vol. 5, no. 6, pp. 1174-1182, 1957.

[23]   C. P. Poole, *Handbook of superconductivity*, first ed. Academic press, 2000, p. 694.

[24] A. M. Campbell and J. E. Evetts, "Flux vortices and transport currents in Type II superconductors," *Advances in Physics,* vol. 21, no. 90, pp. 395-399, 1972.

[25] A. M. Campbell, J. E. Evetts, and D. Dew-Hughes, "Pinning of flux vortices in Type II superconductors," *Philosophical Magazine,* vol. 18, pp. 313-343, 1968.

[26] W. A. Fietz and W. W. Webb, "Hysteresis in superconducting alloys—Temperature and field dependence of dislocation pinning in niobium alloys," *Physical Review,* vol. 178, no. 2, pp. 657-667, 1969.

[27] D. Dew-Hughes, "Flux pinning mechanisms in type II superconductors," *Philosophical Magazine,* vol. 30, no. 2, pp. 293-305, 1974.

[28] W. A. Fietz and W. W. Webb, "Magnetic Properties of some Type-II Alloy Superconductors near the Upper Critical Field," *Physical Review,* vol. 161, no. 2, pp. 423-433, 1967.

[29] J. Bardeen and M. J. Stephen, "Theory of the Motion of Vortices in Superconductors," *Physical Review,* vol. 140, no. 4A, pp. A1197-A1207, 1965.

[30] Y. B. Kim, C. F. Hempstead, and A. R. Strnad, "Flux-Flow Resistance in Type-II Superconductors," *Physical Review,* vol. 139, no. 4A, pp. A1163-A1172, 08/16/ 1965.

[31] G. Wang, M. J. Raine, and D. P. Hampshire, "How Resistive Must Grain-Boundaries be to Limit J_C in Polycrystalline Superconductors?," *Superconductor Science and Technology,* vol. 30, no. 10, p. 104001, 2017.

[32] P. Sunwong, J. S. Higgins, Y. Tsui, M. J. Raine, and D. P. Hampshire, "The critical current density of grain boundary channels in polycrystalline HTS and LTS superconductors in magnetic fields," *Superconductor Science and Technology,* vol. 26, p. 095006, 2013, Art. no. 095006.

[33] A. F. Clark and J. W. Ekin, "Defining Critical Current," *IEEE Transactions on Magnetics,* vol. 13, no. 1, pp. 38-40, 1977.

[34] M. Greco, P. Fabbricatore, S. Farinon, and R. Musenich, "Critical current and n-value modifications from superconducting strands to Rutherford cables," *Physica C: Superconductivity,* vol. 401, no. 1, pp. 124-128, 2004/01/15/ 2004.

[35] J. W. Ekin, "Offset criterion for determining superconductor critical current," *Applied Physics Letters,* vol. 55, no. 9, pp. 905-907, 1989.

[36] E. F. Talantsev, N. M. Strickland, S. C. Wimbush, and W. P. Crump, "The onset of dissipation in high-temperature superconductors: Self-field experiments," *AIP Advances,* Article vol. 7, no. 12, p. 15, Dec 2017, Art. no. 125230.

[37] J. W. Ekin, "Strain scaling law for flux pinning in NbTi, Nb₃Sn, Nb-Hf/Cu-Sn-Ga, V₃Ga and Nb₃Ge," *IEEE Transactions on Magnetics,* vol. 17, pp. 658-661, 1981.

[38] I. Pong *et al.*, "Current sharing temperature of NbTi SULTAN samples compared to prediction using a single pinning mechanism parametrization for NbTi strand," *Superconductor Science and Technology,* vol. 25, no. 5, p. 054011, 2012, Art. no. 054011.

[39] J. Rhyner, "Magnetic properties and AC-losses of superconductors with power law current—voltage characteristics," *Physica C: Superconductivity and its Applications,* vol. 212, no. 3-4, pp. 292-300, 1993.

[40] S. Stavrev *et al.*, "Comparison of Numerical Methods for Modeling of Superconductors," *IEEE Transactions on Applied Superconductivity,* vol. 38, no. 2, pp. 849-852, 2002.

[41] P. W. Anderson, "Theory of Flux Creep in Hard Superconductors," *Physical Review Letters,* vol. 9, no. 7, pp. 309-311, 1962.

[42] A. P. Verweij, "The consequence of self-field and non-uniform current distribution on short sample tests of superconducting cables," in *LHC Project Report 151, CEC/ICMC '97*, Portland, USA, 1997.

[43] J. Barrett, W. and L. Prigozhin, "Electric field formulation for thin film magnetization problems," *Superconductor Science and Technology,* vol. 25, no. 10, p. 104002, 2012.

[44] D. M. J. Taylor and D. P. Hampshire, "Relationship between the *n*-value and critical current in Nb₃Sn superconducting wires exhibiting intrinsic and extrinsic behaviour," *Superconductor Science and Technology,* vol. 18, pp. S297-S302, 2005, Art. no. p. S297-S302.

[45]   C. P. Bean, "Magnetization of high-field superconductors," *Reviews of Modern Physics,* vol. 36, pp. 31-39, 1964.

[46]   C. P. Bean and J. D. Livingston, "Surface barrier in Type-II superconductors," *Physical Review Letters,* vol. 12, no. 1, pp. 14-16, 1964.

[47]   J. W. Ekin *et al.*, "Evidence for weak link and anisotropy limitations on the transport critical current in bulk polycrystalline $Y_1Ba_2Cu_3O_x$," *Journal of Applied Physics,* vol. 62, no. 12, pp. 4821-4828, 1987.

[48]   F. Grilli, E. Pardo, A. Stenvall, D. N. Nguyen, W. J. Yuan, and F. Gomory, "Computation of Losses in HTS Under the Action of Varying Magnetic Fields and Currents," *IEEE Transactions on Applied Superconductivity,* Article vol. 24, no. 1, p. 33, Feb 2014, Art. no. 8200433.

[49]   T. Baumgartner *et al.*, "Evaluation of the Critical Current Density of Multifilamentary Nb_3Sn Wires From Magnetization Measurements," *IEEE Transactions on Applied Superconductivity,* vol. 22, no. 3, p. 6000604, 2012, Art. no. 6000604.

[50]   S. Le Naour *et al.*, "Magnetization measurements on LHC superconducting strands," *IEEE Transactions on Applied Superconductivity,* vol. 9, no. 2, pp. 1763-1766, 1999.

[51]   T. Boutboul, S. Le Naour, D. Leroy, L. Oberli, and V. Previtali, "Critical current density in superconducting Nb-Tistrands in the 100 mT to 11 T applied field range," *IEEE Transactions on Applied Superconductivity,* Article; Proceedings Paper vol. 16, no. 2, pp. 1184-1187, Jun 2006, Art. no. 1643060.

[52]   L. Muzzi *et al.*, "Test Results of a NbTi Wire for the ITER Poloidal Field Magnets: A Validation of the 2-Pinning Components Model," *IEEE Transactions on Applied Superconductivity,* Article vol. 21, no. 3, pp. 3132-3137, Jun 2011.

[53]   M. A. Green, "Calculating the Jc, B, T Surface for Commercial Niobium Tin Conductors Using a Reduced State Model," in *Advances in Cryogenic Engineering Materials*, vol. 40(An International Cryogenic Materials Conference Publication Springer, 1994, pp. 733-739.

[54]   L. D. Cooley, P. S. Chang, and A. K. Ghosh, "Magnetization, RRR and Stability of Nb_3Sn Strands With High Sub-Element Number," *IEEE Transactions on Applied Superconductivity,* vol. 17, no. 2, pp. 2706-2709, 2007, Art. no. 9616446.

[55]   A. Ghosh, K. Robins, and W. Sampson, "Magnetization measurements on multifilamentary Nb_3Sn and NbTi conductors," *IEEE Transactions on Magnetics,* vol. 21, no. 2, pp. 328-331, 1985.

[56]   M. N. Wilson, *Superconducting Magnets*. Oxford, UK: Oxford University Press, 1986.

[57]   F. Gomory and B. Klincok, "Self-field critical current of a conductor with an elliptical cross-section," *Superconductor Science and Technology,* Article vol. 19, no. 8, pp. 732-737, Aug 2006.

[58]   L. F. Goodrich and A. N. Srivastava, "II-3: Critical current measurement methods: quantitative evaluation," *Cryogenics,* vol. 35, pp. S19-S23, 1995, Art. no. pp. S19-S23.

[59]   K. Tsuchiya *et al.*, "Critical current measurement of commercial REBCO conductors at 4.2 K," (in English), *Cryogenics,* Article vol. 85, pp. 1-7, Jul 2017.

[60]   W. M. de Rapper, B. Bordini, S. le Naour, L. Bottura, and H. H. J. ten Kate, "Critical Current in High-J_c Nb_3Sn Rutherford Cables Affected Substantially by the Direction of the Applied Magnetic Field," *IEEE Transactions on Applied Superconductivity,* Article; Proceedings Paper vol. 22, no. 3, p. 4, 2012, Art. no. 6001704.

[61]   A. Ulbricht *et al.*, "The ITER toroidal field model coil project," *Fusion Engineering and Design,* Review vol. 73, no. 2-4, pp. 189-327, Oct 2005.

[62]   J. D. Jackson, *Classical Electrodynamics*. Hoboken, New Jersey, United States: John Wiley and Sons, 1999.

[63]   P. Fabbricatore, R. Musenich, R. Parodi, S. Pepe, and R. Vaccarone, "Self field effects in the critical current measurements of superconducting wires and cables," *Cryogenics,* vol. 29, no. 9, pp. 920-925, 1989/09/01 1989, Art. no. pp. 920-925.

[64]   Y. A. Ilyin, A. Nijhuis, H. H. J. t. Kate, and P. Bruzzone, "Self field measurements by Hall sensors on the SeCRETS long sample CICCs in SULTAN," *IEEE Transactions on Applied Superconductivity,* vol. 12, no. 1, pp. 1667-1671, 2002.

[65]   Y. Ilyin, A. Nijhuis, and H. H. J. ten Kate, "Interpretation of conduit voltage measurements on the poloidal field insert sample using the CUDI–CICC numerical code," *Cryogenics,* vol. 46, no. 7, pp. 517-529, 2006/07/01/ 2006.

[66]   J. W. Ekin, "Current transfer in multifilamentary superconductors. I Theory," *Journal of Applied Physics,* vol. 49, no. 6, pp. 3406-3409, 1978, Art. no. 3406.

[67]   J. W. Ekin, "Current transfer in multifilamentary superconductors II Experimental results," *Journal of Applied Physics,* vol. 49, p. 3410, 1978.

[68]   L. F. Goodrich, J. W. Ekin, and F. R. Fickett, "Effect of twist pitch on short-sample V-I characteristics of multifilamentary superconductors," *Advances in Cryogenic Engineering,* vol. 28, pp. 571-580, 1982.

[69]   S. A. Keys and D. P. Hampshire, "Characterisation of the transport critical current density for conductor applications," in *Handbook of Superconducting Materials*, vol. 2, D. Cardwell and D. Ginley, Eds. Bristol: IOP Publishing, 2003, pp. 1297-1322.

[70]   M. J. Raine, S. A. Keys, and D. P. Hampshire, *Characterisation of the Transport Critical Current Density for Conductor Applications*. Accepted by Taylor and Francis, 2017.

[71]   P. Gislon, L. Muzzi, S. Chiarelli, A. Di Zenobio, M. V. Ricci, and M. Spadoni, "Electrical characterization of the NbTi strand for the ENEA stability SEx-up experiment," *IEEE Transactions on Applied Superconductivity,* vol. 13, no. 2, pp. 1429-1432, 2003, Art. no. 1211867.

[72]   A. Stenvall, M. Siahrang, F. Grilli, and F. Sirois, "Computation of self-field hysteresis losses in conductors with helicoidal structure using a 2D finite element method," *Superconductor Science and Technology,* vol. 26, no. 4, p. 045011, Apr 2013.

[73]   R. Mulet, O. Diaz, and E. Altshuler, "Choice of sample size for high transport critical current density in a granular superconductor: percolation versus self-field effects," *Superconductor Science and Technology,* Article vol. 10, no. 10, pp. 758-762, Oct 1997.

[74]   A. Godeke *et al.*, "Novel Methods for the Measurement of the Critical Current of Superconducting Wires," in *Advances in Cryogenic Engineering, Vol 58*, vol. 1435, U. Balachandran, Ed. (AIP Conference Proceedings, Melville: Amer Inst Physics, 2012, pp. 209-216.

[75]   J. W. Ekin, N. Cheggour, L. Goodrich, J. Splett, B. Bordini, and D. Richter, "Unified Scaling Law for flux pinning in practical superconductors: II. Parameter testing, scaling constants, and the Extrapolative Scaling Expression," *Superconductor Science and Technology,* Review vol. 29, no. 12, p. 38, Dec 2016, Art. no. 123002.

[76]   J. K. Lee, G. S. Cha, and S. Y. Hahn, "Calculation of self-field losses in a superconducting cable considering the twist of strands," *IEEE Transactions on Applied Superconductivity,* Article; Proceedings Paper vol. 9, no. 2, pp. 750-753, Jun 1999.

[77]   J. Rong, X. Huang, Y. Song, and S. Wu, "The Stability Analysis of ITER TF Main Busbar in 15 MA Plasma Current Reference Scenario," *IEEE Transactions on Applied Superconductivity,* vol. 27, no. 2, pp. 1-7, 2017.

[78]   R. Zanino, F. Bellina, P. L. Ribani, and L. Savoldi Richard, "Analysis of sudden quench of an ITER superconducting NbTi full-size short sample using the THELMA code," *Superconductor Science and Technology,* vol. 24, no. 10, p. 105001, 2011.

[79]   R. Wesche, A. Anghel, B. Stepanov, and P. Bruzzone, "DC performance of subsize NbTi cable-in-conduit conductors," *IEEE Transactions on Applied Superconductivity,* vol. 14, no. 2, pp. 1499-1502, 2004.

[80]   B. Bordini, L. Bottura, L. Oberli, L. Rossi, and E. Takala, "Impact of the Residual Resistivity Ratio on the Stability of Nb_3Sn Magnets," *IEEE Transactions on Applied Superconductivity,* vol. 22, no. 3, p. 4, 2012, Art. no. 4705804.

[81]   B. Bordini and L. Rossi, "Self Field Instability in High-J_C Nb$_3$Sn Strands With High Copper Residual Resistivity Ratio," *IEEE Transactions on Applied Superconductivity,* vol. 19, no. 3, pp. 2470-2476, 2009.

[82]   B. Bordini, E. Barzi, S. Feher, L. Rossi, and A. V. Zlobin, "Self-Field Effects in Magneto-Thermal Instabilities for Nb-Sn Strands," *IEEE Transactions on Applied Superconductivity,* vol. 18, no. 2, pp. 1309-1312, 2008.

[83]   N. Mitchell, "Steady state analysis of non-uniform current distributions in cable-in-conduit conductors and comparison with experimental data," *Cryogenics,* vol. 40, no. 2, pp. 99-116, 2/1/ 2000.

[84]   N. Mitchell, "Possible causes of the premature voltage gradient of the CS insert coil [for ITER]," *IEEE Transactions on Applied Superconductivity,* vol. 12, no. 1, pp. 1453-1458, 2002.

[85]   A. K. Ghosh, "Effect of Copper Resistivity and Filament Size on the Self-Field Instability of High-J(c) Nb$_3$Sn Strands," *IEEE Transactions on Applied Superconductivity,* vol. 23, no. 3, p. 7, 2013, Art. no. 7100407.

CHAPTER 3

3. Design of a High Current Probe for Nb-Ti Measurements

In this chapter, the design of the high current probe for transport measurements is outlined. The purpose of this new probe is to make measurements of the critical current density of the strands over a range of magnetic fields with high currents, up to 2 kA. In sections 3.1 and 0, the details of the Nb-Ti strands architecture are outlined. In sections 3.3 and 3.4 the measurement barrel and the probe design is outlined. To quantify the self-field effect both the standard barrel (ITER) and a custom-designed measurement barrel, the minimum separation of turns (MST), were used. The experiment depends on being able to measure the voltage and reverse the current flow direction. Current flowing in either the clockwise or anticlockwise directions is equivalent to the Lorentz force pointing inwards or outwards. Section 3.5 reports measurements of the *same strand* of Nb-Ti using the new probe compared with other in-house measurements made as part of the Fusion for Energy (F4E) contract as well as with the *same type* of Nb-Ti strand measured at other institutes.

3.1.   Niobium-Titanium

Niobium-titanium alloy is the most widely used conductor for superconducting magnets [1]. Elemental niobium and titanium both superconduct with transition temperatures of 9.3 K and 0.4 K respectively [2]. The T_C of Nb-Ti does not change much with Ti content, up to 47%. The effect of Ti concentration is a peak in the B_{C2} value. The alloy composition of the strand studied has both a T_C and B_{C2} value that are close to the maximum [3, 4]. The typical composition of the solution alloy used in commercial conductors is Nb-47wt%Ti [5]. The standard T_C for Nb-Ti is 9.5 K, and $B_{C2}(T = 0\ K)$ = 13.0 T [6].

The ITER machine requires approximately 250 tons of Nb-Ti stand [7, 8] and the strands used have become a standard reference material. The measurements in this thesis are of the ITER poloidal field (PF) type 1 strand, used in PF coils one and six. The requirements of the type 1 strand are summarised in Table 3.1 [9, 10].

Characteristic [unit]	Value
Critical current at 6.4 T and 4.22 K [A]	> 306
n-value at 6.4 T and 4.22 K (10 to 100 μVm^{-1})	> 20
Hysteresis losses at ± 1.5 T and 4.22 K [mJ·cm^{-3}]	< 55
Residual Resistivity Ratio	> 100
Diameter [mm]	0.730 ± 0.005
Twist pitch [mm]	15±2
Cu to non-Cu Ratio	1.55 to 1.75
Nickel Plating Thickness [μm]	1 to 2

Table 3.1 : Nb-Ti strand requirement for the ITER PF type 1 [9].

3.1.1. Strand Identification

Three Nb-Ti ITER type 1 strands were measured. The design and manufacturing process of the three strands are identical. The strands were manufactured by the Chepetsky mechanical plant [11]. The Nb-Ti strands measured were selected from Durham's fusion reference laboratory strand inventory. The strands are allocated a unique four-digit Durham reference (DR) number. A length of the strand is cut from the parent material for transport measurements and a separate length for magnetisation measurements. Although there may be some variation along the parent strand's length, the homogeneity of Nb-Ti is considered to be better than Nb₃Sn [12, 13]. Controlled levels of impurities ensure predictable superconducting properties. The variation between nominally identical strand can be attributed to the microstructure of the alloy. The heat treatment generates α Ti-precipitates, which are sensitive to the composition and affect the fluxon pinning. Macroscopic irregularities and filament cross-sectional area can also affect measured J_C.

The experimental work carried out for this thesis was the extended measurement of strands DR 4810 and DR 5534 over an range of magnetic fields at a fixed temperature (4.22 K) using the new high current probe in different geometries and orientations of F_L. Additional measurements of strand DR 5049 were done for this thesis, measurement over a smaller range of magnetic field, from 3.5 K to 6 K using a variable temperature probe. The reference laboratory, managed by Dr Mark J Raine performed the standard characterisation of strands DR 4810, DR 5534, and DR 5049. All three strands measured have properties which met the requirements outlined in Table 3.1, the details of the three strands are outlined in Appendix A.1 In work by the Durham reference laboratory, an average of I_C of 336.4 A at (B_{App} = 6.4 T) and a standard error on the mean of ± 0.4 A, for the 320 Nb-Ti type 1 strand characterised [14]. Comparisons between the two strands extensively characterised for this thesis are shown in section 6.3.2.

3.2.   The Architecture of Nb-Ti Strands

All low-temperature superconducting strands are manufactured in the form of filamentary composites [15], with superconducting filament embedded in a normal conducting matrix (usually Cu). The filaments in the superconducting strand are an essential architectural feature.

3.2.1.   Filamentary composites

Filaments make the composite stable to thermal fluctuations [1] and increase the usable current densities possible in the strand [16]. In non-DC superconducting magnets, filaments are used to reduce AC losses [4]. The small diameter of the filament minimises the self-field instabilities at low-magnetic fields [17]. Fine filamentary structures can be manufactured as Nb-Ti is both extremely ductile and has a high tensile strength, and the similarities of the Nb-Ti mechanical properties with the copper matrix.

In the strand studied, each Nb-Ti filament is separated with barrier and stabiliser around each filament, shown in Figure 3.1 (a). The Nb foil wrapped around the filaments of Nb-Ti core acts as a diffusion barrier, preventing the formation of intermetallics, like $TiCu_4$, which can distort the filaments during wire drawing [3]. The Nb foil offers excellent ductility and a good mechanical bond with both the Nb-Ti and the copper when manufacturing the strands [1]. The Nb-Ti is inserted into a copper extrusion can, which is evacuated and sealed. Following extrusion, the copper is shaped, with a hexagonal cross-section along the length of the filament. This hexing of the single filament, shown in Figure 3.1 (b) allows stacking into a multi-filamentary stack and a compact configuration. The thickness of copper around each filament controls the drawability. Reducing the spacing between the filaments improves the co-deformation of the filaments and the matrix. If the filaments are too close, Cooper pairs tunnel through the copper, increasing the losses [18, 19]. If the filaments are widely separated, this can result in wire drawing inhomogeneities referred to as 'sausaging', where the filament's cross-sectional area is non-uniform. The sausaging is defined as a coefficient of variation for the filament cross-sectional areas of approximately 2% [1]. A filament with varying cross-sectional area results in a lower overall current carrying capability of the strand [1].

The Nb-Ti ITER PF strand studied in this work shown in Figure 3.2 contains 4488 filaments with a diameter of 6.8 ± 0.2 μm. The scanning electron microscope (SEM) image of the Nb-Ti strand's cross-section shown in Figure 3.2(a), summarises the architecture and design. The darker regions are the matrix material, and the lighter regions an annulus of composite Cu/Nb-Ti filaments. The inset in Figure 3.2 (a) shows the filament and intra-filamentary region. The filamentary composite region is
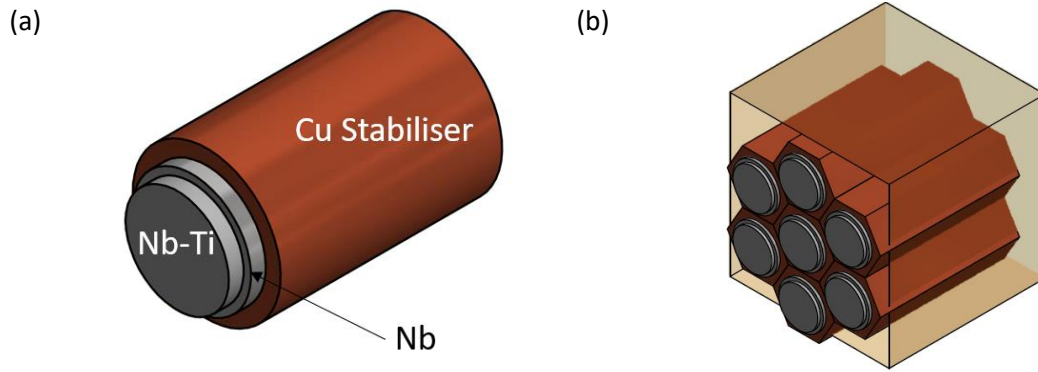
Figure 3.1 : Schematic of the internal architecture of the Nb-Ti strand (a) Layered structure of the filamentary unit. An Nb-Ti alloy core is wrapped in an Nb diffusion barrier. The Nb-Ti and Nb are inside a copper sheath. (b) The filamentary units are hexed and stacked.
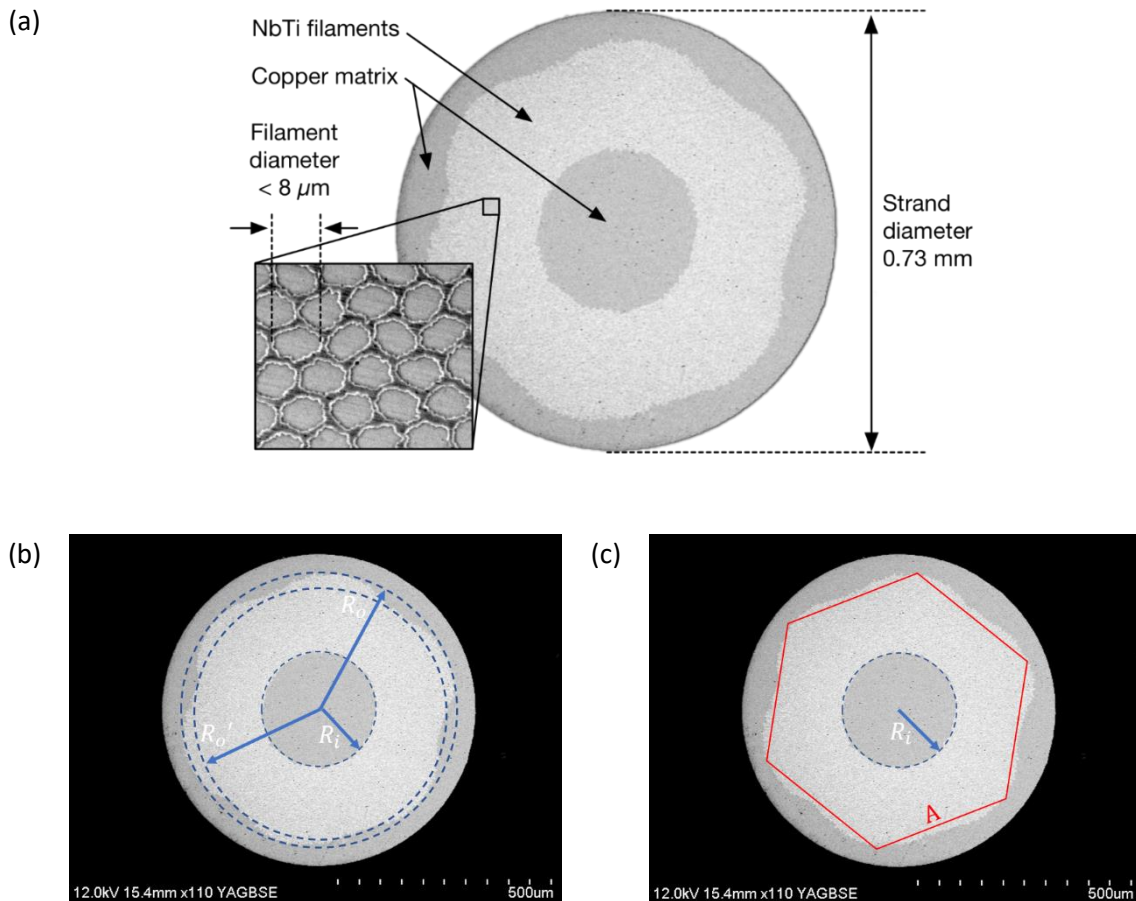
Figure 3.2 : (a) Nb-Ti strand SEM image where an annulus of composite Cu/Nb-Ti filaments can be seen in grey, embedded between the external crown and the internal core copper regions. The inset shows a close-up of the filamentary region, with copper in-between filaments. Figure from Ref. [20]. (b) SEM of Nb-Ti cross-section with an inner R_i and minimum R_O' and maximum R_O outer radii of an annular filamentary region. (c) The Nb-Ti strand considered with a circular internal core, and hexagonal filamentary region with length A.

between the external crown and the internal core copper regions. The internal copper core is used to reduce cavitation or centre burst extrusion [21].

Dimension	Length [mm]	Area	Area [×10⁻⁷ m²]
$\bar{R}_{\mathrm{i}}$	0.131 ± 0.002	A_{fr} : Eq. (3.1)	2.5 ± 0.1
$\bar{R}_{\mathrm{o}}$	$0.\,30 \pm 0.01$	$A_{\mathrm{fr(hex)}}$: Eq.(3.2)	2.3 ± 0.2
A	0.33 ± 0.01		

Table 3.2 : Summary of the lengths and areas used in the simplified Nb-Ti strand model.
The calculations in chapters 5 and 6 use $\bar{R}_{\mathrm{i}}$ = 0.130 mm and $\bar{R}_{\mathrm{o}}$ = 0.310 mm.

In section 2.3.5.1 the engineering and superconducting areas were defined and values for the Nb-Ti PF type 1 strand listed. The FEA models in chapters 5 and 6 model the current flow in the composite filamentary region, using an annular cross-section. Reducing the complexity of the filamentary region to an annulus, with an effective inner (R_{i}) and outer (R_{O}) radii is a simplification which has been used previously in the literature [22, 23]. The software ImageJ [24] has been used to measure the dimension in the SEM images, Figure 3.2 (b, c). For the circular geometries, the area of circular sections was measured, additionally, line profile plots were used to measure lengths. 20 profile plots and 20 circular sections were used to define an average inner $\bar{R}_{\mathrm{i}}$ and outer $\bar{R}_{\mathrm{o}}$ radii. The uncertainty in the dimension of $\bar{R}_{\mathrm{o}}$ [Figure 3.2 (b)] is larger than $\bar{R}_{\mathrm{i}}$, due to the non-circularity. The area of the filamentary region is calculated:

$$A_{\mathrm{fr}} = \pi \left(\bar{R}_{\mathrm{o}}^{\ 2} - \bar{R}_{\mathrm{i}}^{\ 2} \right). \tag{3.1}$$

The area is reported in Table 3.2. It was suggested that the uncertainty in $\bar{R}_{\mathrm{o}}$ can be reduced by considering the filamentary region as hexagonal, shown in Figure 3.2 (c). Using 20 hexagonal polygons in the filamentary composite region the length was measured. The hexagonal filamentary region area, $A_{\mathrm{fr(hex)}}$, assuming that $\bar{R}_{\mathrm{i}}$ is circular is defined:

$$A_{\mathrm{fr(hex)}} = \frac{3\sqrt{3}}{2}(A^2) - \pi \bar{R}_{\mathrm{i}}^{\ 2}. \tag{3.2}$$

The area is reported in Table 3.2, $A_{\mathrm{fr(hex)}}$ is 9 % smaller. When calculating the self-field, the standard in the literature [25] considers a circular cross-section, with the radius to the outermost filament defining the dimension for the calculation. The effect of the radius of the strand on self-field is discussed in section 5.2.3.5. For the areas in Table 3.2, an equivalent radius can be calculated assuming a circular cross-section. For a fixed current, the smaller $A_{\mathrm{fr(hex)}}$ results in a 4 % larger effect of self-field using the correction. A simpler approach would be to use the superconducting area, as the uncertainty is smaller due to the accuracy of measurement of the CnC ratio and the strands diameter.

3.2.2. Matrix Materials

The matrix is an alternative current and heat flow path. The matrix works as an electrical shunt when superconductivity is interrupted and contributes to the recovery of the superconductivity by conducting heat generate to the surrounding coolant. Most commonly, copper is used as a matrix material in Nb-Ti conductors. The cryogenic-temperature resistivity of copper is important, influencing the superconductors stability. Copper has a high heat capacity that both removes heat and, if sufficiently cooled, reduces the heat generated by current shunted through the matrix. The thermal conductivity of the copper at 4 K is 420 $W \cdot m^{-1} \cdot K^{-1}$ [26], although the value depends on purity, and $\boldsymbol{B}$. A value of 0.017 $W \cdot m^{-1} \cdot K^{-1}$ is used for the thermal conductivity of Nb-Ti in the modelling community [26], but measured values reported vary by a factor of 10^2 [27-29]. Copper-nickel (Cu–Ni), is an alternative matrix material used for its anisotropic resistivity [30]. Aluminium can also be used as a matrix material and has the advantage that the electrical resistivity saturates more quickly with B_{App} than copper [3].

3.2.3. Copper to Non-Copper Ratio

Varying the ratio of copper to non-copper (CnC) changes the performance of the conductor. The ideal ratio of CnC depends on the mode of operation of the magnet, the operational current density, and the magnetic field operated at [21]. If the strand is completely composed of superconductor it is unstable. For a composite, increasing the volume of superconductor results in enhanced current carrying capacity and strand stability [21]. With enough copper, the Joule heating is easily extracted by cooling [31]. Although the CnC gives us the fractional area of the strand which is superconducting, it does not contain information about the spatial distribution.

It is possible to optimise the CnC ratio for a high stability, high J_C strand using a numerical method. When designing a strand to be able to sustain a large perturbation without quenching, the figures of merits are the minimum propagating zone (MPZ), and the minimum quench energy (MQE) [15]. The length of the MPZ (l_{MPZ}) gives the maximum dimension over which a normal region will vanish and superconductor will not quench. Similarly, the MQE is minimum local energy, in the form of heat, needed to increase the temperature of a wire segment with length l_{MPZ} from the helium temperature to T_{C}. The MPZ can be calculated from the material properties, the effective thermal conductivity, and is a function of the areas of superconductor and matrix.

Using material properties the Stekly criterion, a CnC ratio for a stable strand was derived. The Stekly criterion offers physical insight and is quasi-quantitative. Manufacturing strands with a CnC ratio of 10:1, Stekly was able to build the first magnets that recovered the superconducting state irrespective

of the size of the thermal perturbation [32, 33]. Strands used commercially typically have *CnC* ratios of 2:1, larger CnC ratios are prohibitively expensive [34], magnets can operate in a metastable mode [35]. An average value of the CnC of the ITER PF strand during production was reported as 1.64 [36].

3.2.4. Residual Resistivity Ratio

The resistivity of the matrix at cryogenic temperature is an important property of the strand that influences the stability. The residual resistivity ratio (RRR) is the ratio of the strands resistivity at two different temperatures

$$RRR = \frac{\rho_{273K}}{\rho_T},$$

(3.3)

where ρ_{273K} is the resistivity at 273 K, ρ_T is the resistivity at temperature T. The resistivity values are characterised using voltage-current ($V - I$) measurements, the international standard techniques. The RRR of the copper matrix affects the heat conduction, magnetic shielding, and current transfer behaviour. Self-field instabilities have been investigated as a function of RRR, with greater stability at higher values, for the range of 8 to 120 [17]. Increasing the RRR above 100 to 300 does not significantly increase stability due to the magnetoresistance of copper [37, 38].

3.2.5. Twist Direction and Pitch

The inter-filament coupling caused by external field variations can be greatly reduced by twisting the filaments together. Filaments are twisted about their drawing axis, which partially transposes the filaments, reducing flux-jump instabilities and eddy-current losses. The twist pitch is chosen depending on the expected rate of change of the field. For a quickly changing field, a high twist pitch is used. The twist pitch of the filaments is normally 10-20 times the strand's diameter [39]. Transposition increases the current path length, and this affects AC losses due to coupling [30]. As the twist pitch is limited, the only means to reduce these coupling losses is to use resistive barriers in the composite. The ITER PF Nb-Ti strand is twisted once in fabrication, with right-handed chirality, when the strand's diameter is just larger than the final diameter.

3.2.6. Nickel Plating

The ITER Nb-Ti PF strand is nickel-plated [19]. The nickel plating both reduce the AC losses [40] and makes it possible to make electrical connections without introducing heat. The drawback to plating is the slight decrease in the *RRR,* probably because of bending the strand when plating [41]. Although

Nickel is ferromagnetic [2], the effects are not considered in this work due to the thickness relative to the diameter of the strand.

3.3.   Measurement Barrels

To reduce the influence of self-field in critical current density measurements, a standardised sample holder with a fixed diameter and pitch was defined [42, 43]. The "ITER barrel" is the result of the Versailles project on Advanced Materials and Standard (VAMAS) [44]. For this thesis, a custom barrel was designed and manufactured to measure the critical current density, as a function of an additional parameter. Additionally, the titanium alloy used in the manufacturing of the measurement barrel used in this research is an alloy different from the standard. The alloy's properties will be outlined in chapter 4.

3.3.1. Barrel Design

To investigate the problem of quantifying self-field a new measurement barrel was designed to enhance the effect of self-field during measurements. The custom-designed minimum separation of turns (MST) with the difference being the separation of turns (S_T). The ITER barrel has a S_T of 3.175 mm (8 turns per inch), with the range 3.18 to 3.20 mm stated in the literature as [45].

The MST barrel has a S_T of 0.830 mm, 0.100 mm larger than the diameter of the strand. Both measurement barrel consists of a 35 mm threaded hollow cylinder of titanium alloy, with two 13 mm oxygen-free high conductivity (OFHC) copper rings, shown in Figure 3.3 (a, b). The assembly screws together and the total height is 51 mm. Along the total height of the barrel, a 90° continuous right-handed V-shaped groove is cut, 0.92 mm deep for the ITER barrel and 0.42 mm for MST barrel. Both barrels have an inner diameter of 24 mm in the copper sections and 28 mm in the titanium section. The strand is positioned at the same major radius for both barrels. A strand length of ~1.6 m is measured on the ITER barrel, and ~6.0 m on the MST barrel. To fix the position of the strand, and enable tension whilst winding, both ends of both barrels include a slot cut into the bottom of the OHFC copper rings and is just wider than the diameter of the strand, shown in Figure 3.3 (c). The design of the ITER and MST barrels are outlined in Table 3.3. Further details are outlined in A.2.1.
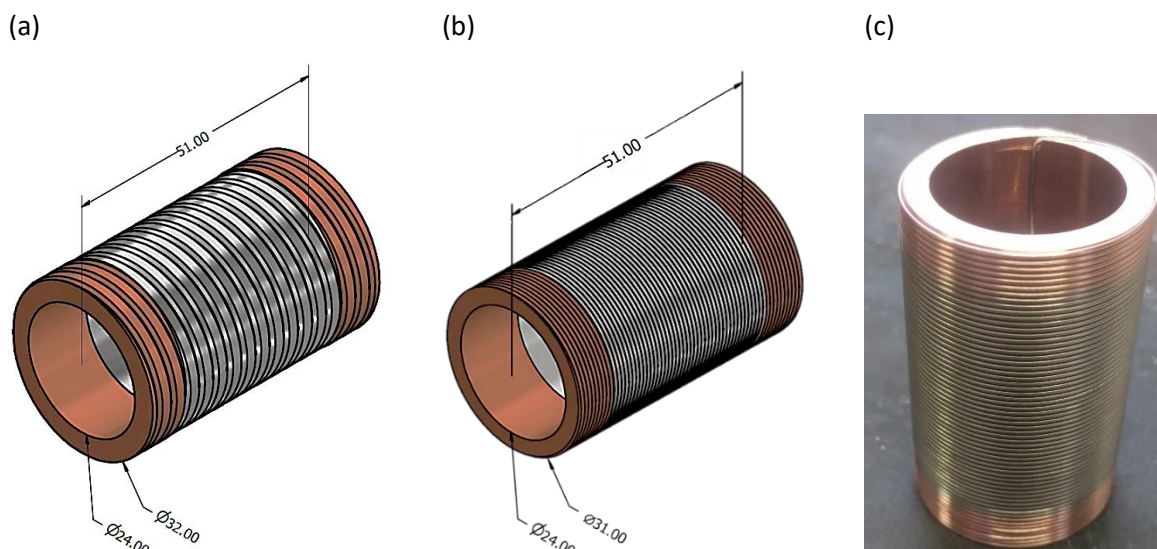
Figure 3.3 : Measurement barrels (a) technical drawing of standard ITER VAMAS barrel (b) technical drawing of the custom-designed minimum separation of turns (MST) barrel for this work[mm] (c). Minimum separation of turns (MST) barrel wound with Nb-Ti strand DR 4810.

Characteristic [unit]	ITER	MST
Separation of turns [mm]: S_T	3.175	0.830
Outer diameter (Cu, Ti-Alloy) [mm]	32	31
Inner diameter (Ti-alloy) [mm]	28	28
Inner diameter (Cu) [mm]	24	24
Groove depth [mm]	0.92	0.42
Total number of turns	16	61
Number of turns in Ti-alloy	11	42
Total number of turns in both OFHC copper rings	5	19

Table 3.3 : Properties of the standard ITER measurement barrel and custom minimum separation of turns (MST) measurement barrel.

3.3.2. Current Transfer

The current is transferred from the current leads to the strand via the current terminals at the ends of the barrel. The current is transferred from the barrel holder to the strands through the lead-tin [$Pb_{40}Sn_{60}$(wt %)] solder, which adheres to both the OHFC current rings and the exposed copper on the strand. The strand is wound under 1 kg of tension, as a result, the contact between the groove and the strand is maximised. Near the current leads, the transport current flows in the normal metal [46]. Current transfer can generate heat, and this limits the use of ITER barrels when measuring conductors with extremely high critical currents [44].
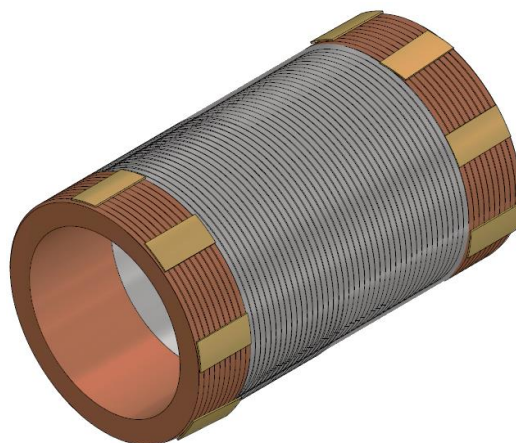
Figure 3.4 : The strapped critical current barrel, eight commercial (SuperPower) YBCO tapes are soldered to the Nb-Ti strand wound on the OHFC copper ring.

Typically in the transport measurements, presented in chapter 6, E-fields up to 120 μV·m^{-1} were measured. In initial measurements where low E-fields were measured, the current transfer to the strand was improved. The YBCO 'straps' are low resistance current paths, and additionally increase the number of contact points. The strapping of barrel is standard practice in the Durham reference laboratory, and in this work, the same method is used. Eight 4 x 8 mm strips of advanced pinning YBCO tape from SuperPower [47] were soldered onto the titanium section of the barrels, shown schematically in Figure 3.4. The straps enabled the current to transfer to the central region while bypassing problematic regions. This enabled higher E-field to be achieved without thermal runaway. The strap length is short enough to ensure current transfer is sufficiently far away from the voltage tap region.

3.4.   Description of the Probe

The two key design aspects of the probe are the cryogen and current flow. The transport measurements were performed in a wet bore magnet, where the liquid helium flows through the probe. Increasing the cross-sectional area of the current leads would be ideal for increasing current into the strand, but the probe's dimensions are limited by both the magnet system bore and the measurement barrel. Maximal current flow is achieved using both superconducting and normal materials. The materials used in the design of the probe was guided by the properties outlined in Ref. [48].

The probe was manufactured in Durham's Physics departments mechanical workshop. The workshop has experience of producing probes for measuring a range of superconductor materials [49, 50]. The
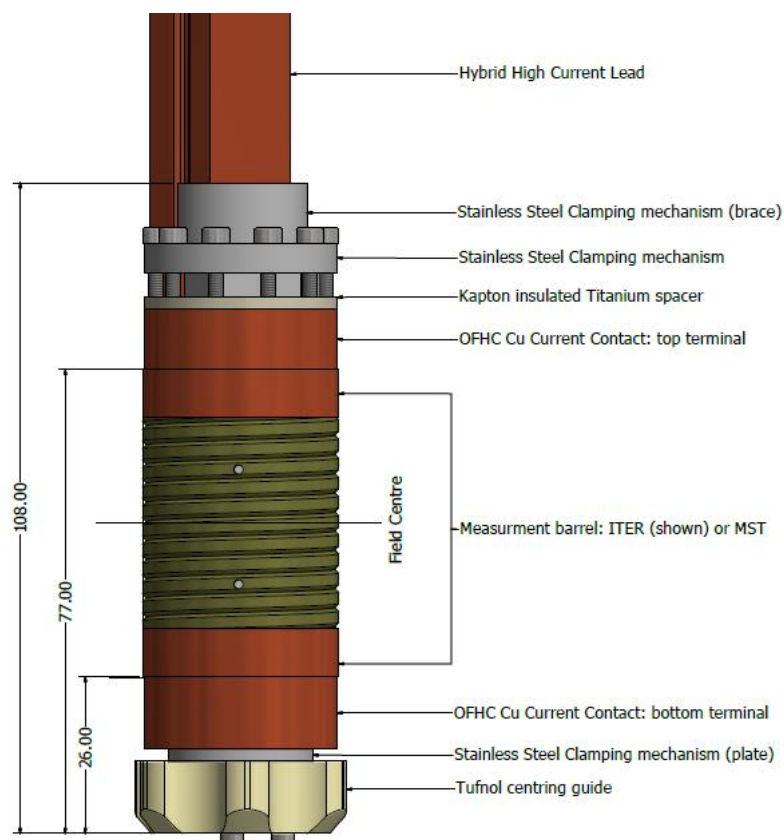
Figure 3.5 : CAD model of the bottom end of the new design probe with components and dimensions labelled in the z-direction.

probe is assembled from two parts, the probe head and the probe's bottom end. The head of the probe was manufactured for the Jefferson Laboratory "JLab" measurements of Rutherford cables. Previous measurements were performed using probe currents up to 1000 A and in magnetic fields from 0 to 4 T [51]. Before the experimental campaign, the probe head was disassembled, inspected, cleaned, and then reassembled to ensure no visible faults and no loose connections. The assembly of parts at the bottom end of the probe that includes the newly designed components are shown in Figure 3.5. Photographs of the manufactured and assembled probe are shown in Figure 3.6 (a) and the probe in the magnet, with external current leads attached to the probe head current contact shown in Figure 3.6 (b). A clamp and bubblers (not visible) details outlined in section 3.4.2.

3.4.1. Probe Assembly

The probe is assembled with the measurement barrel between the current contacts. External to the probe, the high current flows through copper cables. Due to the resistive material and high currents, the cables heat up due to Joule heating. As these resistive cables are thermally connected to the internal current leads, which go down into the liquid helium, it is necessary to allow time for them to cool between each transport measurement.

(a)   (b)
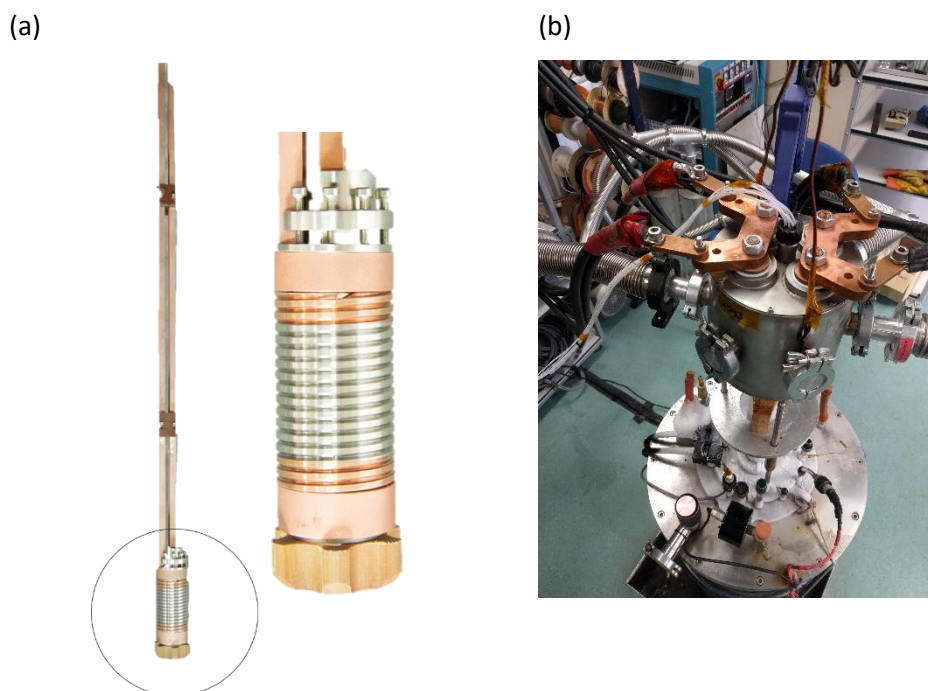
Figure 3.6 : (a) Photograph of the bottom half of the probe assembly, with a larger view of the barrel and terminal connection. (b) The probe head with electrical connections, clamps, and flexible corrugated hoses for the bubblers to maintain the helium pressure.

3.4.2. External Constraints and Circuity

The measurements were performed in a wet bore (38 mm diameter) 15 T vertical superconducting magnet system cooled by liquid helium. The applied magnetic field has an accuracy of 1 % and a precision of 0.5 % [52]. The field homogeneity has a uniformity better than ± 2 % over the length of the specimen between the voltage contacts. The requirement for measurement is a maximum periodic and random deviation of the magnetic field less than ± 1 % [53]. The magnet is homogenous to 10^{-3} over a 10 mm diameter sphere volume (DSV). The magnetic field profile was checked using a Hall probe that was calibrated against an NMR system in Durham University's chemistry department. The magnet is supplied by a 120 A power supply unit, controlled by a computer. The magnet has both a liquid nitrogen and helium jacket. Further details of the magnet system are outlined in [49].

Flexible corrugated hoses were used to attach the Dewar and probe to the bubblers. Typically, two bubblers are attached to the probes head. One bubbler is attached the relief valve on the Dewar, and the other attached to an output port on the probe head. The liquid in the bubbler is salinised water. Using the bubblers minimises variations in pressure, from atmospheric pressure, of the helium in the magnet system. Further details of temperature-pressure relationships for helium are outlined in Section 6.2.3.

The circuitry of the experiment is represented with a block diagram is shown in Figure 3.7. In addition to the magnet system, the sample current source is controlled by the computer. The bubbler is used to stabilise the pressure in the magnet system. The computer uses the software program LabVIEW for data acquisition. The software interfaces with the hardware via a general-purpose interface bus (GPIB) and USB connection to the Keithley 2100 Voltmeters. The data is captured and plotted in real-time during the critical current density measurements. An Oxford Instruments (OI) IPS120-10 power supply unit (PSU) provides the transport current to the strand for up to 120 A. Above 120A, and up to 2000 A, a Power Ten 2000 A PSU is used. The current was increased linearly at a fixed ramp rate during the experiments. The current is ramped at a rate of 4 A·s^{-1}, the standard ramp rate used in the European Organization for Nuclear Research (CERN) is 12.5 A·s^{-1} [23]. The effect of the ramp rate is less than 0.1% [12], repeated measurements at the same B_{App} with different ramp rates did not produce variants in the measured J_{C}.

The voltage is measured with three voltage taps on the strand. The voltage signal across the sample is amplified using an A10 nano-volt amplifier with a gain of 50 k. The amplifier is battery supplied and the output is connected to the Keithley 2100. A standard resistor is used as a resistive shunt. The current through the strand is determined with a high accuracy using the standard shunt.

From the voltage and the gauge length, the electric field is calculated. The length between each tap is 250 ± 1 mm for the ITER barrel and 250 ± 2 mm for the MST barrel. For the standard ITER barrel design, a marker was designed by the reference laboratory which when placed over the barrel and aligned gives the positions of the voltage taps. A permanent marker with 0.6mm width tip marks the region of the strand which is then stripped of its copper coating, pre-tinned and voltage taps attached with Pb-Sn solder. The central position on the MST barrel was marked using this system. For the top and bottom 250 mm voltage taps, a new system was designed. From the radius of the barrel with the strand wound on to it, the vertical and horizontal displacement from the centre for the 250 mm length taps was calculated. A simple grid was designed shown in Figure 3.8, which was transferred to the barrel by printing and copying on to Kapton tape. When the sample was removed from the MST barrel the length of voltage taps was measured and was 501.00 ± 0.05 mm. The uncertainty of positioning the voltage taps is small, relative to the length of the sample is measured over, and the system for positioning contacts above reduces the error.
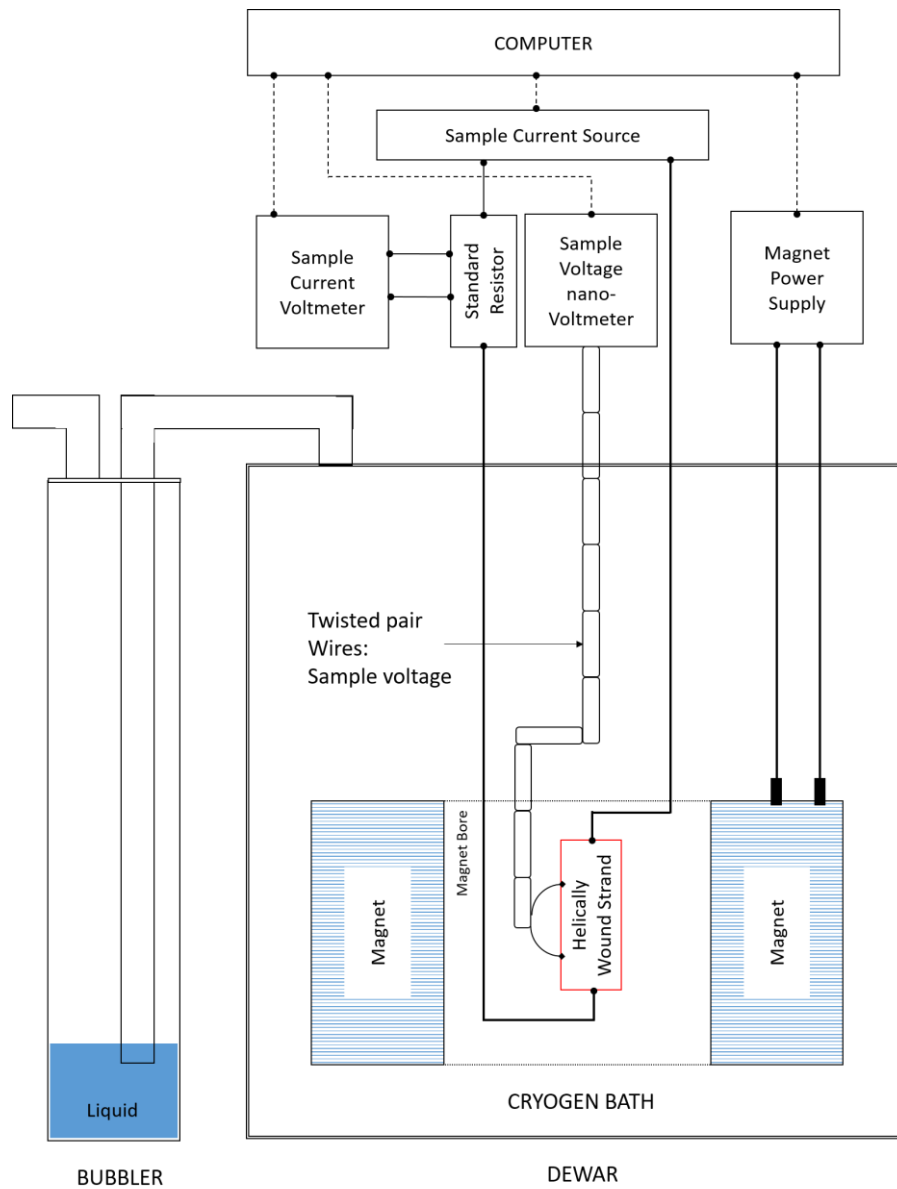
Figure 3.7 : Block diagram of equipment for transport measurement of the critical current density. The data acquisition is controlled using the computer. Pressure and temperature are maintained in the Dewar using bubblers. Dashed lines are used for signal communication and solid lines for electrical leads.
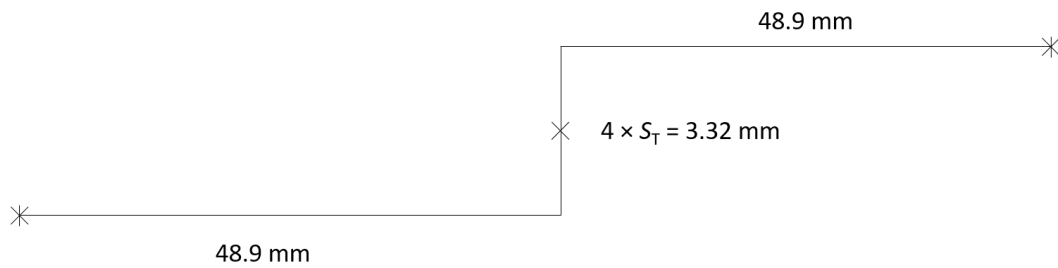
Figure 3.8 : Voltage tap guide for marking positions on the MST barrel [Figure not to scale].

The electric field can be determined from the top 250 mm, the bottom 250 mm, or the whole 500 mm length. The voltage taps were twisted at the position of the top contact, and the middle and bottom voltage taps are wound parallel to the sample on the measurement barrel. The parallel winding minimises inductive voltages for the helical geometry. Twisting the voltage leads reduces the electrical noise arising from magnetic-field variations or motion of the strand. Continuous leads were not used in the probe. There is a ten-pin plug at the top of the probe, and voltage taps attached near the bottom. The noise floor is given by the Johnson noise voltage due to resistance, R, at a finite temperature T,

$$V_{\mathrm{rms}} = (4k_{\mathrm{B}}T(\Delta f)R)^{1/2},\tag{3.4}$$

which is where k_{B} is the Boltzmann constant, and Δf is approximately the inverse time-constant of the amplifier.

3.4.3. High Current Leads and Current Terminals to Measurement Barrel

The current leads internal to the probe head were designed previously, and are manufactured from brass. Brass was selected as it has a much lower thermal conductivity (109 W·m^{-1}·K^{-1} [26]) than copper at low temperature, and the resistivity is less temperature-dependent than copper [54, 55].

The high current leads that connect to the head are newly designed, specifically to transport large current without thermal runaway or burnout. The two halves of the high current leads and current terminals to the barrel were manufactured from single pieces of OFHC copper. In addition to OFHC, both LTS and HTS are soldered into the current leads. Hybrid current leads can reduce heat load as long as they operate below the critical current density of the superconductor in the leads [56]. Significant static boil-off due heat transfer from room temperature to the helium bath is a problem using an entirely copper current lead and terminal.

Both the current leads and current terminals have a recessed design shown in Figure 3.9. In the three deepest channels of the recess, two strands of Nb-Ti are soldered side-by-side using Pb-Sn solder and then covered with Pb-Sn solder. A 12 mm wide HTS American Superconductor Corporation (AMSC) superconducting tape is soldered on top of the Pb-Sn layer using Bolton Metals Cerrolow-136 [Pb$_{18}$Sn$_{12}$Bi$_{49}$In$_{21}$ (wt %)] [57]. The Cerrolow-136 solder is used for bonding the HTS as the maximum temperature required to melt the solder is 75°C, low enough to ensure the tape is not delaminated or damaged [58].
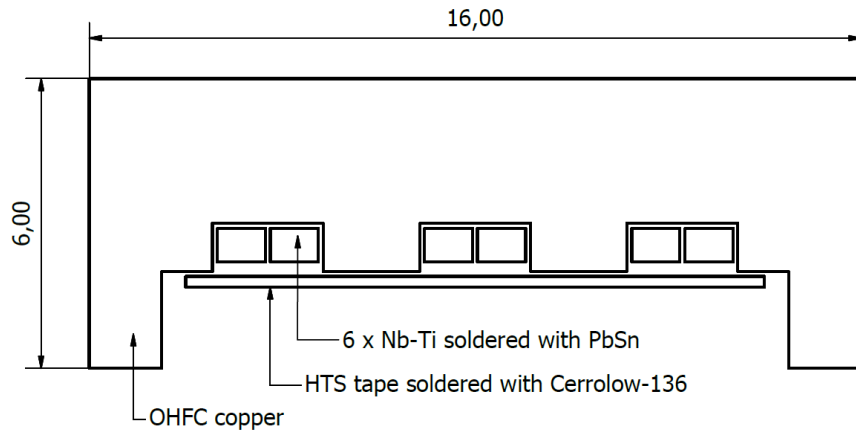
Figure 3.9 : Cross-sectional design of the hybrid high current leads recessed for LTS and HTS material to be soldered into. Using both LTS and HTS increases the current carrying capacity of the leads, and over the range at which the current transfer can operate. [mm]

(a)

(b)

(c)

(d)
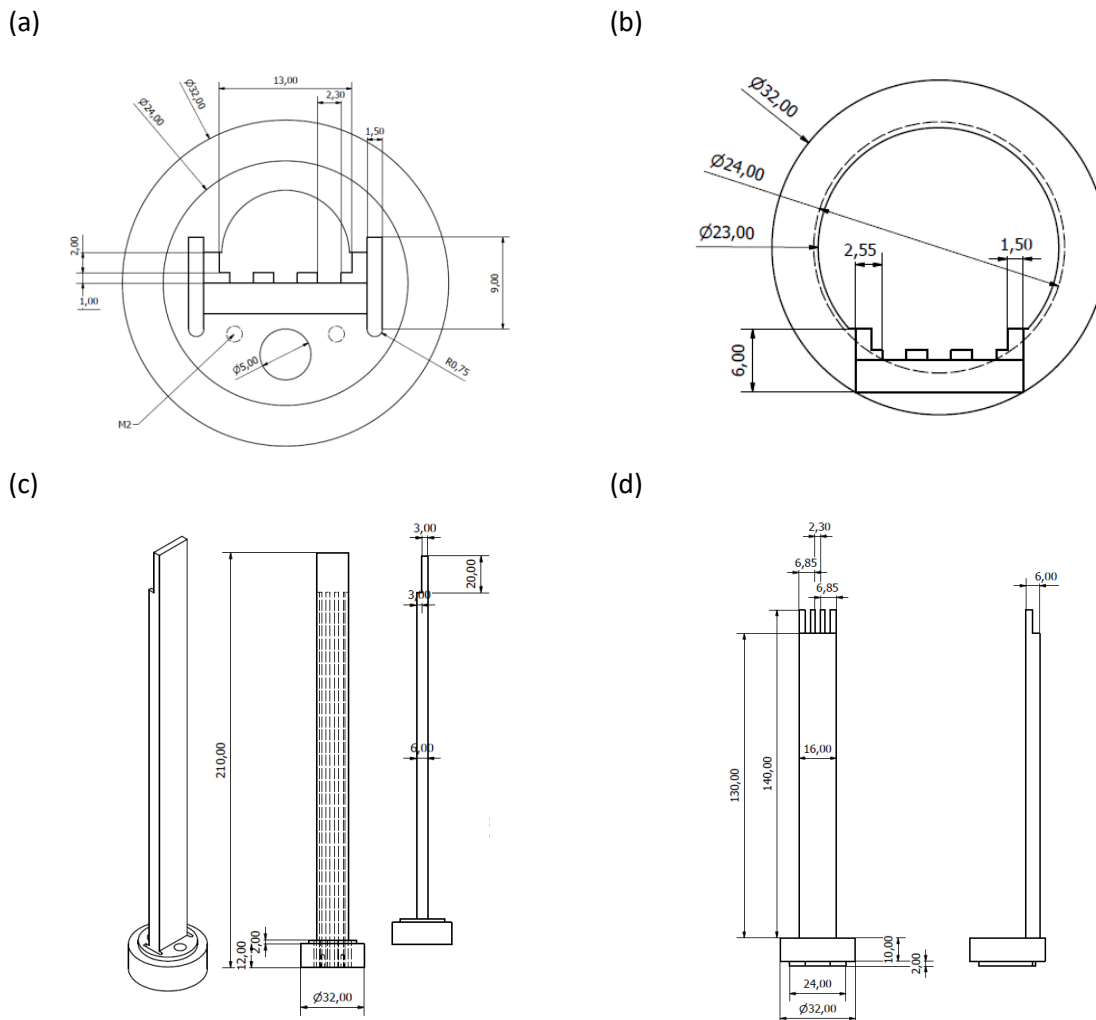
Figure 3.10 : Drawings of measurement probe current terminals. (a) Bottom current terminal for the barrel. (b) Top current terminal for the barrel. (c) Bottom current terminal for the barrel with high current lead. (d) Top current terminal for the barrel with high current leads. [mm].

The design of the current terminals maximises the cross-sectional area for current transfer, with the same outer diameter as the barrel, and a 2 mm high lip with an internal diameter of 24 mm to align the barrel centrally shown in Figure 3.10. The recessed profile (Figure 3.9) is cut into the top and bottom copper terminal to the barrel shown in Figure 3.10 (a, b). The bottom terminal has a is slightly off centre current lead that goes through the barrel shown in Figure 3.10 (a, c). The bottom terminal has a 5 mm diameter hole for helium flow. The M2 holes are for attaching the Tufnol centring guide, and a rectangular cut-out is to push through the stainless-steel brace. The top terminal, shown in Figure 3.10 (b, d) has an inner diameter of 23 mm, to ensure that the current leads do not short to the bottom terminal current lead.

Resistive joints are a problem due to Joule heating. To minimise heating in the region where the strand is measured the joint in the current lead is 198 mm above the bottom terminal to the barrel and 172 mm above the centre of the measurement barrel. The lengths of the current leads for both the top and bottom terminal is designed to ensure that the assembly aligns for connecting to the probe head. The bottom and top terminals are machined from single pieces of OHFC and are shown in Figure 3.10 (c, d).

3.4.4. Helium Flow and Static Boil-Off

When the probe is in the magnet, the cryogens boil-off. The probe is designed with a maximum diameter of 32 mm, 6 mm smaller than the magnet's bore. M2 clearance or greater in the probe components ensure helium flow. The gas flow past the current leads prevents overheating and reduces helium consumption [59]. As a change in the helium level can result in a different strand performance, during the experiment the volume of helium in the magnet is monitored. When measuring in low B_{App} the high transport currents and the time taken to measure the transition, typically between 120 and 480s, resulted in significant boil-off of helium.

3.4.5. Lorentz Force

The strand is measured with current flowing in the strand in both directions with a fixed B_{App} orientation. Strand movement may lead to additional voltage noise, variations in the measured J_{C} or even thermal runaway. In the measurements presented here, the strand is not bonded to the measurement barrel. In the helix geometry, the Lorentz force (F_{L}) on the strand will be "compressive or explosive" [60]. The F_{L} is directed inwards in the standard characterisation measurements. The titanium section of the measurement barrel provides support for the strand. The maximum F_{L} in the measurement is calculated using the magnetic field at the maximum measured critical current of 2.3 kN·m^{-1}. The F_{L} is constrained by the axial strength of the wire itself. At zero applied magnetic field,

the Lorentz force is entirely due to self-field. The results at zero applied field were repeatable and independent of the direction of current flow. The hybrid high current leads were parallel to the stray field of the magnet ($J \parallel B = 0$) and therefore did not require significant additional mechanical support [20].

3.5.   Benchmarking and Verification

The superconducting Nb-Ti and Nb$_3$Sn strands for the ITER machine are manufactured by several domestic agencies [61]. To ensure uniform production quality, reference laboratories have measured the properties of the superconducting strands. Worldwide benchmarking is performed to ensure reliable results [7]. Strands are characterised by several institutes [36, 62-65]. Benchmarking is performed at magnetic fields of 6.4 T for Nb-Ti at 4.22 K [9] and 12 T for Nb$_3$Sn [66]. In benchmarking, the strands are distributed, mounted, and measured. The results are then reported, with some variations in the data [67]. The largest differences in the measured I_C were at the high magnetic fields [7]. The national high magnetic field laboratory (NHFML) in the USA has performed verification tests on ITER materials [68]. Durham's fusion reference laboratory has reported cryogenic and room temperature measurements of the ITER PF coil conductors as part of the European contribution to ITER via a Fusion for Energy (F4E) contract.

Similar transport $J_C(B)$ measurements of the ITER PF Nb-Ti strands have been reported in the literature for a range of fields and temperatures. Data from B_{App}= 1.5 to 11 T and T = 3.5 to 7.0 K [69]; B_{App} = 4 to 10 T and T = 4.2 K to 7.5 K [70]; and B_{App}= 4 to 8 T and T = 3.5 to 6.0 K [71]. The measurements presented in this thesis consider a large range of fields, with a minimum B_{App}= 0 T.

3.5.1. Comparison with Durham Measurements

The critical current of strand DR 4810 is plotted as a function of the applied field shown in Figure 3.11 The comparison shows good agreement between the results from the Durham reference laboratories measurement and those undertaken for this work using the new probe. The differences in the critical current at the benchmarking applied magnetic fields (4 to 6.4 T) were less than 1 A, for details see Table 3.4.

3.5.2. Comparison with Literature Values

The measurement of the critical current of strand DR 4810 using this new probe is compared with the same *type* of Nb-Ti strand in the literature [62, 65]. One thing to note is that the data in these papers are from measurements on a non-standard barrel. The ITER measurement barrel, has an outer diameter of 32, while [65] are measurements on a barrel with an outer diameter of 18 mm. The other
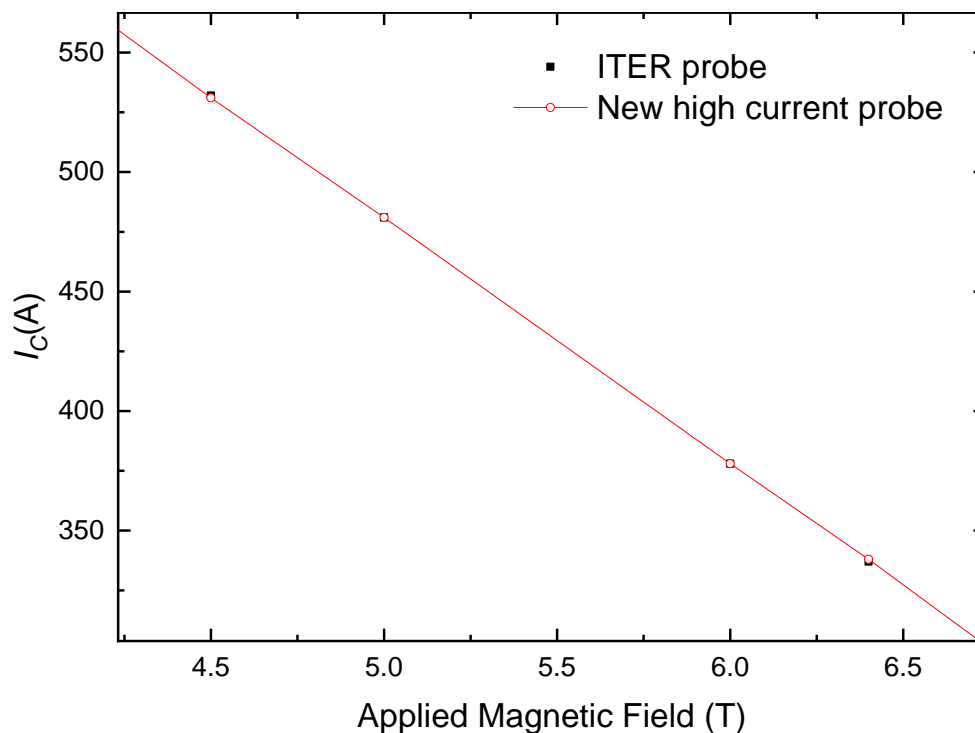
Figure 3.11 : Comparison of the critical current of the *same strand* (DR 4810) measured on two probes in Durham (new high current probe and ITER probe).

dimensions of the barrel are not provided. In chapter 5 the differences in self-field with geometry are calculated, the smaller outer diameter measurement barrel results in a different self-field distribution.

The $I_C(B)$ data in the paper by Karasev [62] has been corrected using the self-field correction term, defined in [25] which will be outlined in section 5.2.3.5. The difference in the measurement data on the new probe and the literature data is shown in Figure 3.12. The difference between the measured I_C and literature values is larger than the difference between the measurements of the strand in Durham. The measurement data is plotted in [62] and [65], additionally the values of $I_C(B)$ have been calculated using the fit parameters, calculated using the Bottura fit [72]. How well the data is fit with the single or two-component model may result in differences in the value of $I_C(B)$. The data are summarised in Table 3.4.

It can also be assumed that it is possible at B_{App} = 6.4 T, the Durham measurements produced values within 2 A of the average value (336.4 A) [14], the values of 351 A, and 329 A are within the 2σ value.
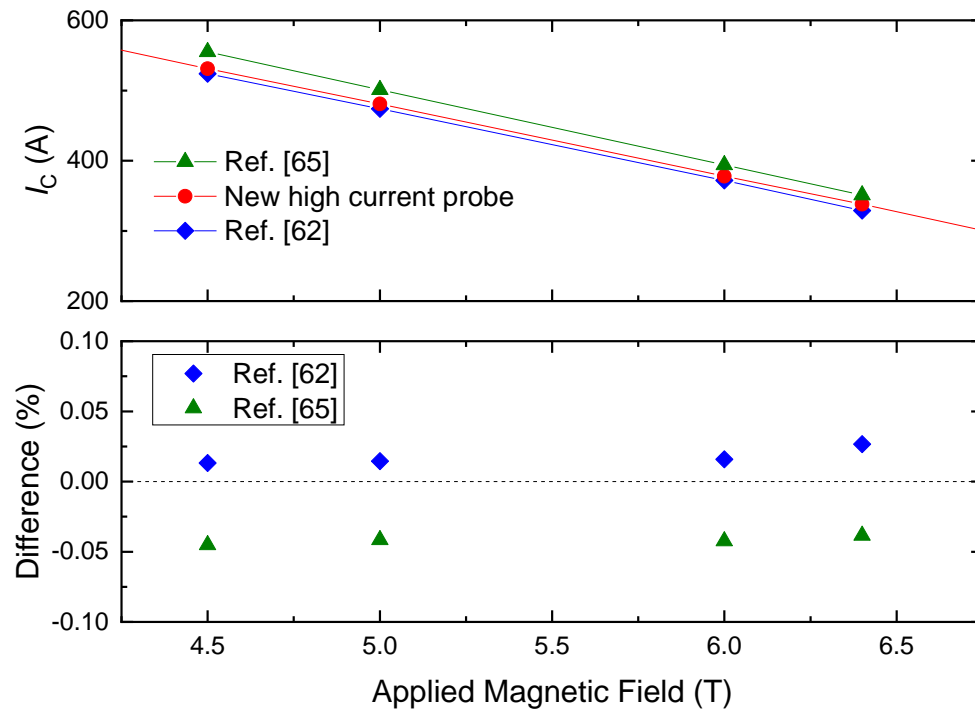
Figure 3.12 : (Top) Comparison of literature values of critical current with new high current probe measurements of strand DR 4810. (Bottom) Percentage difference of critical current between the new high current probe measurements and the literature values as a function of the applied magnetic field.

Applied Field, B_{App} [T]	I_C [A]			
	Strand DR 4810:			
	Durham Reference Laboratory	New high current probe	[65]*	[62]
4.5	532	531	555	524
5	481	481	501	474
6	378	378	394	372
6.4	337	338	351	329

Table 3.4 : Measured critical current values of ITER type 1 Nb-Ti strands at benchmarking fields, * self-field correction defined in [25] has been applied to data [65].

3.6.   Conclusions

The properties of the Nb-Ti strand characterised in this thesis were outlined. The measurement barrel designed to investigate the self-field was described. The main difference between the standard ITER barrel and the custom-designed minimum separation of turns barrel is the separation of turns. A high-current probe has been designed, commissioned, and constructed for low-field high-current transport measurements of Nb-Ti ITER PF type 1 strands at 4.22 K. The probe is designed for Durham's vertical 15 T magnetic system. The use of both LTS and HTS in the high current leads enable transport measurements at high currents. The clamping mechanism and the material choices ensured current transfer through the terminal to the barrel is achieved. The measured critical current values measured were compared with internal benchmarking experiments and good agreement is found. Further details of the Nb-Ti strand can be found in A.1, and details of the probe and barrel can be found in A.2.

References for chapter 3:

[1]   P. J. Lee and D. C. Larbalestier, "Niobium-Titanium Superconducting Wires: Nanostructures by Extrusion and Wire Drawing," *Wire Journal International,* vol. 36, no. 2, pp. 61-66, 2003.

[2]   C. Kittel, *Introduction to Solid State Physics*, Eighth ed. John Wiley & Sons, 1996, p. 673.

[3]   L. D. Cooley, P. A. Lee, and D. C. Larabalestier, "Processing of low Tc conductors: the alloy Nb–Ti," in *Handbook of Superconducting Materials*, vol. I: Superconductivity, Materials and Processes, D. A. Cardwell and D. Ginley, Eds. London: Institute of Physics 2003, pp. 603-638.

[4]   K. Osamura, *Composite Superconductors* (Applied Physics). New York: M. Dekker, 1994, p. 440.

[5]   W. T. Liu, X. H. Liu, Y. Feng, H. J. Xie, T. C. Wang, and J. F. Li, "Development of Fine Filament NbTi Superconducting Strands for ITER," *IEEE Transactions on Applied Superconductivity,* vol. 20, no. 3, pp. 1504-1506, 2010.

[6]   C. P. Poole, H. A. Farach, and R. J. Creswick, "Type II Superconductivity," in *Superconductivity*New York: Dover Publications, 2007, pp. 337 - 384.

[7]   I. Pong *et al.*, "Worldwide Benchmarking of ITER Internal Tin Nb_3Sn and NbTi Strands Test Facilities," *IEEE Transactions on Applied Superconductivity,* Article; Proceedings Paper vol. 22, no. 3, p. 4802606, Jun 2012, Art. no. 4802606.

[8]   N. Mitchell, A. Devred, P. Libeyre, B. Lim, and F. Savary, "The ITER Magnets: Design and Construction Status," *IEEE Transactions on Applied Superconductivity,* vol. 22, no. 3, pp. 4200809-4200809, 2012.

[9]   M. Sborchia *et al.*, "Overview of ITER Magnet System and European Contribution," *IEEE/NPSS 24th Symposium on Fusion Engineering,* pp. 1-8, 2011.

[10]   A. Devred *et al.*, "Status of ITER Conductor Development and Production," *IEEE Transactions on Applied Superconductivity,* vol. 22, no. 3, pp. 4804909-4804909, 2012.

[11]   (21/05/2018). *Cheptsky Mechanical Plant: Production Superconductors*. Available: http://www.chmz.net/en/product/sp/

[12]   L. F. Goodrich, D. F. Vecchia, E. S. Pittman, J. W. Ekin, and A. F. Clark, "Critical current measurements on a NbTi superconducting wire standard reference material," N.B.S. special publication, BoulderNo. 260 - 91, 1984.

[13]   J. W. Ekin, "Relationships between critical current and stress in NbTi," *IEEE Transactions on Magnetics,* vol. 23, no. 2, pp. 1634-1637, 1987, Art. no. 1064844.

[14]   M. J. Raine, T. Boutboul, and D. P. Hampshire, "Verification of Nb_3Sn and Nb-Ti strands for the ITER toroidal and poloidal field magnets," Private Communication, 2018.

[15]   M. N. Wilson, *Superconducting Magnets*. Oxford, UK: Oxford University Press, 1986.

[16]   M. N. Wilson, "NbTi superconductors with low ac loss: A review," *Cryogenics,* vol. 48, no. 7, pp. 381-395, 2008/07/01/ 2008.

[17]   B. Bordini, L. Bottura, L. Oberli, L. Rossi, and E. Takala, "Impact of the Residual Resistivity Ratio on the Stability of Nb_3Sn Magnets," *IEEE Transactions on Applied Superconductivity,* vol. 22, no. 3, p. 4, 2012, Art. no. 4705804.

[18]   C. Zhou, Y. Miyoshi, E. P. A. v. Lanen, M. Dhallé, and A. Nijhuis, "Direct measurement of inter-filament resistance in various multi-filamentary superconducting NbTi and Nb_3Sn strands," *Superconductor Science and Technology,* vol. 25, no. 1, p. 015013, 2012.

[19]   C. Zhou, Y. Miyoshi, E. P. A. van Lanen, M. Dhalle, and A. Nijhuis, "Inter-filament resistance, effective transverse resistivity and coupling loss in superconducting multi-filamentary NbTi and Nb_3Sn strands," *Superconductor Science and Technology,* Article vol. 25, no. 6, p. 9, Jun 2012, Art. no. 065018.

[20]   M. J. Raine, S. A. Keys, and D. P. Hampshire, *Characterisation of the Transport Critical Current Density for Conductor Applications*. Accepted by Taylor and Francis, 2017.

[21]   W. V. Hassenzahl, "Study of the effects of copper to superconductor ratio on stability," *Cryogenics,* vol. 29, no. 6, pp. 637-641, 1989/06/01/ 1989.

[22]   T. Baumgartner *et al.*, "Evaluation of the Critical Current Density of Multifilamentary Nb₃Sn Wires From Magnetization Measurements," *IEEE Transactions on Applied Superconductivity,* vol. 22, no. 3, p. 6000604, 2012, Art. no. 6000604.

[23]   T. Boutboul, P. Lezza, and R. Wolf, "Low-current Resistance of Multifilamentary Superconducting Cu/NbTi Strands," in "Accelerators and Storage Rings," CERN2003.

[24]   C. A. Schneider, W. S. Rasband, and K. W. Eliceiri, "NIH Image to ImageJ: 25 years of image analysis," *Nature Methods,* vol. 9, p. 671, 06/28/online 2012.

[25]   B. Bordini, "Self-Field Correction in Critical Current Measurements of Superconducting Wires Tested on ITER VAMAS Barrels," in "CERN-ITER Collaboration Report," ITEREDMS Nr: 1105765, 2010.

[26]   "CRYODATA software," in *CryoComp*, 5.2 ed: Cryodata Inc. , 1999.

[27]   C. Schmidt, "Simple Method to Measure the Thermal Conductivity of Technical Superconductors, e.g., NbTi," *Review of Scientific Instruments,* Article vol. 50, no. 4, pp. 454-457, 1979.

[28]   Y. F. Bychkov, R. Herzog, and I. S. Khukhareva, "Thermal conductivity and electrical resistivity of Nb-Ti alloys at low temperatures," *Cryogenics,* vol. 21, no. 12, pp. 741-745, 1981/12/01/ 1981.

[29]   P. Duthil, "Material Properties at Low Temperature," in *Proceedings of CAS - CERN Accelerator School: Course on Superconductivity for Accelerators*, European Organization for Nuclear Research (CERN), 2014, p. 592.

[30]   H. Krauth, "Conductors for d.c. applications," in *Handbook of Applied Superconductivity*, vol. 1, B. Seeber, Ed. London: IOP publishing, 1998, pp. 397-427.

[31]   Z. J. J. Stekly and J. L. Zar, "Stable superconducting coils," *IEEE Transactions on Nuclear Science,* vol. 12, p. 367, 1965.

[32]   Y. Iwasa, *Case studies in superconducting magnets: design and operational issues*. New York: Plenum Press, 1994.

[33]   Z. J. J. Stekly, R. J. Thome, and B. Strauss, "Principles of Stability in Cooled Superconducting Magnets," *Journal of Applied Physics,* vol. 40, p. 2238, 1969.

[34]   Y. Iwasa, "Stability and protection of superconducting magnets-a discussion," *IEEE Transactions on Applied Superconductivity,* vol. 15, no. 2, pp. 1615-1620, 2005.

[35]   L. Dresner, "SUPERCONDUCTOR STABILITY, 1983 - A REVIEW," (in English), *Cryogenics,* Review vol. 24, no. 6, pp. 283-292, 1984.

[36]   Y. Karasev *et al.*, "Characterization of Nb-Ti Strands in the Process of Industrial Production for the ITER Poloidal Field Coils," *IEEE Transactions on Applied Superconductivity,* vol. 26, no. 4, 2016, Art. no. 6000104.

[37]   A. K. Ghosh, "Effect of Copper Resistivity and Filament Size on the Self-Field Instability of High-J(c) Nb₃Sn Strands," *IEEE Transactions on Applied Superconductivity,* vol. 23, no. 3, p. 7, 2013, Art. no. 7100407.

[38]   M. D. Sumption, "Stability Nb₃Sn Conductors; Magnetic and Self-Field Instability Consideration at 4 k and 2 K," in *Advances in Cryogenic Engineering*, vol. 1219, U. Balachandran, Ed. (AIP Conference Proceedings, Melville: Amer Inst Physics, 2010, pp. 199-207.

[39]   P. Lee, "Superconducting Wires and Cables: Materials and Processing " in *Concise Encyclopedia of Composite Materials* Oxford: Pergamon Press, 1994, p. 826.

[40]   D. Ciazynski *et al.*, "Test results on the first 50 kA NbTi full size sample for the International Thermonuclear Experimental Reactor," *Superconductor Science and Technology,* vol. 17, no. 5, pp. S155-S160, 2004/02/20 2004.

[41]   Y. V. Karasev *et al.*, "The Effect of Final Processing Steps on RRR of NbTi Strands for ITER PF Coils " in *Advances in Cryogenic Engineering, Vol 58*, vol. 1435, U. Balachandran, Ed. (AIP Conference Proceedings, Melville: Amer Inst Physics, 2012, pp. 182-189.

[42]   IEC, "Superconductivity - Part 2: Critical current measurement - DC critical current of Nb$_3$Sn composite superconductors," in *International Standard*1 ed.: International Electrotechnical Commission, 2006, pp. IEC 61788-2:2006.

[43]   A. Godeke *et al.*, "Interlaboratory Comparisons of NbTi Critical Current Measurements," *IEEE Transactions on Applied Superconductivity,* vol. 19, no. 3, pp. 2633-2636, 2009.

[44]   A. Godeke *et al.*, "Novel Methods for the Measurement of the Critical Current of Superconducting Wires," in *Advances in Cryogenic Engineering, Vol 58*, vol. 1435, U. Balachandran, Ed. (AIP Conference Proceedings, Melville: Amer Inst Physics, 2012, pp. 209-216.

[45]   A. Godeke *et al.*, "A Review of Conductor Performance for the LARP High-Gradient Quadrupole Magnets," *Superconductor Science and Technology,* Article vol. 26, no. 9, p. 15, Sep 2013, Art. no. 095015.

[46]   M. Polak *et al.*, "Current transfer lengths and the origin of linear components in the voltage-current curves of Ag-sheathed BSCCO components," *Superconductor Science and Technology,* vol. 10, no. 10, pp. 769-777, 1997.

[47]   SuperPower-Furukawa. (11/10/2017). *SuperPower 2G HTS Coated Conductors*. Available: www.superpower-inc.com/content/2g-hts-wire

[48]   P. Sunwong, J. S. Higgins, and D. P. Hampshire, "Probes for investigating the effect of magnetic field, field orientation, temperature and strain on the critical current density of anisotropic high-temperature superconducting tapes in a split-pair 15 T horizontal magnet," *Review of Scientific Instruments,* vol. 85, no. 6, p. 065111, 2014, Art. no. 065111.

[49]   N. Cheggour and D. P. Hampshire, "A probe for investigating the effect of magnetic field, temperature and strain on transport critical currents in superconducting tapes and wires," *Review of Scientific Instruments,* vol. 71, p. 4521, 2000.

[50]   D. M. J. Taylor and D. P. Hampshire, "Properties of helical springs used to measure the axial strain dependence of the critical current density in superconducting wires," *Superconductor Science and Technology,* vol. 18, pp. 356-368, 2005.

[51]   P. K. Ghoshal *et al.*, "Design and Evaluation of Joint Resistance in SSC Rutherford-Type Cable Splices for Torus Magnet for the Jefferson Lab 12-GeV Upgrade," *IEEE Transaction on Applied Superconductivity,* vol. 26, no. 4, p. 4800304, 2016.

[52]   "VAMAS Technical Working Party for Superconducting Materials - Recommended standard method for determination of d.c. critical current of Nb$_3$Sn multifilamentary composite superconductor," *Cryogenics,* vol. 35 S105, 1995.

[53]   IEC, "Superconductivity - Part 1: Critical current measurement - DC critical current of Nb-Ti composite superconductors," in *International Standard*: International Electrotechnical Commission, 2006, pp. IEC 61788-1:2006.

[54]   J. W. Ekin, *Experimental Techniques for Low-Temperature Measurements*. New York: Oxford University Press, 2007.

[55]   (2013, 21/05/2018). *Materials Properties*. Available: https://trc.nist.gov/ThermoML.html

[56]   P. F. Herrmann, "Current leads," in *Handbook of Applied Superconductivity*, E. B. Seeber, Ed. Bristol: Institute of Physics, 1998, p. 801.

[57]   Y. Tsui, R. Mahmoud, E. Surrey, and D. P. Hampshire, "Superconducting and mechanical properties of low-temperature solders for joints," *IEEE Transaction on Applied Superconductivity,* vol. 26, no. 3, p. 6900204, 2016.

[58]   Y. Tsui, E. Surrey, and D. P. Hampshire, "Soldered Joints - an essential component of demountable high temperature superconducting fusion magnets," *Superconductor Science and Technology,* vol. 290, p. 075005, 2016.

[59]   H. D. Ramsbottom and D. P. Hampshire, "A probe for measuring magnetic field profiles inside superconductors from 4.2 K up to T$_C$ in high magnetic fields," *Measurement Science and Technology,* vol. 6, pp. 1349-1355, 1995.

[60]   J. W. Ekin, "Experimental Techniques for Low-Temperature Measurements," New York: Oxford University Press, 2007, p. 567.

[61]   (16/03/2020). *About: ITER Members*. Available: https://www.iter.org/proj/Countries

[62]   Y. V. Karasev *et al.*, "J_C(B,T) Characterization of Commercial NbTi Strands for the ITER Poloidal Field Coils by Transport and Magnetization Methods," *IEEE Transactions on Applied Superconductivity,* vol. 23, no. 3, June 2013, Art. no. 6001304.

[63]   Y. V. Karasev *et al.*, "Study of the Temperature and Field Dependence of the Critical Currents in Nb-Ti Strands for the ITER Poloidal Field Magnet System," *IEEE Transactions on Applied Superconductivity,* Article vol. 24, no. 3, Jun 2014, Art. no. 6000204.

[64]   L. Muzzi *et al.*, "Test Results of a NbTi Wire for the ITER Poloidal Field Magnets: A Validation of the 2-Pinning Components Model," *IEEE Transactions on Applied Superconductivity,* Article vol. 21, no. 3, pp. 3132-3137, Jun 2011.

[65]   N. Salunin *et al.*, "The J_C(B, T) Characterization of Commercial NbTi Strands for ITER PF 1&6 Coils," *IEEE Transactions on Applied Superconductivity,* Article; Proceedings Paper vol. 22, no. 3, p. 4, Jun 2012, Art. no. 4804604.

[66]   M. C. Jewell *et al.*, "World-Wide Benchmarking of ITER Nb_3Sn Strand Test Facilities," *IEEE Transactions on Applied Superconductivity,* vol. 20, no. 3, pp. 1500-1503, 2010.

[67]   H. Wada, L. F. Goodrich, C. Walters, and K. Tachikawa, "Second intercomparison of critical current measurements," *Cryogenics,* vol. 35, pp. S65-S80, 1995.

[68]   D. R. McGuire *et al.*, "Verification Testing of ITER Nb_3Sn Strand at the NHMFL," *IEEE Transactions on Applied Superconductivity,* vol. 25, no. 3, pp. 1-4, 2015.

[69]   C. Zhou, D. Bessette, A. Devred, G. Romano, and A. Vostner, "The Scaling Parameterization of ITER Superconducting Nb-Ti Strands Throughout Worldwide Production," *IEEE Transactions on Applied Superconductivity,* vol. 26, no. 4, 2016, Art. no. 6000204.

[70]   L. Zani, E. Mossang, A. Tena, J. P. Serries, and H. Cloez, "J(C)(B, T) Characterization of NbTi Strands used in ITER PF-relevant Insert and Full-Scale Sample," *IEEE Transactions on Applied Superconductivity,* Article; Proceedings Paper vol. 15, no. 2, pp. 3506-3509, Jun 2005.

[71]   F. J. Ridgeon, M. J. Raine, M. Lakrimi, A. Thomas, T. Boutboul, and D. P. Hampshire, "Self-field Effects on J_C(*B*,*T*) Measurements of Nb-Ti Strands in High Magnetic Fields," *IEEE Transactions on Applied Superconductivity,* 2018.

[72]   L. Bottura, "A practical fit for the critical surface of NbTi," *IEEE Transactions on Applied Superconductivity,* vol. 10, no. 1, pp. 1054-1057, 2000, Art. no. 828413.

CHAPTER 4

4.   Superconducting Properties of Titanium Alloys Ti-64 and Ti-6242

In this chapter, the properties of two titanium alloys, Ti-6Al-4V (Ti-64) and Ti-6Al-2Sn-4Zr-2Mo-0.2Si (Ti-6242) are outlined. Typically, the ITER measurement barrels are manufactured from Ti-64, which is problematic as the alloy superconducts, T_C (Ti-64) = 5.12 K. This alternative superconducting current path during the measurement introduces uncertainty in the measurement of J_C. An alternative titanium alloy Ti-6Al-2Sn-4Zr-2Mo-0.2Si (Ti-6242) was measured which has similar physical properties to Ti-64, such as thermal conductivity and electrical resistivity as a function of temperature. With a lower T_C (Ti-6242) = 2.38 K, Ti-6242 alloy is a better choice for manufacturing components for superconducting transport measurements. In chapter 3 the characteristics of the Nb-Ti used in the ITER poloidal field magnets were outlined, this strand is not heated prior to characterisation. The toroidal magnetic field in the ITER magnet system, which provides primary plasma confinement, is manufacture from Nb_3Sn strands which are heat treated (HT) prior to characterisation. The heat-treatment for the Nb_3Sn strand is performed on the ITER measurement barrel, HT Ti-64 alloys were also characterised. The improved understanding of the behaviour of the two titanium alloys as a function of magnetic field improves the analysis of J_C measured using transport methods.

4.1.   Introduction

In standard critical current density (J_C) measurements at liquid helium temperatures, samples are measured on a Ti-6Al-4V wt % (Ti-64) ITER barrel [1, 2]. Ti-64 is the workhorse of the titanium industry covering more than 50 % of uses [3]. The excellent mechanical properties and good machinability of this material make it the material of choice for barrels [4]. Ti-64 is a highly resistive material, even at cryogenic temperatures, due to the high titanium content in solid solution [5]. The alloy's thermal contraction is similar to Nb_3Sn minimising pre-straining of the strands [6] and has low thermal conductivity.

In 1970, Clark published the electrical resistivity of many engineering alloys including the Ti-64 alloy and reported that it exhibits a superconductivity [7] at 4.22 K in magnetic fields of up to a few tesla [4]. Other reports of Ti-64 superconducting properties followed. In 1992 Umezawa showed that the

measured T_C (Ti-64) varied between 4.35 and 6.30 K, depending on oxygen concentration and heat treatment [8]. Divakar showed that T_C of Ti-64 could vary from 1.3 to 5.7 K [9, 10]. Barucci measured a T_C of about 4.38 K using a mutual inductance method [11]. The alloy superconducts, but a history of the material is required to understand the measured value.

As Nb₃Sn conductor is typically reacted on the Ti-64 measurement barrel, and then measured, in addition to the as-supplied material, heat-treated samples were also characterised. As the Nb-Ti conductor studied in this work is not heat treated, the Ti-6Al-2Sn-4Zr-2Mo-0.2Si wt % alloy was measured in the as supplied state only [Ti-6242 (AS)].

4.2.   Materials and Measurements

4.2.1. Ti-64 Phase Diagram

Two elementary structures are found in pure titanium, the alpha (α) and beta (β) phase. The crystal unit cell structure of the α-phase is hexagonal close packed (HCP), and the β-phase body-centred-cubic (BCC). When heated, the allotropic transformation from α to β phase occurs at 882 °C, the β-transus temperature, T_β. In Ti-alloys the α-phase and β-phase are separate by a two-phase ($\alpha + \beta$) region. Ti-64 is categorised as an $\alpha + \beta$ two-phase alloy, while the Ti-6242 is categorised as a near-alpha, or super-alpha alloy, or as a weakly beta-stabilised alpha-beta alloy [5].

Alloying of the titanium both promotes the β crystal structure and optimises the electron density of states [12]. The 6% aluminium addition in both the Ti-64 and Ti-6242 alloys is a potent α-phase stabiliser. Aluminium improves oxidation properties and is probably not superconducting [3]. Alloying with vanadium helps stabilise the β-phase in Ti-64, by lowering the α-β transition temperature. The phase diagram of Ti-6Al-4V is shown in Figure 4.1. In Ti-6242 the 2% molybdenum is a moderate β-phase stabiliser. The tin is an alpha stabiliser, while the zirconiums effect is α or β phase strengthening. The silicon is neutral and improves creep resistance [13].

The properties of $\alpha + \beta$ can be controlled by heat treatment (HT) which adjusts the microstructural and precipitational states of the β component. It is known that temperatures of 620 °C are sufficient to change the microstructure of Ti-alloys [3]. When heated the volume fraction of the β-phase increases, for $\alpha + \beta$ Ti-alloy, with increasing temperature up to the β transus temperature [14]. If the Ti-alloy is heated and cooled below T_β the microstructure will depend on the initial microstructure, and heat treatment conditions. Conditions such as the heating rate, holding temperature, holding time at the temperatures, and cooling conditions. The HT of Ti-64 is outlined in section 4.2.3.
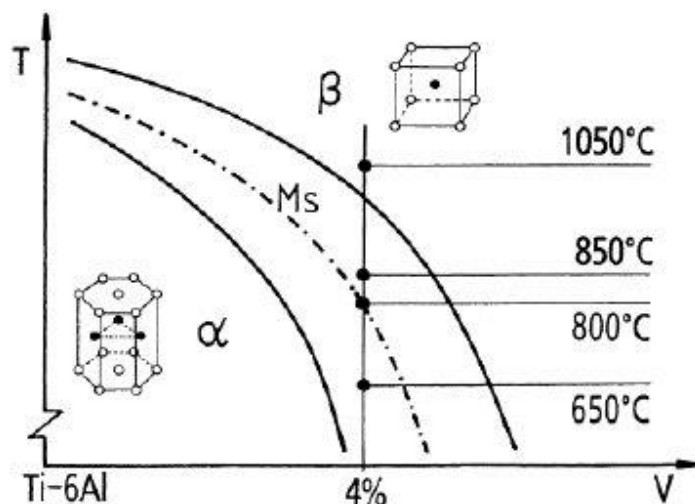
Figure 4.1 : Schematic phase diagram of Ti-6Al-V alloy. The β phase is BCC, while α is HCP. The dashed line is the martensite start temperature. Figure from Ref. [15].

The superconducting state in the Ti-64 is due to the proximity effect of the β phase [16]. The superconductor in proximity to a normal metal may induce pairing correlation in the normal metal. The electrons in the normal metal can carry screening currents. The retained β state has a higher T_C than the α matrix [8].

4.2.2. Material Properties

Ti-64 alloy has excellent strength, good ductility, and desirable corrosion properties. The ideal alternative Ti-alloy for a measurement barrel should have similar normal state electrical, thermal, and mechanical properties to Ti-64. Ti-6242 alloy was identified as a suitable alternative due to its similar properties, detailed in Table 4.1 [5]. Both Ti-6242 and Ti-64 alloys have a high electrical resistivity that does not change significantly from 10 K to room temperature. The properties of both alloys are given in Table 4.1

The origin of the superconducting properties of Ti-alloys can be understood to some degree in terms of the Matthias rules [17]. The elemental components titanium, aluminium, and vanadium all superconduct: T_C (Al) = 0.4 K, T_C (Ti) = 1.2 K, and T_C (V) = 5.38 K. As the vanadium has the highest T_C, it is probable the Ti-64 T_C (Ti-64) $\sim$ 5.12 K, measured in this work, is due to the vanadium [18]. The Ti-6242 alloy is investigated because contains elements with lower values of T_C. The element in Ti-6242 with the highest T_C is tin (Sn) = 3.772 K. The measurements in section 4.3.1 show that the T_C (Ti-6242) $\sim$2.38 K.

The thermal coefficient of linear expansion for both Ti alloys is similar to the intermetallic superconductor Nb_3Sn (i.e., 7.6×10^{-6} K^{-1}). Although the Ti-6242 matches the value more closely, the

Property [Unit]	Ti-64 (AS)	Ti-6242 (AS)
Thermal Conductivity [$W·m^{-1}·K^{-1}$]	7.4	7.0
Thermal Coefficient of linear expansion [$10^{-6} K^{-1}$]	8.0	7.7
Specific Heat Capacity [$kg^{-1}· K^{-1}$]	529	460
Young's Modulus: Tensile [$10^{11} N·m^{-2}$]	1.10	1.14
Young's Modulus: Compressive [$10^{11} N·m^{-2}$]	1.11	1.24

Table 4.1 : Thermal and mechanical properties of titanium alloys [5].

volume of Ti-64 produced results in a less expensive material. Like Nb-Ti, Nb_3Sn strand are composite, the soft copper in the matrix has a higher thermal contraction coefficient, so the linear expansion is not perfectly matched to the Ti alloy [19]. In quantifying the effect of self-field, the low aB_{App} was of interest. The possibility of Ti-64 being superconducting introduces an uncertainty in characterising the strand at low B_{App}. The use of Ti-6242 is not envisaged for all measurement barrels, transport measurements of Nb_3Sn at low B_{App} are limited typically by current supply, in the kA range [20].

4.2.3. Heat Treatment used for Ti-64

The heat-treated Ti-64 samples measured in this work were cut from measurement barrels used to react bronze route [Ti-64(BR)] and internal tin [Ti-64(IT)] Nb_3Sn strands. The heat-treated ITER barrels were processed by the Durham reference laboratory team. The Ti-6242 alloy is only studied in its as-supplied state. Although it was not HT, it is expected that no significant phase change can occur with HT due to its near alpha state [21]. Due to the low thermal conductivity of titanium alloys, the extraction of the small bars from the HT measurement barrels was completed using low machine cutting speeds and large quantities of cutting fluid coolant. The heating produced by extracting the titanium bars from the barrels is assumed negligible.

The barrels are first oxidised in air at 300 °C for 5 hours. The barrels were heat-treated in an argon atmosphere. HT above 400 °C requires atmospheric protection to limit oxygen and nitrogen forming a surface, an α-case. The heat treatment schedules for the Nb_3Sn strands are outlined in Table 4.2 and Table 4.3. The bronze route (BR) heat treatment is longer at 480 hours than the internal tin (IT) 300 hours. The time of the HT affects the particles size, larger particles can result in an increased T_C. The HT profiles are shown in Figure 4.2, with maximum temperature (BR) 620 °C and (IT) 650 °C. A ramp rate of 5 °C·h^{-1} between the dwell temperature was used throughout. After the final heat treatment dwell, the temperature was rapidly decreased to room temperature by switching off the furnace.
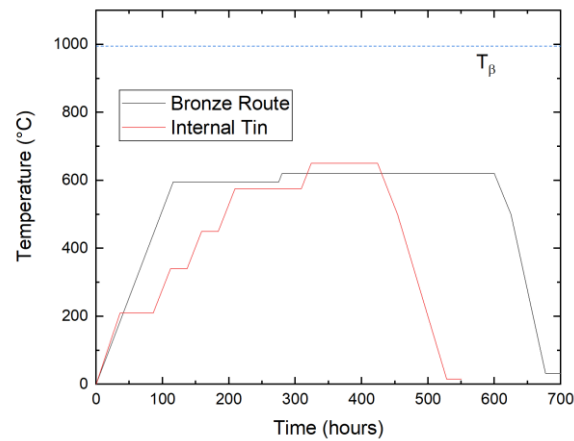
Figure 4.2 : Heat treatment (HT) profiles for winding and reacting Nb3Sn superconductors, using Internal Tin and Bronze Route compared with the Ti-64 beta transus temperature (T_β). For details of HT see Table 4.2 and Table 4.3.

Temperature [°C]	595	620	500
Time [hours]	160	320	0

Table 4.2 : Bronze route heat treatment schedule for the Nb$_3$Sn strand, mounted on Ti-64 barrel measured in this work.

Temperature [°C]	210	340	450	575	650	500
Time [hours]	50	25	25	100	100	0

Table 4.3 : Internal tin heat treatment schedule for the Nb$_3$Sn strand, mounted on Ti-64 barrel measured in this work.

The highest temperature in both HTs of Ti-64 are below T_β = 995 ± 20 °C. In Ref. [22] the phase compositions of Ti-64 was measured with varied temperature HT. Analysing the microstructure, the α-phase grows within the β-phase. It is possible to use synchrotron X-ray diffraction spectra of the $(110)_\beta$, the $(002)_\alpha$, and $(101)_\alpha$ reflections to extract phase α and β-phase percentages [23]. These measurements were not performed for this thesis. When considering the resistivity measurements, the HT can result in defects and inhomogeneities in the Ti alloy sample, the thermal precipitates created have a distribution of sizes. The transition to the superconducting state is broadened, when samples that are β quenched [16].

Figure 4.3 : Titanium alloy bar mounted on PPMS resistivity puck for transport measurements.

4.2.4. Transport Measurements

Resistivity and the E-J characteristics were measured as a function of temperature and magnetic field using a standard four-terminal measurement. The temperature and magnetic field were controlled using the Quantum Design, physical property measurement system (PPMS). Magnetic fields of up to $B_{App} = 9$T were possible in Durham's PPMS system.

For the resistivity measurements, the internal PPMS circuitry was used. The titanium bar samples (approximately 1 × 1 × 10 mm) were sequentially mounted on to a PPMS resistivity puck shown in Figure 4.3. Current and voltage leads were connected with silver paint to the small Ti bars, the voltage gauge length was approximately 5 mm. Room temperature measurements of Ti bars approximately 1 × 1 × 35 mm, with a 20 mm voltage gauge length, were also measured. With measurements data at 293 K for both Ti-64 [AS] samples from the same source, and a smaller uncertainty in the gauge length the difference in the measured resistivity was calculated. The short sample, variable temperature data were scaled by normalisation factors outlined in Table 4.4, and the uncertainty in the resistivity was reduced to ≈ 4 %.

For the E-J measurements of the Ti bars in the PPMS, external circuitry was used. The current was provided by a Keithley 220 programmable current source. A resistor was also added in series to the sample to ensure the nominal current programmed into the current source and the current derived from the voltage across the resistor were consistent through the measurements from 10 nA to 0.1 A. The voltage across the sample was measured using an amplifier of gain 5 × 10⁴ and a Keithley 2100 6½-digit multimeter.

Ti-Alloy	Normalisation
Ti-6242 (AS)	1.18
Ti-64 (AS)	1.03
Ti-64 (BR)	1.11
Ti-64 (IT)	1.18

Table 4.4 : Normalisation factor for Ti-Alloy.

In addition to short Ti bar samples, the ITER barrels the bar samples were cut from were measured in the vertical magnet system. The ITER barrels were modified to allow voltage taps to be connected to the Ti-alloy sections. The purpose of this additional measurement was to investigate the effect of applied-field direction on the critical current density E-J measurements.

4.3.   Results and Discussion

4.3.1. Zero-field resistivity
There is excellent agreement, to within 4 %, between experimental data, for the temperature dependence of the normal state resistivity of the as supplied Ti-64 alloy, and the data from Ekin [4] and Clark [7], shown in Figure 4.4 (a). The transition from normal to superconducting in zero-field is seen in the resistivity data for the titanium alloys, shown in Figure 4.4 (b). T_C (Ti-6242) $\sim$2.38 K is well below that of T_C (Ti-64) $\sim$5.12 K.

The HT Ti-64 alloys transitions to a non-zero resistivity state. The HT of the sample results in a material which has connected β phase, demonstrated by the superconductive behaviour [24]. The lack of the bulk transition can be ascribed to the α-phase. At low temperature some of the β phase remains in the form of interconnecting filaments [25], which causes the superconductivity. The variance in the transition and measured T_C is due to the binary structure and differences in the β phase due to the working of the material.

4.3.2. In-field Resistivity
The titanium alloy samples were measured in applied-fields to investigate the upper critical fields. The magnetic field was applied orthogonally to the direction of current flow in the PPMS measurement system. The superconducting T_C and upper critical field B_{C2} of the as-supplied Ti-64 are consistent with the literature values, the range measured from 4.35 and 6.30 K. The two as-supplied alloys make a complete transition to zero resistivity, shown in Figure 4.5 (a) and Figure 4.6. The heat-treated Ti-64 alloys were also both measured in an applied magnetic field.

(a)

(b)
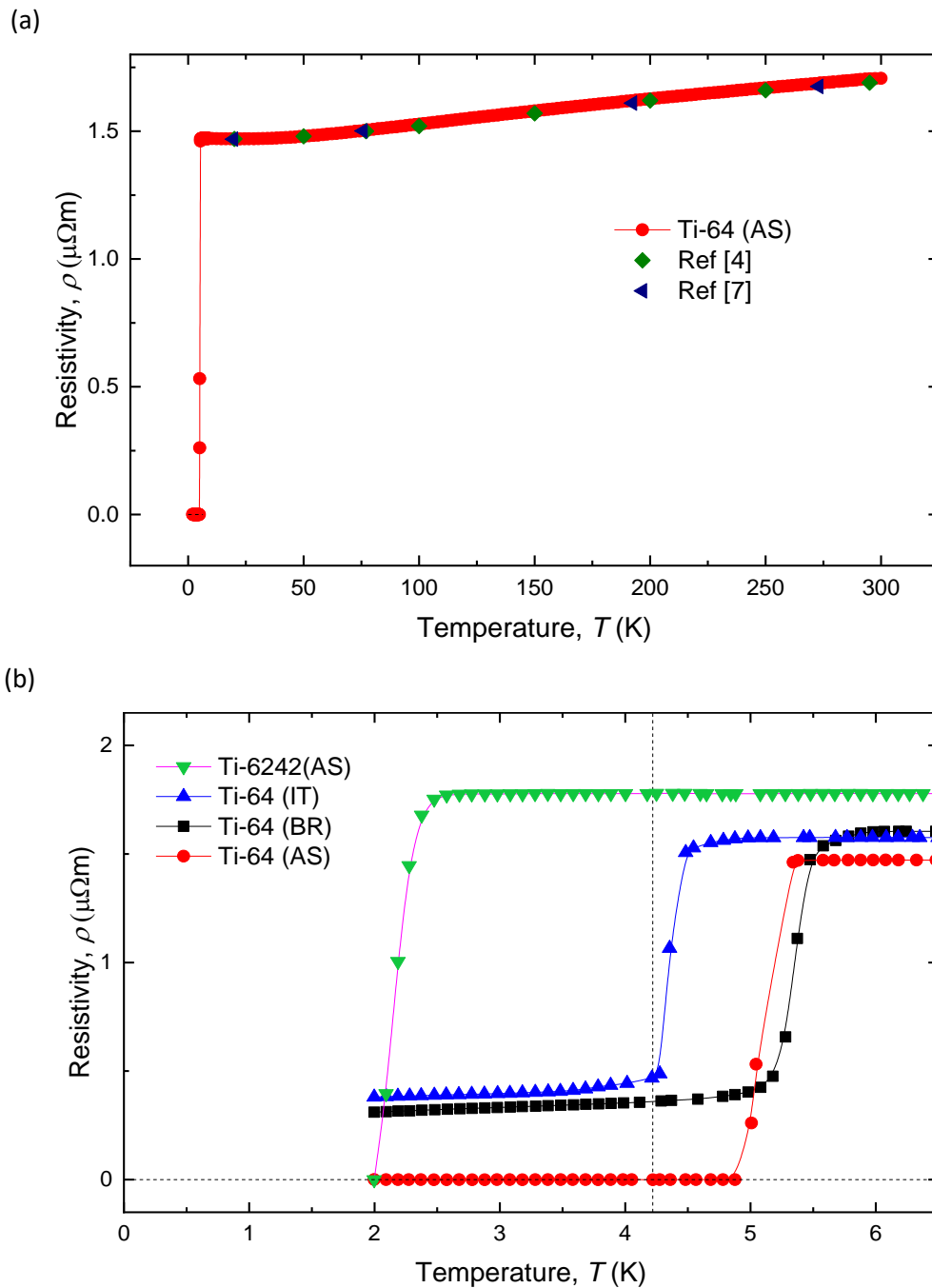
Figure 4.4 : (a) The resistivity of titanium alloys Ti-64 (Ti-6Al-4V) compared with the literature measurements [4, 7]. (b) The resistivity of titanium alloys Ti-64 (Ti-6Al-4V) and Ti-6242 (Ti-6Al-2Sn-4Zr-2Mo-0.2Si). The Ti-6242(AS) and Ti-64(AS) materials in the as-supplied state achieve zero resistivity. The Ti-64(BR) and Ti-64(IT) were heat-treated using the schedules for bronze-route Nb_3Sn and internal tin Nb_3Sn strands respectively, as detailed in Table 4.2 and Table 4.3. The heat-treated materials show partial resistivity transitions from their normal state resistivity to a lower resistivity value. The vertical dashed line is at 4.22 K.

(a)

(b)

(c)
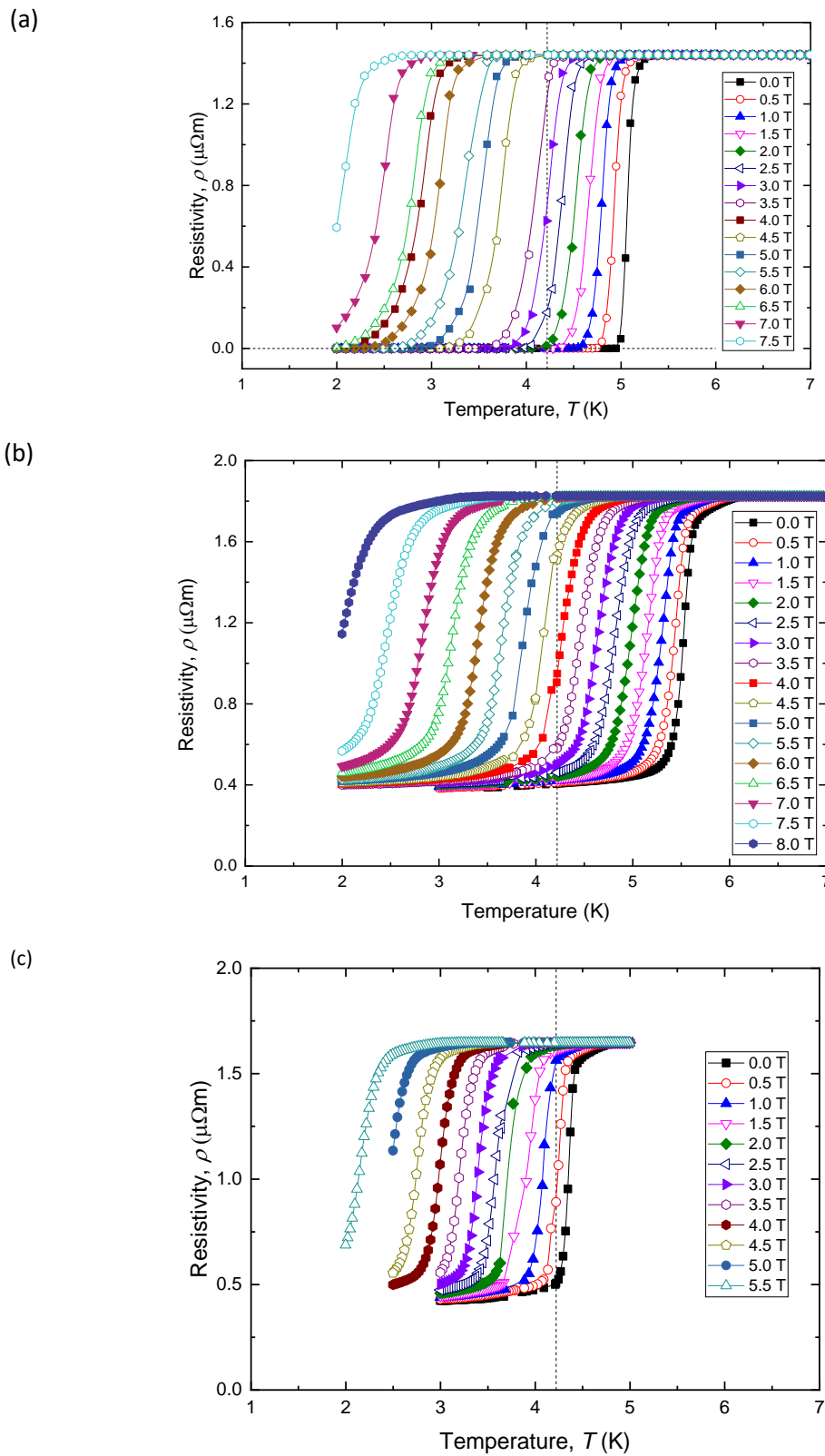
Figure 4.5 : The resistivity of Ti-6Al-4V alloys as a function of the applied magnetic field (a) Ti-6Al-4V [Ti-64(AS)] (b) heated treated [Ti-64(BR)] using the schedule used for bronze route Nb₃Sn strands as given in Table 4.2. (c) [Ti-64(IT)] using the schedule used for Internal Tin route Nb₃Sn strands as given in Table 4.3. Note that at low temperatures the sample remains resistive. The vertical dashed line is at 4.22 K.
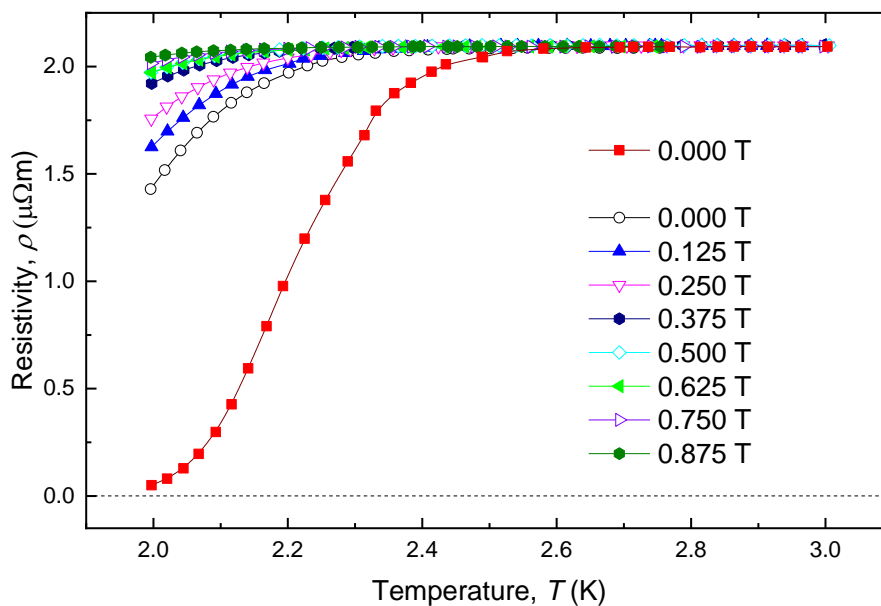
Figure 4.6 : The resistivity of as-supplied Ti-6Al-2Sn-4Zr-2Mo-0.2Si (Ti-6242(AS)) as a function of temperature measured in magnetic fields from 0 T to 0.875 T. The nominal 0 T data (1st run, red square) data were measured at the beginning of the experiment. The 0 T (second run, black open circle) data were taken at the end of the experiment.

The heat-treated sample Ti-64(BR) shown in Figure 4.5 (b) shows a partial transitions, the resistivity dropping by about 60 %. The heat-treated sample Ti-64(IT) shown in Figure 4.5(c) also shows similar partial transitions behaviour. This behaviour may be associated with some non-contiguous parts of this alloy becoming superconducting. Although incomplete, the transitions for Ti-64 (IT) and Ti-64 (BR) remain relatively sharp and have a temperature dependence that can be associated with superconducting components in these alloys. The superconducting path is not continuous throughout the entire sample down to a base temperature of 2 K.

The in-field transitions of the as-supplied Ti-6242(AS) alloy were also measured, shown in Figure 4.6. The transition is very broad, consistent with multi-phase samples [26] containing materials with a range of compositions. The Ti-6242(AS) alloy also showed considerable hysteresis in the resistive traces, particularly in nominal zero-field, shown in Figure 4.6. The hysteresis is attributed to trapped flux in these inhomogeneous samples. For each of the in-field traces, the samples were first heated to above 3 K to ensure the whole sample was driven normal.

From the in-field resistivity measurements, a value for the onset of superconductivity was found $[B_{C2}^*(T)]$ for each alloy, shown in Figure 4.7.
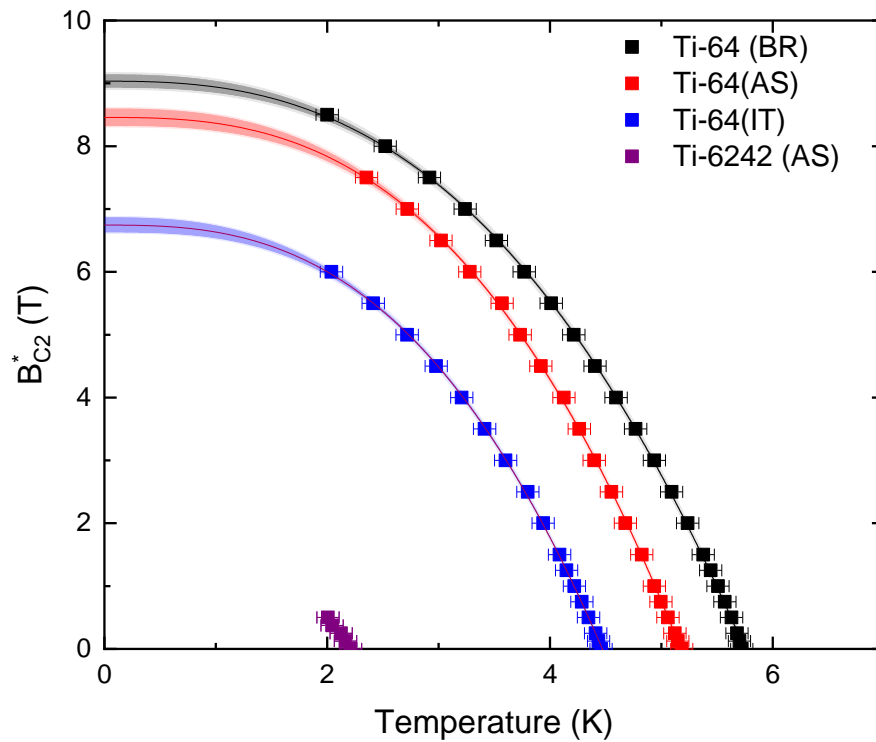
Figure 4.7 : B_{C2}^*(T) – the onset of superconductivity for the Ti-alloys Ti-64 and Ti-6242 as a function of temperature. The Ti-alloy state: as supplied (AS), heat-treated for Bronze route (BR) or internal Tin (IT). The solid line is a fit to Eq. (4.1), with 95% confidence band for the Ti-64 alloys. It was not possible to fit the Ti-6242 data meaningfully.

Characteristic [Unit]	Ti-64 (AS)	Ti-64 (BR)	Ti-64 (IT)	Ti-6242 (AS)
T_C [K]	5.1 ± 0.1	5.8 ± 0.1	4.5 ± 0.1	2.2 ± 0.1
$B_{C2(0)}$ [T]	8.5 ± 0.1	9.0 ± 0.1	6.7 ± 0.1	1 ± 1
B_{C2} [W-H-H]	14.4 ± 0.4	19.8 ± 0.8	13.6 ± 0.7	4.5 ± 0.2
Index S	2.7 ± 0.1	2.6 ± 0.1	2.7 ± 0.1	5 ± 6
Data points	19	22	17	5
ρ (0 T, 273 K) [μΩ m]	1.60 ± 0.01	1.67 ± 0.01	1.74 ± 0.01	1.75 ± 0.01
ρ (0T, 10 K) [μΩ m]	1.40 ± 0.01	1.45 ± 0.01	1.50 ± 0.01	1.51 ± 0.01

Table 4.5 : Superconducting and normal state properties of titanium alloys from transport measurements for the titanium alloy Ti-64 (Ti-6Al-4V) and Ti-6242 (Ti-6Al-2Sn-4Zr-2Mo-0.2Si). Ti-64(BR) and Ti-64(IT) were heat-treated using the schedules that are used for the bronze route strands and internal tin strands outlined in Table 4.2 and Table 4.3.

The onset was defined as 95% of the normal state resistance. The data have been fitted with using the expression [27]:

$$B_{C2}^*(T) = B_{C2}(0)\left[1 - \left(\frac{T}{T_C}\right)^S\right]$$

(4.1)

The characteristic superconducting and normal state parameters for the four alloys measured in this work are given in Table 4.5. A rule of thumb for data sets with ten or fewer measurements, the error is rounded to one significant figure [28]. With five data points for the Ti-6242, it is clear using Eq. (4.1) results in an over extrapolation with the uncertainty in S and B_{C2}^* equal to or larger than the value. The 95% confidence band, 2σ, for the Ti-alloys is shown in Figure 4.7, apart from Ti-6242 as it is not meaningful.

It is possible to calculate the B_{C2} using the well-known Werthamer, Helfand and Hohenberg (WHH) empirical fit, Eq. (4.2) [29]. (W-H-H) theory is used to extrapolate to find the upper critical field, at 0 K, from the T_C and gradient of B_{C2}^* at T_C.

$$B_{C2}^*(T)[WHH] = -0.693\, T_C \left(\frac{dB_{C2}^*}{dT}\right)_{T_C}$$

(4.2)

This analysis results in values of $B_{C2}^*(T)[WHH]$ has the same trend, i.e., the smallest value for Ti-6242, but approximately a scale factor of 2 larger (Table 4.5).

4.3.3. Critical Current Measurements

The critical current density (J_C) measurements on bars of Ti-64(AS) and Ti-64(BR) at 4.22 K as a function of the B_{App} are shown in Figure 4.8. The magnetic field was applied orthogonal to the direction of current flow. Ti-64(AS) shows a zero-resistivity baseline in contrast with and the Ti-64(BR) alloy which shows a resistive baseline from origin, both results are consistent with the data shown in Figure 4.4 (b).

Both datasets shown in Figure 4.8 are consistent with the data shown in Figure 4.4 (b). The Ti-64(AS) is non-ohmic, i.e., superconducting. The range of J_C values reported here are comparable to those of Goodrich [30], who found J_C values for barrels from > 680 mA·mm^{-2} for AS material to 2 mA·mm^{-2} for annealed (HT) and oxidised barrels. It is important to note that the J_C are not small values in the context of making high accuracy transport measurements, since in zero applied-field the Ti-64 barrel can carry a supercurrent of > 112 A. A J_C value a factor of 3 - 4 higher than the data shown in Figure 4.8 (a) (42 mA·mm^{-2}) is consistent with well-established Lorentz-force-free flux pinning considerations.

(a)

(b)
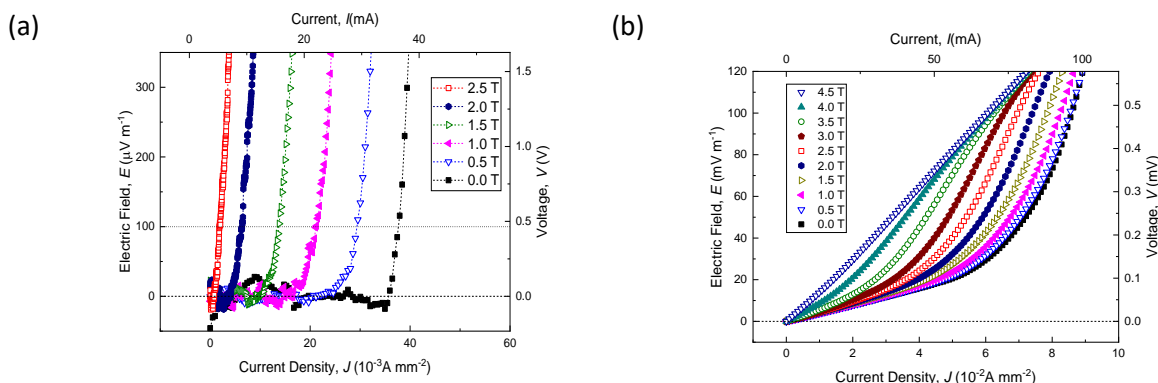
Figure 4.8 : E-J characteristics at 4.22 K as a function of the applied magnetic field (a) as-supplied Ti-6Al-4V [Ti-64(AS)]. The line between points is a guide for the eye. Horizontal lines at $E = 0$, and E_C (b) [Ti-64(BR)]
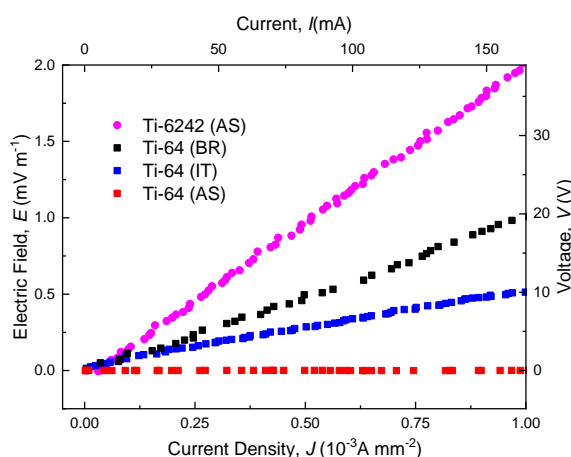
Figure 4.9 : E-J characteristics at 4.22 K of titanium alloy barrels. Samples measured were Ti-64(AS) (as supplied Ti-6Al-4V); Ti-6242(AS) (as supplied Ti-6Al-2Sn-4Zr-2Mo-0.2Si) and Ti-64 that was heat-treated using the internal tin (IT) and bronze route (BR) strand schedules given in Table 4.2 and Table 4.3. Not the E-field range in the measurement

In addition to measurements of Ti-alloy bar samples, critical current density measurements were performed on intact ITER barrels, shown in Figure 4.9. Measurements in the vertical magnet setup, are at a fixed temperature, 4.22 K, and the applied magnetic field is parallel to the direction of current flow. The J_C measurements of the Ti-64(AS) and Ti-64(BR) samples were measured. The behaviour of Ti-64(AS) is consistent with the data shown in Figure 4.4. The data has a noisy baseline and a transition. The Ti-64 (BR) measurement barrel is resistive but non-ohmic.

4.4. Conclusions

The superconducting transition temperatures and upper critical fields of Ti-64 and Ti-6242 titanium alloys, as well as the effect of two heat treatments on Ti-64, were measured. The critical temperature of Ti-64 is 5.14 K and Ti-6242 is 2.38 K. After the heat treatments, the standard Ti-64 no longer achieved the zero-resistivity state but a partial transition in the resistivity was seen, which was attributed to the isolated parts of the material remaining superconducting. For high accuracy J_C measurement at 4.22 K in magnetic fields up to 3 T, the barrel should be made using Ti-6242 rather than Ti-64 because it is in its normal state under these conditions. The two measurement barrels, detailed in chapter 3, were manufactured using Ti-6242 and were used to perform transport measurements, detailed in chapter 6.

References for chapter 4:

[1]   S. A. Keys and D. P. Hampshire, "Characterisation of the transport critical current density for conductor applications," in *Handbook of Superconducting Materials*, vol. 2, D. Cardwell and D. Ginley, Eds. Bristol: IOP Publishing, 2003, pp. 1297-1322.

[2]   IEC, "Superconductivity - Part 2: Critical current measurement - DC critical current of Nb_3Sn composite superconductors," in *International Standard*1 ed.: International Electrotechnical Commission, 2006, pp. IEC 61788-2:2006.

[3]   C. Leyens and M. Peters, C. Leyens and M. Peters, Eds. *Titanium and Titanium Alloys: Fundamentals and Applications*. Wiley VCH GmbH & Co. KGaA, 2003.

[4]   J. W. Ekin, *Experimental Techniques for Low-Temperature Measurements*. New York: Oxford University Press, 2007.

[5]   R. Boyer, G. Welsch, and E. W. Collings, *Materials Properties Handbook: Titanium Alloys*. ASM Internation, 1993, p. 1176.

[6]   A. K. Ghosh, "Effect of Barrel Material on Critical Current Measurements of High-J(c) RRP Nb_3Sn Wires," *IEEE Transactions on Applied Superconductivity,* Article vol. 21, no. 3, pp. 2327-2330, Jun 2011.

[7]   A. F. Clark, G. E. Childs, and G. H. Wallace, "Electrical resistivity of some engineering alloys at low temperatures," *Cryogenics,* Article vol. 10, no. 4, pp. 295-305, 1970.

[8]   O. Umezawa and K. Ishikawa, "Electrical and thermal conductivities and magnetization of some austenitic steels, titanium and titanium alloys at cryogenic temperatures," *Cryogenics,* vol. 32, no. 10, pp. 873-880, 1992.

[9]   U. Divakar, S. Henry, H. Kraus, and A. J. B. Tolhurst, "Measurement of the superconducting transition temperature of Dural and titanium 6Al-4V alloys," *Superconductor Science and Technology,* Article vol. 21, no. 6, pp. 1-3, Jun 2008, Art. no. 065021.

[10]   U. Divakar, S. Henry, H. Kraus, and A. J. B. Tolhurst, "Corrigendum - Measurement of the superconducting transition temperature of Dural and titanium 6Al-4V alloys (vol 21, 065021, 2008)," *Superconductor Science and Technology,* Correction vol. 23, no. 12, p. 1, Dec 2010, Art. no. 129801.

[11]   M. Barucci, L. Lolli, L. Risegari, and G. Ventura, "Measurement of thermal conductivity of the supports of CUORE cryostat," *Cryogenics,* Article vol. 48, no. 3-4, pp. 166-168, Mar-Apr 2008.

[12]   E. W. Collings, *A Sourcebook of Titanium Alloy Superconductivity* (Library of Congress Cataloging in Publication Data). New York: Plenum Press, 1983.

[13]   R. Pederson, O. Babushkin, F. Skystedt, and R. Warren, "Use of high temperature X-ray diffractometry to study phase transitions and thermal expansion properties in Ti-6Al-4V," *Materials Science and Technology,* vol. 19, no. 11, pp. 1533-1538, 2003/11/01 2003.

[14]   A. Kumar, T. Jayakumar, B. Raj, and D. Banerjee, "A new methodology for identification of β-transus temperature in α + β and β titanium alloys using ultrasonic velocity measurement," *Philosophical Magazine,* vol. 88, no. 3, pp. 327-338, 2008/01/21 2008.

[15]   A. Ducato, L. Fratini, M. La Cascia, and G. Mazzola, "An Automated Visual Inspection System for the Classification of the Phases of Ti-6Al-4V Titanium Alloy," Berlin, Heidelberg, 2013, pp. 362-369: Springer Berlin Heidelberg.

[16]   Y. Hariharan, M. C. Valsakumar, and T. S. Radhakrishnan, "A proximity effect model for superconductivity in titanium-transition metal alloys," *Journal of Low Temperature Physics,* vol. 43, no. 3, pp. 341-352, 1981/05/01 1981.

[17]   T. H. Geballe and J. K. Hulm, "Bernd Theodore Matthias," *National Academies Press,* 1996.

[18]   R. R. Hake, D. H. Leslie, and T. G. Berlincourt, "Electrical resistivity, Hall effect and superconductivity of some b.c.c. titanium-molybdenum alloys," *Journal of Physics and Chemistry of Solids,* vol. 20, no. 3, pp. 177-186, 1961.

[19]   D. M. J. Taylor and D. P. Hampshire, "Properties of helical springs used to measure the axial strain dependence of the critical current density in superconducting wires," *Superconductor Science and Technology,* vol. 18, pp. 356-368, 2005.

[20]   B. Bordini and L. Rossi, "Self Field Instability in High-J_C Nb_3Sn Strands With High Copper Residual Resistivity Ratio," *IEEE Transactions on Applied Superconductivity,* vol. 19, no. 3, pp. 2470-2476, 2009.

[21]   M. J. Donachie. ASM International, 2000.

[22]   S. Malinov, P. Markovsky, W. Sha, and Z. Guo, "Resistivity study and computer modelling of the isothermal transformation kinetics of Ti–6Al–4V and Ti–6Al–2Sn–4Zr–2Mo–0.08Si alloys," *Journal of Alloys and Compounds,* vol. 314, no. 1, pp. 181-192, 2001/01/16/ 2001.

[23]   M. M. Attallah, S. Zabeen, R. J. Cernik, and M. Preuss, "Comparative determination of the α/β phase fraction in α+β-titanium alloys using X-ray diffraction and electron microscopy," *Materials Characterization,* vol. 60, no. 11, pp. 1248-1256, 2009/11/01/ 2009.

[24]   W. E. Gardner and C. J. Raub, "The resistance minimum in dilute Ti-Mn alloys," *Proceedings of the Physical Society,* vol. 86, no. 3, pp. 647-651, 1965/09 1965.

[25]   F. Heiniger and J. Muller, "Bulk Superconductivity in Dilute Hexagonal Titanium Alloys," *Physical Review,* vol. 134, no. 6A, pp. A1407-A1409, 06/15/ 1964.

[26]   R. R. Hake, D. H. Leslie, and T. G. Berlincourt, "Low-Temperature Resistivity Minima and Negative Magnetoresistivities in some Dilute Superconducting Ti Alloys," *Physical Review,* vol. 127, no. 1, pp. 170-179, 1962.

[27]   J. W. Ekin, "Unified scaling law for flux pinning in practical superconductors: I. Separability postulate, raw scaling data and parameterization at moderate strains," *Superconductor Science & Technology,* vol. 23, p. 083001, 2010.

[28]   I. G. Hughes and T. P. A. Hase, *Measurements and their Uncertainties: a practical guide to modern error analysis*. New York, USA: OUP, 2010.

[29]   M. S. Lubell, "Empirical scaling formulas for critical current and critical field for commercial NbTi," *IEEE Transactions on Magnetics,* vol. 19, pp. 754-757, 1983.

[30]   L. F. Goodrich, J. A. Wiejaczka, A. N. Srivastava, and T. C. Stauffer, "Superconductor Critical Current Standards for Fusion Applications," *NIST-Internal report (NISTIR 5027),* no. NISTIR 5027, pp. 1-95, 1994.

CHAPTER 5

5. Magnetic Field Calculations: Analytic and Finite Element Analysis

To apply a self-field correction to experimental transport data it is necessary to calculate the magnitude, orientation, and distribution of the magnetic field due to current flow. Analytic methods are of limited use for calculating the self-field as the magnetic field equations are for unphysical – pointlike or infinite – geometries. Finite element analysis (FEA) is the method used to calculate magnetic field distributions for current flow through the complex geometry. To verify the methodology of the FEA modelling, several consistency tests are used to demonstrate agreement between FEA and analytic expressions.

In section 5.1, a brief overview highlighting key features and terminology of the FEA model implemented is presented. Additional information about the FEA model is included in the appendix, A.3. Working in collaboration with Dr Adel Nader (AN), and with improved computing resources, the complexity of the FEA models used for calculations increased.

In section 5.2, several consistency tests using simpler geometries demonstrate the validity of the FEA modelling technique and its development. Numerical values of analytic equations were used as comparisons, implemented using Mathematica [1]. This section concludes by comparing results of a helix with a circular cross-section, with the literature, in particular, the results of a model developed by the CERN group [2].

In section 5.3, results are presented from more complex geometries. Calculations are presented for helices and arrays that better approximate the experimental geometry and architecture of the strand. The architecture of the stand has been considered modelling the composite cross-section as a homogenised region in an annulus shape that is subdivided into three nested insulated tubes: tubes-within-tubes (TwT). The TwT geometry is used, a simplification that captures that the composite strand is composed of multiple filaments that are partially transposed. The effect of the current orientation relative to the B_{App} and the resultant Lorentz force (F_{L}) is outlined. The different spatial distributions of the self-field results in a change in the J_{C} measured, which provides insight into the role of self-field in testing superconducting properties.

5.1.   FEA Model Overview

Comsol Multiphysics was used as it is the default FEA software in the modelling community. Several FEA model files shared by the superconductivity model workgroup [3], were used as a reference in the development of the model used in this work. There are two formulations of the constitutive equations to model superconductors used in this thesis, summarised in Table 5.1. The A-V formulation describes the electrical conductivity in terms of the electric field. The state variable in the H-formulation is the magnetic field strength and is solved directly, rather than the magnetic field potential A from which B can be calculated. Using the H-formulation the resistivity can be defined as a function of the current density. The H-formulation is well-established; the development is outlined in references [4-7]. Reference [8] is useful for an in-depth review of the H-formulation. For details of implementing the H-formulation using Comsol see appendix (A.3.2.3).

One of the constitutive equations essential to the model is the relationship between the magnetic flux density, $\mathbf{B}$ and the magnetic field strength $\mathbf{H}$:

$$\mathbf{B} = \mu \mathbf{H}.$$
(5.1)

where μ is the magnetic permeability. As there are no magnetic materials in the experimental set-up, μ is imposed as the free space value (μ_0). The other constitutive relationship is the generalised Ohm's law. The relationship between the electric field $\mathbf{E}$ and the current density $\mathbf{J}$:

$$\mathbf{E} = \rho \, \mathbf{J}.$$
(5.2)

The E-field is assumed to be parallel to the current density, i.e., ρ is taken to be isotropic [9]. The normal conducting domains in the models are implemented using resistivity $\rho = \rho_N$. The superconducting domains $\rho = \rho_{sc}$ are implemented using different methods for the two formulations. When using the A-V formulation, a constant resistivity value similar to copper, 1.7 x 10^{-8} Ωm [10] is defined in the superconducting domains. When using the H-formulation, the superconducting domain is described by a non-linear magnetic field-dependent resistivity equation, a modified version of the power-law model [11] Eq. (5.3).

$$\rho_{\mathbf{sc}}(B, n) = \frac{E_{\mathrm{C}}}{J_{\mathrm{C}}(B)} \left(\frac{J}{J_{\mathrm{C}}(B)} \right)^{(n-1)}.$$
(5.3)

Formulation	Constitutive Equations	Definitions
Vector and scalar potential A-V	$$\nabla^2 \mathbf{A} = \mu\sigma \left(\frac{\partial \mathbf{A}}{\partial t} + \nabla V \right)$$ $$\nabla \cdot \left(\frac{\partial \mathbf{A}}{\partial t} + \sigma\nabla V \right) = 0$$	$$\mathbf{B} = \nabla \times \mathbf{A}$$ $$\mathbf{E} = -\frac{\partial \mathbf{A}}{\partial t} - \nabla V$$ $$\sigma = \sigma(\mathrm{E})$$
H-field	$$\nabla \times \rho\nabla \times \mathbf{H} = -\mu\frac{\partial \mathbf{H}}{\partial t}$$	$$\mathbf{J} = \nabla \times \mathbf{H}$$ $$\rho = \rho\left(J \right)$$

Table 5.1 : Summary of the two formulations used for modelling superconductors, modified from Ref. [9].

Several FEA calculations have been completed for this thesis with the development framework outlined in Table 5.2. The magnetic field distributions were initially calculated for all the geometries in Table 5.2 using the A-V formulation. Using the A-V formulation for stationary solutions, the magnetic field distribution is independent of the value of the domain's resistivity. For calculations with a constant resistivity, both the A-V and H-formulation have been used. For calculations using the power-law definition of the superconducting domain resistivity, Eq. (5.3), the H-formulation has been used. For the H-formulation models, the $J_\mathrm{C}(B)$ relationship was developed, from a linear to an exponential form. All bulk transport properties of the superconductor are contained within $J_\mathrm{C}(B)$. The calculations presented in chapter 5 have been implemented using a linear definition of $J_\mathrm{C}(B)$,

$$J_\mathrm{C}(|\boldsymbol{B}|) = J_\mathrm{C0} \left(1 - \frac{|\boldsymbol{B}|}{B_\mathrm{C2}} \right). \tag{5.4}$$

The details and numerical values used in Eq. (5.4) are outlined in section 6.3.1. The B_App field studied was from 0 to 8 T, and using experimental data for currents from 150 A to 1 600 A. The consistency tests typically fixed the current to 1 kA, and B_App either 0 or 1 T.

As computation time increases with geometric complexity, eventually Comsol cannot be used to calculate the properties of a multifilamentary strand with partially transposed filaments. Reducing the dimensions of the FEA calculations, i.e., modelling a 3D helix as a 2D axisymmetric or a 3D axisymmetric (z-component removed) ring reduces runtime. Implementing the mathematical formulation of the H-field in 2D axisymmetric coordinates using Comsol is relatively straightforward. During testing inconsistencies were found, outputs were dependent on input parameters, such as the E-field being linearly dependent on the ramp rate. In collaboration with Dr Adel Nader, the problem was addressed, and useful results were generated using 2D axisymmetric models.

Geometry	Resistivity Definitions						
	Constant	Power law: $n = 1$ const. J_C $B_\text{App}= 0\text{T}$	Power law: $n = 5$ const. J_C $B_\text{App}= 0\text{T}$	Power law: $n = 1$ $J_C(B)$ $B_\text{App}= 0\text{T}$	Power law: $n = 5$ $J_C(B)$ $B_\text{App}= 1\text{T}$	Exponential: $J_C(B)$ $B_\text{App}= 1\text{T}$	Exponential: $J_C\left(\lvert B\rvert_{max}\right)$ $B_\text{App}= 1\text{T}$
2D Straight Wire: Circular cross-section	√	√	√	√	√	√	√
3D Straight Wire: Circular Cross-section	√	√	√	√	√	√	√
2D Ring: Circular Cross-section	*AN*	*AN*	*AN*	*AN*	*AN*	*AN*	*AN*
3D Helix: Circular Cross-section	√	√	√	√	√	√	√
3D Rings: Annular Cross-section	*AN*	*AN*	*AN*	*AN*	*AN*	*AN*	*AN*
3D Helix: Annular Cross-section	√	√	√	√	√	√	√
3D Helix: Tubes-within-Tubes Cross-section	√	√	√	√	√	√	√

Table 5.2 : The geometries of the models studied with the *H*-Formulation. For each geometry the complexity of the definition of the resistivity was increased incrementally. *AN* indicates models that were developed in collaboration with by Dr Adel Nader.

The filamentary region of the strands was modelled as a homogenous region, with a circular or annular cross-section in the simple geometries studied in section 5.2. Nb-Ti strands with similar architecture to the ITER PF conductor have been modelled in the literature where the filamentary structure of the strand is simplified by considering a homogenised bundle [12, 13]. The electrical conductivity of the bundle σ_b is characterised using:

$$\sigma_b = \lambda_{\text{SC}}\, \sigma_{\text{SC}} + (1 - \lambda_{\text{SC}})\sigma_{\text{m}}, \tag{5.5}$$

where λ_{SC}, is the fraction of the strand that is superconductor and the electrical conductivities of the matrix and superconductor are σ_{m}, and σ_{SC} respectively. The authors of [12, 13] conclude the bundle approximation was of qualitative use, providing a suitable approximation for comparing layouts for optimisation, and results in reduced computation time. This bundle approximation has not been followed in this thesis, as redistribution of the current is required for accurate modelling of the self-field.

5.2. Consistency Tests: Simpler Geometries

5.2.1 Infinite Straight Wire
A first approximation for the effect of the magnetic self-field in the ITER helix geometry is to model it as a straight wire. It is a simple calculation with demonstrated usefulness [14]. It has been stated that for currents less than 2 kA, the magnetic field generated by current flowing in the helix geometry is "not much different from that of a straight strand" [15]. At the National Agency for New Technologies, Energy and Sustainable Economic Development (ENEA) facility, transport measurements are corrected by applying a straight wire correction term [16]. The justification for the simplification is that the ITER barrel's major radius is large, relative to the strand's diameter, and the separation between turns minimises the effect of neighbouring turns. The magnetic field generated by the nearest neighbour turn in the ITER helix is between 1% [16] to $\sim$ 5% [17] of the self-field on the strand. In section 5.2.1 the magnetic field of a straight wire is modelled accurately and quickly using Comsol.

5.2.1.1. Magnetic Field Spatial Variation: 2D-FEA
Using the Biot-Savart law, the equation for a thin infinite straight conductor with a circular cross-section is described by:

$$|\mathbf{B}|(I,r) = \frac{\mu_0}{2\pi}\left|\frac{\boldsymbol{I} \times \hat{r}}{r}\right|, \tag{5.6}$$

where r is the distance from the current element to the point the magnetic field is calculated and $\boldsymbol{I}$ is the current [14, 18]. The infinite long straight wire geometry was investigated using both the *A-V* and *H*-formulation. The radial field profile outside of a strand of radius R = 10 mm is compared to Eq. (5.6) and the results from Comsol, shown in Figure 5.1 (a). The magnetic field outside of the strand shows the standard inverse radial dependence (r^{-1}). The magnetic field inside the strand, with a circular cross-section, is described by:

$$B(I, r, R) = \frac{\mu_0 I r}{2\pi R^2}.$$

(5.7)

As both R and I are constant, the field inside the wire is linearly dependent on the radial distance. The radial dependence of the magnetic field $r < R$ of the wire, for both formulations, are compared to Eq. (5.7) and shown in Figure 5.1 (b).

5.2.1.2.   Magnetic Field Spatial Variation: Annular

The magnitude of the magnetic field for a wire with an annular cross-section can be characterised with three separate terms. The magnetic field inside the inner radius ($r < R_i$) is zero, due to zero current flow. For distances outside of the annulus ($r > R_o$), the magnetic field can be modelled by assuming an infinite straight wire r^{-1} dependency. In the region of the conductor where current flows ($R_i < r < R_o$), the magnetic field is dependent upon the radial position, r, and the inner and outer radii of the annulus. The magnetic field is described by:

$$B_{\text{Annulus}}(I, r, R_i, R_o) = \frac{\mu_0 I}{2\pi r}\left(\frac{r^2 - R_i^2}{R_o^2 - R_i^2}\right).$$

(5.8)

The radial field profile of an annular wire (R_i = 5 mm, and R_o = 10 mm) is calculated using FEA methods and compared with the Eq. (5.8) shown in Figure 5.2. The results of the *A-V* formulation are identical to the analytic equation. To generate results using the *H*-formulation calculation, which closely follows the analytic results, a sufficiently high mesh density using linear element order must be used. For further details of element order see (A.3.2.4).

(a)

(b)

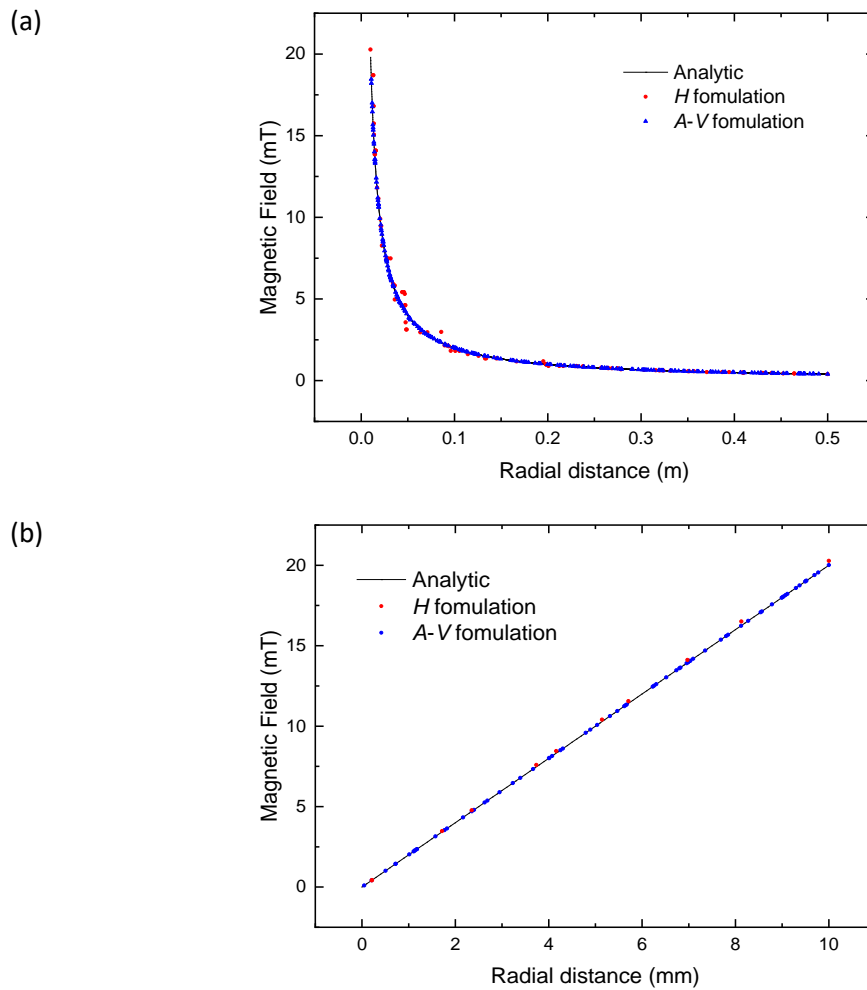Figure 5.1 : Comparison of the radial magnetic field distribution, for a conductor of 10 mm radius, with the two formulations (a) outside strand, Biot-Savart Eq. (5.6). (b) inside strand, Biot-Savart Eq. (5.7).
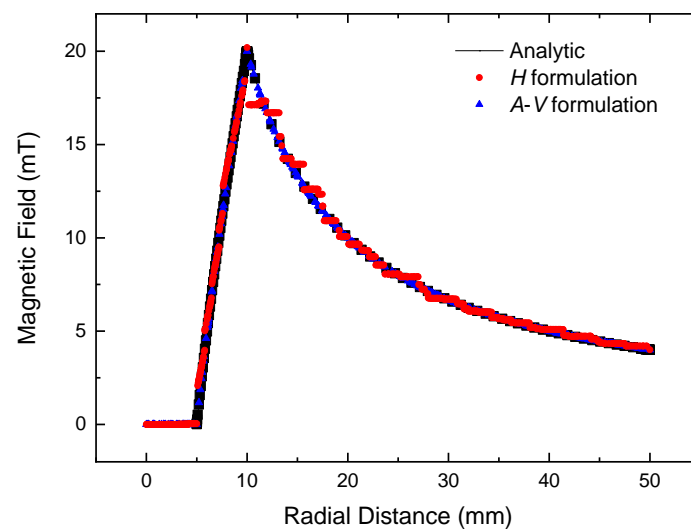

Figure 5.2 : Comparison of the radial magnetic field profile of an infinite wire with an annular cross-section for the two FEA formulations s and Eq. (5.8). R_i = 5 mm, and R_o= 10 mm

5.2.1.3.   Probability Distribution: 2D-FEA

For the simple geometry of a straight wire, it is possible to calculate the value of the magnetic field at any point inside the strand, and therefore the probability distribution. Understanding the distributions of magnetic fields within the volume of the strand is key to understanding which field statistic can describe the effect of self-field. The probability of the magnetic field B is equal to the probability of r in element dr , i.e.,

$$|p(B)dB| = |p(r)dr| \qquad (5.9)$$

In the simple case that the magnetic field is given by the Biot-Savart law for a straight wire, of radius R, the magnetic field is given by Eq. (5.7). This equation can be simplified by defining a constant $B_0 = \mu_0 I/2\pi R^2$. The value of B is linearly dependent on the position r. For a normalised distribution of magnetic field within the strand, (i.e., fixing the total value equal to one) it is possible to write the integral of the probability between the centre of the strand and its radius,

$$\int_0^{B_0 R} p(B)dB = 1 \qquad (5.10)$$

The probability element in the radial direction $(r + dr)$ is given a fraction of the total area πR^2 in the circular cross-section:

$$p(r)dr = \frac{2\pi r}{\pi R^2} dr = \frac{2r}{R^2} dr \qquad (5.11)$$

Equating using Eq. (5.9) results in the probability density distribution of the magnetic field inside a straight wire, with a circular cross-section, is described by:

$$p(I, B, R) = \left(\frac{8\pi^2 R^2}{\mu_0^2 I^2}\right) \cdot B \, dB. \qquad (5.12)$$

From the form of Eq. (5.12) the probability is linearly related to the magnetic field for a straight wire. The analytic solution Eq. (5.12) is compared with the FEA calculations using the *A-V* formulation and agreement is found, as shown in Figure 5.3. Inside the volume of the strand, for a straight wire geometry, the most probable field is the maximum field.
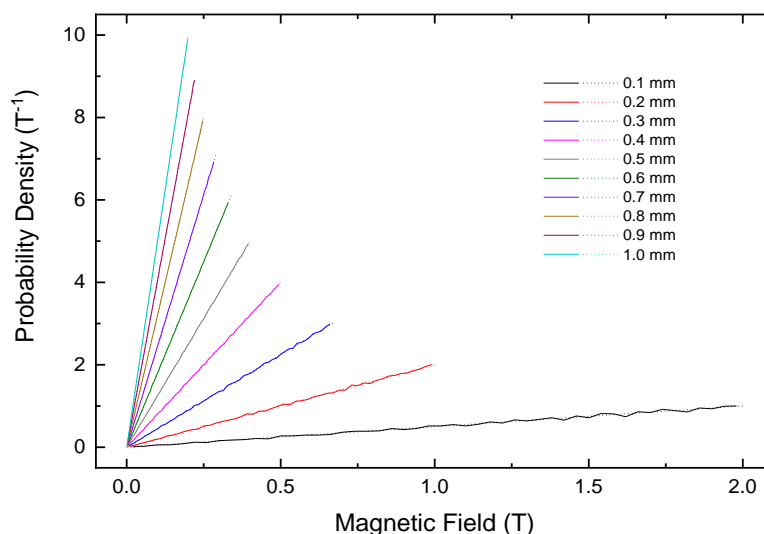
Figure 5.3 : Comparison of the probability density for FEA solutions (solid line) and analytic solutions Eq. (5.12) (dotted line), for a straight wire with uniform current density. The strands radius (R) is varied from 0.1 to 1.0 mm.

5.2.1.4.   Current Ramp Rate Dependence: 2D-FEA

In the time-independent calculations, the current is imposed using a constant flux constraint by imposing boundary conditions at the edges of the computational volume. For time-dependent solutions, the current ramp rate affects the current distribution, and consequently the electric and magnetic fields. A conductor of radius 5 mm, with a circular cross-section, was investigated. With a fixed ramp rate of 50 A·s^{-1}, the current is increased from 0 to I_C. The 2D plot of the current distribution is shown in Figure 5.4 at (a): 0.1 I_C A, (b) 0.5 I_C, (c) 1.0 I_C. In the lower panel, the 2D current distribution is a line plot of the normalised spatial current distribution. These plots are used to verify that the current penetrates the strand fully.

For some of the FEA calculations, a stepped current ramp is defined, shown in Figure 5.5(a). Integrating the electric field with time show the variance as the current is ramped, shown in Figure 5.5(b). The analysis of the E-J is shown in Figure 5.5 (c). The data points are extracted in a way that the system has relaxed back to its equilibrium and within a reasonable computation time.

The skin depth (δ) which characterises the skin effect, can be calculated using the resistivity of the conductor and the frequency:

$$\delta = \sqrt{(2 \cdot \rho)/(2 \cdot f_{skin} \cdot \mu_0)}. \tag{5.13}$$
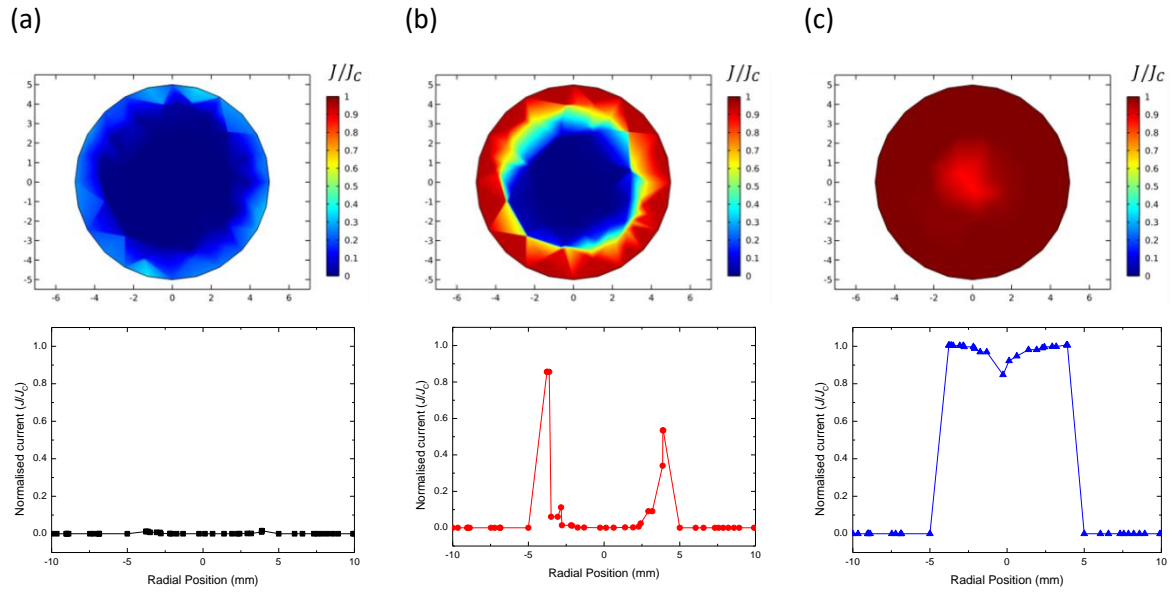
Figure 5.4 : Distribution of the current within the strand for (a) $J//J_C = 0.1$, (b) $J//J_C = 0.5$ and (c) $J//J_C = 1$. (upper) normalised current distribution in the strand (lower) current density profile across the diameter of the strand ($y = 0$). The mesh elements can be seen in these figures.
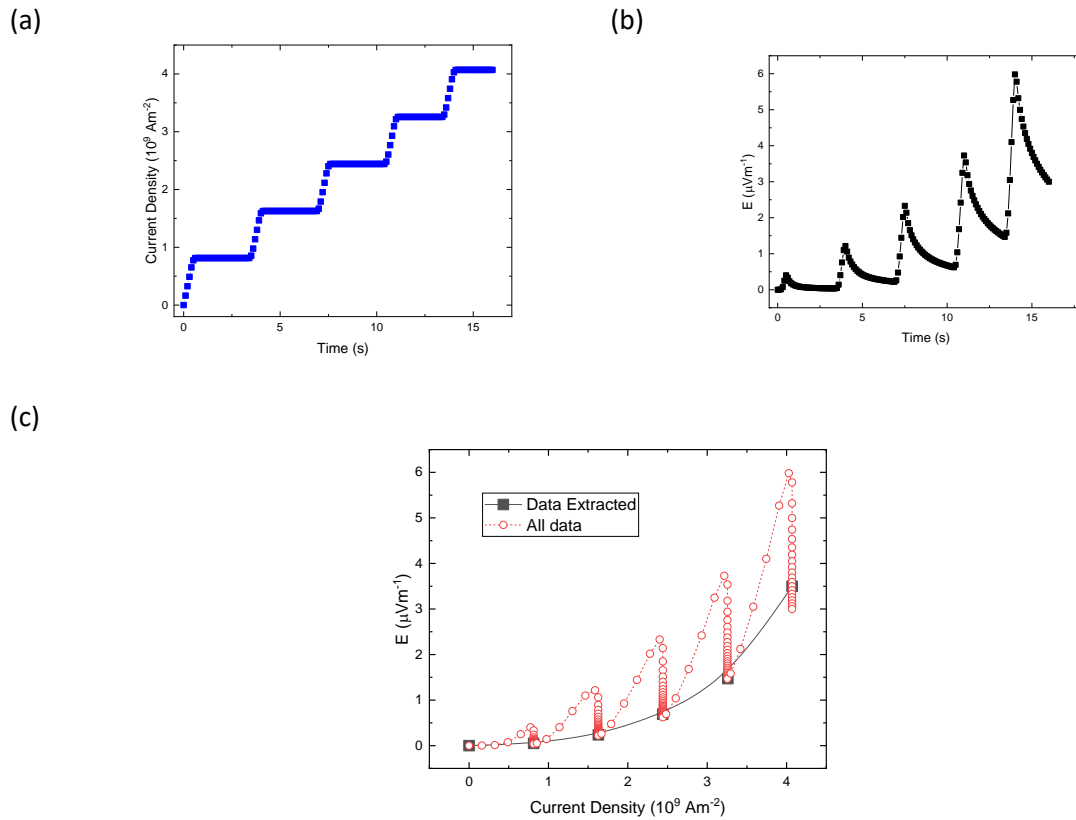
Figure 5.5 : Typical output from FEA calculations (a) the defined step increase in current density with time (b) the *E*-field in the centre turn with time (c) Comparison of all *E*-field data with the *E*-field data extracted.

Defining the skin depth as the radius of the ITER PF strand studied (0.365 mm), and an average resistivity of $\rho = 2 \times 10^{-15}$ Ω·m (from the FEA solutions), the characteristic time ($1/f_{skin}$) for the current to penetrate the conductor is 84 s. FEA calculations used have both computation times greater and less than the characteristic value. It was necessary to establish that shorter calculations produce results with the expected current distribution. Ramping of current and waiting ensures that errors due to eddy currents were not significant. This method was used throughout for results reported.

5.2.1.5.   Charge Conservation: 3D-FEA

Implicit in Maxwell's equation is conservation of charge, characterised by the equation:

$$\frac{\partial \rho}{\partial t} + \mathbf{\nabla} \cdot \mathbf{J} = 0.$$

(5.14)

To verify that conservation is obeyed in the FEA model, the transport current density J_T is integrated normal to the current direction over the surface at interfaces in the modelling domain and compared with the current imposed.

The circular cross-section surfaces are perpendicular to the current directions, and their positions are shown in Figure 5.6 (a). The current integral as a function of time, from positions 1 (source) to 6 (drain) demonstrates the conservation of current along the length of the strand, shown in Figure 5.6 (b). For these calculations, the magnetic field is evaluated at t = 2.5 s in the region of interest between points 3 and 4. The current is imposed as 1 kA, although at positions 1 and 6 for t = 2.5 s, the current is 2% larger, it is not clear why.

5.2.1.6.   Magnetic Field Spatial Variation: 3D-FEA

The spatial distribution of magnetic field in both zero-field and an applied magnetic field of 1 T has been calculated in both the A-V formulation and for H-formulation. The A-V formulation 2D and 3D data for B_App = 0 T, is shown in Figure 5.7 and is consistent with analytic solutions.

(a)

(b)
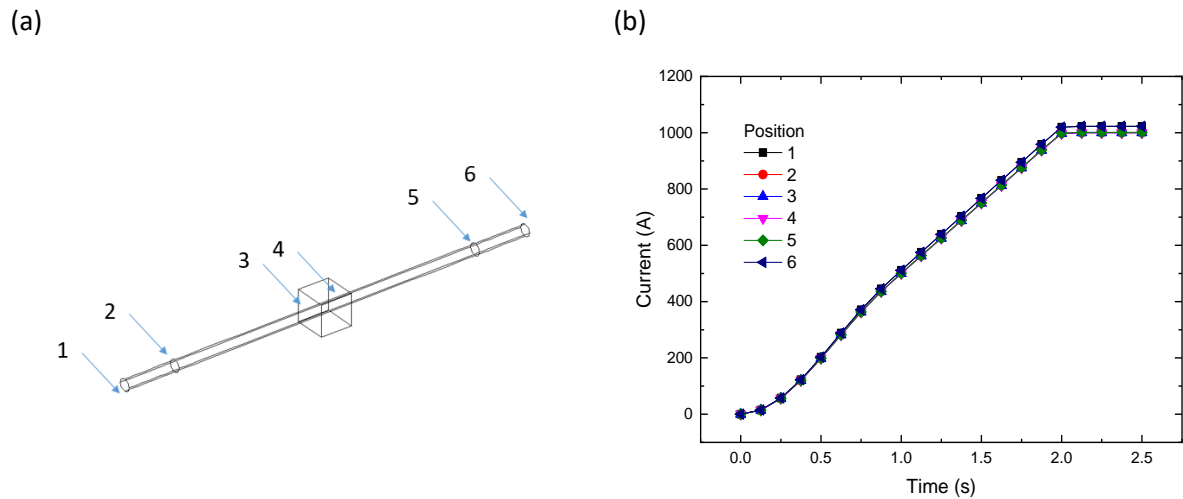
Figure 5.6 : Verification of conservation of current in modelling interfaces (a) positions where current is integrated (b) current as a function of time.

(a)

(b)
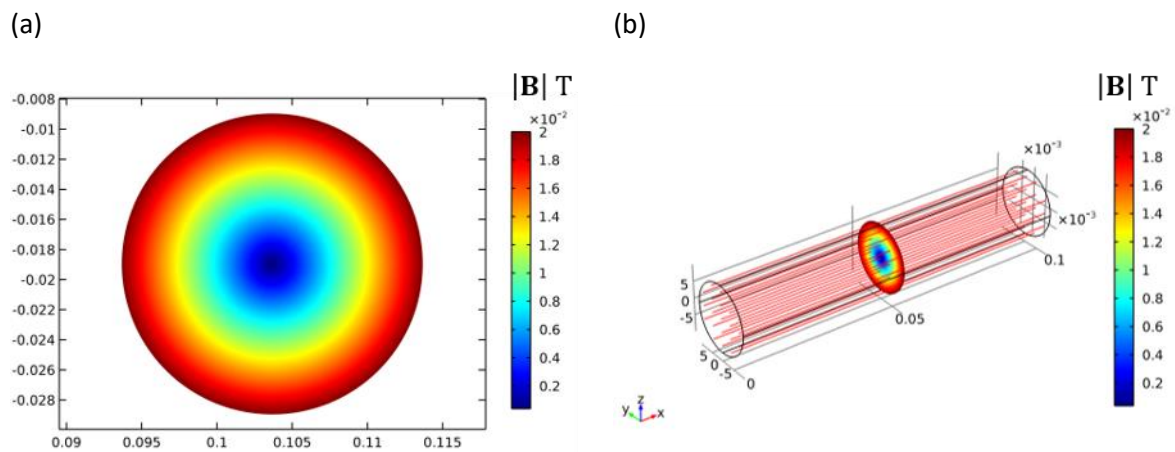
Figure 5.7 : *A-V* Formulation calculations of the magnetic flux density in zero applied field (a) 2D y-z slice (b) 3D plot with current streamlines in the x-direction.

5.2.1.7.   Comparisons between 2D and 3D

Consistency between results in different dimensions ensures the reliability of calculation. The magnetic field probability distribution has been investigated, as the mesh size is increased, for an infinite straight wire in both 2D and 3D cases. Excellent agreement between 2D and 3D models using both formulations is seen in Figure 5.8 (a). The magnetic field probability distribution for an infinite straight wire with varied mesh density is shown for both *A-V* and *H*-formulation is shown in Figure 5.8(b). Figure 5.8 differs from the earlier analytic calculation (Figure 5.3) as a volume of the strand is at a higher magnetic field than the most probable. The increase in the maximum is small (between 1 and 6%) and due to the meshing.
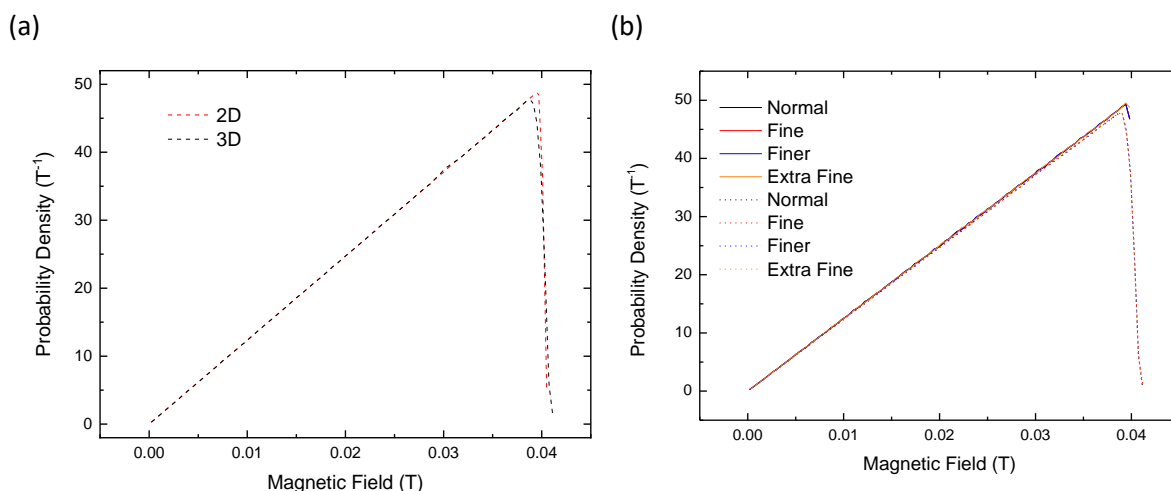
Figure 5.8 : Probability density distribution of the magnetic field for an infinite wire (a) comparison between a 2D wire and 3D (radius 5 mm) *H*-formulation computation (b) Comparison of 3D *A-V* formulation (solid lines) and *H*-formulation (dotted lines), with varied mesh density.

Dimensions	Mesh Size [min. element size (mm)]	*A-V* Formulation		*H* Formulation	
		Runtime [s]	File size [MB]	Runtime [s]	File size [MB]
2D	Extremely Fine [0.01]	2	0.1	2	0.8
3D	Normal [0.67]	422	26.4	13 196	114
	Fine [0.53]	384	26.1	13 615	115
	Finer [0.37]	402	26.0	23 361	115
	Extra Fine [0.02]	563	32.8	8 127	115

Table 5.3 : Comparison of the computational expense for the two formulations (*A-V* and *H*)
with varied mesh densities, and dimensionalities for the infinite straight wire geometry.

Developing an efficient mesh, was essential for calculations of the complex geometries. For the straight wire geometry, it was possible to infer the effects of meshing. A low-density mesh generates results quickly. How an increased mesh density affected the resultant magnetic field and runtime was investigated. The numerical values for runtime and file size are summarised in Table 5.3. It is clear from Table 5.3 that the *A-V* formulation calculations generate results quickly, with higher-order elements (for details see A.3.2.4.), and with smaller file sizes than the *H*-formulation. Pre-defined and custom meshes were used. It is interesting to see the results of the 3D extra fine mesh calculation, a result inconsistent with an increased complexity resulting in longer simulation times. It is unclear why this happened.

(a)   (b)
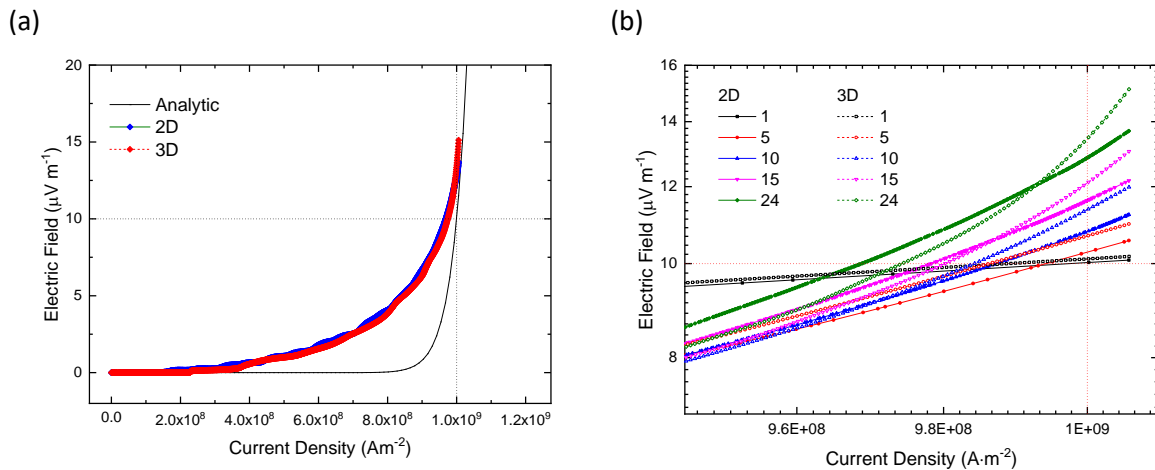
Figure 5.9 : Comparison of analytic [Eq. (5.3)] and computational (2D and 3D) E-J transitions (a) for fixed n-value = 24 (b) (log-log) E-J as a function of the index of transition for both 2D model (solid symbols and 3D model (open symbols) of an infinite straight wire (radius 5 mm). The dotted horizontal line is the electric field criterion, and the vertical dotted line is the critical current density value.

Index of transition (n)	2D Runtime [s]	3D Runtime [s]	2D J_C [10^8 A·m^{-2}]	3D J_C [10^8 A·m^{-2}]
1	31	77 577	9.98	9.98
5	21	140 483	9.94	9.86
10	182	163 345	9.87	9.84
15	179	163 345	9.78	9.80
24	208	177 324	9.69	9.74

Table 5.4 : Computational expense and calculated $J_C(n)$ as a function of dimension from Figure 5.9 (b). The analytic value of J_C imposed is 1x10^9 A·m^{-2}

5.2.1.8. n-Index of Transition: 2D and 3D

Computational and analytic E-J traces are compared for both 2D and 3D calculations as shown in Figure 5.9. An H-formulation calculation, with a magnetic-field-dependent J_C [Eq. (5.4)], was implemented varying the n-index from 1 to 24. The results from H-formulation calculations are affected by the n-index [19]. The strand was modelled with a circular cross-section with a radius of 5 mm, the current was ramped at 50 A·s^{-1}. The electric field was averaged over the wire's surface in 2D and the central volume of the wire in the 3D model. The 3D in Figure 5.9 is shown with a dashed line, and 2D with a solid line. The 3D data have higher E-field for equivalent J. The dotted lines show the J_C imposed is 1x10^9 A·m^{-2} and the E_C. The FEA calculations can reproduce to a high fidelity the non-linear equilibrium transition, shown in Figure 5.9. The minimum element size limits how small each mesh element can be, with lower values a finer mesh is generated.

The analytic equation Eq. (5.3) with an n-value of 24 is compared using the 2D and 3D models, shown in Figure 5.9 (a). The 2D and 3D models agree but are different from the analytic equation definition of I_C. A finite electric field is seen at currents 0.36 × analytic I_C, and at the *E*-field criteria (10 μV·m^{-1}) the current is 0.97 × analytic I_C for both 2D and 3D models. The results from 2D and 3D are compared on a log-log (*E-J)* plot, shown in Figure 5.9 (b). The 2D calculations result in higher J_C at low n. The computational runtimes for the data obtained in Figure 5.9 (b) are summarised in Table 5.4. The time difference between the 2D and 3D results is very large, as expected. Increasing the index of transition results in a longer runtime. In 3D for $n > 5$, increases were < 25 % in 3D.

An error in the FEA methodology is highlighted by considering a single data-set for direct comparison, shown in Figure 5.10. Both plots shown in Figure 5.10 are log-log, with normalised J_C data. The difference being highlighted is the *E*-field behaviour over the range of current densities modelled and measured experimentally.

The baseline-corrected experimental *E-J* data for the Nb-Ti stand where n = 24, is shown in Figure 5.10 (a). The FEA calculated *E-J* is shown in Figure 5.10 (b), where n is imposed as 24. The experimental data has noisy *E*-field baseline for $J < J_C$ which may be skewed to some finite (positive or negative value) it is random below the take-off transition. In contrast to this, the FEA calculations for $J < J_C$ has a linear *E-J* relation. Evidently, it is not possible to model noise.

For the FEA data shown in Figure 5.10 (b) the region where $E > 0.1$ μV·m^{-1} the calculated n-values are n = 2.8 in 2D and n = 3.1 in 3D, despite n imposed as 24. Analysing the experimental data, in the region $E < 0.1$ μV·m^{-1} a linear relationship is fitted, and n = 24.7 ± 0.1 is calculated, B_{App} = 8T. A linear region is seen for $E < 0.1$ μV·m^{-1}, Figure 5.10 (b), 23.41 ± 0.08 in 3D. This fault in the FEA calculations was not addressed during this thesis, and it is possible that the results presented cannot be considered as accurate.

Further work is required to understand how to use the FEA models in the region of current densities near the transition to the normal state. It is possible to define a function where E = 0 for $J < J_C$ [20], but this requires the value of J_C to be known and defined. With the FEA models in the literature, calculations were typically sinusoidal and J was not increased to a value greater than the defined J_C value.

(a)   (b)
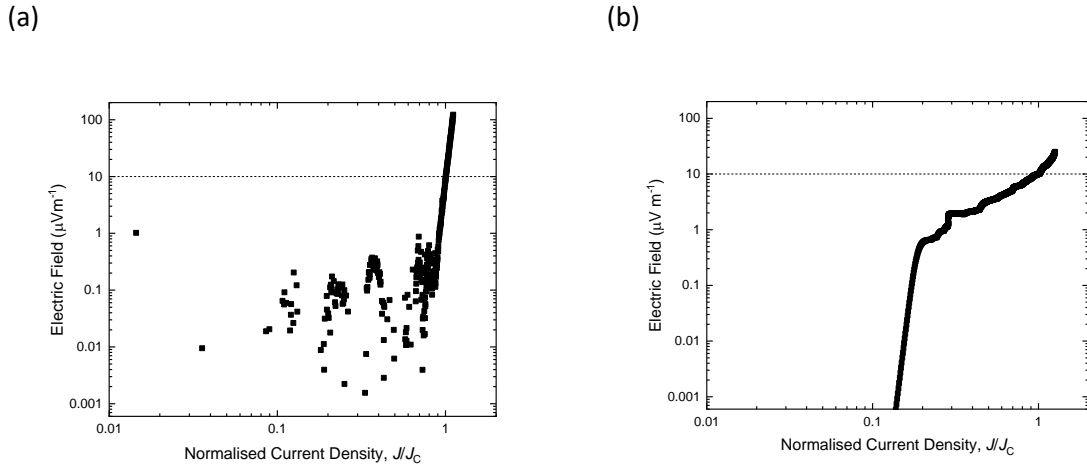
Figure 5.10 : Comparison of experimental and computation electric field for $J < J_C$ (log-log) E-$J/\!/J_C$ (a) Experimental $B_{\mathrm{App}}=$ 8 T, $n = 24$ (b) computational $B_{\mathrm{App}}=$ 0T, n imposed as 24.

5.2.2   Single Ring

Modelling the experimental helical geometry as a single ring is a better way to approximate a helix than a straight wire - the field and current have components in more than one direction, i.e., B_x and B_r [21]. There are limitations to using the ring geometry to model a helix as the ring is isolated. The geometry of the ring is defined in terms of the major radius (R_{Maj}) which is the distance from the free-space centre of the ring to the axis. The minor radius (R_{Min}) is the distance from the axis of the ring, i.e., the strand's radius.

5.2.2.1.   Magnetic Field: Point Evaluation

Undergraduate physics textbooks present simple equations that describe some features of the single ring geometry shown in Figure 5.11. The magnetic field at the centre of the ring in the x-y plane is described by:

$$B\big(I, R_{\mathrm{Maj}}\big) = \frac{\mu_0 I}{2 R_{\mathrm{Maj}}}.$$

(5.15)

Where ($z = 0$) The parameters are the same as previously defined. Using Eq. (5.15) and the R_{Maj} of the ITER barrel, the magnetic field in the centre is 36 mT.
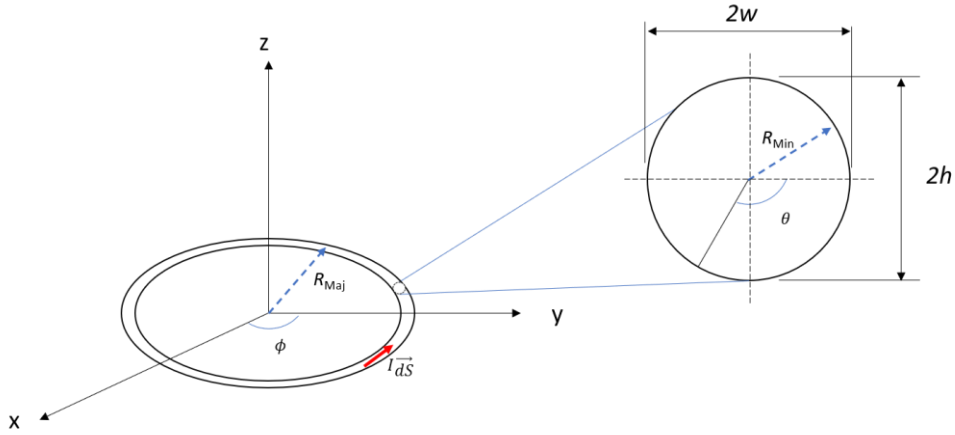
Figure 5.11 : Schematic of a single ring in the $x - y$ plane. Current flows in the ϕ direction. The cross-section shows the width $2w$ and height $2h$ of the strand with minor radius R_{Min}.

5.2.2.2. Magnetic Field Spatial Variation

The magnetic field variation of a single ring with a circular cross-section was calculated using the Biot-Savart law. The volume integral form is written:

$$\boldsymbol{B}(\hat{r}) = \frac{\mu_0}{4\pi} \iiint_V \frac{\vec{J} \times (\vec{r} - \overrightarrow{r'})}{\left|\vec{r} - \overrightarrow{r'}\right|^3} dV, \tag{5.16}$$

where $\vec{r}$ is the coordinate where the magnetic field is calculated, $\overrightarrow{r'}$ is the coordinate vectors pointing to the volume current element. Two coordinate systems are used to simplify the notation of the integral in Eq. (5.22). The cartesian coordinates (x, y, z) are used defining the position vector to the point the current is calculated for $\vec{r}$ where:

$$\vec{r} = \begin{pmatrix} x \\ y \\ z \end{pmatrix}, \tag{5.17}$$

Cylindrical coordinates: radial, azimuthal, and vertical, (r, θ, h) are used for the integral in the internal volume of the ring. The dimensions of the ring in cartesian co-ordinates are defined as width $2w$, and height $2h$. Using the standard definition of the geometry of a circle, i.e., $x^2 + y^2 = r^2$, and rearranging, it is possible to define the vector to the current elements which are inside the volume of the strand, $r < R_{Min} - \sqrt{w^2 + h^2}$.

The vector $\overrightarrow{r'}$ in Eq. (5.16) is defined:

$$\overrightarrow{r'} = \begin{pmatrix} r\cos\theta \\ r\sin\theta \\ h \end{pmatrix} \tag{5.18}$$

For a ring of finite cross-sectional area, the current density can be assumed to have a radial variation where:

$$J = \frac{\alpha}{r}\overrightarrow{u_\theta} = \frac{\alpha}{r}\begin{pmatrix} -\sin\theta \\ \cos\theta \\ 0 \end{pmatrix}. \tag{5.19}$$

The integral of the current density across the cross-section is equal to the current. The parameter α in Eq. (5.19) is a variable to account for the finite cross-section of the ring, where the radius is expressed in x and y dimensions as a width w, and height, h. The parameter α is defined:

$$\int_{-w}^{w}\int_{a-\sqrt{w^2-h^2}}^{a+\sqrt{w^2-h^2}} \frac{\alpha}{r}\,dr\,dh = I. \tag{5.20}$$

The numerator of the Biot-Savart integral Eq. (5.16) can be calculated directly to give:

$$\vec{J}\times(\vec{r}-\overrightarrow{r'}) = \frac{\alpha}{r}\begin{pmatrix} (z-h)\cos\theta \\ (z-h)\sin\theta \\ r-(x\cos\theta+y\sin\theta) \end{pmatrix}. \tag{5.21}$$

Using Eq. (5.17) and (5.21) it is possible to rewrite Eq. (5.16) with the integral over separable variables. The z-component of the magnetic field can be calculated by integrating first over the circumference (i.e., phi not shown), then over w, h and finally the angle θ.

$$\begin{aligned} B_z(\hat{r}) \\ = \frac{\mu_0}{4\pi}\alpha\int_0^{2\pi}\int_{-w}^{w}\int_{a-\sqrt{w^2-h^2}}^{a+\sqrt{w^2-h^2}} \frac{r-(x\cos\theta+y\sin\theta)\,dr\,dh\,d\theta}{[(x-r\cos\theta)^2+(y-r\sin\theta)^2+(z-h)^2]^{3/2}} \end{aligned} \tag{5.22}$$

Extensive series solutions are calculated for $B_z(\hat{r})$ using Mathematica [1]. The general integral Eq. (5.22), for a single ring with an annular cross-section is compared with the FEA calculations shown in Figure 5.12 and excellent agreement is seen.
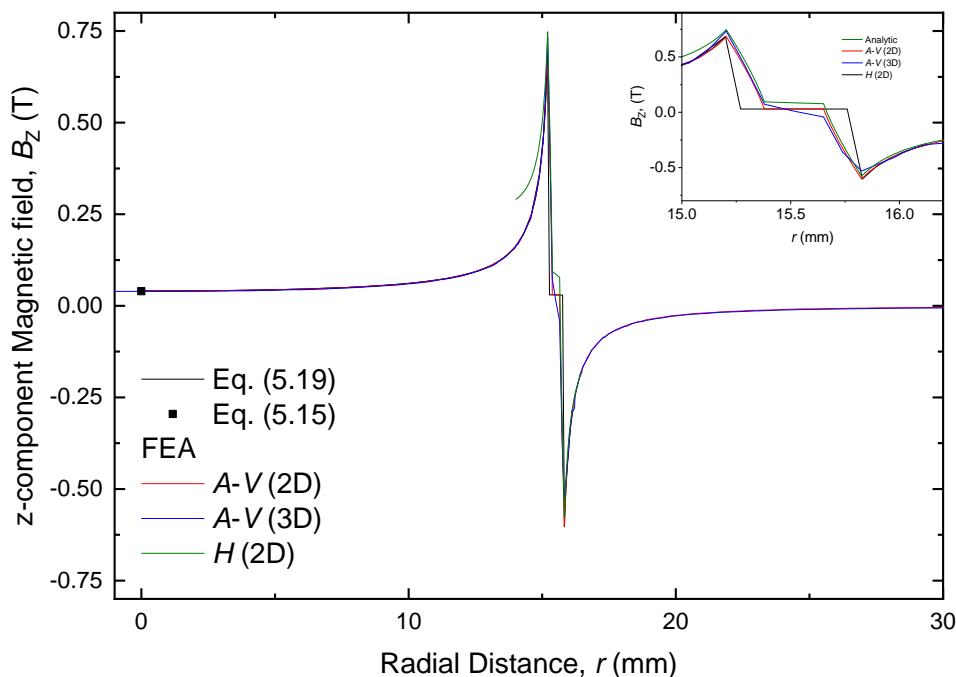
Figure 5.12 : Comparison of the analytic Eq. (5.22) and FEA computation *A-V* (2D and 3D) and *H* (2D) for a single loop with an annular cross-section. The points are solutions of Eq. (5.15) and Eq. (5.19). R_i = 0.136 mm and R_o = 0.311 mm.

The results from FEA calculations using the three methods are compared for the single ring, shown in Figure 5.12. The radial distribution of the z-component of the magnetic field, using both formulations are very similar. The peak in the magnetic field, the field inside and outside of the ring agree. For the analytic solutions for the strand with an annular cross-section, the radial distribution of the magnetic field in the filamentary region is dissimilar, shown in Figure 5.27.

5.2.3   Helices and stack of Rings: Circular Cross-section

The last of the simpler geometries used as consistency tests are helices and a stack of rings with a circular cross-section. Using a stack of rings to represent helical geometry is typical as it removes the z-component of the geometry and has the benefit of including rotational symmetry [22]. A stack of rings better approximates a helix than a single ring, however, the mathematical description is only true at large radial distances [22]. It has been argued that the stack is too simplified to describe helical data [23, 24]. In the literature calculations of the effect of self-field for the ITER helical geometry have used a stack of rings. The consistency test in this section compares FEA results implementing using literature methods, and with the same analysis, to the literature values.

(a)

(b)
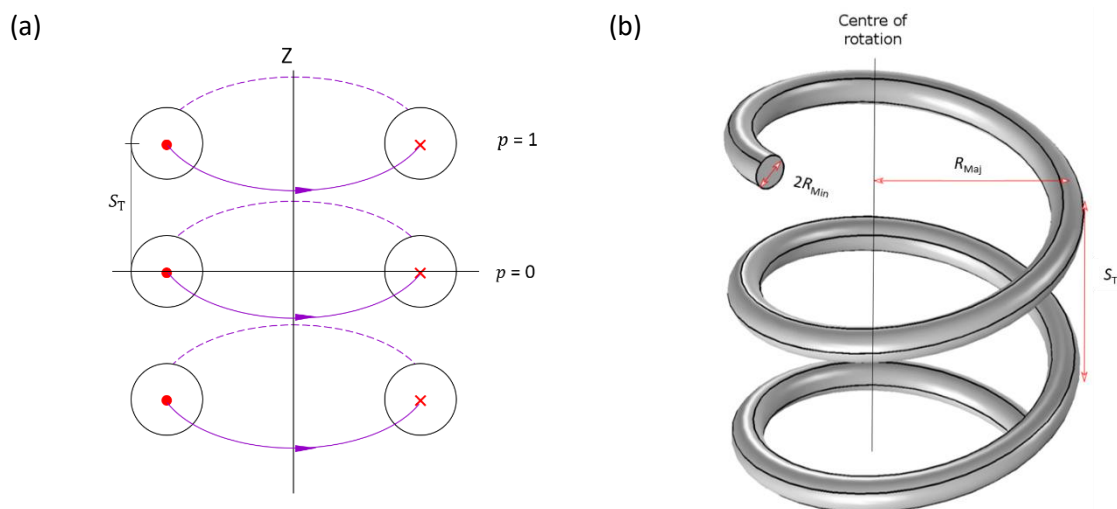
Figure 5.13 : (a) Schematic of the stack of rings, with a separation of turns (S_T) in the z-direction, and indexing of the rings with the central ring p =0. (b) schematic of helix with right handed chirality.

5.2.3.1.   Stack of Rings: Analytic

For defining the self-field correction with an axisymmetric system, the peak in B_z is most commonly used. With current only flowing in the ring the B_x and B_y components average to zero [25]. For this thesis, the B_z was calculated at the centre of a stack of rings, using a summation of the magnetic field due to each ring in the stack. Integrating over the angle ɸ over 0 to 2π and discounting the B_x and B_y components, the equation for the field is:

$$B_z(z, I, R_{\mathrm{Maj}},) = \frac{\mu_0 I R_{\mathrm{Maj}}^2}{2} \left[\sum_{p=1}^{turns/2} \frac{1}{R_{\mathrm{Maj}}^2} + \frac{2}{[R_{\mathrm{Maj}}^2 + (S_T \times p)^2]^{\frac{3}{2}}} \right]. \tag{5.23}$$

The rings are separated in the z-direction by the separation of turns (S_T) of the measurement barrel. The position of the ring relative to the centre is notated with the index p, the central ring in the stack, $p = 0$. The values of B_z for the ITER and MST are reported in Table 5.5.

Geometry	Turns	Magnetic Field [T·kA^{-1}]
ITER	13	0.212
MST	51	0.765

Table 5.5 : Analytic calculation of B_z Eq. (5.23) at the centre of the stack of rings.

5.2.3.2.   Finite Length Solenoids

Analytic solutions for finite length solenoids are available in the literature [26, 27]. B_z is derived by integrating the magnetic field over the length of the solenoid,

$$B_z\big(L, n, I, R_{\mathrm{Maj}}, z\big) = \left(\frac{\mu_0 n_d I}{2}\right)$$

$$\times \left[\left(\frac{(L/2) - z}{((z - (L/2))^2 + R_{\mathrm{Maj}}{}^2)^{1/2}}\right) + \left(\frac{(L/2) + z}{((z + (L/2))^2 + R_{\mathrm{Maj}}{}^2)^{1/2}}\right)\right]$$

(5.24)

where $(L/2)$ is half the height of the solenoid, z is parallel to the long axis of the solenoid, and n_d the turn density [28]. The magnetic field at the centre for the two measurement geometries are reported in Table 5.6. Solutions to Eq. (5.24) have been calculated and compared with FEA results for a stack of nine rings shown schematically in Figure 5.14 (a) and a nine turn helix, as shown in Figure 5.14 (a) and Figure 5.14 (b), agreement is seen between FEA and the analytic solutions.

Geometry	Turn density, n_d [turns· m^{-1}]	Magnetic Field [T]
ITER	315	0.336
MST	1205	1.286

Table 5.6 : Magnetic field in the centre of a finite solenoid with nine turns.

5.2.3.3.   Number of Rings

The number of rings that should be included in the FEA model is an important consideration. Some of the helical calculations presented in this chapter have a simplified geometry with fewer turns than the experimental geometry. The number of turns in the experimental geometry - 13 turns on the ITER barrel and 51 turns on the MST barrel – can results in long FEA solver calculation times.

The axial field component, B_z as a function of the number of turns, in the stack of rings, has been calculated using the analytic method outlined in section 5.2.3.1. The calculation shown in Figure 5.15 demonstrates that the B_z value has not reached the peak value for the number of turns in the titanium alloy section of the measurement barrel, therefore the helix cannot be considered to be infinitely long, and the number of turns considered in the calculation is an important parameter.
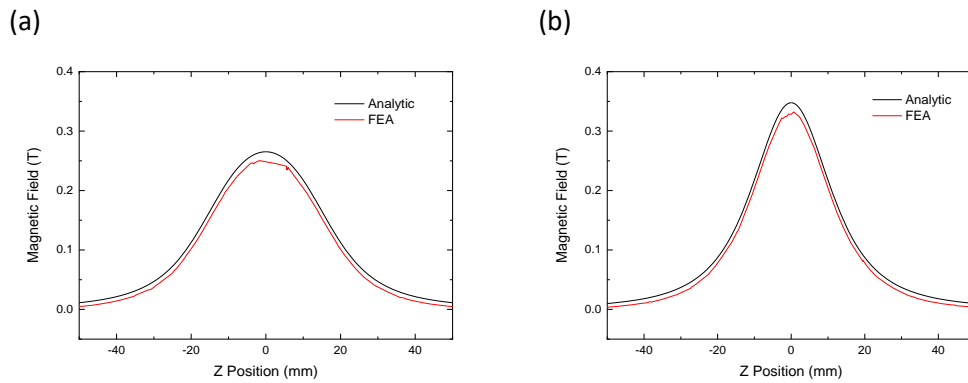
Figure 5.14 : The analytic spatial variation in the magnetic field through the centre of a finite length solenoid Eq. (5.24) is compared with FEA solutions for a stack of 9 rings. (a) ITER geometry (b) MST geometry.
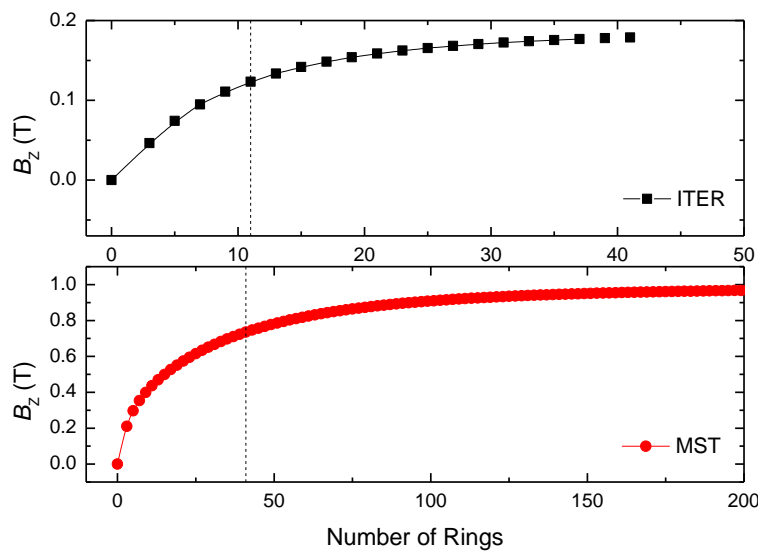
Figure 5.15 : The magnitude of the z-component of the magnetic field as a function of the number of turns for (top) ITER geometry (bottom) MST geometry. The vertical dashed line indicated the number of turns in the titanium alloy section of the measurement barrel.

5.2.3.4. Mesh Density

The effect of varying the mesh density, relative to the fixed strand diameter, of a stack of nine rings with a circular cross-section (R_{Min} = 0.311 mm) was modelled. The MST separation of turns was used. The magnetic field distribution was calculated using the A-V formulation, shown in Figure 5.16. The distribution in B_x in the central ring is shown, with a fixed field colour bar range ± 0.8 T. Visually the distributions of the magnetic field in the three panels are broadly similar, reading the colour bar suggests a maximum magnitude of $|B_x|$ < 0.8, which is different from the results derived from the FEA, quoted in Table 5.7. It is important to determine if there is an error in the data output from the analysis. The average of the magnetic field should be zero, and with a higher density mesh, the value approaches zero.

(a)   (b)

(c)
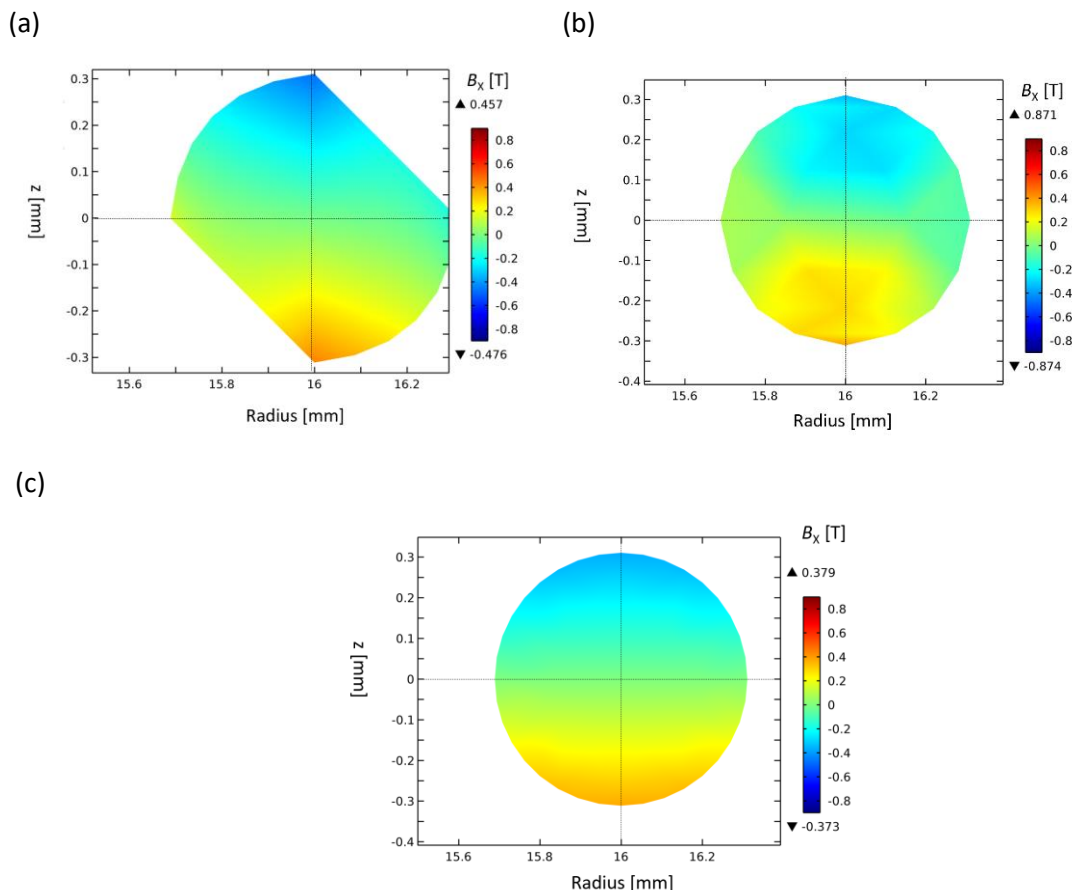
Figure 5.16 : The different distributions of the B_x with mesh size for a circular cross-section. The approximation of the circular cross-section improves with mesh density (a) Fine (b) Finer (c) Extra fine. The geometry is a stack of nine rings with a separation between rings, the same as the MST (0.830 mm). The crosshairs note the centre of the cross-section

Mesh	MESH SIZE [mm]	Degrees of Freedom	Calculation time [s]	Min. B_x Field [T]	Average B_x Field [T]	Max. B_x Field [T]
Fine	0.065	502,541	119	-0.758	-0.001	1.214
Finer	0.046	1,664,118	256	-0.874	-0.0002	0.871
Extra fine	0.037	1,972,561	1,315	-0.430	0.00005	0.454

Table 5.7 : The computational expense of a nine turn geometry MST with mesh density, for data shown in Figure 5.16. Differences of the x-component of the magnetic field with mesh density.

5.2.3.5.   CERN Correction

The magnetic field generated in the standard transport measurements, ITER VAMAS geometry, has been studied by the CERN group, as part of their research to understand self-field [2, 18, 29]. The CERN self-field correction ($B_{\mathrm{SF}}^{\mathrm{CERN}}$) is calculated from the peak transversal field, B_z [2]. The $B_{\mathrm{SF}}^{\mathrm{CERN}}$ self-field correction is widely used when analysing transport measurement data [29-37].

As the internal note [2] is not publicly available the important details are noted here for the reader. The FEA calculation uses the A-V formulation, implemented with Comsol AC-DC module. Several

simplifications to the ITER measurement geometries are made. To simplify the calculation, the dimension was reduced from 3D to 2D. In a 3D model of the helix, the angle of the current relative to B_{App}, flowing in the strand wound on the ITER barrel is 88.2°. In the 2D axisymmetric model, current flows at an angle of 90° relative to B_{App}. The argument presented was that the difference in the peak B_z of a 3D model and a 2D axisymmetric model is that no significant differences were found between the two models, so the analysis can be done using the 2D model. The second simplification is the number of turns considered. The 2D model considers the helix as nine rings spaced by the separation of turns. The geometric details of the measurement barrel, (Table 3.3) state there are 16 turns in the barrel, with 11 in the titanium section. The third simplification of the FEA model was that the peak field on the surface of the conductor (diameter 0.8 mm), is "practically equal" to the peak field in the superconducting filaments of a composite strand.

For the calculations, a fixed current of 1 kA is used. The current source and drain are defined in each ring separately. The magnetic field is defined as B_{App} = 0 T. The material properties of the rings are defined using copper. A parametric study is carried out, with the parameter varied the length between the centre of the strand to the outermost superconducting filament r_{of} . The peak field in the central ring of the stack in the FEA calculation was output for the inward F_{L}, with the data reported in Table 5.8. The justification of defining the effect of self-field with the peak in B_z is the high n-index of Nb-Ti, which will be discussed further in section 6.1.3.1.

The CERN self-field correction term, Eq. (5.25), is calculated by calculating the difference between the straight wire term Eq.(5.6), the peak in the FEA:

$$B_{\mathrm{SF}}^{\mathrm{CERN}}(I, r_{\mathrm{of}}, \alpha_a) = I \cdot \left[\frac{\mu_0}{2\pi r_{\mathrm{of}}} + \alpha_a \right], \tag{5.25}$$

The value of the constant α_a in Eq. (5.25) is dependent on the orientation of the F_{L}. Depending on the current and field orientation the position of the peak magnetic field varies from the inside of the strand i.e., $R_{\mathrm{Maj}} - R_{\mathrm{Min}}$, to the outside $R_{\mathrm{Maj}} + R_{\mathrm{Min}}$. Although all the results are not reported explicitly in the paper, for calculations in zero applied field, it is unclear how the differences with orientation was calculated. For inward F_L measurements, α_a = - 9.0 × 10⁻⁵ [T· A⁻¹] and for outward F_L, α_a = 1.5 × 10⁻⁴. The self-field correction vs radius to the outermost filament is shown in Figure 5.15 (upper panel). It is clear from Table 5.8 that for r_{of} = 0.5 mm and current of 1 kA, the difference between Eq. (5.6) and B_Z FEA is on 0.096 T·kA⁻¹. Using this data point, to one significant figure, α_a is defined. No numerical values are provided for the outward F_{L} calculations.
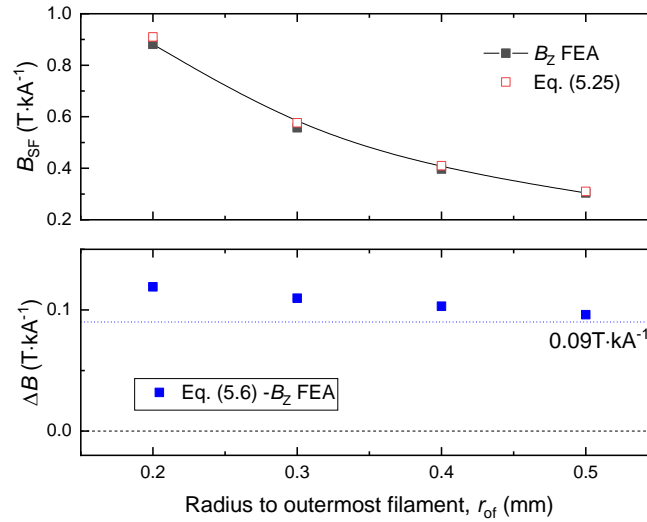
Figure 5.17 : (Upper panel) The B_{SF} calculated using FEA is compared with the defined self-field correction term [B_{SF}^{CERN}: Eq. (5.25)]. (Lower panel) The difference between the straight wire equation [Eq. (5.6)] and the FEA. The blue dotted line is α_a for 1 kA inward F_L; the constant term 0.09 T·kA⁻¹.

Radius r_{of} [mm]	B [Eq.(5.6)] [T]	B_Z FEA [T]	B_{SF}^{CERN}: [Eq. (5.25)] [T]
0.5	0.400	0.304	0.310
0.4	0.500	0.397	0.410
0.3	0.666	0.557	0.580
0.2	1.000	0.881	0.910

Table 5.8 : The results from Ref. [2] self-field correction as a function of radius to the outermost filament, r_{of}, for a sample with current of 1 kA. Inward F_L.

A simple problem with the B_{SF}^{CERN} analysis is highlighted by the lower panel of Figure 5.15. Using the data in the note, for a fixed value of α_a the difference between the FEA results and Eq. (5.25) can be substantial. For r_{of} = 0.2 mm, the 29 mT difference between FEA and Eq. (5.25), is results in a 32 % larger self-field correction term. It should be possible to characterise the difference between the FEA and the straight wire term Eq.(5.6) more accurately.

5.2.3.6.   Previous Helical Models

Several self-field corrections calculated for the helical geometry are reviewed in [29]. A Fortran calculation by den Ouden [38] modelled the ITER helix geometry. Although no details are available, numerical values were reported in [39]. The self-field correction in [29] is of the same form as Eq. (5.25) with a different value of the constant for inward Lorentz force: α_a -10.0 × 10⁻⁵ T·A⁻¹.
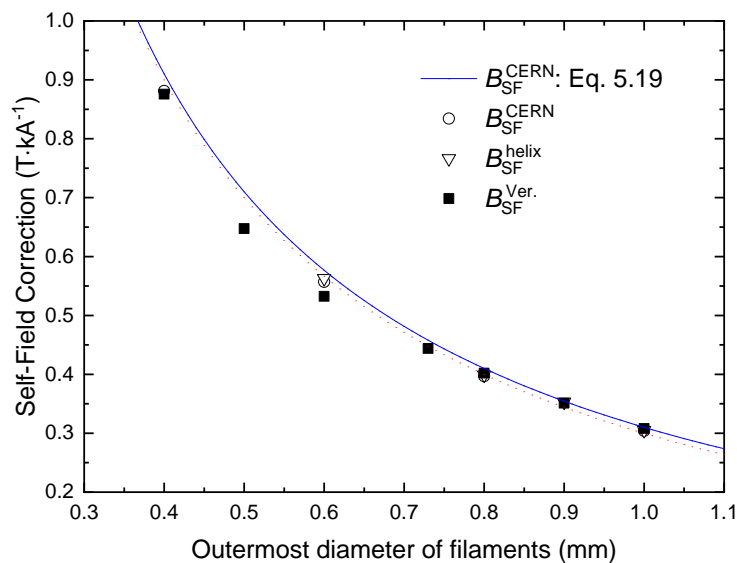
Figure 5.18 : Comparison of peak net magnetic field as a function of the outermost diameter of filament with literature definitions. The work calculated in this thesis: $B_{\text{SF}}^{\text{Ver.}}$ using the *A-V* formulation and a circular cross-section five turn helix.

The values for the peak magnetic field, $B_{\text{SF}}^{\text{CERN}}$ (Table I in Ref. [2]), Eq. (5.25) and $B_{\text{SF}}^{\text{helix}}$ (Table 5.1 in Ref. [39]) and the self-field correction results generated in this work used to verify the 3D FEA methodology ($B_{\text{SF}}^{\text{Ver.}}$). The calculations using the *A-V* formulation for a 9-turn helix are shown in Figure 5.18, and agreement is seen with the literature data.

The experimental results presented in chapter 6, highlight that by considering solely the ITER barrel measurement geometry agreement between different methodologies is not unexpected. The design of the barrel, large separation of turns, and the ratio of the major radius of the helix to the strands radius results in a measurement geometry where the effect of neighbouring turns is minimised, depending on the currents.

5.2.3.7.   Reduced Dimensions

The calculations presented by CERN uses a 2D axisymmetric model, a stack of rings, that is verified in their working using a 3D helical calculation. Another method to reduce the number of dimensions is to map from Cartesian coordinates, $\{x, y, z\}$ to some $\{u, v, w\}$, which encompass the twist pitch and the parameters of the helix [40]. Filamentary models using a 2D discretisation of a 3D model are beneficial [41]. The work presented in this thesis are helices modelled in 3D.

(a)   (b)
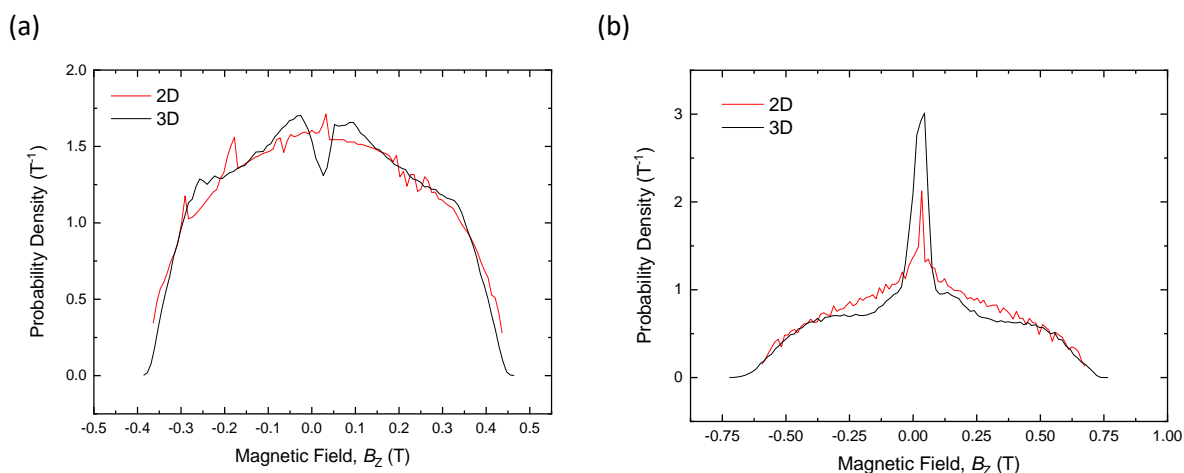
Figure 5.19 : Comparison of the probability density distribution for a single ring with 2D and 3D calculations using *A-V* formulations (a) circular cross-section R_o = 0.311 mm (b) Annular cross-section R_o = 0.311 mm and R_i = 0.136 mm.

5.2.3.8.   Probability Distribution: 2D and 3D

The magnetic field probability distribution of B_z inside the volume of a single ring is investigated using both 2D and 3D FEA, shown in Figure 5.19. Both circular, Figure 5.19 (a) and annular Figure 5.19 (b) cross-sections have been considered. Reasonable agreement between the 2D and 3D models, which can be improved by taking a finer mesh, is shown in Figure 5.19. With the 2D calculations, an 'extremely fine' mesh is built, while a lower density mesh 'finer' is used in the 3D calculations. Magnetic field distribution statistics are reported in Table 5.9. The difference in the average field for the circular cross-section is relatively small, while the peak changes by 10 %. For the annular cross-section, shown in Figure 5.19 (b), due to the smaller cross-sectional area, a higher current density in the strand results in a higher peak magnetic field. For the 3D geometries, the distribution is for the volume centred about the coordinate (x, y, z) = (0, - R_{Maj},0). The coordinate at which the volume of the strand is exported for the calculation of the distribution does not affect the resultant B_Z value. For the volume centred about the coordinate (x, y, z) = (0, 0, R_{Maj}), there is a large B_y component, and similarly for the volume centred about the coordinate (x, y, z) = (R_{Maj}, 0,0) a large B_x component.

Cross-section	Dimension	Minimum Field [T]	Average Field [T]	Maximum Field [T]	Runtime [s]
Circular	2	-0.368	0.030	0.441	7
	3	-0.390	0.029	0.469	13
Annular	2	-0.682	0.033	0.682	68
	3	-0.730	0.031	0.774	167

Table 5.9 : The magnetic field distribution statistics for *A-V* formulations of the single ring geometry plotted in Figure 5.19.

5.3.   Consistency Tests: Complex Geometries

The geometries and cross-sections considered in section 5.2 allowed several simple self-field corrections to be calculated and confirmed using FEA and analytic solutions. Using the results from the simpler geometries it is possible to replot $J_C(B_{App})$ measurement data accounting for the effect of self-field, as a function of $J_C(B_{Net})$. Analysing the experimental data, presented in chapter 6, it was clear that it is necessary to combine the helical geometry and capture the complex multifilamentary architecture of the strand to understand the experimental data. In this section, both analytic and FEA calculations for an array of straight wires and a stack of rings, and helices are presented.

5.3.1   Tubes-within-Tubes

Due to the complexity of the Nb-Ti strand's architecture, and the computing resources available, it is not possible to model each partially transposed filament in the strand. As the strands are twisted during manufacturing, the filaments are partially transposed in an annulus. Each of the 4488 filaments remains broadly at a constant distance from the central axis of the strand. The strand is considered as numerous and concentric thin layers. The strand is modelled as three annular nested tubes, tubes-within-tubes (TwT), shown in Figure 5.20, is proposed as an approximation to the partially transposed filaments. The TwT geometry allows current redistribution in the superconducting domain, without incurring a very high computational expense. Similar models where the current circulates the strand in addition to in and out of each filament have been reported [42]. In the TwT models, the superconducting region within the strand is described by three tubes that have equal wall thickness. The inner and outer radii of the tubes are reported in Table 5.10 and the fractional areas in Table 5.11. Although in the strand the central core is copper a resistive air domain is used in the FEA model. It is assumed that the current will flow in the nominally zero-resistance superconducting domain.

Inner Copper: [mm]	Tube 1: [mm]	Tube 2 [mm]	Tube 3 [mm]	Strand OD [mm]
R_0: 0.136	R_1: 0.194	R_2: 0.253	R_3: 0.311	R_4: 0.365

Table 5.10 : The outer radii in the tubes-within-tube models of the Nb-Ti strand.

Tube	Area [1 × 10^{-8} m^2]	Fractional Area [Unitless]
1	6.01	24.47
2	8.28	33.71
3	10.27	41.82

Table 5.11 : Cross-sectional, and fractional area of the tubes in the tube-within-tube model.
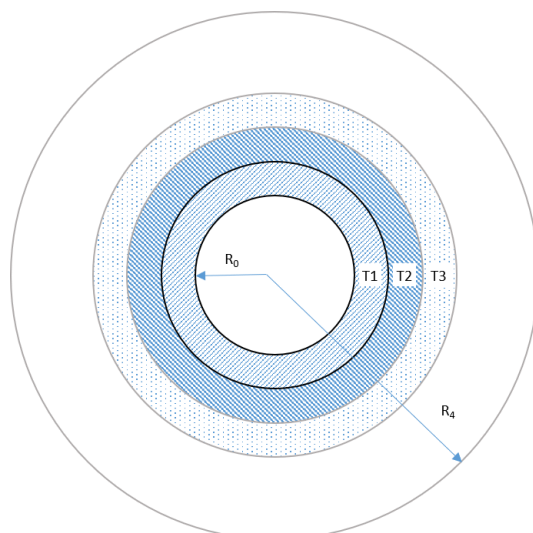
Figure 5.20 : Nb-Ti strand cross-section model three nested tubes (T1, T2, T3) of superconductors, tube-within-tube, with central resistive air ($R < R_0$) domain (figure not to scale).
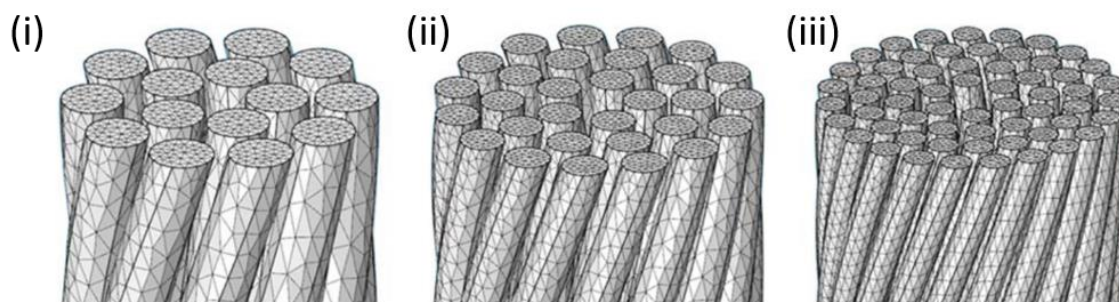
Figure 5.21 : Literature 3D FEA model of twisted filaments, with a varied number of Filaments (i) 15 (ii) 30 (iii) 60 filaments. The figure is from Ref. [43].

In the literature, Lyly looks at transposed filament bundles [43] shown in Figure 5.21. The FEA model is a straight wire composed of twisted filaments. The similarity between the filament geometry shown in Figure 5.21 and the tubes-within-tubes model is the group of filaments with fixed radii.

For the TwT geometry, the position and current dependent magnetic field is reported as a matrix

$$B\left(I_X, T_J\right) = \begin{pmatrix} F_{11} & F_{12} & F_{13} \\ F_{21} & F_{22} & F_{23} \\ F_{31} & F_{32} & F_{33} \end{pmatrix} \tag{5.26}$$

where F_{12} for example, is the magnetic field produced at the position of the outer radius of tube one (R_1) due to the current flow in tube two (T_2). The position-dependent values have units of T·kA^{-1}. The positions where the matrix values are calculated are the outer radius of each of the tubes 1-3, Table 5.10. Details for deriving the matrix values are outlined in section 5.3.5.3. Using the magnetic field matrices, the current distributions were calculated in chapter 6.

(a)

(b)
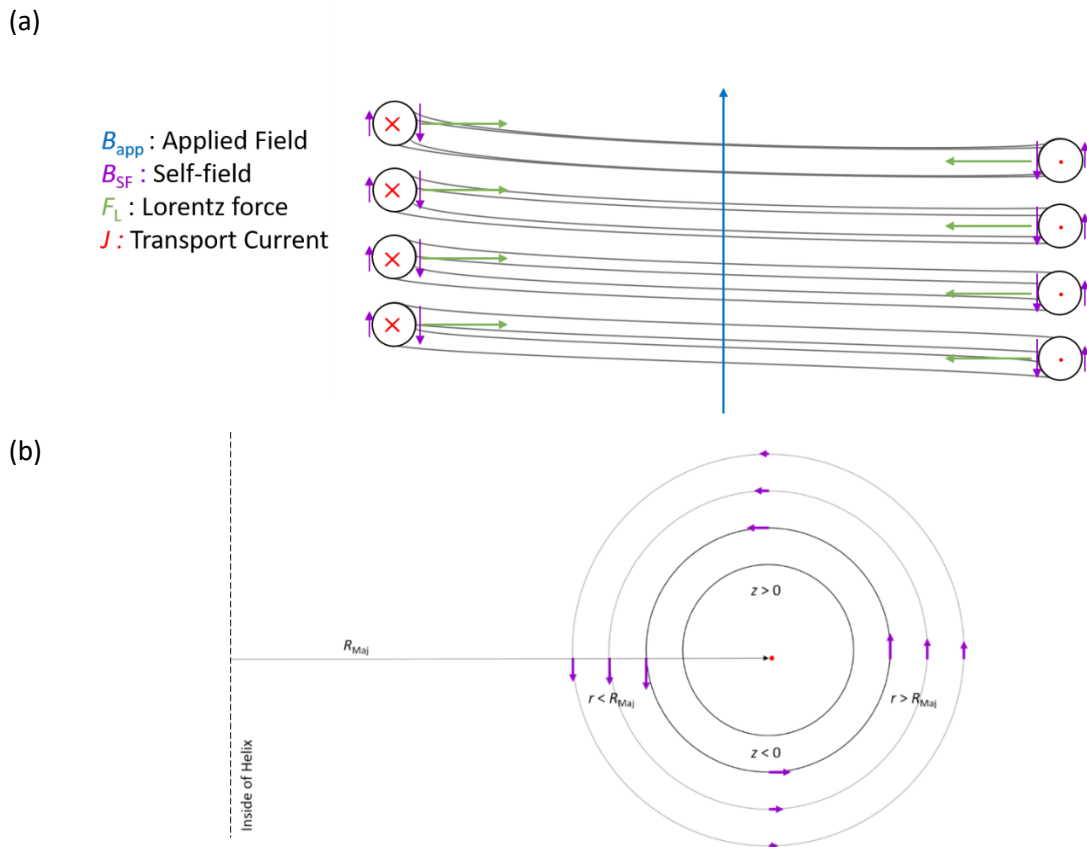
Figure 5.22 : Simplified vector diagram of the magnetic field and resultant Lorentz force for the standard measurement set-up (applied field, and current flow in the z-direction). (a) The inward F_L acting on the strand during measurement, result in the self-field that opposes the applied field at $r = R_{\mathrm{Maj}} - R_{\mathrm{Min}}$. (b) Schematic of the geometry of the tube-within-tube cross-section. The magnitude of the z-component of the magnetic field in the radial direction and the y-component of the magnetic field in the z-direction is represented vectorially at the outer radii of the three tubes considered. Current is flowing in tube 1 (black outline, the grey outline shows the positions of the other tubes).

5.3.2   Lorentz force Orientation

A schematic of the experiment, when the magnetic field direction and current orientation result in an inward F_{L} acting on the strand is shown in Figure 5.22. The F_{L} induced pushes the strand towards the measurement barrel [2]. The orientation of the applied field is fixed in the experiments, depending on the current and magnitude of the B_{App}, the magnitude and orientation of the B_{SF} can either increase or decrease the net magnetic field. From the form of the typical $J_C(B)$ relationship, it is assumed that the J_C locally decreases as the B_{Net} increases. With the inward F_{L} shown in Figure 5.22 (a), the net field is reduced on the side of the strand closest to the centre of the barrel. For the inward F_{L} force, the region of the highest magnetic field, and where dissipation will occur first, is at the outside of the helix, $r \approx R_{Maj} + R_{Min}$, and vice versa for F_{L} radially outwards.

For the central turn of the nested TwT geometry, shown in Figure 5.22 (b), the orientation and magnitude of the magnetic field are represented with vectors at the outer radii of the tubes. The

magnitude of the field is dependent on where the current is flowing, and the magnetic field is not equal, i.e., $\pm R_1$. The simplified geometry is shown in Figure 5.22 (b) does not consider the angular direction of the magnetic field vector. To calculate the magnetic field angle, θ,

$$\theta = \tan^{-1}\left(\frac{B_z}{B_r}\right). \tag{5.27}$$

where B_r is in the magnetic field in the radial direction. The matrices in Table A.13 are for both the magnitude and angle of the magnetic field, relative to B_{App} (in the $+B_z$ direction).

5.3.3 Array of Straight Wires

A helix can be considered as an array of straight wires. A slice along the x-z plane of the helix is shown schematically in Figure 5.23 (a). The elements of the straight wire array are positioned with the same separation in the x-direction i.e., the diameter ($2 \times R_{Maj}$). The vertical distance (z-direction) between neighbouring turns on the same side is S_T, while on the opposite side the increase is a half a turn ($0.5 \times S_T$). To approximate the helical current flow, the direction of current flow is opposite at $\pm R_{Maj}$.

In the region where the matrix is calculated, B_{Net} is the vector summation of the magnetic field $B_{Annulus}$ [Eq. (5.8)] which is the field inside the wire, and the magnetic field due to the other wires in the array, B_{Array}. The B_{Array} is calculated as the summation of the magnetic field due to the array of infinite straight wire using Eq. (5.6), with the z-distances defined by the separation of turns and R_{Maj}.

$$B_{Net} = B_{Annulus} + B_{Array}. \tag{5.28}$$

For the fixed strand geometry considered the $B_{Annulus}$ term is the same for both the approximation of the ITER and MST helix geometry. With two experimental S_T, the B_{Array} term is geometry dependent. The result of Eq. (5.28) are plotted in Figure 5.27, good agreement with the FEA results is seen for the ITER geometry but not for the MST geometry. The simplification of the radial distribution in Eq. (5.8), i.e., $B = 0$ for $r < R_1$ may account for the error. B_{Net} in the radial and z-directions see Table A.12 and A.13.
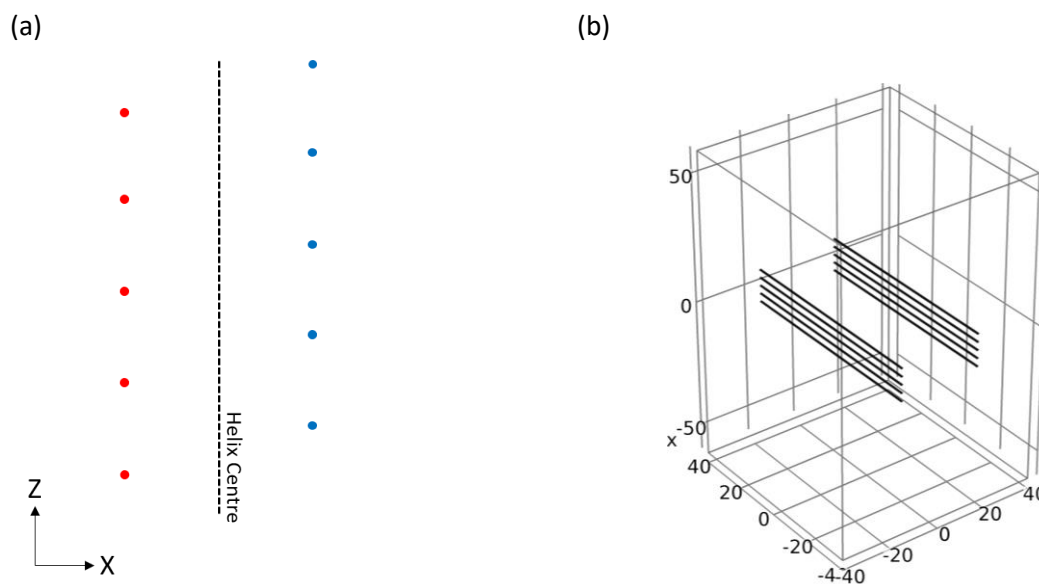
Figure 5.23 : (a) Simplified schematic of a straight wire array. Red points current into the plane, and blue out of the plane. Not to scale. (b) FEA model geometry of the straight wire array for an ITER type measurement.

5.3.4   Stack of Rings

Developing on section 5.2.3, the magnetic field distribution for a periodically arranged stack of rings was studied with the TwT cross-section. The calculated field matrices for the array of rings, the magnetic field is the vector summation of the individual ring (section 5.2.2.2) and the straight wire term for the rings above and below. For the ITER geometry 13 rings are considered, and MST 51 rings. The results for the stack of rings with the TwT cross-section are shown in Figure 5.27. Like the array of straight wires, the results of the stack of rings produces results consistent with the FEA for the ITER geometry, but not the MST geometry. For numerical values of the field matrices in the radial and z-directions see Table A.12 and A.13.

5.3.5   Helices

5.3.5.1.   Charge Conservation: 3D-FEA

An important check on the validity of the calculations was to ensure the conservation of charge. The positions of the six interfaces in the helix are shown in Figure 5.24 (a). In the geometry considered the FEA model consists of six domains. The extrudes (domains 1 and 6) connect the helix to the outside of the air domain. The helix (domains 2, 3, and 5) are where the current flows. The high-density mesh is implemented in domain 3. A high-density mesh air domain, around the centre of the helix (domain 4) is to locally increase the mesh density. The conservation of current is demonstrated by integrating the current density across interfaces. The interfaces are at the boundaries of the domains, i.e., the outer modelling domain, into the helix (domain 2), into and out of (domain 3), the volume analysed, and the

(a)

(b)   (c)
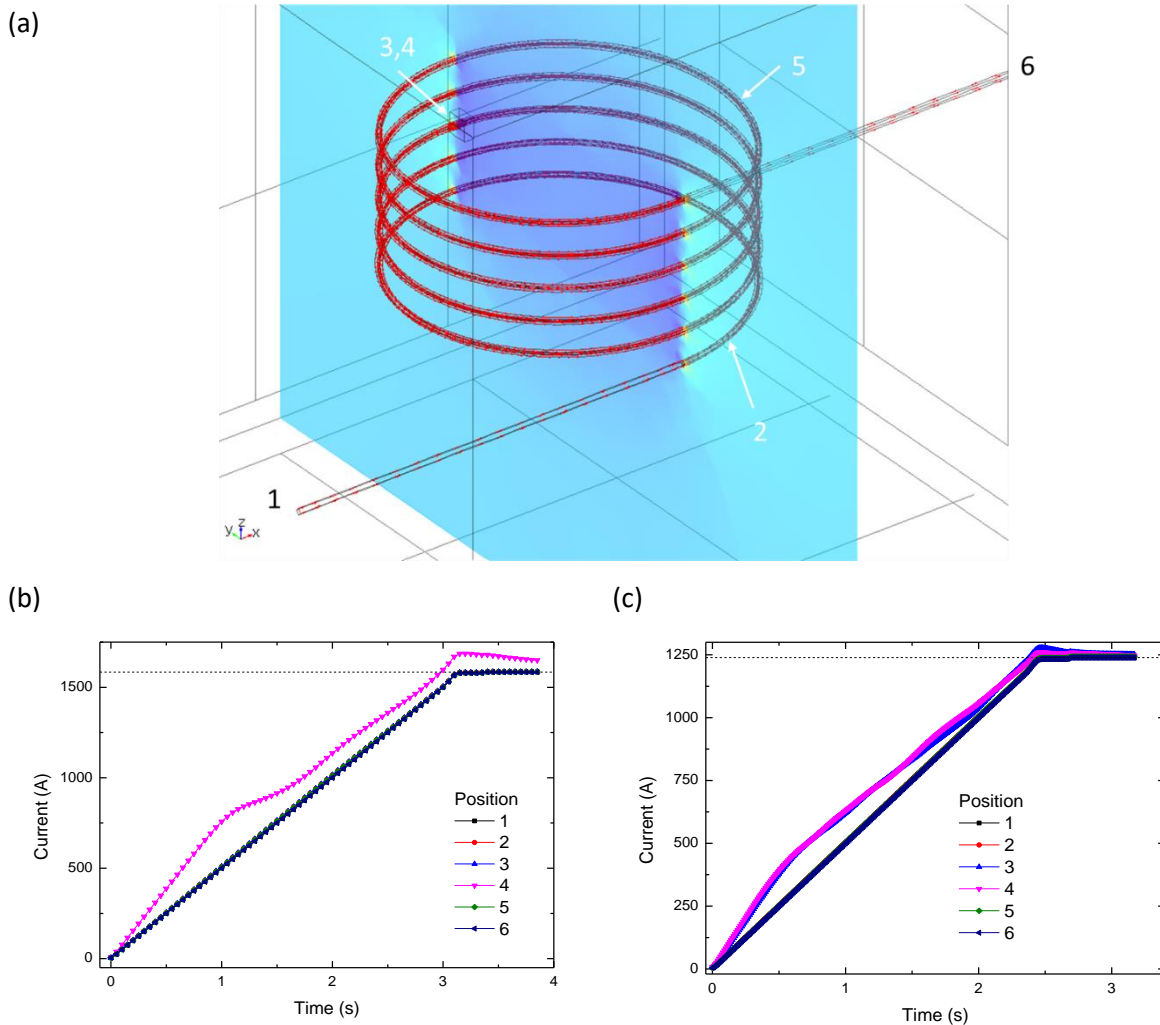
Figure 5.24 : (a)Labelled helix model in Comsol. The extrudes (1,6) connect the helix to the outside of the air domain. Domains 2, 3, and 5 are the helix. Domain 4 is a box volume of air around the centre of the helix region defined for a localised increased mesh density. The red arrows streamline indicate current flow direction. The colour plot is the distribution in the magnetic field. (b) Integral of the current density along the length of the helix at the positions of the interfaces for the two geometries (b) ITER (c) MST. The dashed horizontal line is the maximum critical current ramped to.

upper extrude and outer modelling domain. The current as a function of time and position, shown in Figure 5.24 (b, c) for the ITER and MST geometry shows there is reasonable continuity of current during the ramp.

5.3.5.2.   Probability Distribution and Number of Turns

The combination of the number of turns and the pitch of the MST barrel necessarily results in a large dense mesh. How the number of turns changes the magnetic field distribution was investigated, shown in Figure 5.25, with computation time reported in Table 5.12. In section 5.2.3.3, the analytic calculation for the ring geometry suggested that increasing the number of turns increased the magnitude of the magnetic field at a faster rate for the MST geometry, which is shown in Figure 5.25.
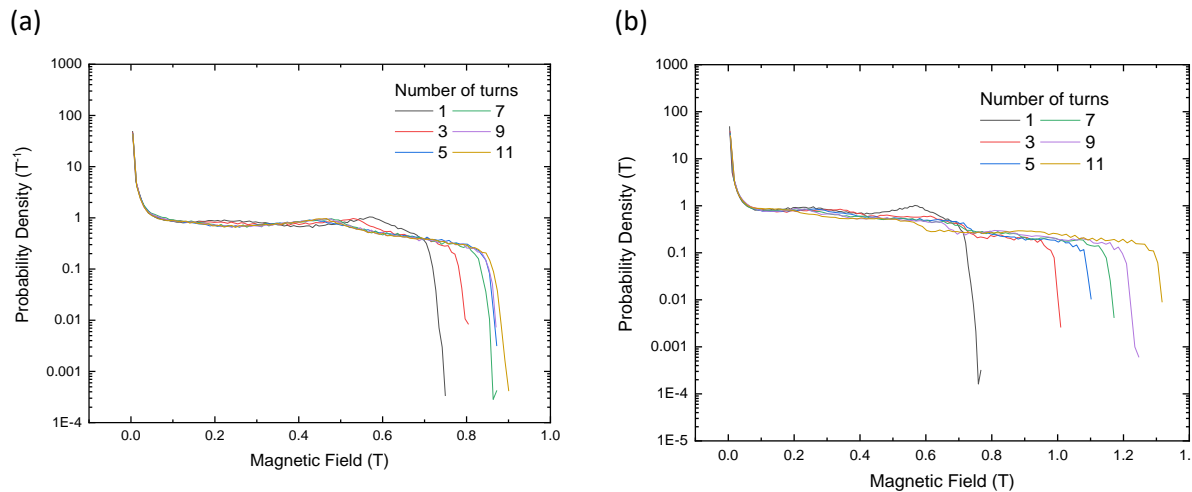
Figure 5.25 : (log-lin) Probability density as a function number of turns, B_{App}= 0 T, annular cross-section (a) ITER separation of turns (b) MST separation of turns.

Geometry	Runtime [s]		Average Magnetic field [T]	
Number of Turns	ITER	MST	ITER	MST
1	64,068	41,753	0.192	0.193
3	89,436	56,218	0.194	0.211
5	73,049	78,635	0.200	0.223
7	90,416	87,324	0.198	0.232
9	97,799	144,123	0.199	0.239
11	125,994	157,197	0.200	0.257

Table 5.12 : Computation time for a varied number of turns in
the two measurement geometries. Note: 86,400 seconds is a day

For the ITER geometry [Figure 5.25 (a)], changing the number of turns has a limited effect when there are at least five turns. For the MST geometry [Figure 5.25 (b)] a linear increase in the average magnetic field, ~5 mT·turn is seen. From these results, it is concluded that it is necessary to model the experimental geometry as closely as possible. The data demonstrates that the MST barrel modelled with 51 turns is extremely computationally expensive. The matrix elements in Table A.12 and Table A.13 are calculated for finite barrels using the experimental geometry.
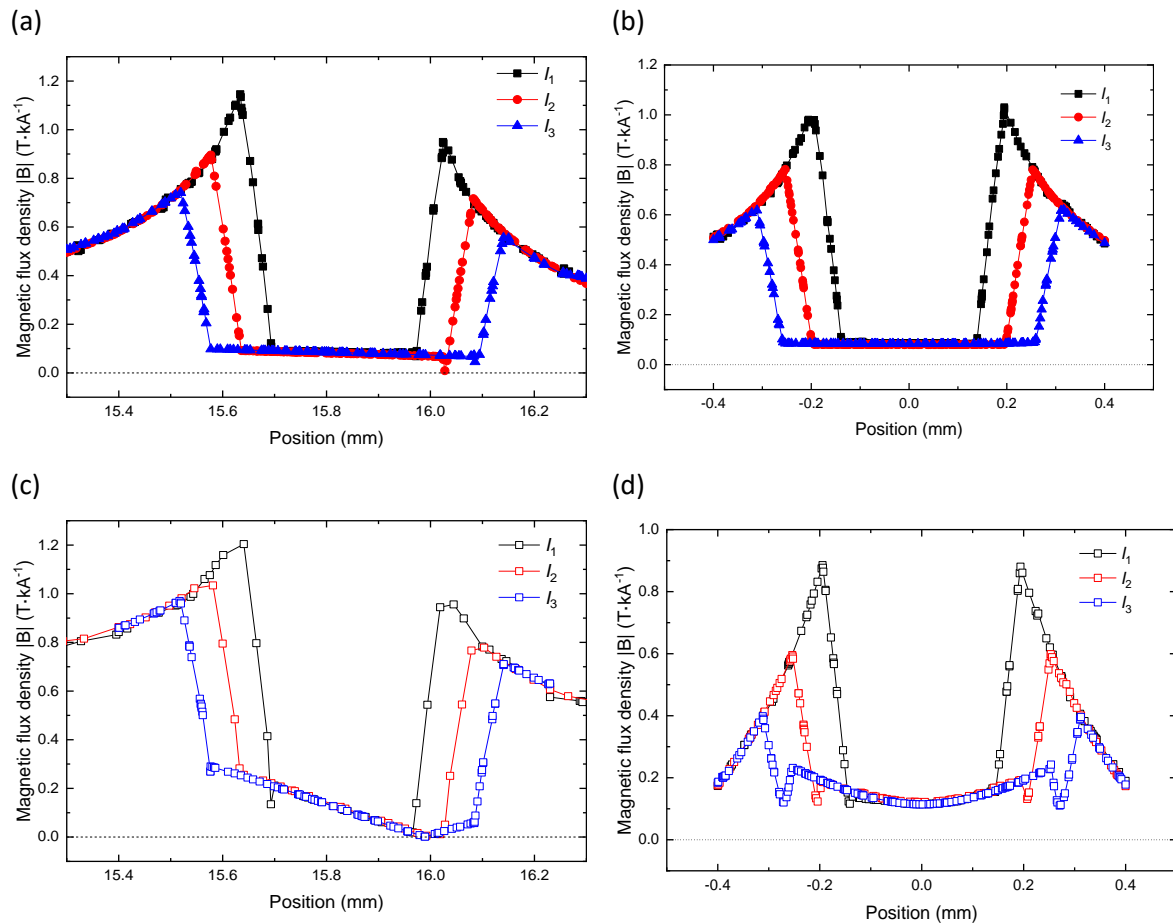
Figure 5.26 : FEA distribution of the magnetic field for three separate tubes (a) ITER in the radial direction (b) ITER in the z-direction (c) MST in the radial direction (d) MST in the z-direction. The current label i.e., I_1 denotes the tube which it flows in.

5.3.5.3. Matrix Elements

The helical TwT geometry was modelled with three separate FEA models, each with different R_i and R_o. The ITER and MST geometries were modelled. For the results shown in Figure 5.26, the ITER geometry was approximated with 11 turns and the MST geometry with 21 turns.

The FEA calculations shown in Figure 5.26 were repeated for 13 turns and 51 turns for the ITER and MST geometries respectively, but not included here. The peak values obtained were used to generate the matrix elements in Table A.12 and Table A.13. The magnetic field profiles through the centre of three separate strands modelled are shown in Figure 5.26. The magnetic field in the radial direction is shown in Figure 5.26 (a, c) and the z-directions is shown in Figure 5.26 (b, d). For current flowing in tube 1 i.e., R_i= 0.136 mm and R_o = 0.194 m, the profile is labelled I_1. The peaks in the magnetic field shown in Figure 5.26 are at the outer radius of each of the tubes. From the value of the magnetic field at the positions of the $R_{Maj} \pm R_o$ (for the three values of R_o) the matrix elements were calculated, equivalently for $z = 0 + R_O$ (for the three values of R_O).

For the ITER geometry shown in Figure 5.26 (a, b), the gradient of the magnetic field in both the x and r direction is small (for $r < R_{\text{Maj}} + R_{\text{i}}$) it is 58 mT·mm^{-1}. For $r < R_i$), the magnetic field is linear, and the range is small between 75-100 mT. For the MST geometry, the magnetic field for $r < R_{\text{Maj}} + R_i$ in the varies from $0 - 300$ mT in the radial direction (722 mT·mm^{-1}) and 100-240 mT in the vertical direction.

The results from the single ring and stack of ring matrix elements agree with FEA for the ITER geometry shown in Figure 5.27 (a). For the methods considered the results agree, this may be due to the relatively large separation of the turns and ratio of major to minor radius of the ITER geometry. For the MST geometry, shown in Figure 5.27 (b), the discrepancy between the FEA and analytic solutions are varied. The peak value of the magnetic field for the MST geometry on the outermost part of the helix agree while the other points do not. The straight wire array does not result in a uniform magnetic field between the array ($r < R_{\text{Maj}}$). The stack of rings most closely approximates the results of the FEA. With the single ring, the magnetic field is not added vectorially by rings above or below and has the smallest magnitude.

5.3.5.4.   Current Ramp: 3D-FEA

The experimental data acquisition procedure was mimicked using time-dependent calculations. Experimentally the current was ramped to an approximated I_{C} value, interpolated or experimentally measured, over a period of 120 seconds. The FEA calculations could not be ramped similarly due to the required computing time. Three methods for ramping the applied current in the computation were considered.

The current was ramped linearly at a rate of 50 A·s^{-1}. The second method included a stepped increase in which the current was rapidly ramped, imposed at a rate of 400 A·s^{-1} up to 90% of the critical current, and then was ramped between 90 % and 110 % of the critical value (from experimental data) at a slower rate of 4 A·s^{-1}. The density of data around the E-field criterion is higher for the stepped increase. These two methods are compared in Figure 5.28 (a), with agreement seen. For the linear ramp, the low current data obtained is of little use to the self-field calculations. In the third calculation, the current was increased up to 120 % of the measured critical current and then slowly decreased to 90 % of I_C, Figure 5.28 (b). The I_C at the E-field criterion is different by 140 A (8 %).

(a)

(b)
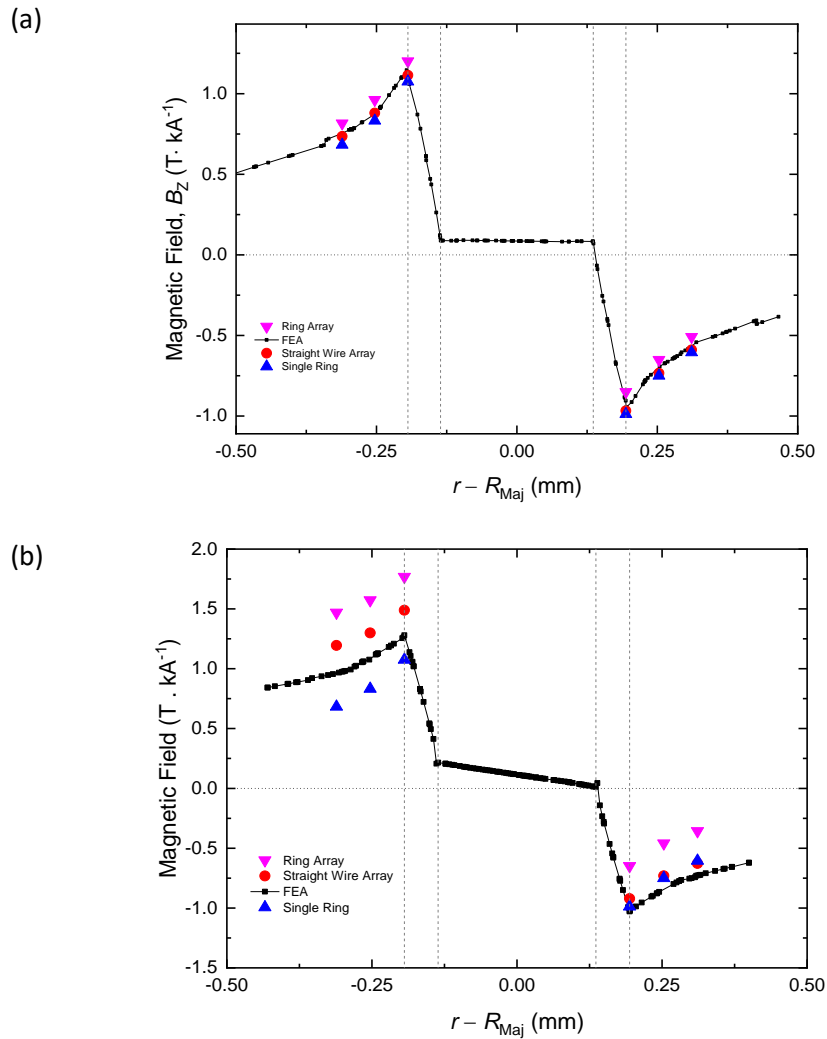
Figure 5.27 : Comparison of the magnetic field as a function of radial distance in the region of the strand calculated using different methods. The vertical dashed lines are a guide for the eye at $r = R_i$ and R_o of the tube. (a) the ITER geometry (b) the MST geometry.

a)

(b)
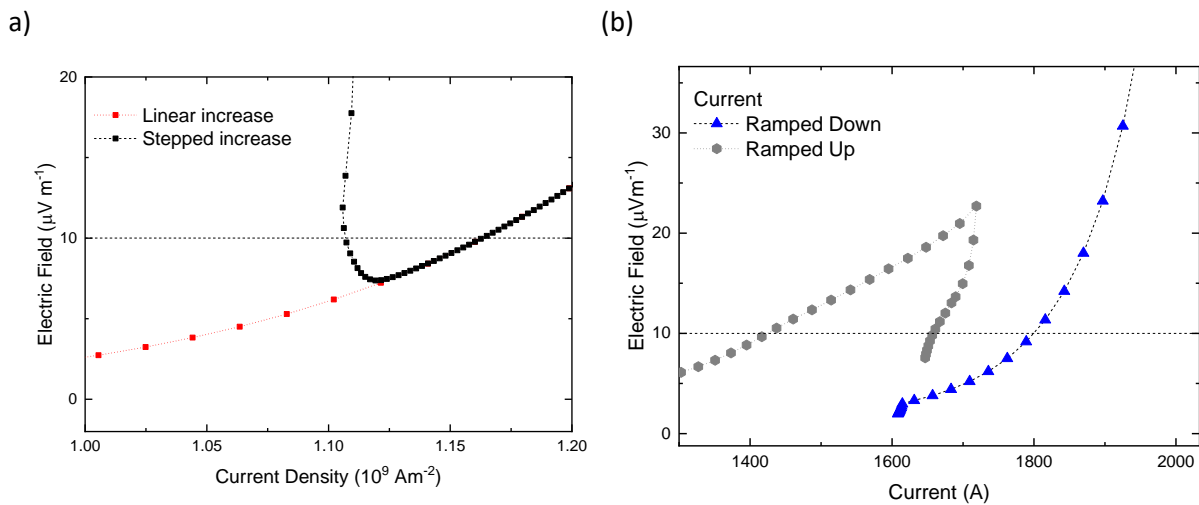
Figure 5.28 : The effect of the current ramp (a) ramp rate (b) current ramp direction.

5.4.   Conclusions

If the geometry and superconducting properties are known, numerical models are a useful and flexible tool to calculate the performance of a system. Finite element analysis is essential to accurately describe magnetic field profiles and distributions due to helical current flow. In chapter 5, the reliability of the models, from simple to complex geometries has been shown. The radial distribution of the magnetic field calculated using FEA of isolated geometries and stacks of rings and arrays of straight wires produce results which agree with the analytic models.

There are several disadvantages to using FEA, the choice of the input parameters, the meshing, and the order of the elements, all affect the solution. It is necessary to check that results are consistent. As the results of FEA calculations are always approximate solutions, the accuracy depends on how well the problem was posed and discretised. The approximations of the experimental geometry have been investigated, and the necessary complexity to capture the detail was implemented. An important point to consider is the difficulty in using the models to capture the non-linear behaviour as the current in the system is increased to a value up to and then exceeds the J_C value, highlighted in Figure 5.10.

Using the FEA modelling technique developed, magnetic fields of the complex experimental geometries are calculated to analyse experimental data in chapter 6.

References for chapter 5:

[1]   "Mathematica," 11.0.0.0 ed. Champaign, Illinois: Wolfram Research, Inc., 2018.

[2]   B. Bordini, "Self-Field Correction in Critical Current Measurements of Superconducting Wires Tested on ITER VAMAS Barrels," in "CERN-ITER Collaboration Report," ITEREDMS Nr: 1105765, 2010.

[3]   (22/01/2018).   *HTS   Modelling   Workgroup*   [Website].   Available: http://www.htsmodelling.com/

[4]   F. Grilli, R. Brambilla, F. Sirois, A. Stenvall, and S. Memiaghe, "Development of a three-dimensional finite-element model for high-temperature superconductors based on the H-formulation," *Cryogenics,* vol. 53, pp. 142-147, Jan 2013.

[5]   F. Sirois, M. Dione, F. Roy, F. Grilli, and B. Dutoit, "Evaluation of two commercial finite element packages for calculating AC losses in 2-D high temperature superconducting strips," *Journal of Physics: Conference Series,* vol. 97, no. 1, p. 012030, 2008.

[6]   V. Zermeno, F. Grilli, and F. Sirois, "A full 3D time-dependent electromagnetic model for Roebel cables," *Superconductor Science and Technology,* vol. 26, no. 5, p. 052001, 2013.

[7]   Z. Hong, A. M. Campbell, and T. A. Coombs, "Numerical solution of critical state in superconductivity by finite element software," *Superconductor Science and Technology,* vol. 19, no. 12, pp. 1246-1252, 2006/10/23 2006.

[8]   M. D. Ainslie and H. Fujishiro, "Modelling of bulk superconductor magnetization," *Superconductor Science and Technology,* Review vol. 28, no. 5, p. 20, May 2015, Art. no. 053002.

[9]   R. Brambilla, F. Grilli, and L. Martini, "Development of an edge-element model for AC loss computation   of   high-temperature   superconductors,"   *Superconductor   Science   and Technology,* vol. 20, no. 1, p. 16, 2007.

[10]   C. Kittel, *Introduction to Solid State Physics*, Eighth ed. John Wiley & Sons, 1996, p. 673.

[11]   J. Rhyner, "Magnetic properties and AC-losses of superconductors with power law current—voltage characteristics," *Physica C: Superconductivity and its Applications,* vol. 212, no. 3-4, pp. 292-300, 1993.

[12]   M. Lyly, A. Stenvall, and R. Mikkonen, "Validation of Homogenized Filament Bundle Model in AC Loss Computations," *IEEE Transactions on Applied Superconductivity,* vol. 22, no. 3, p. 4705505, 2012.

[13]   M. Lyly, V. Zermeno, A. Stenvall, V. Lahtinen, and R. Mikkonen, "Finite Element Simulations of Twisted NbTi Conductors," *IEEE Transactions on Applied Superconductivity,* vol. 23, no. 3, 2013.

[14]   IEC, "Superconductivity - Part 1: Critical current measurement - DC critical current of Nb-Ti composite superconductors," in *International Standard*: International Electrotechnical Commission, 2006, pp. IEC 61788-1:2006.

[15]   B. Bordini, E. Barzi, S. Feher, L. Rossi, and A. V. Zlobin, "Self-Field Effects in Magneto-Thermal Instabilities for Nb-Sn Strands," *IEEE Transactions on Applied Superconductivity,* vol. 18, no. 2, pp. 1309-1312, 2008.

[16]   P. Gislon, L. Muzzi, S. Chiarelli, A. Di Zenobio, M. V. Ricci, and M. Spadoni, "Electrical characterization of the NbTi strand for the ENEA stability SEx-up experiment," *IEEE Transactions on Applied Superconductivity,* vol. 13, no. 2, pp. 1429-1432, 2003, Art. no. 1211867.

[17]   T. Boutboul, P. Lezza, and R. Wolf, "Low-current Resistance of Multifilamentary Superconducting Cu/NbTi Strands," in "Accelerators and Storage Rings," CERN2003.

[18]   T. Boutboul, S. Le Naour, D. Leroy, L. Oberli, and V. Previtali, "Critical current density in superconducting Nb-Tistrands in the 100 mT to 11 T applied field range," *IEEE Transactions on Applied Superconductivity,* Article; Proceedings Paper vol. 16, no. 2, pp. 1184-1187, Jun 2006, Art. no. 1643060.

[19]   G. Iannone, S. Farinon, G. D. Marzi, P. Fabbricatore, and U. Gambardella, "Modeling Experimental Magnetization Cycles of Thin Superconducting Strips by Finite-Element Simulations," *IEEE Transactions on Applied Superconductivity,* vol. 25, no. 1, pp. 1-7, 2015.

[20]   R. Pecher, M. D. McCulloch, S. J. Chapman, L. Prigozhin, and C. M. Elliott, "3D-modelling of bulk type II superconductors using unconstrained H-formulation," *Proc. 6th EUCAS, Sorrento, Italy, 2003,* 2003 2003.

[21]   J. D. Jackson, *Classical Electrodynamics*. Hoboken, New Jersey, United States: John Wiley and Sons, 1999.

[22]   T. Tominaka, "Magnetic field calculation of an infinitely long solenoid," *European Journal of Physics,* vol. 27, no. 6, p. 1399, 2006.

[23]   M. Lieberherr, "The magnetic field lines of a helical coil are not simple loops," *American Journal of Physics,* vol. 78, no. 11, pp. 1117-1119, 2010.

[24]   M. W. Garrett, "Calculation of Fields, Forces, and Mutual Inductances of Current Systems by Elliptic Integrals," *Journal of Applied Physics,* vol. 34, no. 9, pp. 2567-2573, 1963.

[25]   L. F. Goodrich and A. N. Srivastava, "II-3: Critical current measurement methods: quantitative evaluation," *Cryogenics,* vol. 35, pp. S19-S23, 1995, Art. no. pp. S19-S23.

[26]   J. M. Ferreira and J. Anacleto, "Using Biot–Savart's law to determine the finite tube's magnetic field," *European Journal of Physics,* vol. 39, no. 5, p. 055202, 2018.

[27]   A. Pathak, "An elementary argument for the magnetic field outside a solenoid," *European Journal of Physics,* vol. 38, no. 1, p. 015201, 2017.

[28]   S. R. Liao, P. A. Dourmashkin, and J. W. Belcher, *Introduction To Electricity and Magnetism*. Pearson 2011.

[29]   A. Godeke *et al.*, "A Review of Conductor Performance for the LARP High-Gradient Quadrupole Magnets," *Superconductor Science and Technology,* Article vol. 26, no. 9, p. 15, Sep 2013, Art. no. 095015.

[30]   A. J. Wuis, B. Bordini, A. Ballarino, L. Oberli, and H. H. J. ten Kate, "Characterization of Nb_3Sn Rutherford Cables for the LHC 11-T Dipole Magnet," *IEEE Transactions on Applied Superconductivity,* Article vol. 24, no. 3, p. 5, Jun 2014, Art. no. 4003505.

[31]   B. Bordini *et al.*, "Extensive Characterization of the 1 mm PIT Nb3Sn Strand for the 13-T FRESCA2 Magnet," *IEEE Transactions on Applied Superconductivity,* Article; Proceedings Paper vol. 22, no. 3, p. 4, Jun 2012, Art. no. 6000304.

[32]   I. Pong *et al.*, "Worldwide Benchmarking of ITER Internal Tin Nb_3Sn and NbTi Strands Test Facilities," *IEEE Transactions on Applied Superconductivity,* Article; Proceedings Paper vol. 22, no. 3, p. 4802606, Jun 2012, Art. no. 4802606.

[33]   W. M. de Rapper, B. Bordini, S. le Naour, L. Bottura, and H. H. J. ten Kate, "Critical Current in High-J_c Nb_3Sn Rutherford Cables Affected Substantially by the Direction of the Applied Magnetic Field," *IEEE Transactions on Applied Superconductivity,* Article; Proceedings Paper vol. 22, no. 3, p. 4, 2012, Art. no. 6001704.

[34]   Y. V. Karasev *et al.*, "J_c(B,T) Characterization of Commercial NbTi Strands for the ITER Poloidal Field Coils by Transport and Magnetization Methods," *IEEE Transactions on Applied Superconductivity,* vol. 23, no. 3, June 2013, Art. no. 6001304.

[35]   C. Zhou, D. Bessette, A. Devred, G. Romano, and A. Vostner, "The Scaling Parameterization of ITER Superconducting Nb-Ti Strands Throughout Worldwide Production," *IEEE Transactions on Applied Superconductivity,* vol. 26, no. 4, 2016, Art. no. 6000204.

[36]   J. W. Ekin, N. Cheggour, L. Goodrich, J. Splett, B. Bordini, and D. Richter, "Unified Scaling Law for flux pinning in practical superconductors: II. Parameter testing, scaling constants, and the Extrapolative Scaling Expression," *Superconductor Science and Technology,* Review vol. 29, no. 12, p. 38, Dec 2016, Art. no. 123002.

[37]   I. Pong *et al.*, "Current sharing temperature of NbTi SULTAN samples compared to prediction using a single pinning mechanism parametrization for NbTi strand," *Superconductor Science and Technology,* vol. 25, no. 5, p. 054011, 2012, Art. no. 054011.

[38]   A. den Ouden, "Fortran code for the self-field calculations on ITER barrels," ed, 2012.

[39]   A. Godeke, "Performance Boundaries in Nb_3Sn," PhD, Physics, University of Twente, Enschede, The Netherlands,, 2005.

[40]   A. Stenvall, F. Grilli, and M. Lyly, "Current-Penetration Patterns in Twisted Superconductors in Self-Field," *IEEE Transactions on Applied Superconductivity,* vol. 23, no. 3, 2013.

[41]   A. Stenvall, M. Siahrang, F. Grilli, and F. Sirois, "Computation of self-field hysteresis losses in conductors with helicoidal structure using a 2D finite element method," *Superconductor Science and Technology,* vol. 26, no. 4, p. 045011, Apr 2013.

[42]   A. M. Campbell, "Coupling losses in filamentary superconductors with a resistive barrier," *Superconductor Science and Technology,* Article vol. 10, no. 12, pp. 932-935, Dec 1997.

[43]   M. Lyly *et al.*, "Suitability of Bundle Approximation in AC Loss Analysis of NbTi Wires: Simulations and Experiment," *IEEE Transactions on Applied Superconductivity,* vol. 25, no. 3, pp. 1-5, 2015.

CHAPTER 6

6.   Quantifying the Effects of Self-Field

In this chapter, extensive critical current density (J_C) measurements of the Nb-Ti strands characterised are presented. Measurements in the two experimental geometries and Lorentz force (F_L) orientations resulted in different values of J_C at every applied magnetic field (B_App). Using the experimental data, the self-fields were calculated as a function of J_C and B_App. A universal curve describing the strand's J_C as a function of the magnetic field accounting for the effect of self-field is presented.

In section 6.1, experimental I_C data for the standard ITER barrel design, field, and F_L orientation in the benchmarking range of B_App is replotted with five of the literature self-field corrections terms used. The methodology, applicability, and the magnitude of the literature self-field corrections are discussed. In addition, the one example of a F_L direction-dependent literature self-field correction was calculated for the experimental data, and its implications are discussed.

In section 6.1.4, the experimental transport and magnetisation measurements of the Nb-Ti strands studied are reported. Measuring the same strand, wound on the ITER and MST barrels, makes it possible to isolate and investigate the effect of the helical geometry. Using data from the strands, the repeatability of the results is also seen. The transport J_C data are also compared to magnetisation data for B_App= 0 to 8 T.

In section 6.5 the finite element analysis model used to calculate the magnetic field distribution and self-field terms are described. The initial analysis including J_C as a function of the average of the magnitude of the net magnetic field ($\bar{B}_{Net}$) is presented. The effects of the FEA input parameters are investigated. The results of the model with the different $J_\text{C}(B)$ are compared and how well they can generate a universal $J_\text{C}(B)$ curve is evaluated. The section concludes by considering how closely the FEA results describe $J_\text{C}(\bar{B}_{Net})$.

In section 6.6, a linearised semi-analytic model, that combines both the FEA and experimental results as inputs, is used to calculate the distribution of current within the strands' filamentary region. The FEA matrix elements define the radial distribution of the magnetic field with current. Several piecewise $J_\text{C}(B)$ were calculated and compared with the experimental data. The $J_\text{C}(B)$ calculated results in a

universal plot for the Nb-Ti strands measured in this thesis. In section 6.7, the implications of the work presented in this chapter are discussed.

6.1.   Self-field Corrections in the Literature

The primary purpose of this thesis is to quantify the effect of self-field, finding self-field corrections for an arbitrary size and shape helical measurement geometry. The effect of self-field is to change the spatial distribution of the B_{Net} [1]. To contextualise the research, the self-field corrections used in the literature are compared. The self-field corrections can be characterised by considering the magnitude of the magnetic field per unit current, i.e., T·kA^{-1}. Most self-field correction equations in the literature are independent of B. Although it is clear that it is difficult to analyse data when B_{SF} is of the same magnitude as B_{App} [2-4]. Other self-field corrections from the literature state the range of B_{App} and currents within which they can be used. Infrequently self-field corrections have been applied to data without a detailed methodology [5, 6]. The self-field has been analysed for ITER measurement barrel geometries [7, 8] and reported to have intractable solutions. The range of self-field data corrections presented in this section is not exhaustive.

6.1.1.   Literature Methodologies

The first four methods discussed in section 6.1.1 account for the effect of self-field by evaluating the peak magnetic field in the strand. The fifth method considers an average value of the self-field in the strand. Two of the self-field corrections in this section consider the helical geometry of the transport measurement, with the others assuming a straight wire geometry.

Transport measurement of strand DR 4810 in the standard geometry and inward Lorentz force orientation F_{L}, I_{C} vs B_{App} (closed symbols) are compared with five self-field corrections (open symbols) shown in Figure 6.1. Transport measurements in the range of B_{App} shown in Figure 6.1 are typically used to verify the manufactured Nb-Ti strand's quality. The magnitude of the literature self-field correction for the data shown in Figure 6.1 varies from 0.205 to 0.733 T·kA^{-1}.

The experimentally measured I_{C} at B = 7.0 T (vertical dashed line in Figure 6.1) was 275 A. The values of I_{C} are calculated, with a linear $I_{\mathrm{C}}(B)$ assumed for the five cases, from the single experimental data set, the interpolated I_{C} values and the percentage increase are reported in Table 6.1. The I_{C} data at B_{App} = 7.0 T was considered throughout this chapter to enable direct comparison of effects and magnitudes of the different self-field corrections applied to single experimental data sets.
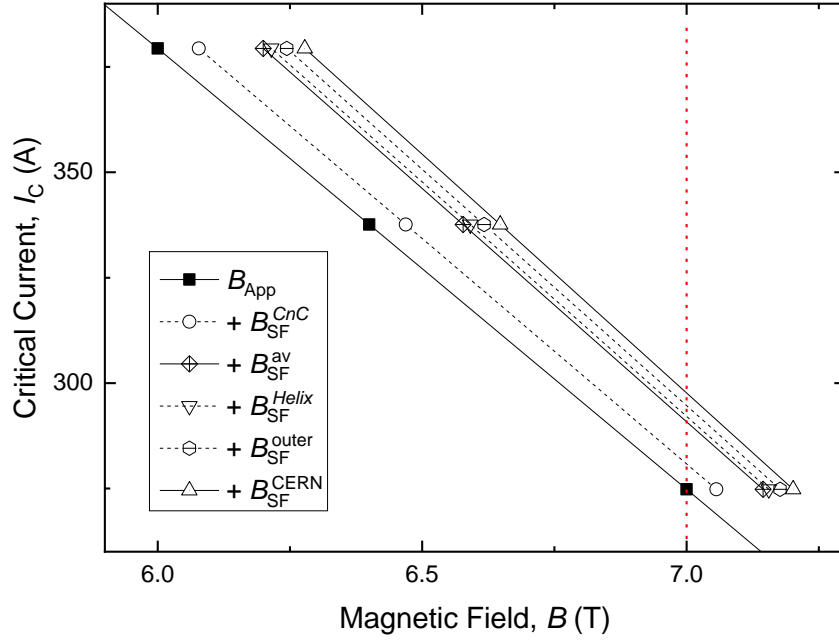
Figure 6.1 : Experimental data set with the literature self-field correction applied for the Nb-Ti strand DR 4810 wound on the ITER barrel. The dotted vertical line: B = 7.0 T. The experimental data is plotted as a function of the applied field [closed symbols: $I_C(B_{App})$]. The self-field corrected data is plotted as a function of the net magnetic field [open symbols: $I_C(B_{Net})$]. A linear $I_C(B)$ fit between data points is assumed in the range of B_{App}.

Correction term	B_{SF} [mT]	Interpolated I_C (B = 7.0T)	Increase in I_C [%]
$CnC: B_{SF}^{CnC}$	56.2	280.8	2.1
Composite: B_{SF}^{av}	144.5	290.8	5.7
Helix: B_{SF}^{Helix}	155.5	292.1	6.2
Outer: B_{SF}^{Outer}	167.7	294.6	7.1
CERN: B_{SF}^{CERN}	201.5	297.6	8.2

Table 6.1 : The resultant self-field, interpolated I_C and increase in I_C for the different self-field correction terms outlined in section 6.1.1. I_C (B_{App}= 7.0 T) = 275 A is compared with the interpolated $I_C(B_{Net})$ = 7.0 T (vertical dashed line in Figure 6.1).

6.1.1.1.   Copper to Non-copper Ratio

To account for the fact that the strand is a composite, the copper to non-copper ratio (CnC) is incorporated into the equation for the magnetic field of a thin infinite conductor with a circular cross-section. The peak magnetic field is modified by the volume fraction of the superconductor. The self-field is described by,

$$B_{SF}^{CnC}(J, CnC, D) = \mu_0 JR/2(1 + CnC),$$
(6.1)

where J is the current density and R is the strand's radius [9].

As the orientation of the F_L is not considered in this model, a single value of the self-field correction is calculated. The result of the correction is an increase from the B_{App} by 0.8 % at 7.0 T, and by an average of 1.1 % for the data shown in Figure 6.1 for a CnC value of 1.68. The increase in calculated I_C for the B_{App}= 7 T data is 2.1 %. In the 1989 paper by Garber [3] this methodology is suggested for multifilamentary wires, and good agreement is seen when comparing transport data corrected for the effect of self-field and the magnetisation data.

6.1.1.2.   Outermost Filament

By considering the architecture of the Nb-Ti strand (outlined in section 3.2), the simple modification to the infinite wire Biot-Savart law is to use the radius to the outermost filament in the filamentary region (r_{of}). Not including the copper crown, the region of copper around the annulus of filaments, increases the calculated effect of the self-field. The strands R= 0.365 mm is larger than r_{of} = 0.311 mm. Ignoring this copper region is justified as the current flow would be dissipative. The self-field correction term is described [10],

$$B_{SF}^{Outer}(I, r_{of}) = \mu_0 I/(2\pi r_{of}),\qquad\qquad (6.2)$$

where the notation is the same as used previously. The orientation of the F_L is not considered in this correction, a single value of the self-field is calculated. The result of this self-field correction is an increase from the B_{App} by 2.5 % at 7.0 T, and an average increase in B of 3.3 % for the data shown in Figure 6.1. The increase in I_C for the B_{App} = 7 T data is 7.1 %.

6.1.1.3.   Helix Model

The self-field correction which considers the helical geometry of the ITER barrel and is the standard which has been widely used in the community outlined in section (5.2.3.5). The CERN (B_{SF}^{CERN}) [11], Eq. (5.25) was used. The B_{SF}^{CERN} correction is the largest correction to I_C for the data presented. The increase from B_{App}= 7.0 T is 2.9 %, with an average increase in B of 3.8 % for the data shown in Figure 6.1. The increase in I_C for the B_{App}= 7 T data is 8.2 %.

In more recent work [12] the peak magnetic field was calculated for the helical geometry of the Brookhaven National Laboratory (BNL) Nb$_3$Sn test barrel [13, 14]. The BNL barrel has similar geometric properties to the ITER barrel, but the strand is soldered onto the stainless steel enabling higher currents during transport measurements. The self-field correction for two types of strand in the range of B_{App} from 7.0 to 11.5 T has been calculated for two strands of different diameters.

The self-field is described by,

$$B_{SF}^{\text{Helix}}(k, I) = kI, \qquad (6.3)$$

where the numerical values for k are dependent on the diameter of the strand, 0.570 T·kA^{-1} for 0.70 mm and 0.500 T·kA^{-1} for 0.88 mm. Assuming a linear relationship between the k values and diameter, for the strand characterised (0.710 mm) k = 0.566 T·kA^{-1}. The increase in I_C for the B_{App} = 7 T data is 6.2 %.

6.1.1.4.   Composite Zone Calculation

An analytic self-field correction term, which considers the cross-section of the strand with a single composite zone of superconducting filaments, has been calculated [15]. In the infinite straight wire geometry, the self-field is the average of the magnetic field due to the uniform current density in the superconducting region. The magnetic field due to current flow in the annulus region between the inner (R_i) and outer (R_o) radii was calculated. The average self-field is described by

$$B_{SF}^{av}(R_i, R_o) = \frac{\mu_0 I_C}{2\pi (R_o^2 - R_i^2)^2} \left(\frac{R_o^3}{3} - R_i^2 R_o + \frac{2R_i^3}{3} \right). \qquad (6.4)$$

Although Eq. (6.4) has been stated as valid for transport data at B_{App}< 1 T, it has been included in Figure 6.1 as an example of a self-field correction defined by the average. The increase from B_{App}= 7.0 T is 2.1 %, and an average increase of 2.7 % for the data shown in Figure 6.1. The increase in I_C for the B_{App}= 7 T data is 5.7 %.

6.1.2. Lorentz Force Orientation

With a fixed orientation of the magnetic field and the helical geometry, reversing the transport current direction changes the orientation of the Lorentz force (F_L), outlined in section 5.3.2. Measuring a difference in I_C with the orientations of F_L is one method to demonstrate the change in magnitude and orientation of the self-field [16]. Experimentally it is important to ensure that changes are due to the field distribution and not degradation of the strand. It has been reported in the literature that cycling the F_L orientation, even at high F_L, does not decrease the performance stability of Nb-Ti [17].

With measurements of the multiple Nb-Ti strands, and with varied magnetic field history, the differences in the measured I_C with Lorentz force was seen consistently. Inward F_L results in a higher measured I_C than outward F_L. Both the precision of the measurement, and the result of the inward F_L consistently resulting in a higher I_C ensured confidence in the experimental measured difference
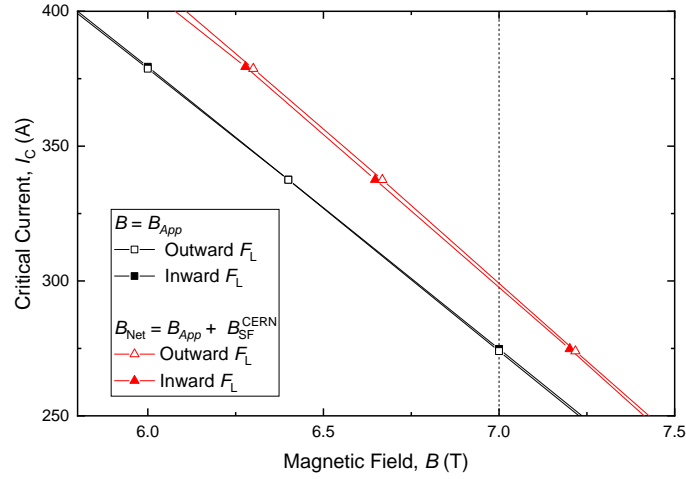
Figure 6.2 : Experimental $I_C(B_{\text{App}})$ and CERN self-field corrected [Eq. (5.25)] $I_C(B_{\text{Net}})$ critical current data for strand DR 4810 in both orientation of Lorentz force. The linear fit are a guide for the eye. The dotted vertical line: B = 7.0 T.

F_{L} orientation	I_C (B_{App}= 7.0T)	I_C (B = 7.0T)	Increase in I_C [%]	$B_{\text{SF}}^{\text{CERN}}$[mT]
Inward	274.8	297.6	8.3	201
Outward	274.0	299.1	9.2	217

Table 6.2 : Comparison of I_C in both orientations of Lorentz force for B_{App} and $\bar{B}_{Net}$ applying the $B_{\text{SF}}^{\text{CERN}}$ self-field correction Eq. 5.22.

due to the current and applied magnetic field orientations.

The self-field corrected data $I_C(B_{\text{Net}})$ for the two F_{L} orientation using the $B_{\text{SF}}^{\text{CERN}}$ correction term with the two α_a values is shown in Figure 6.2. The $B_{\text{SF}}^{\text{CERN}}$ correction outlined in 5.2.3.5 defines the effect of self-field by the peak in B_z distribution and as a result for any value of I_C the effect is to increase B_{Net}. Seeing an increased I_C in both orientation due to the effect of B_{SF} is not intuitive. When considering reversing the current orientation relative to a fixed B_{App} the effect of the field should act in the opposite direction. The interpolated difference in I_C for the two orientations at B_{App}= 7.0 T, is very small (< 2A) within the measurement error. The difference in the B_{Net} from Eq. (5.25) for the B_{App} = 7.0 T of 16 mT. The data shown in Figure 6.2 is summarised in Table 6.2.

It is difficult to analyse self-field entirely from the differences in I_C that are measured when the orientation of F_{L} is changed. If the form of the equation for self-field is $B_{\text{Net}} = B_{\text{App}} + B_{SF}^*$, where B_{SF}^* has a term due to both the Lorentz force distribution B_{F_L} and the helical geometry B_{Helix}.

6.1.3. Applicability of the Literature Methodologies

The maximum increase in I_C of 8.2 % (Table 6.1) is a conservative estimate of the effect of self-field. The discrepancies due to self-field, where the peak field has been applied to characterise the correction to the net field, is still an open question in the community. Inconsistencies in measurement results when the literature methods have been used are not "completely unexpected" [18].

6.1.3.1. Architecture

Understanding the effect of the architecture is necessary to account for the effect of self-field. The effect of self-field is dependent on the architecture of the strand [19]. The layout of the filaments in the strand has a substantial effect. While the twisting of the filaments decouples the magnetic field with respect to the transverse fields, the filaments are affected by self-field [20]. The self-field flux is linked between the inner and outer filaments [21]. Although the self-field losses are not considered in thesis, the self-field losses are influenced by twisting of the filaments [22]. Experimentally, at high B_{App}, the twist pitch has little effect on J_C [23].

The literature methodologies that consider the filament layout, account for the architecture with a homogenised term. In analysis that considers an annulus of filaments, the ratio of matrix area to the area of the homogenized filament bundle is also considered [24, 25]. While the new approach implemented in this thesis is to consider a self-field correction which accounts for the architecture of the strand with the TwT geometry.

6.1.3.2. Peak field

The peak in the magnetic field distribution is most used to define the effect of self-field. The peak is both a conservative estimate of the self-field [27] and typically the simplest to calculate [28]. Additionally, the behaviour of the current and the architecture of the strand can be used to argue for the peak field, which will be discussed further in this section. Conversely, it has also been argued that using the peak field has no real theoretical justification [29, 30].

For a constant transport current density (J_{Tr}) flowing along the conductor, where $J_{Tr} \approx J_C$, the current cycles in and out of the highest magnetic-field region due to the transposition of the filaments [31]. The electric field generated by this current flow will vary with the magnetic field [32, 33]. In calculations of the distribution of voltages due to self-field, the peak magnetic field contributes the majority of the voltage [34].

For the peak to characterise B_{SF}, the filaments are required to be fully transposed; filaments are not fully transposed in any Nb-Ti strand [21]. The way that the filaments are twisted during manufacturing result in each filament at a fixed radius from the strand's centre, and a number of filaments at that radius. The result of the twisting is that that many of the filaments experience the same electromagnetic conditions [35]. The filament transposition and the gauge length would suggest that the effect of peak magnetic field is localised; not all filaments experience the peak in B_{Net}. The purpose of calculating the probability density distribution of the magnetic field in this work is to quantify the volume of the strand which is at the peak magnetic field, shown in Figure 5.19. The skew and shape of the probability distributions calculated demonstrate that only a small fraction of the strand experiences the peak magnetic field value, shown in Figure 6.22 (b). The analysis demonstrates that the effect of the peak field is localised, such that the conductor cross-section exposed to the peak field is a very limited fraction [34].

An additional effect to consider in the multifilamentary conductor is that the current can redistribute. The typical form the $J_{\text{C}}(B)$ relationship (higher B results in lower J_{C}) it is possible that there is magnetic field gradient in the volume of the strand [3].

The $B_{\text{SF}}^{\text{CERN}}$ correction [11] argues that the large value n-index, justifies the peak field defining the self-field correction. Using the peak field to characterise the self-field correction can be justified if the index of transition is infinite, and filaments are fully transposed. For a fully transposed filament when any part of the outermost filaments becomes normal, all filaments become normal. The n-index measured for the Nb-Ti strand, shown in Figure 6.14, has finite values between $20 < n < 100$.

6.1.3.3. Average Field

The alternative to using the peak magnetic field to describe the self-field is to use an average field, with a magnitude between $B_{\text{App}} \pm B_{\text{SF}}$ [36]. If the local magnitude of B_{Net} determines J_{C}, parts of the strand experience a self-field that adds in parallel to the B_{App} and produces an E-field $> E_{\text{C}}$. Conversely, regions of the strand where the self-field opposes the applied field, the E-field $< E_{\text{C}}$. In regions where the self-field is orthogonal to the B_{App}, the B_{Net} increases, with no compensation occurring in regions where the self-field has opposite polarity. However, if the self-field is characterised by an average in the distribution of B_{Net}, it is possible that the self-field correction opposes the direction of the applied field, i.e., $B_{\text{Net}} < B_{\text{App}}$. The results from section 6.1.2 suggest that B_{Net} is always larger than B_{App}, and accordingly the J_{C} measured is lower than its true value.

Figure 6.3 : Photograph of a superconducting wire mounted on a tee-shaped Walters spring. S_T = 6.35 mm, R_{Maj} = 12.5 mm. Figure taken from Ref. [37]

6.1.3.4.   Measurement Geometry

Before and after the standardisation of the ITER VAMAS measurement barrel geometry, strands have been characterised in different helical geometries [38]. In order for data in different helical geometries to be useful for understanding the performance of the strand, a geometry-dependent self-field correction is needed [38]. Transport data for Nb-Ti strands measured in the BNL, ITER, and CERN geometries are compared in Ref. [39]. As self-field corrections are not usually applied to benchmarking data [40], it is possible to quantify systematic differences due to the geometries of the different measurement barrels. As CERN typically uses a larger diameter measurement barrel for its Nb-Ti measurements, a smaller B_{SF} is expected and found to produce a systematically higher J_C than all other participants [39].

The variables in the literature self-field correction methods (section 6.1.1) consider the geometric properties of the strand. The approach in this thesis is to use one type of strand varying the separation of the turns, S_T of the measurement barrel geometry. If it is possible to parametrise the self-field correction as a function of the experimental helical geometry, the J_C measured in any helical geometry can, in theory, be corrected for.

A self-field correction for another widely used helical geometry the Walters spring (WS), shown in Figure 6.3, has been defined [10]. The WS can be used to measure strands with both compressive and tensile axial strains. The WS has a smaller diameter (25 mm) and a larger separation of turns (6.35 mm) than the ITER barrel [41]. An equivalent equation for the WS self-field correction is reported, with the

α term in Eq. (5.25) comparable: α(ITER) = - 9.0 × 10^{-5}, α(WS) = - 10.0 × 10^{-5}. The analysis demonstrated that the geometric differences averaged out [10].

Experimental measurements of Nb$_3$Sn strands on custom barrels, with 25 mm outer diameter and a separation of turns of 3 and 5 mm, and 35 mm outer diameter with a separation of turns of 3 mm have been reported [42]. The transport measurements from B_{App}= 8.0 to 12.0 T result in I_C values between 114 and 332 A. For currents in this range, the effect of B_{SF} is expected to be small relative to the large B_{App}. The larger diameter should reduce the effect of self-field and result in a higher measured I_C. However, the experimental results for the 35 mm diameter measurement barrel were a 1.5 % lower I_C than the 25 mm barrel. For the measurement barrel with a greater separation of turns, the effect of self-field should be smaller. Experimentally this was seen with the 5 mm separation of turns measurement barrel resulted in a 1 % higher I_C than the 3 mm geometry. The author concluded that the effect of dimension and pitches was not appreciable. This conclusion was specific to the Nb$_3$Sn measurement, which will be discussed in section 6.2.1.

6.1.4. Comparing Measurements Techniques

Agreement between the transport and magnetisation measurements of J_C is seen in some data in the literature [43-46]. There are also papers which discuss the large differences (7-10 %) [47] between magnetisation and transport measurements of J_C, particularly at low B_{App}[15, 48, 49]. In [47] the author argues that there are "no valid transport measurements" for B_{App}< 1 T. Low B_{App} magnetisation data can have errors as the analysis neglects coupling effects due to filament proximity and contact, undermining the reliability of extracting $J_C(B)$. At low B_{App}, proximity coupling increases the magnetic moment by *tens* of percent [15, 50]. In [51] the magnetisation data does not agree with transport data, underestimating J_C. Elsewhere the results for measured J_C are described as "technique dependent" [52]. Research quantifying the universal self-field J_C[53] used only transport data for the analysis. It is important for the analysis of self-field to understand the limitations of each of the methods.

The J_C measured using the magnetisation method is an average value in the strand rather than the weakest point [47, 48], and the analysis of the measurements assumes that J_C is constant across the volume of the strands. At high B_{App}, when the effect of self-field is small, B_{App} is expected to be "roughly uniform" [15].

6.2.   Critical Current Density

6.2.1. Strain Dependence

Nb-Ti strands were used to investigate the effect of self-field because it limited any variability due to strain. The changes in J_C are only a few percent at tensile strains of $\sim$ 3% [54]. The strain dependence of Nb-Ti [$J_C(\epsilon)$] is an order of magnitude smaller than the commercial A-15 materials: Nb_3Sn and V_3Ga [55]. The highest J_C measured is when the Nb-Ti strand is in the strain-free state [13]. The tensile strain (ϵ) on the strand wound on the measurement barrel geometry is given by [39]:

$$\epsilon = \frac{R_{\text{Maj}} + d_s}{R_{\text{Maj}} + 0.5d_s} - 1.$$

(6.5)

For the ITER strand's diameter (d_s) and the measurement barrel's major radius (R_{Maj}) the strain is 2.3 %. For the smaller radius WS, the strain is of 2.9 %. Transport measurements of the Nb-Ti on the WS resulted in a reduction of I_C about 5 % at B_{App} = 7 T [39]. The differences in the measurement geometries cause the strand to be in different strain states which could explain the variance in the interlaboratory comparisons of Nb-Ti strands [39]. The differences in the I_C measurements of Nb_3Sn strands [42] in different geometries could be explained by the strain state of the strand.

For an elastic model, there is a compressive strain of equal magnitude on the inside of the strand. Interpolating the $J_C(\epsilon)$ data from [54], a strain of 2.3 % results in the J_C decreasing by $\approx$ 17 % at B_{App}= 5 T. Extrapolating the $J_C(\epsilon)$data from [54] to B_{App}= 0.5 T the 2.3 % strain results in the J_C decreasing by $\approx$ 9 %. The J_C values at 0.0 and 2.3 % strain are fitted at the low field assuming a linear $J_C(B)$ relationship. Although the decrease in J_C with strain on both the ITER and the MST barrels is not small, as R_{Maj} is fixed the strands are in the same state. The strands characterised had diameters between 0.732 to 0.736 mm, details in Table A.1, the resultant differences in ϵ is a maximum of 0.01 %. The strand could be in a different strain state due to winding on to the barrel. Analysis of preparation techniques in the literature quantified the effect to be small < 1 A [38]. With a fixed winding method (section 3.3.2) differences were minimised.

The strain-dependent upper critical field $B_{C2}^*$is described [55],

$$B_{C2}^*(\epsilon) = B_{C2M}^*(\epsilon)(1 - a|\epsilon|^u)$$

(6.6)

where $B_{C2M}^*(\epsilon)$ is the maximum value of the upper critical field. The Nb-Ti fitting parameters for Eq. (6.9) from [55] are: a(ϵ < 0) = 23, and u = 1.7. The average change in $B_{C2}^*(\epsilon)$ (4.22 K) has been calculated as 488 mT (4.6 %) for the strand wound on an ITER barrel using strain dependent parameters [54].

In other work looking at the effect of self-field when characterising Nb-Ti strands, mechanical stresses are not considered to affect the results [31]. It should be noted that strain can decrease the strand's stability; as the strand is bent during manufacture the *RRR* of the strand is reduced by 10 % [56]. The strain state is not considered further in this work.

6.2.2. Angular Dependence

The orientation of current flow relative to B_{App} affects the J_C value measured. The angular dependence of J_C in multifilamentary Nb-Ti wires is small due to the competing effects of the pinning and the Lorentz force averaging out [57, 58]. Generally, the maximum pinning force for Nb-Ti is strongly dependent on the angle between the transport current and B_{App} [59]. In transport measurements, the strand is approximately perpendicular to the applied magnetic field [60, 61]. The angle between the strand and the field direction is 88.46° for the ITER barrel and 88.44° for the MST barrel. The angular dependence of J_C was not considered in the self-field analysis as the angle, relative to the B_{App} at 90°, in both measurement geometries is small.

6.2.3. Temperature Dependence

The atmospheric pressures during the experimental campaign were noted from a local weather station [62] and ranged from 99.1 to 102.8 kPa. To account for changes in the temperature of the helium bath, the temperature-pressure relationship was calculated using the data shown in Figure 6.4 (a), digitised from [63]. A cubic-fit was used to calculate the helium temperature, the values for the cubic function fitted are reported in Table 6.3. The calculated temperature of the helium on the days experiment was carried out are shown in Figure 6.4 (b).

The critical current measured at the bath temperature (I_m) is corrected to the 4.22 K critical current (I_C) value, with the relationship

$$\frac{I_C}{I_m} = \frac{T_C(B) - 4.22}{T_C(B) - T_m},$$
(6.7)

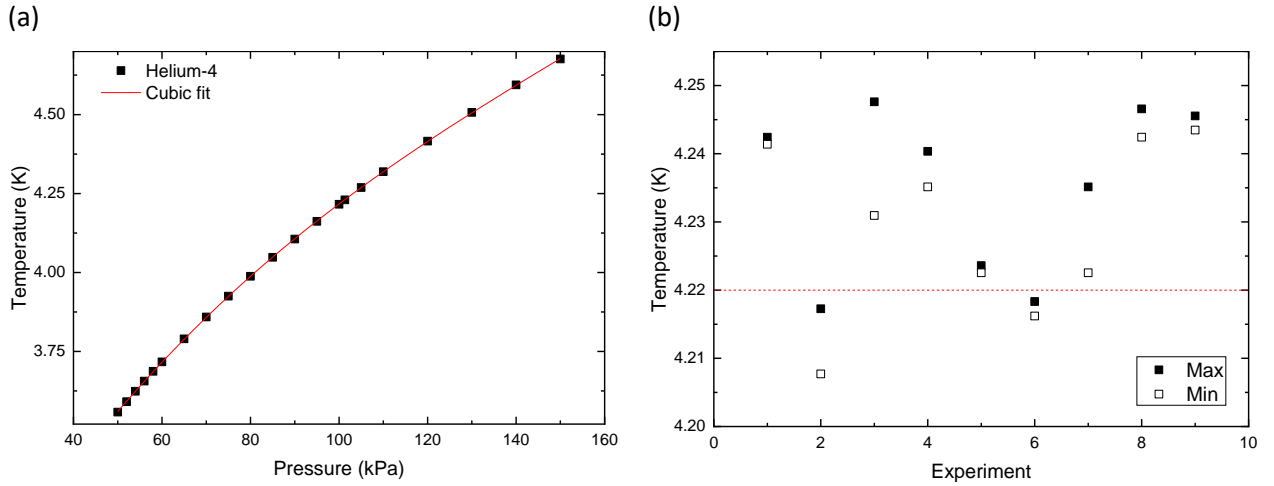where $T_C(B)$ is the field dependence of the critical temperature [40].

(a)

(b)

Figure 6.4 : Temperature correction term for Liquid Helium-4 (a) Reduced temperature vs pressure digitised data from Ref. [63]. (b) The maximum and minimum helium temperatures calculated using atmospheric data and cubic fit for days the experiment was run.

Parameter	Value	Error
A $[x^0]$	2.53	0.01
B $[x^1]$	25.6×10^{-3}	0.3×10^{-3}
C $[x^2]$	-1.11×10^{-4}	0.04×10^{-4}
D $[x^4]$	2.4×10^{-7}	0.1×10^{-7}

Table 6.3 : Helium Temperature-Pressure fit parameters.

For Nb-Ti, $T_C(B)$ is described by the relationship[64],

$$T_C(B) = T_C \times \left(1 - \frac{B}{B_{C2}}\right)^{0.59},$$

(6.8)

where the numerical values are the B_{C2} =14.5 T and T_C = 9.2 K. The helium bath's minimum temperature was calculated as 4.208 K, an average of 4.232 K, and a maximum of 4.248 K. Using the temperature of the helium bath (T_m) the I_C was corrected from the bath temperature to 4.22 K. The largest correction to I_m is at high B_{App} and is of order 2%. The maximum difference between I_m and I_C is 10 A.

At high B_{App} the I_C values are small (< 40 A), and the field sensitivity of J_C measurements is lower [15], so the data is of limited use for verification of the self-field correction. At low B_{App}, the correction defined by Eq. (6.7) is equivalent to 0.8 % I_C. The variation in pressure and temperature correction did not make a significant difference, less than 4 A, to the measured transport I_C data. As the same strands

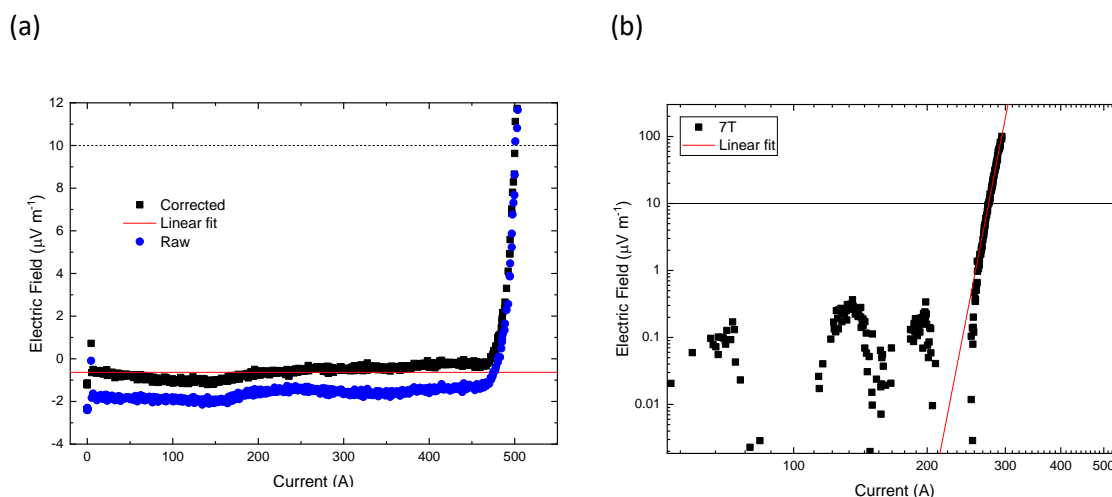(a)   (b)

Figure 6.5 : (a) Comparison of the raw and self-field corrected data. (b) log-log data with n-index fitting shown.

are measured on multiple days and removed from the magnet system, the strands are thermally cycled. The effect of temperature cycling on Nb-Ti is less than 0.3 % [65].

6.2.4. Baseline correction and fitting

The transport measurement data is baseline correct. The raw data is shifted vertically, by subtracting a linear fit between 0 and $\sim 90 \%$ I_C with the gradient fixed as 0. The raw data, linear fit, and baseline corrected data is shown in Figure 6.5 (a). It is clear that the baseline is not sloped curved or multisegmented, which would indicate current transfer [66].

To extract n-value, the E-I data was plotted on a log-log scale, and using the data from 10 μV·m⁻¹ to the 100 μV·m⁻¹ a straight line was fitted with error, shown in Figure 6.5 (b).

6.2.5. Measurement Error

In order to investigate the effect of self-field each aspect of the experiment has been analysed, in order for the measurement error to be minimised. The first test of the accuracy of the Nb-Ti strand measurements was the comparison with the benchmarking measurements shown in section 3.5.1. The remeasurement of the same strand with a different experimental set-up and analysis process gave values which differed by 1 A.

The transport E-J data shown in Figure 6.6 is a comparison of the same Nb-Ti strand remeasured and the differences. The data shown in Figure 6.6 (a) is the MST measurement geometry at the benchmarking range of B_{App} . Measurement 1 was using probe 1 in 2016/05. Using this probe, the

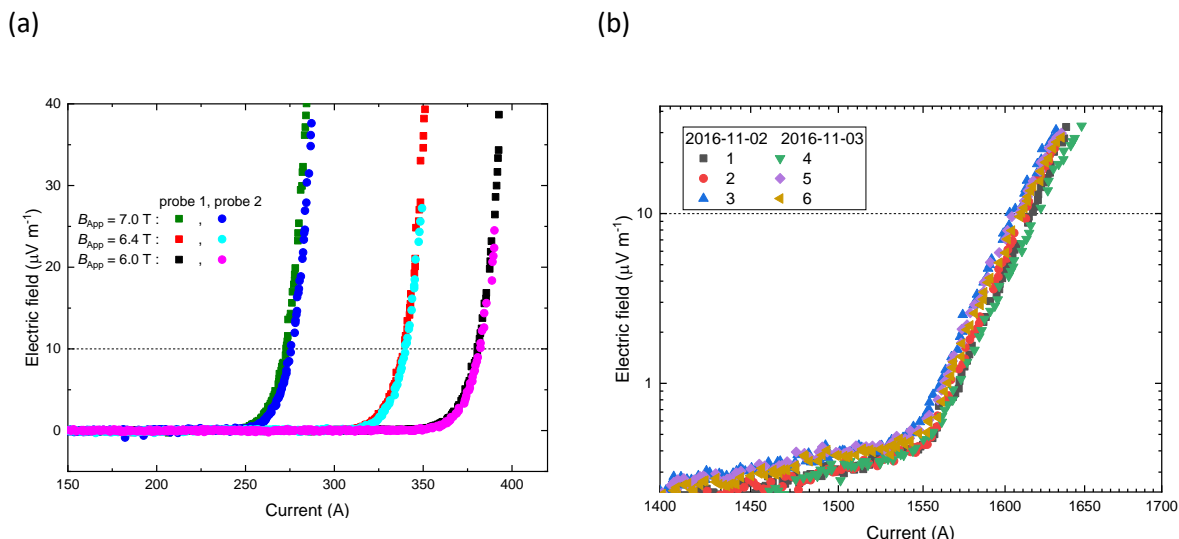(a)   (b)

Figure 6.6 : Comparison of strand DR 4810 data (a) different probes, different months measured in the MST geometry (b) Measurements on the strand DR 4810 on the same probe, following inward and outward F_L measurements in the ITER geometry.

Date	Measurement	I_C [10 µV·m^{-1}] [A]
2016-11-02	1	1616 ± 1
	2	1612 ± 1
	3	1605 ± 1
2016-11-03	4	1620 ± 1
	5	1609 ± 1
	6	1610 ± 1

Table 6.4 : Comparison of I_C measured at B_{App} = 0 T in the ITER geometry on different days and following different F_L measurements.

sample quenched when measuring at lower B_{App}. Using the new probe, it was possible to measure the strand completely, in 2016/11. Measurements using the first probe (square symbols) gave slightly higher I_C than the second probe (circular symbols). The results highlight both that the measurement error is small, relative to the effect being investigated, and the improved design increases the E-field measured.

One check of the effect of Lorentz force was repeated measurements at B_{App} = 0 T, shown in Figure 6.6 (b). The measurement is of strand DR 4810 wound on the ITER measurement barrel. Measurements followed the applied magnetic field being reserved, and the current orientation reversed. The differences in I_C are outlined in Table 6.4, with an average of 1612 A, and standard

deviation of 5 A. The differences in the value are less than 0.3 % of the I_C value. There was no clear trend from the data, with respect to the data or the direction of the F_L in the previous measurements.

6.3.   Transport Measurements

6.3.1. Variable Temperature Data

Variable temperature transport measurements are used to determine the temperature margin of the strand when used in magnet applications [67]. The temperature margin is defined as the difference between the operating temperature and the temperature at which I_C is equal to the operating current. Transport measurements over the range of temperatures 3.5 to 6.0 K were performed in B_{App} = 4.0 to 8.0 T. The strand DR 5049 was characterised in the ITER measurement geometry. The design of the probe and experimental set-up were developed by Dr Mark J Raine. The measurement data in the inward F_L data was supplied by Dr Mark J Raine, the outward I_C measurements data is new and was completed for this research by F Ridgeon. The data in this section with details of the probe and experimental set-up were published [68].

The data for both orientations of F_L were analysed by F Ridgeon, and the strand was remeasured in the outward F_L at the same B_{App} and T. Log-log E-J traces comparing the two F_L orientations measurements at T = 3.5 K, are shown in Figure 6.7. For inward F_L closed symbols are used, and open symbols for outward F_L. For the data shown in Figure 6.7, the differences in J_C with opposite F_L orientation is < 1 % at E_C. It was clear from the extensive measurements that the data is high quality. Each measurement, for a fixed field and temperature, resulted in a lower J_C for the outward F_L measurements. Although differences in measured J_C are seen, the stability of the strand at the range of B_{App} and T measured at reduces the variability.

Within the measured range of B_{App} and T, the magnitude of the transport currents results in B_{SF} being small relative to B_{App}. The $I_C(B_{App}, T)$ data for the strand in the two orientations of F_L is summarised in Figure 6.8. The data was parameterised using the single pinning-mechanism, Bottura phenomenological relationship [69]:

$$I_C = \frac{C_0}{B} b^\alpha (1 - b)^\beta (1 - t^\nu)^\gamma \qquad (6.9)$$

where $\alpha, \beta, \gamma, \nu$ and C_0 are scaling parameters, normalised critical temperature ($t = T/T_C$), and reduced field b.
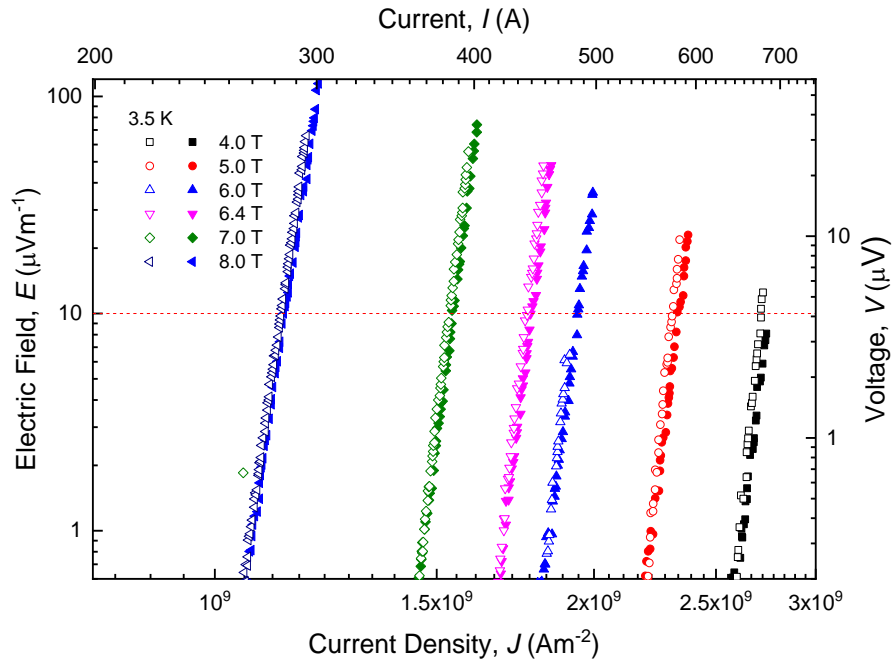
Figure 6.7 : E-J traces for DR 5049 at 3.5 K. Open symbols - outward Lorentz force, closed symbols - inward Lorentz force. Inward data provided by Dr Mark J Raine.
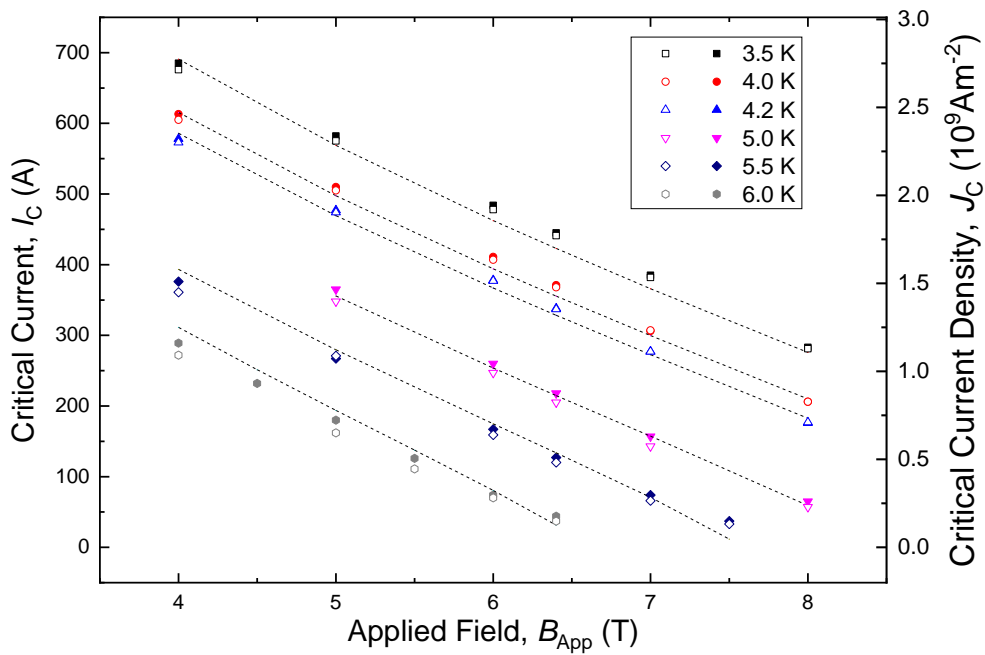
Figure 6.8 : Critical current data for DR 5049. Open symbols -outward Lorentz force, closed symbols - inward Lorentz force. The dashed lines are the Bottura fit Eq. (6.9) to both data sets. Inward data provided by Dr Mark J Raine.

C_0 [A·T^{-1}]	$B_{c2}(0)$ [T]	T_{C0} [K]	α	β	γ	ν
14054	14.33	9.05	0.75	0.84	1.83	1.53

Table 6.5 : Fitting parameter of Nb-Ti strand for both Lorentz force polarities at varied temperature.

The temperature-dependent upper critical field is used. Eq. (6.9) was fitted using the standard method, outlined in [18]. The value of ν, and the parameters of Eq. (6.9) are listed in Table 6.5. The fitting parameters values in Table 6.5 are within the typical range in the literature. The standard deviation (σ = 2.0 %) for the measurement in two orientations of F_{L}, is typical for fitting the data set in one F_{L} orientation. Any effect due to the orientation of F_{L} on the distribution of self-field is too small to be resolved. In section

The variable temperature data is at high B_{App}, and it is of limited use for the analysis of the self-field. However, the data demonstrates that it is possible to measure the strand over a range of temperatures, fields, and orientations of Lorentz force.

6.3.2. 4.22 K Data

Transport measurements of strands DR 4810 and DR 5534 at 4.22 K in B_{App} from 10.5 to 0.0 T were performed to characterise J_{C} and the effect of self-field. The measurements at high B_{App} (>5.5 T) are at the standard values of magnetic field used in benchmarking and verification of the strand. A higher density of measurements was taken at low field (< 2.0 T), as the FEA calculations suggested a peak in the measured J_{C} and large differences in J_{C} were being observed experimentally. The measurements in the inward F_{L} at low fields (<1 T), the outward F_{L} for the ITER geometry and all J_{C} measurements in the MST geometry provide new information.

The strand DR 4810 was measured in ITER geometry in a reversed applied magnetic field ($B_{\mathrm{App}} = -B_{\mathrm{z}}$). Due to possible damage of the magnet, further transport measurements were not repeated at $B_{\mathrm{App}} = -B_{\mathrm{z}}$. A selection of the E-I traces for the strand DR 4810 at 4.22 K are shown in Figure 6.9. The raw data has been corrected, the baseline has been shifted vertically by the average of the electric field, between 0 and $\approx$ 90 % of J_{C}.

The effect of magnetic field hysteresis on J_{C} at any B_{App} was investigated. Measurements were repeated at B_{App} = 0 T following B_{App} > 0.4 T, and B_{App} < 0.4 T. The resultant differences were small, σ = 5.1 A, 0.3 %. Following changes to the experimental set-up (refilling the helium in the magnet, adjustment to the probe assembly) measurements were repeated at several B_{App} values. Differences were typically less than 1 A, e.g., repeated I_{C} measurements at B_{App} = 1.4 T, inward F_{L} ITER geometry results in an I_{C} of 1039.4 ± 0.9 A.
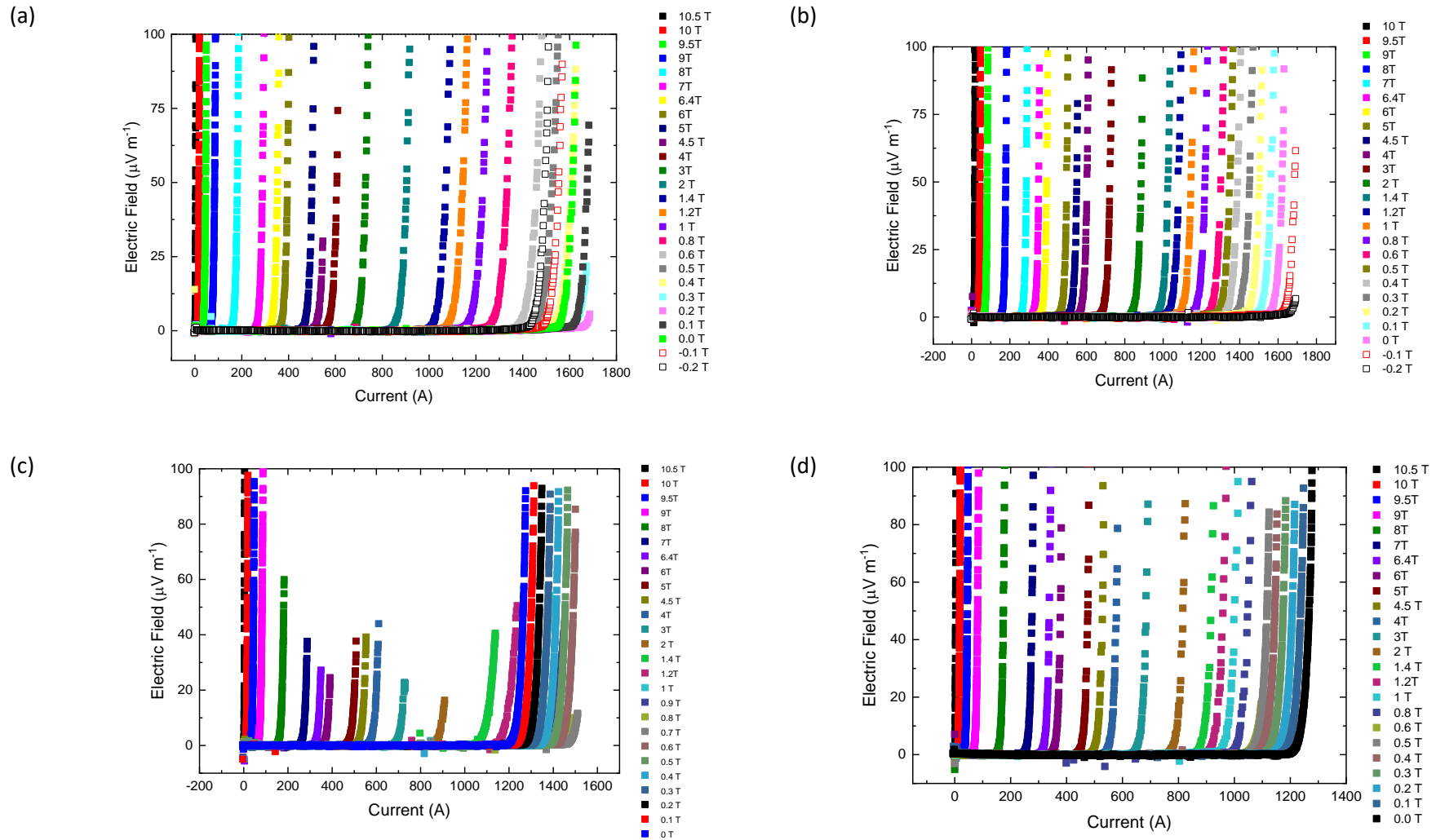
Figure 6.9 : Experimental E-I traces of the Nb-Ti strand DR 4810 measured in the (a) Inward Lorentz force orientation ITER geometry (b) Outward Lorentz force orientation ITER geometry (c) Inward Lorentz force orientation MST geometry (d) Outward Lorentz force orientation MST geometry. Open symbols B_{App}< 0 T.
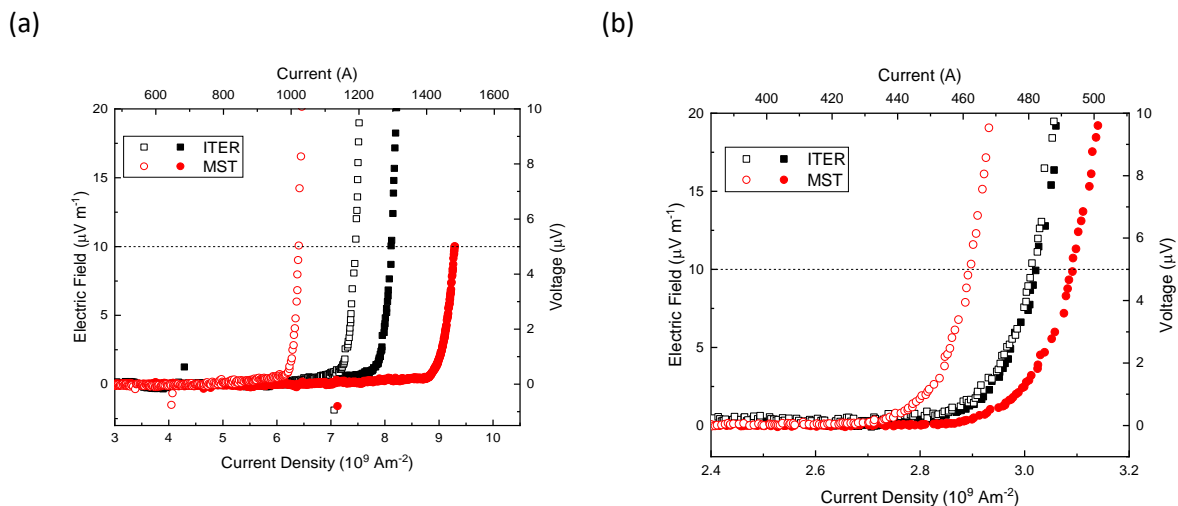
(a) (b)

Figure 6.10 : E-J data for strand DR4810 in the four measurement geometries at two values of the applied field (a) B_{App}= 0.8 T (b) B_{App}= 5.0T.

Geometry	F_{L} orientation	J_{C} (0.8 T) [10^9 Am^{-2}]	Δ (0.8 T) = $J_{\mathrm{C}} - \bar{J}_{\mathrm{C}}$(%)	J_{C} (5.0 T) [10^9 Am^{-2}]	Δ (5.0 T) = $J_{\mathrm{C}} - \bar{J}_{\mathrm{C}}$(%)
ITER	Inward	8.15	+ 3.8	3.02	+ 0.3
	Outward	7.47	- 4.8	3.01	+ 0.0
MST	Inward	9.29	+ 18.3	3.09	+ 2.7
	Outward	6.49	- 17.3	2.90	- 3.7

Table 6.6 : Critical current density at B_{App}= 0.8 T and 5.0 T. Percentage difference from the average J_{C}, J_{C} (B_{App}= 0.8 T) = 7.85 × 10^9A·m^{-2} and J_{C} (B_{App}= 5.0 T) = 3.01 × 10^9 A·m^{-2}

The measurement of DR 4810 in the ITER geometry inward F_{L} is shown in Figure 6.9 (a). For the high-currents, low B_{App}, E-fields of >5 µV·m^{-1} were measured. As E-fields of 100 µV·m^{-1} were not measured the uncertainty in the analysis of the index of transition is large. The measurement of DR 4810 in the ITER geometry outward F_{L} is shown in Figure 6.9 (b). For $B_{\mathrm{App}} < 0$ T, E-fields < 100 µV·m^{-1} were measured. For the MST geometry in the inward F_{L} orientation [Figure 6.9 (c)], in the intermediate B_{App} range (8.0 to 2.0 T) low E-fields (<10 µVm^{-1}) were measured. The outward F_{L} MST geometry [Figure 6.9 (d)] followed the inward measurements, and E-fields of 100 µV·m^{-1} were measured.

The E-J traces at a fixed B_{App} with the four configurations (helical geometry, and Lorentz force orientation) is shown in Figure 6.10, for the strand DR 4810. At B_{App}= 0.8 T, shown in Figure 6.10 (a), changing the orientation of F_{L} results in a difference in J_{C} of 8.7 % in the ITER geometry and by 35.7 % in the MST geometry. At B_{App}= 5.0 T, shown in Figure 6.10 (b), the measured J_{C} is comparable in the two orientations of F_{L} in the ITER geometry, i.e., differences of 0.3 % similar to measurement error,

(a)
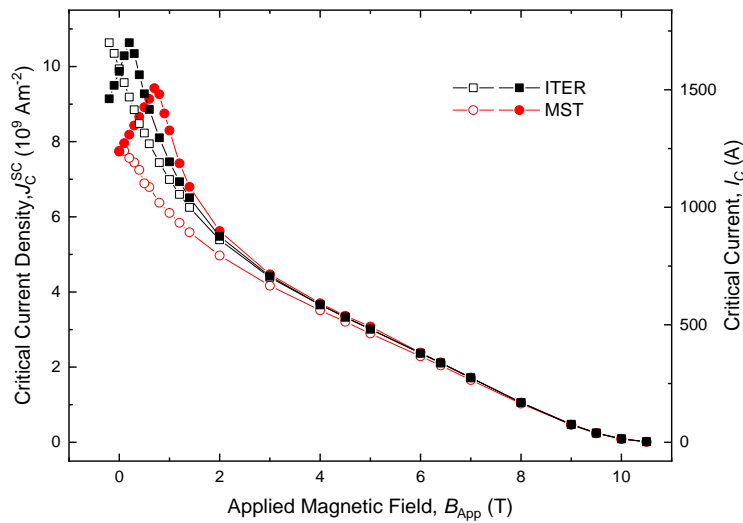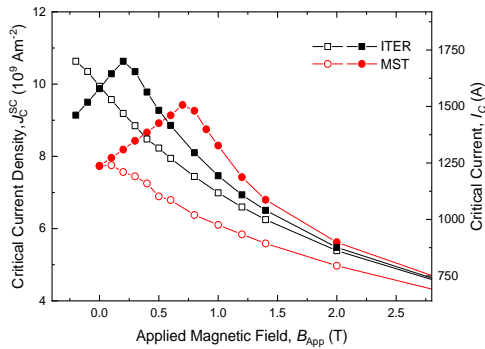
(b)   (c)
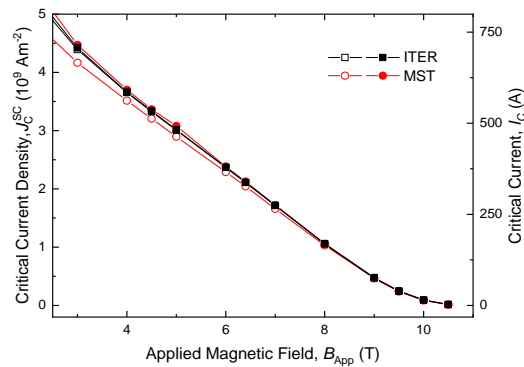
Figure 6.11 : Critical current density as a function of the *applied* magnetic field for strand DR 4810. (a) Complete data range (b) Low applied, high self-field data (c) High applied-field, low self-field effect data. Lines between data points are a guide for the eye.

whereas the difference in the MST geometry is larger at 6.3 %. The J_C value and the percentage difference from the average are reported in Table 6.6. An average of the four data sets was used to calculate J_C.

The J_C vs B_{App} of strand DR 4810 is shown in Figure 6.11. The data for the whole range of B_{App} is shown in Figure 6.11 (a). The largest changes in the measured J_C, due to the effect of self-field occurred at the low field range (>2.0 T). The low *applied*-field, high *self*-field data are replotted in Figure 6.11 (b), and the low *self*-field and high *applied*-field data in Figure 6.11 (c). From these J_C vs B_{App} data, the effect of the different density of turns on the measurement barrel can be seen.

Strand ID	Geometry	Inward F_L	Outward F_L
DR 4810	ITER	■	☐
	MST	●	○
DR 5534	ITER	◆	◇
	MST	⬡	⬡

Table 6.7 : Summary of notation used for measured properties of strands DR 4810 and DR 5534 in different geometries and Lorentz force orientations for analysis figures. Not used in E-J data shown in Figure 6.9

The outward Lorentz force orientation results in an increased B_{Net} which reduces the measured J_C. The inward Lorentz force orientation results in a reduced B_{Net}, this increases the measured J_C. The ITER measurement geometry results in a smaller B_{SF} , as the peak in the measured J_C in the inward F_L is lower than the MST geometry. For B_{App} below the peak in measured J_C, a constant gradient (ITER: 0.607 T·kA^{-1}, MST: 0.328 T·kA^{-1}) was measured for the inward F_L measurements.

Transport measurements of composite Nb-Ti strands, at low B_{App}, can be limited by self-field instabilities [70]. The J_C at B_{App}= - 0.2 T for ITER outward F_L was found by extrapolating the E-J data to E_C. Similarly, the data at B_{App}= 0.2 T for ITER inward F_L was found by extrapolation of E-J data to E_C. The uncertainty in J_C due to this extrapolation is 0.7 %. For the high B_{App} data, shown in Figure 6.11 (c) the J_C (B) is nearly linear. The change in the gradient at B_{App}> 9 T, in all four measurements, is an artefact of the E-field criterion used [66].

The E-I measurements about the peak in the measured J_C in the inward F_L, for the ITER and MST geometry, are shown in Figure 6.12. The peak occurs around B_{App}= 0.2 T for the ITER geometry and B_{App}= 0.7 T for MST geometry. For both data sets, the peak B_{App}± 0.1 T, have similar behaviour and I_C. Measurements of I_C about the peak were not always possible due to the instability of the strand, and the volume of helium and time required. It is expected there is an equivalent peak in I_C at B_{App}- 0.2 T for the ITER geometry and in the outward F_L, but measurements were not performed at B_{App}< -0.2 T to verify.

(a)   (b)
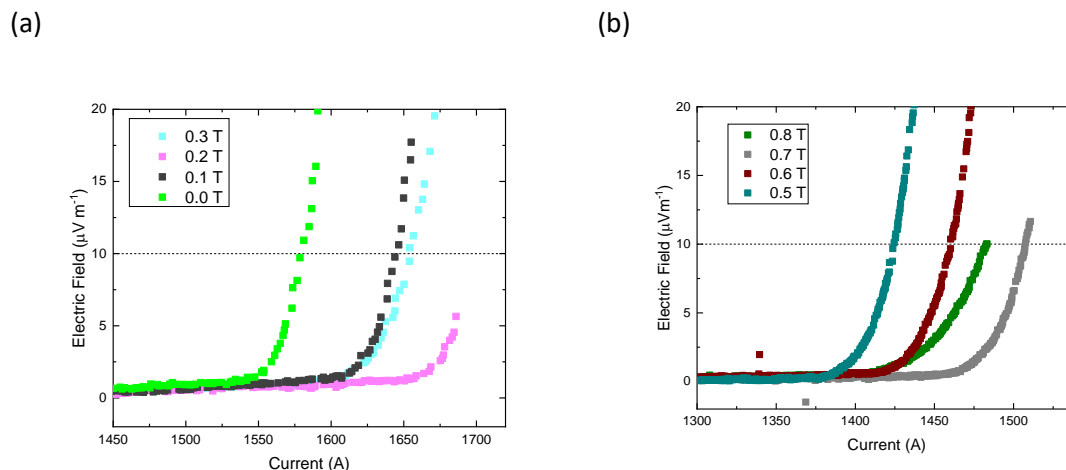
Figure 6.12 : E-I measurement data for strand DR 4810 about the peak in the I_C in the inward Lorentz force orientation (a) ITER geometry (b) MST geometry.

The difference in I_C with the orientation of Lorentz force (normalised by the inward F_L measurement) $\Delta I_C/I_C$ is shown in Figure 6.13 (a) at high B_{App}, where $(F_{L(in)} - F_{L(out)})$ determines the sign of ΔI_C. The percentage difference in I_C for the ITER geometry is small (<0.35 %, <1.0 A) at the benchmarking range of B_{App} (the shaded region) shown in Figure 6.13 (a). For the MST data shown in Figure 6.13 (a), the difference in I_C is larger, 6% (22 A). The experimentally measured difference in I_C with F_L orientation can be understood by considering the distribution of current in the stand, and the resultant distributions of the magnetic field with F_L orientation. One of the results of the FEA calculations was the position of the maximum magnetic field changes with the F_L orientation. Plotting the difference in the I_C for the complete data set of B_{App} shown in Figure 6.13(b), a maximum difference of 460 A (MST geometry), and 240 A (ITER geometry) is measured. The largest differences occur when comparing measurements where the self-field is acting in the opposite directions and the B_{App} is small.

The I_C for the four measurement geometries has been normalised by the ITER inwards F_L data, shown in Figure 6.13 (c). For the benchmarking range of B_{App}, the differences in I_C due to F_L is small. The differences in I_C due to the two geometries is clear. The difference due to the MST geometry in the outwards F_L orientation is still smaller than 2 %.

The normalised Lorentz Force ($\equiv J_C B$) for the four measurements are compared in Figure 6.13 (d), and the peak in F_L varies from B_{App}= 4.3 to 4.7 T. The analysis in Ekin 2016 paper which defines a master scaling curve replots the reduced pinning force vs reduced field, the shape is invariant and "thus can be registered into a single master unified-scaling curve" [71]. Typical data is for $b > 0.3$
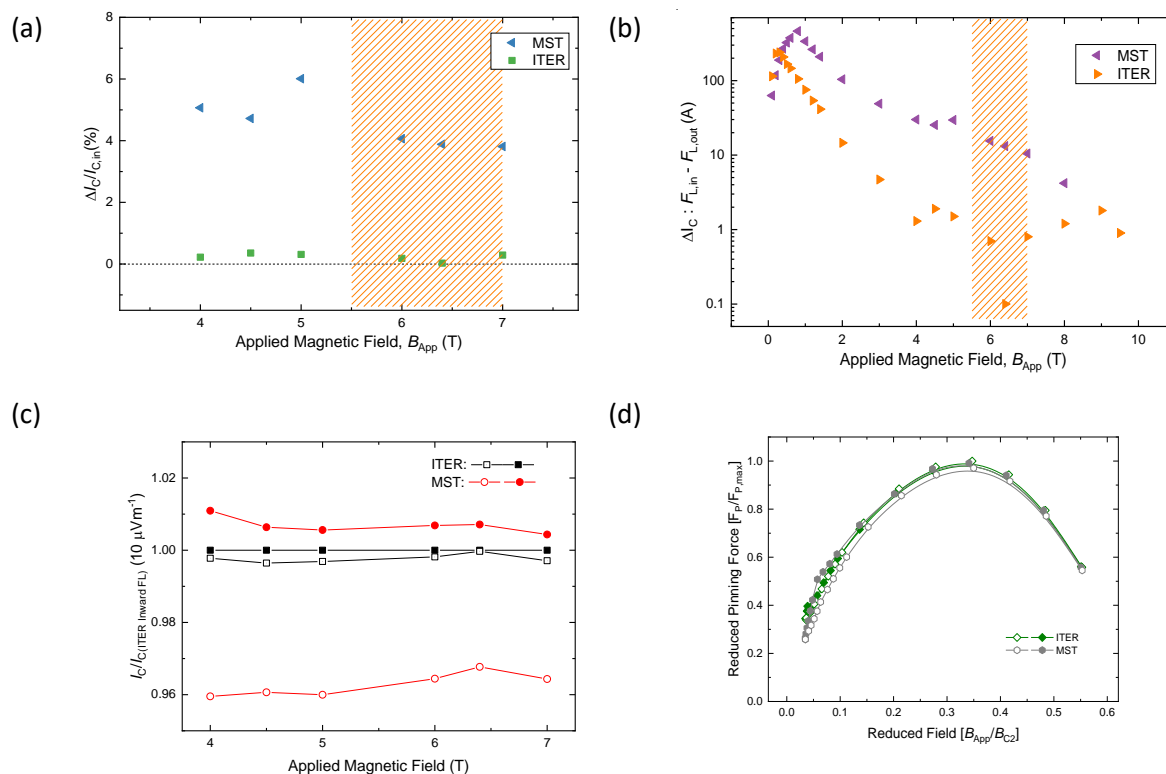
Figure 6.13 : DR 4810 (a) Percentage differences in critical current, with Lorentz force orientation for both geometries as a function of the applied field. (b) (log-lin) differences in critical current with Lorentz force orientation as a function of applied field for both geometries. Highlighted region – benchmarking and verification range of B_{App}. (c) Normalised I_C (inward ITER geometry) (d) average of outward and inward F_L I_C. (d) Reduced pinning force vs reduced field (b).

The index of transition (n) is compared for the measurement geometries and different F_L directions. The results are reported in Figure 6.14. For the n versus B_{App} data, shown in Figure 6.14 (a), for B_{App}> 2.0 T the n-value decreases - a typical inverted parabola shape. For B_{App}< 2.0 T, there is a sharp increase in the n-value. At all values of B_{App}, the inward F_L measurements have lower n-values than the corresponding outward measurements. The analysis of n has large error bars at low B_{App}, because heating due to the high currents occurs. The increase in n at B_{App}< 2.0 T could be due to the instability of the strand when measured under those conditions. It is difficult to measure n-value at low B_{App} of Nb-Ti strands, due to the low E-fields measured before samples quenching, and the value can be very large [42].

There is a power-law relation between the n-value and the critical current density shown in Figure 6.14 (b). The data in Figure 6.14 (b) are fitted with Eq. (2.18) with fitting parameters r = - 2.72 and s = 0.46 and are within the typical range of values [72].

(a)   (b)
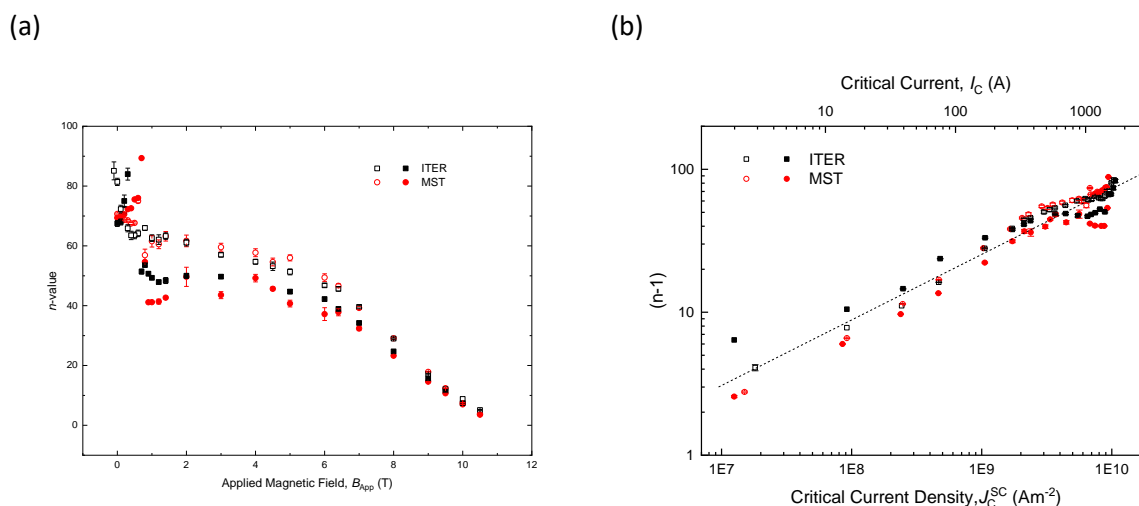
Figure 6.14 : Index of transition for the four transport measurements of strand DR 4810 (a) n versus B_{App} (b) (n-1) versus the critical current density.

Transport measurements of strand DR 5534 were repeated at the same B_{App} where possible in the same geometries using both F_{L} orientations, using the same probe as strand DR 4810, on separate measurement barrels. Similar E-J traces were measured, and the same analysis performed. The I_{C}-B_{App} of the two strands are compared in Figure 6.15. There are some broadly similar features: a sharp increase in I_{C} at B_{App}< 2.0 T, higher I_{C} in the inward F_{L} orientation, and a linear increase in I_{C} at low B_{App}. Due to the instability of strand DR 5534 at high currents, the peaks in I_{C} were not measured in either measurement geometry. Strand DR 5534 could not be kept sufficiently stable to measure a transition and E-field without quenching. In the ITER geometry, it was not possible to measure the I_{C} above 1190 A and in the MST geometry, it was not possible to measure I_{C} above 1370 A.

The high self-field region is compared for strands DR 4810 and DR 5534 in the ITER geometry shown in Figure 6.15 (b) and MST Figure 6.15 (c). The gradient in the linear region $J_{\text{C}}(B)$ at B_{App}< 0.4 T is slightly higher for DR 5534 than DR 4810, (with MST: 0.351 T·kA^{-1}). The physical properties of the strand (section 3.2) may explain why the measured I_{C} was lower. Although both strands are nominally the same, strand DR 5534 has both a lower CnC ratio and RRR. The relationship between self-field instabilities and RRR is well documented [12, 73, 74].

The transport measurements at 4.22 K, of the three strands considered in this chapter are compared in Figure 6.16. The effect of variance in the strand I_{C} (i.e., I_{C}at B_{App}= 7 T varies by 6 A, 2.2 %), was not considered in the calculation of the self-field correction. As the J_{C}measurements of strand DR 4810 are the most complete, the experimental data for strand DR 4810 is used as the input for the FEA and semi-analytic analysis.

(a)
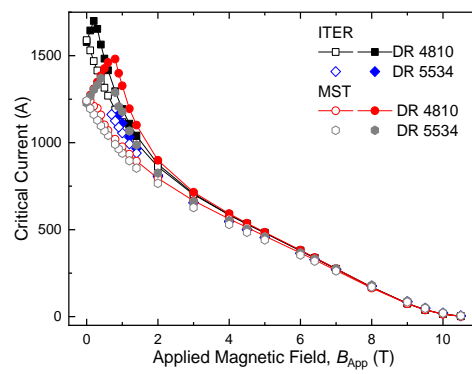
(b)
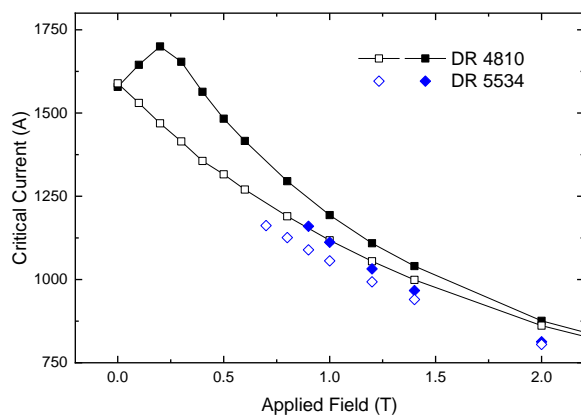
(c)
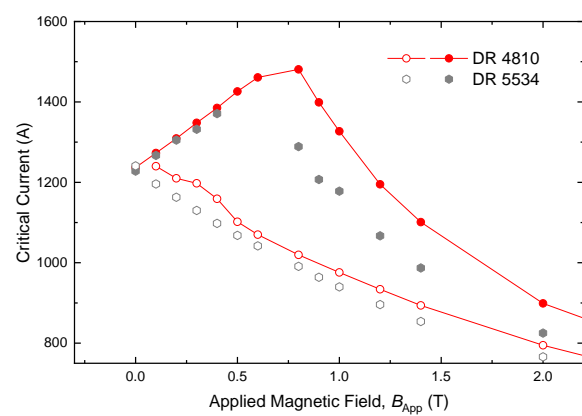
Figure 6.15 : Comparison of the J_C of strands DR 4810 and DR 5534. (a) Full magnetic field range (b) limited field range in the ITER geometry (c) limited field range in the MST geometry. Lines between DR 4810 data points are a guide for the eye.
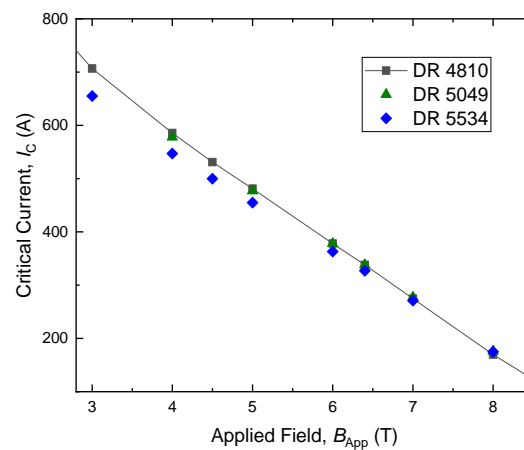
Figure 6.16 : Compilation of the inward F_L ITER geometry measured I_C at 4.22 K. Line between DR 4810 data points are a guide for the eye. I_C (B_{App}= 7.0T) = 274.8 [DR 4810], 277.0 [DR 5049], 271.0 A [DR 5534].

6.4.   Magnetisation Measurements

The self-field can be expected to be much less in magnetic measurements than transport measurement due to the magnitude of the current flowing in the strand. The magnetisation J_C (B_{App}, T) of the strands provides additional data about the strands behaviour, to aid in understanding the universal J_C (B).

To measure J_C magnetically, a Quantum Design PPMS system [75] is used in DC-extraction mode. The DC B_{App} is swept at a rate of 4 mT.s^{-1} (0.240 T min^{-1}). 170 mm of strand is cut, cleaned using isopropanol, and wound tightly around a stainless-steel rod, as shown in Figure 6.17. The characteristics of the coiled strand are outlined in Table 6.8. The coiled strand is orientated parallel to the applied magnetic field (+B_Z). Dr Mark J Raine produced the magnetic moment data.

Raw magnetic moment data (not normalised by volume) for the three strands are shown in Figure 6.18. The area under the curve is used to calculate the AC losses. The strands DR 5534 and DR 5049 have very similar behaviour. Strand DR 4810 has both the highest AC losses and measured J_C. The losses of the three strands are within the ITER requirements (<55 mJ·cc_st^{-1}), Table 6.9. The skewed or asymmetric nature of the data are due to the nickel plating.

Characteristic [Unit]	Value
Length [mm]	130
Major radius [mm]	2.365
Height [mm]	6.75
Pitch [mm]	0.732
Number of turns	8.7

Table 6.8 : Characteristics of magnetisation helical
measurement geometry.

Strand Identity	Losses Q_{hys} [mJ·cc_st^{-1}]
DR 4810	47 ± 0.1
DR 5049	44 ± 0.1
DR 5534	44 ± 0.1

Table 6.9 : Hysteresis losses. cc_st: cubic centimetre of strand.

Figure 6.17 : Photograph of an Nb-Ti strand wound for magnetisation measurement. Taken from [76].
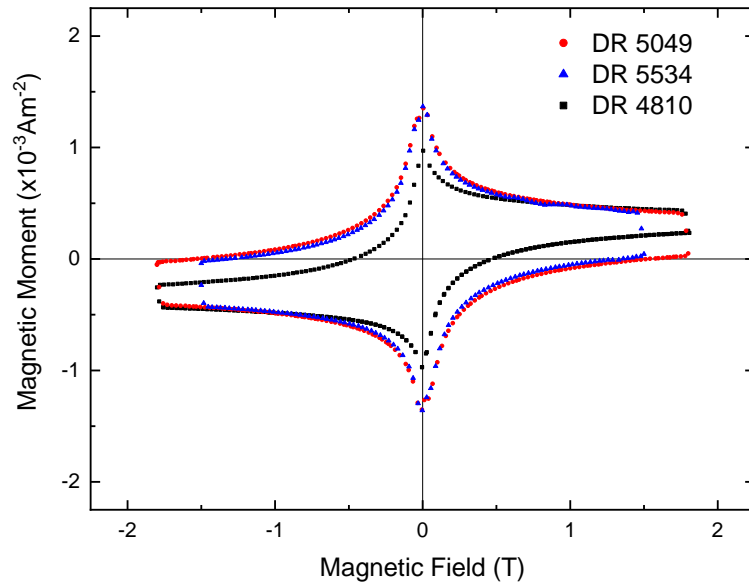
Figure 6.18 : Magnetic moment versus applied magnetic field for strands DR 4810, DR 5049 and DR 5534. Raw data.

(a)
(b)
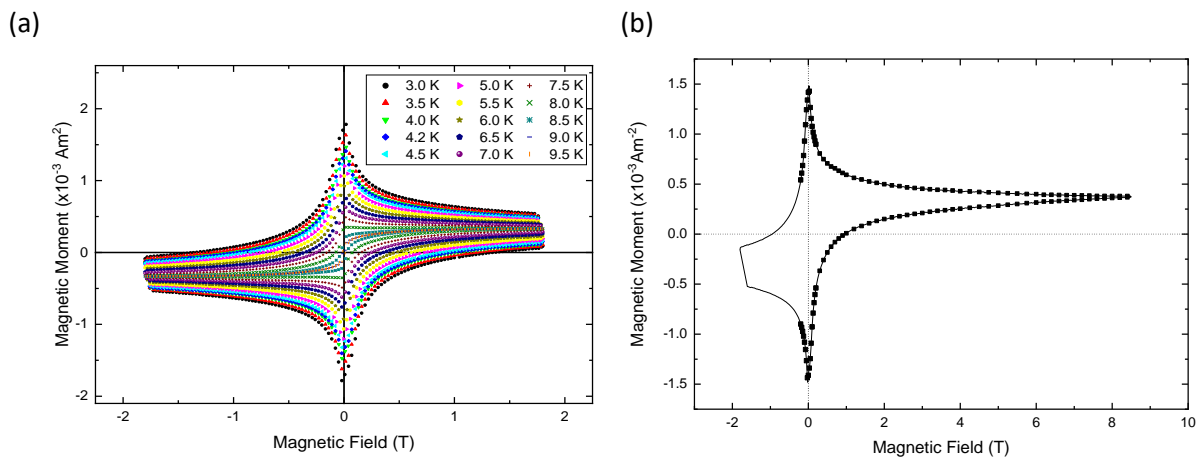
Figure 6.19 : Magnetic moment versus applied magnetic field for strand DR 4810. (a) various temperature (3.0 to 9.5 K in 0.5 K intervals) measurements over a limited field (± 1.8 T) range (b) 4.22 K measurement data.

All three strands were measured from 3.0 to 9.5 K at 0.5 K intervals. The magnetic moment data for strand DR 4810, B_{App} = -1.80 to 1.80 T, shown in Figure 6.19 (a) are typical. The peaks in the magnetic moment near B_{App}= 0 T, are above (+ 16 mT) and below (-18 mT) skewed in the direction which the magnetic field is swept. Measurement data of DR 4810 for B_{App}= -1.8 T to 8.5 T at 4.2 K, is shown in Figure 6.19 (b). The data points on the graph indicate where J_C was extracted.

6.4.1. Filament Properties and J_C

To calculate J_C from magnetisation measurement, the architecture of the conductor must be known. Magnetisation measurements are influenced by the geometry of the filaments [69]. Using an electron microscope image of the strand, the area of the superconducting region was measured and analysed using photo editing software. The filaments are assumed to be perfectly round [15]. An average filament diameter was calculated using the number of filaments (N), the measured superconducting area, A_{sc}:

$$d_f = \sqrt{\frac{4A_{sc}}{\pi N}}.$$

(6.10)

The average filament diameter of strand DR 4810 is 6.73 μm, the filament diameter 7 μm was used for the analysis. The uncertainty in the measurement resolution of the electron microscopy is considered negligibly small. Polishing of the sample can increase the uncertainty to < 1%.

There is a normal distribution in the diameter of the filament around the average, with the average filament diameter varying with radial position [77]. As the filaments are non-uniform, the analysis is further complicated with and variance in J_C along the length of each filament [78]. In Ref. [77] the distribution of filament sizes was from 0.75 to 1.2 $D/< D >$, where $< D >$ is the average filament diameter. This paper was studying filaments of average diameters 27, 33, 37 μm, and it is not clear how relevant this result is to the 7 μm filaments in the composite.

Filament distortion [45] can result in an increase in the transport measurements and can be up to 1.4 [69]. The ratio of magnetisation to transport measurements of the ITER PF type 1 strand were measured as 0.92-0.94 indicating uniformly shaped Nb-Ti filaments [45].

The 4.22 K transport and magnetisation $J_C(B)$ measurements for strand DR 4810 are compared in Figure 6.20 (a). The differences in the results for the two methods are expected, with the uncertainty in B at high fields in magnetisation measurements, and uncertainty in B due to self-field effect at low B_{App} in transport measurements. The transport J_C are lower for B_{App}< 2 T, and higher for B_{App}> 2 T than the magnetisation J_C. Literature data [79] comparing transport and magnetisation measurement methods shows similar behaviour to the data shown in Figure 6.20 (a).

(a)   (b)
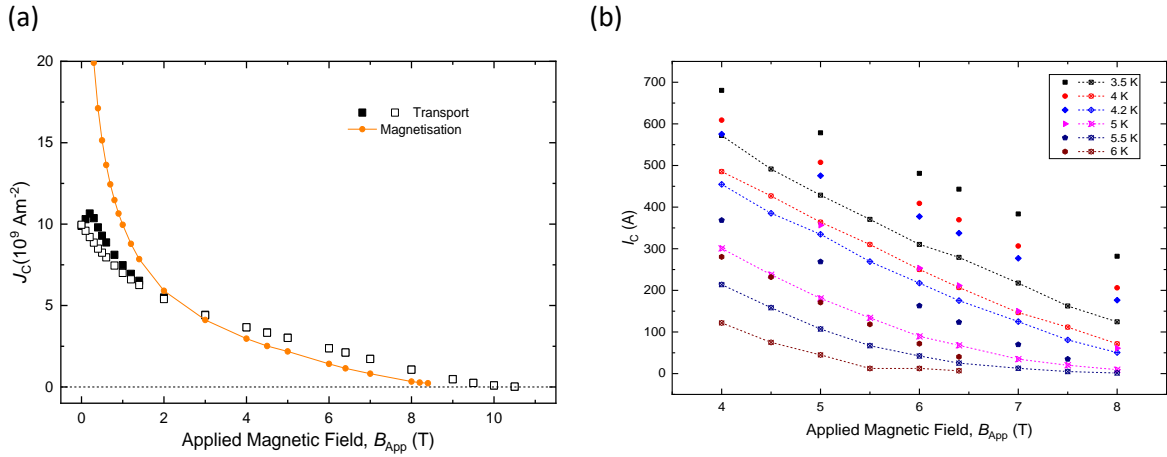
Figure 6.20 : (a) Comparison between transport (ITER geometry) and magnetisation J_C for strand DR 4810 at 4.22 K. The dashed horizontal line is at J_C= 0. The open symbols: outward F_L, closed symbols: inward F_L (b) Comparison between transport and magnetisation J_C measurements of strands DR 5049. The closed symbols are the transport data (ITER, inward F_L) and crossed symbols the magnetisation data. The dashed straight lines are a guide for the eye.

In the literature the single term exponential fit to the two experimental data sets (magnetisation and transport measurements) that captures the sharp increase of J_C at low B (< 4.0 T) results in a low less accuracy fit for B > 4.0 T [79]. For the FEA calculations in this chapter, the $J_C(B)$ data, shown in Figure 6.20 (a), is fitted with a two term exponential as a model input.

Variable temperature data, $I_C(B,T)$, measured using both transport and magnetisation techniques are compared in Figure 6.20 (b). Typically the two measurement methods provide data in different field ranges, and the magnetisation and transport data can be fitted with small errors using either a single-pinning [69] or double-pinning mechanism [46]. For the range of B_{App} and temperatures studied, the magnetisation I_C is lower than transport, as expected from considering the data shown in Figure 6.20 (a).

6.4.2. Electric field
The J_C was evaluated in the transport measurements using an E-field criterion of 10 µV·m^{-1}. The E-field generated in the magnetisation measurement was calculated for comparison using Faraday's law. The tightly wound coil was approximated by the magnetic field of an infinite solenoid geometry, the E-field was equated to a flux change,

$$E = \left(-n_d A \frac{dB}{dt}\right)/l. \qquad (6.11)$$
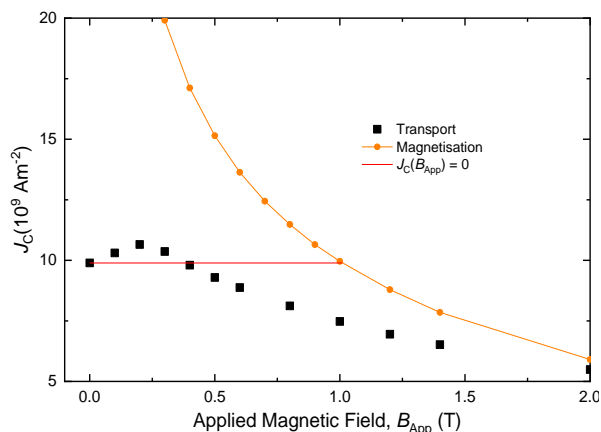
Figure 6.21 : Calculation of self-field effect using the differences in transport and magnetisation measurement at B_{App}= 0 T.

The magnetisation measurement geometry and Eq. (6.11) suggest the evaluation is at $E \approx 10$ nV·m^{-1}, three orders of magnitude smaller than the E_C. As the magnetisation measurements were of strands with constant areas and lengths, at a fixed magnetic field ramp rate (dB/dt = const.), a single E-field is generated, and further analysis is not possible.

6.4.3. Self-field

Although there are errors associated with magnetisation measurements, the higher J_C measured relative to the transport technique provides further evidence that the self-field effects are large at low B_{App}, and self-field corrections are necessary to understand low B_{App} transport measurement J_C.

One comparison between transport and magnetisation measurements is calculating at what value of B the magnetisation J_C is equal to the transport J_C [48] The data input is the transport at B_{App}= 0 T and what value of B this is equivalent too in the magnetisation data, shown in Figure 6.21. Analysing the data in using this method results in a B_{SF} = 1.00 ± 0.01 T for the ITER geometry, i.e., 0.63 T·kA^{-1} and B_{SF} = 2.31 ± 0.01 T for the MST geometry, i.e., 1.87 T·kA^{-1}. The magnitude of the ITER self-field correction is within the range reported in the literature. It is clear that the J_C measured is not accurate, due to the facts $B \neq 0$ T. The relationship generated is of limited use.

Detailed quantification of the magnitude of the effect of self-field in the magnetisation measurement is a topic for future research. In sections 6.5 (FEA model) and 6.6 (semi-analytic method) the magnetisation $J_C(B)$ data were plotted without correcting for the effect of self-field and used as a reference.

6.5.   Finite Element Analysis Model

The consistency checks in chapter 5 verified the FEA modelling methodology implemented using the H-formulation. In this section different models are presented which vary in complexity, both the definition of $J_C(B)$ and how the current redistributes within the strand. The strands architecture is modelled in a way that allows the current can redistribute. A precursory model with an annular cross-section is considered in section 6.5.1. With a reduced experimental J_C data set, the FEA results are compared with literature methodologies, and an analytic method is attempted to understand the effects of filament transposition. Extensive analysis of the self-field with an annular cross-section is outlined in section 6.5.2 with the complete transport and magnetisation measurement data. In the insulated TwT cross-section the current can redistribute within each tube.

For the FEA models in section 6.5.2 the geometry is fixed, the variable changed is the $J_C(B)$ relationship. The fixed value of $n = 5$ in Eq. (5.3) was used in all the models presented here. The magnetic field is calculated by defining a ramping to the I_C, at each of the F_L orientation and values of B_{App}. The distribution of the probability density was analysed and an average of the magnitude of the net magnetic field ($\bar{B}_{Net}$) at selected B_{App} value was calculated. The values of $\bar{B}_{Net}$ were used to replot the experimental data. An accurate self-field correction would result in the replotted J_C data points at each B_{App} converging on to a single curve. $J_C(B)$ relationship that accounts for the effect of self-field have been investigated for several materials in the literature [80, 81].

6.5.1.   Precursory Self-field Correction: Annular Cross-section
The first self-field correction calculated used the variable temperature transport measurement data (section 6.3.1) of strand DR 5534 at 4.22 K. The experimental data is taken in the ITER geometry and in both orientations of F_L. The measured differences in the I_C data are small, ~5A, >1 %. At high B_{App} it is expected that the distribution in the net-field results in a correction would result in a $\bar{B}_{Net} < B_{App}$ for inwards F_L, and higher $\bar{B}_{Net} < B_{App}$ for outwards F_L, with the two data sets converging onto a single $I_C(B)$.

The FEA model simplified the experimental geometry; the ITER helix was modelled with five turns only. The strand cross-section was considered as annular, with an inner and outer filamentary region radius. The field distribution was calculated for current density at which the E_C criterion is met. The probability distribution of the superconducting region in the two orientations of F_L is analysed to calculate B_{Net}.

(a)

(b)

(c)
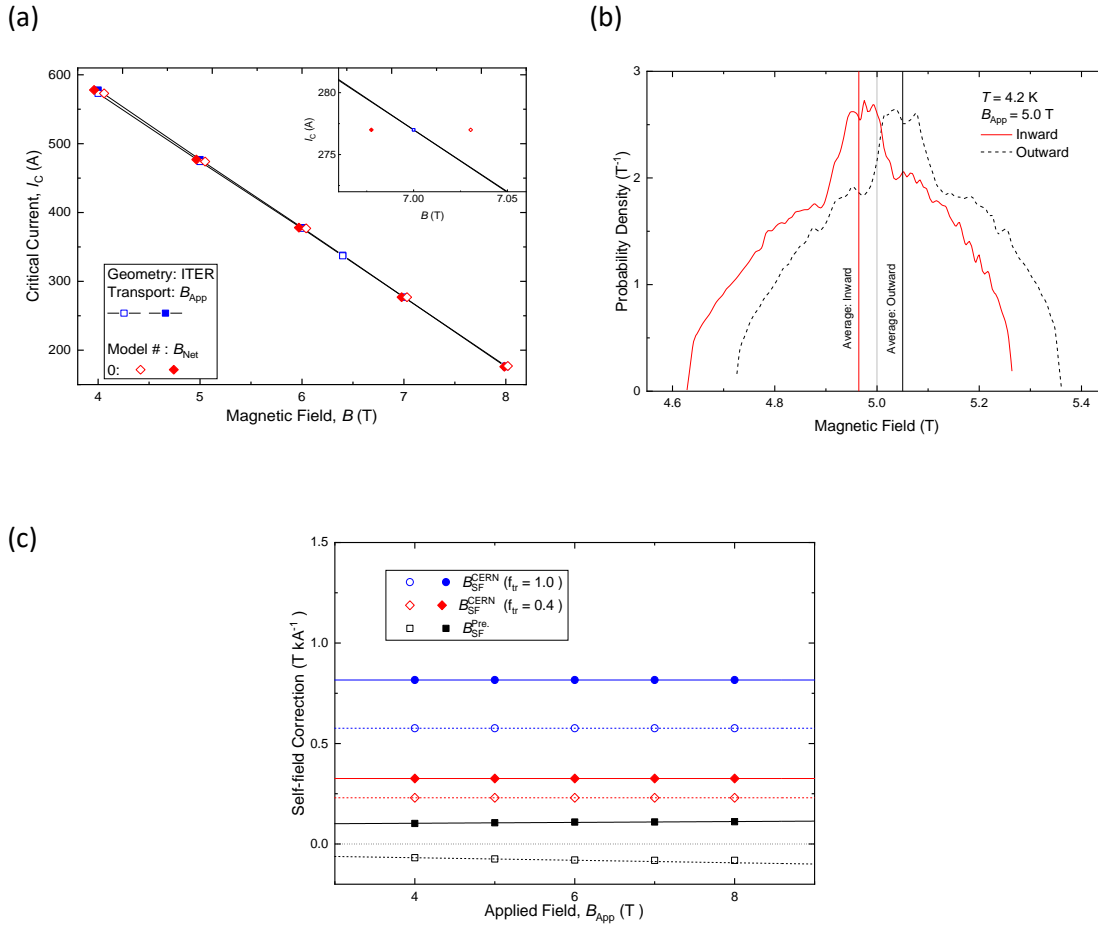
Figure 6.22 : Model 0 (a) Comparison of I_C vs B_{App} and I_C vs $\bar{B}_{Net}$ with self-field correction. Inset − I_C data about B = 7 T. (b) Probability density function for the modulus of the net magnetic field for each of the two polarities of force on the strand - inward Lorentz force (solid) and outward Lorentz force (dashed). The distribution is calculated for the central turn of the strand at B_{App} = 5 T. (c) The self-field correction as a function of the applied magnetic field. The B_{SF}^{CERN} correction is Eq. 5.22, calculated with a transposition factor (f_{tr}) of 1.0 and 0.4. The inward (closed symbols) and outward (open symbols) Lorentz force.

The $J_C(B)$ relationship implemented is a linear fit of the form

$$J_C(|\boldsymbol{B}|) = J_{C0}\left(1 - \frac{|\boldsymbol{B}|}{B_{C2}}\right)$$ (6.12)

to the experimental 4.22 K data, shown in Figure 6.8, where J_{C0} is the critical current density at B = 0 T. This model will be referred to as model 0 in this section. The experimental data for B_{App} = 4 to 8 T is replotted as a function of the average of the magnitude of the net magnetic field ($\bar{B}_{Net}$) in the two F_L orientations shown in Figure 6.22 (a). The convention of open symbols for outward F_L and closed for inward F_L is followed. The results of the FEA model is peaks in B_{Net} > B_{App}, but the averages greater than, $\bar{B}_{Net}$ > B_{App} in the outward F_L measurements, and less than, $\bar{B}_{Net}$ < B_{App} in the inward Lorentz force measurements, shown in Figure 6.22 (b). The B_{SF} at B_{App} = 7.0 T is +30 mT in the

outward F_{L}, and -23 mT for inward F_{L}. This result is in contrast to those in section 6.1.2, both in magnitude, and orientation. Visually it is clear that the resultant $\bar{B}_{Net}$ for the two datasets is not described by a single $J_C(B)$, [inset in Figure 6.22 (a)]. The self-field correction is considered as an overestimate, as the resultant $J_C(B)$ for the two F_{L} orientations do not converge. Using the measured I_C as the input in the FEA, the values being so similar in both F_{L} orientations makes the analysis more difficult to analyse. Determining an effect which has typically been neglected with almost identical input was going to be tricky.

The precursory self-field correction $B_{\mathrm{SF}}^{\mathrm{Pre.}}$, as a function of B_{App} and F_{L}, is compared with the $B_{\mathrm{SF}}^{\mathrm{CERN}}$ (Eq. 5.25) and is smaller, as shown in Figure 6.22 (c). To try and explain the difference between the $B_{\mathrm{SF}}^{\mathrm{Pre.}}$ and $B_{\mathrm{SF}}^{\mathrm{CERN}}$ result, a term was added to Eq. 5.25, to characterises the degree to which the filaments are transposed, f_{tr}:

$$B_{\mathrm{SF}}/I = f_{\mathrm{tr}}\left(\frac{\mu_0}{2\pi r} + \alpha\right).$$
(6.13)

As the $B_{\mathrm{SF}}^{\mathrm{CERN}}$ assumes the full transposition of filaments, $f_{\mathrm{tr}}= 1$ this results in the maximum self-field correction. The self-field correction is also not a function of B. In the Nb-Ti strands, the filaments are partially transposed, and transposition factor was estimated: $f_{\mathrm{tr}} \approx (0.6 \times 2)/\pi \approx 0.4$. As expected, the transposition factor results in a lower self-field correction, although the results of $B_{\mathrm{SF}}^{\mathrm{Pre.}}$ is significantly lower than Eq. (6.13) and opposes B_{App}. The transport I_C data, was used to calculate an experimental transposition factor. Using the values of α_{in} and α_{out} from Eq. 5.25, and the change in I_C with magnetic field ($\partial I_C/\partial B$), of $\sim100\,\mathrm{A \cdot T^{-1}}$ (for the Nb-Ti strand studied in the range of B_{App}), the difference in I_C due to the difference in Lorentz force direction, F_{L} results in the relationship:

$$\Delta I_{\mathrm{C}}/I_{\mathrm{C}} = f_{\mathrm{tr}}\left(\frac{\partial I_{\mathrm{C}}}{\partial B}\right)_{I_{\mathrm{C}}}[-\alpha_{in} + \alpha_{out}].$$
(6.14)

As the experimental difference in I_C with F_{L} at $B_{\mathrm{App}}= 5.0$ T is 1%, a value of f_{tr} can be calculated from Eq. (6.14) to be $f_{\mathrm{tr}} \approx 0.42$.

This precursory FEA analysis considers only the ITER barrel measurement geometry at high B_{App} and low measured J_C. The analysis suggests that the effect of self-field is smaller than the conservative CERN estimate, and that the architecture can be included using a transposition factor. Using the data in section 6.3.2 was necessary to quantify the effect of self-field.

6.5.2. Extensive Self-field Correction: Annular Cross-section

The ITER and MST geometries are modelled using a five-turn helix, with an annular cross-section R_i = 0.136 mm and R_o = 0.311 mm. The FEA calculations of B_{SF}, implemented using $J_{\mathrm{C}}(B)$ model 1, are carried out at B_{App}= 0.0 to 8.0T. The current input is the geometry dependent average I_{C} of the inner and outward F_{L}. At B_{App}= 0 T, a single value of $\bar{B}_{Net}$ is calculated for each geometry. The average of the probability distribution is used to define B_{SF}. The self-field is calculated for each Lorentz force orientation, and the critical current data replotted I_{C}vs $\bar{B}_{Net}$, shown in Figure 6.23.

With J_{C} measured in two geometries for strand DR 4810, the self-field correction was calculated with many grid data points to verify the FEA model. The $J_{\mathrm{C}}(B)$ relationship is defined using the experimental transport J_{C} data for strand DR 4810. The $J_{\mathrm{C}}(B)$ relationships are a linear relationship of the form Eq. (6.12). The fit is the average (inward and outward F_{L}) of the transport J_{C} for the two geometries of strand DR 4810, the blue line shown in Figure 6.23. To reduce the error of the linear fit, low B_{App} (< 3.0 T) and high B_{App} (> 3.0 T) regimes were defined. The numerical parameters of $J_{\mathrm{C}}(B)$ model 1 are listed in Table 6.10. This model will be referred to as model 1.

Over the benchmarking range of magnetic fields, as shown in Figure 6.23 (a), due to the small I_{C} and resultant B_{SF}, describing the four data sets with a single curve is a reasonable approximation for the ITER geometry. Comparing the results of this analysis with the literature (Table 6.2) at B_{App}= 7.0 T, the inward I_{C} is decreased by 0.6 % and the outward I_{C} is increased by 0.8 %. The resultant self-field correction is more than ten times smaller than the standard literature correction. The difference in results is not unexpected as the analysis considers the average. For the inward F_{L}, the resultant $\bar{B}_{Net}$ > B_{App}, whereas $\bar{B}_{Net}$ < $B_{\mathrm{App}}$for outward F_{L}.

The low B_{App}, (high B_{SF}) data is plotted in Figure 6.23 (b). It can be reasonably assumed that a universal $J_{\mathrm{C}}(B)$ relationship does not peak at $B > 0$ T and turnover. Below the peak in J_{C}, the effect of transport current flow changes the orientation of B_{Net}. It was not possible to describe the $J_{\mathrm{C}}(B)$ MST data shown in Figure 6.23 (b), with a single universal curve for $J_{\mathrm{C}}(B)$. For $B < 0.7$ T, the analysis of the data suggests J_{C} can have two values. The J_{C} at $\bar{B}_{Net}$≈ 0.6 T has values of 5.63 or 4.84 ×10^9 A·m^{-2} in the MST geometry. The analysis does not result in a universal curve and suggests that the effect of the B_{Net} is not recreated with the FEA model.
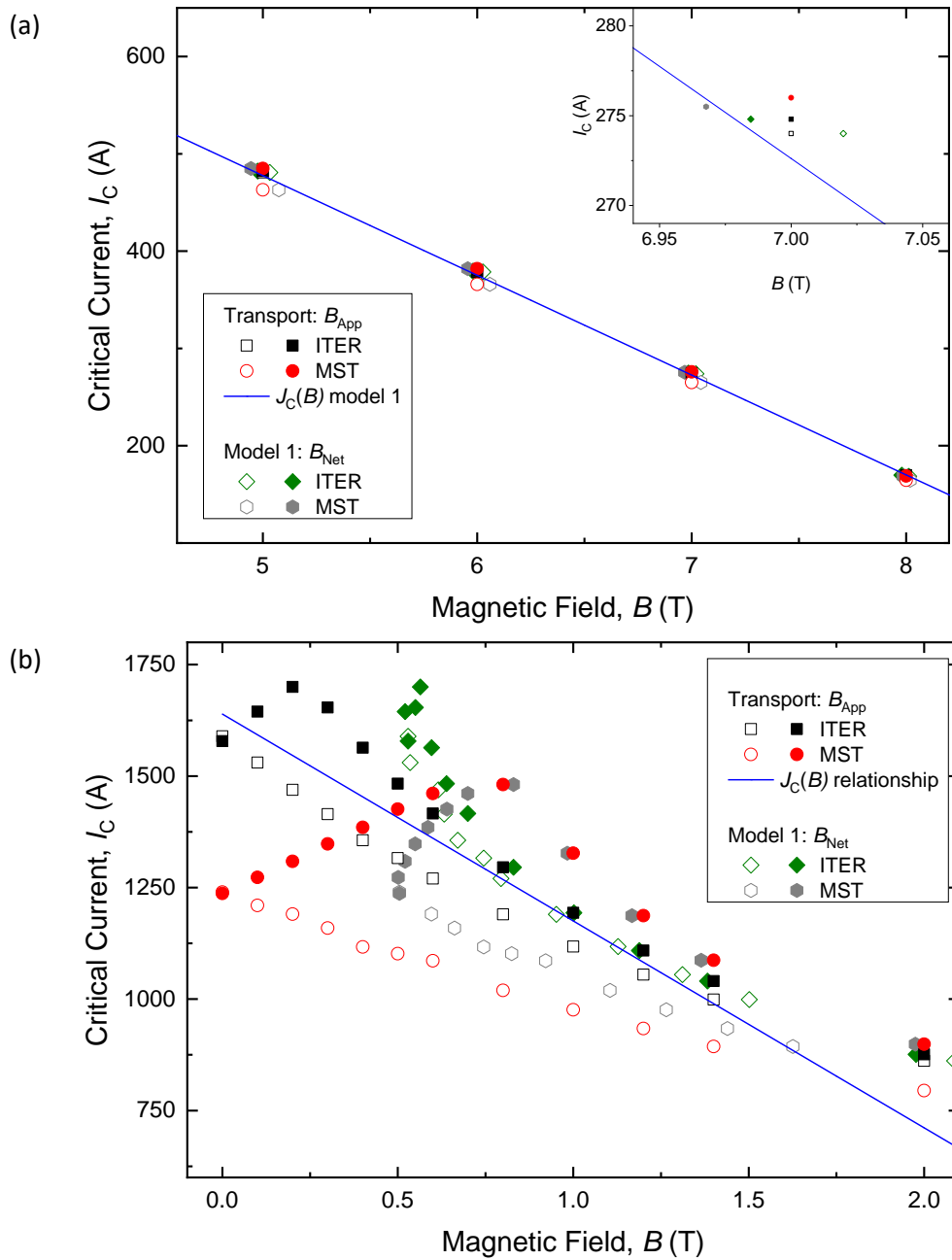
Figure 6.23 : Model [1] Comparison of experimental data I_C vs B_{App} for strand DR 4810 and self-field corrected data I_C vs $\bar{B}_{Net}$ with $J_C(B)$ relationship model 1 – linear fit to the average of the experimental: Table 6.10. (a) benchmarking region of B_{App}. Inset – I_C data about $B = 7$ T. (b) Low B_{App} region.

B_{App} range	J_{C0} [1× 10^9 A·m^{-2}]	Upper Critical field, B_{C2} [T]
Low (< 3.0 T)	9.94	4.50
High (> 3.0 T)	6.65	9.66

Table 6.10 : Linear fit parameters for $J_C(B)$ model 1, 6.

(a)
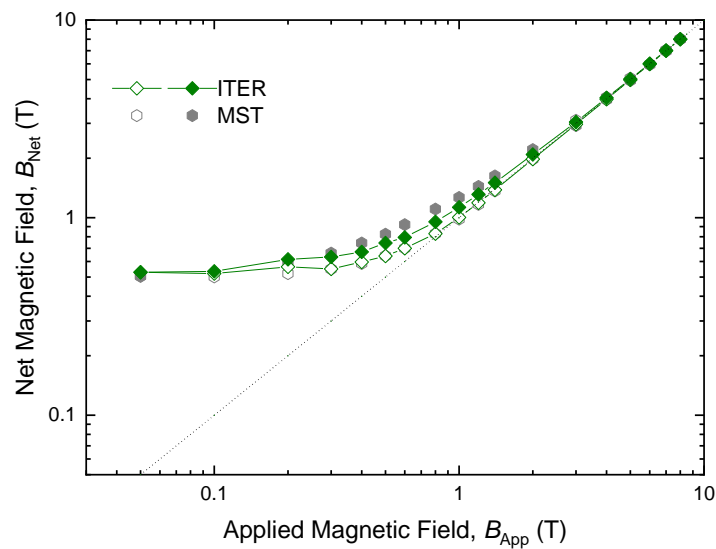
(b)
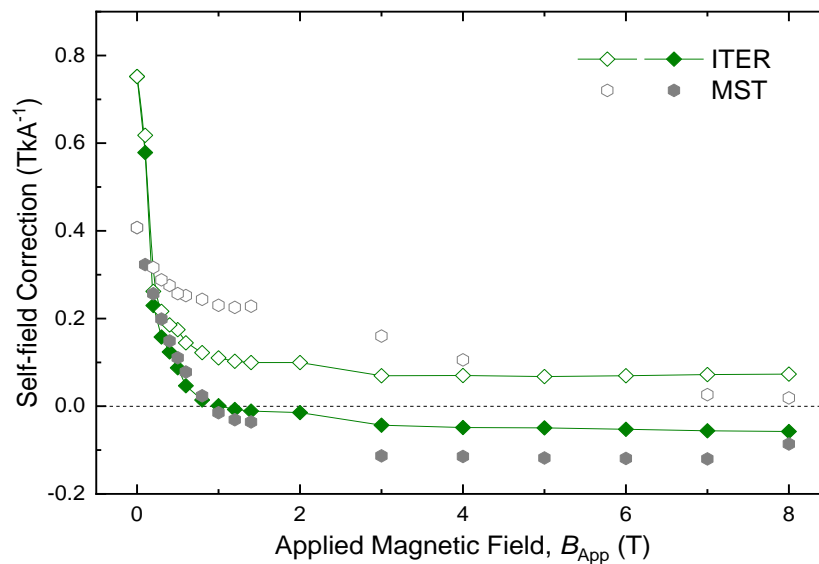
Figure 6.24 : Model [1] (a) (log-log) Net magnetic field as a function of the applied field for the two geometries and orientations of Lorentz force. The dotted line indicates a 1:1 ratio(b) Self-field correction as a function of applied field for the ITER and MST geometry [$J_C(B)$ model 1]. Open symbols: outward F_L, closed symbols: inward $F_L$orientation. Lines between data points are a guide for the eye.

The results of the FEA calculations are considered further by investigating the B_{SF} and $\bar{B}_{Net}$. At $B_{App}=$ 0 T, the $\bar{B}_{Net}$ is entirely due to the B_{SF}, a minimum value of $\bar{B}_{Net} = 0.505$ T was found, shown in Figure 6.24 (a). Experimentally the difference in I_C value between the ITER and MST measurement barrel geometries is ~345 A. The similar size of $\bar{B}_{Net}$ suggests that the geometric effect is not being captured with the FEA, the effect of the neighbouring turns are not as significant as the geometry of the strand itself, i.e., both measurement geometries consider the cross-section as an annulus.

Model	J_{C1} [10^9 A·m^{-2}]	J_{C2} [10^9 A·m^{-2}]	B_1[T]	B_2[T]	C_0 [10^9A·m^{-2}]	I_C(B_{App}= 0 T) [A]
2	10.2	17.3	1.158	0.158	1.730	7 173
3	45.0	10.9	0.144	1.776	0.475	12 213
4, 5	10.7	15.3	8.025	0.332	-2.790	3 685

Table 6.11 : Exponential fit parameters for the critical current density Eq. (6.15) for the Nb-Ti ITER PF strand DR 4810 shown in Figure 6.20

The self-field correction was calculated as a function of B_{App}, shown in Figure 6.24 (b). For both geometries in the inward F_L orientation: $\bar{B}_{Net} < B_{App}$, for B_{App}> 1.0 T. Similarly, in the outward $F_L$orientation: $\bar{B}_{Net} > B_{App}$, for B_{App}> 1.0 T. For B_{App}≤ 1.0 T, both orientations of the $F_L$result in a $\bar{B}_{Net} > B_{App}$.

The rest of section 6.5.2 uses FEA models with different definitions of $J_C(B)$ but with the same geometry as model 1. In total 4 different $J_C(B)$ are used, and two implementations of the magnetic field dependency. The focus has changed to investigate the self-field correction at low B_{App}. Using the FEA model I_C-$\bar{B}_{Net}$ were calculated for the two geometries and inward and outward F_L at values of B_{App}= 0, 0.5 and 1.0 T. At low B_{App}, the FEA calculations generate $\bar{B}_{Net} > B_{App}$ for all F_L orientations. As the $J_C(B)$ relationship is iterated, how well the correction works is evaluated by attempting to describe a new $J_C(B)$. The purpose of this analysis is quantifying if the magnetisation $J_C(B)$ produces consistent results for both F_L and geometries at the low B_{App}.

One-term exponential decay functions to fit $J_C(B)$ data have been used in the literature [82]. Using a two-term equation to describes $J_C(B)$ minimised any differences between the fit and the magnetisation $J_C(B)$ data. The FEA analysis of B_{SF} in models 2 - 5 use a $J_C(B)$ behaviour given by:

$$J_C(B) = J_{C1}\, e^{\left(-\frac{|\boldsymbol{B}|}{B_1}\right)} + J_{C2}\, e^{\left(-\frac{|\boldsymbol{B}|}{B_2}\right)} + C_0 \,. \tag{6.15}$$

The free parameters in Eq. (6.15) have no independent physical meaning. Table 6.11 summarises the numerical values for the fitting parameters for models 2-5.

The $J_C(B)$ used in models 2 and 3 was two fits to the magnetisation data. The $J_C(B)$ model 2, was a fit to the magnetisation data with the data from B_{App}= 0.0 to 3.0 T. The fitting parameters for model 3 were calculated using the magnetisation data for B_{App}= 0.0 to 2.0 T. With a reduced B_{App}fitting range, the result was an increased $I_C$at B = 0.0 T.

Figure 6.25 : Models [1-4] Comparison with the experimental data (I_C vs B_{App}) and four helical models with varied $J_C(B)$ relationship (I_C vs $\bar{B}_{Net}$). (a) ITER measurement geometry (b) MST measurement geometry. Dashed lines are a guide for the eye, open symbols: outward F_L, closed symbols: inward F_L.

The fitting parameters used to evaluate $J_C(B)$ used in model 4 was calculated using the I_C-$\bar{B}_{Net}$ ITER data shown in Figure 6.25 fitted from $B = 0.0$ to 8.0 T. Model 5 uses the same numerical parameters as model 4, further details will be outlined in section 6.5.2.1. The I_C intercept at $B_{App}= 0$ T, for $J_C(B)$ relationships in models 2, 3, and 4, are listed in Table 6.11. The intercept is larger than the experimentally measured transport [I_C ($B_{App}= 0$ T) = 1600 A], which is expected because the experimental I_C at $B_{App}= 0$ T, is at B_{Net} dependent on the current and measurement geometry.

Model	$\bar{B}_{Net}$ (B_{App}= 0 T) [T]		B_{SF} [T·kA^{-1}]	
	ITER	MST	ITER	MST
1	0.529	0.505	0.333	0.408
2	0.584	0.401	0.367	0.324
3	0.530	0.374	0.334	0.302
4	0.495	0.355	0.311	0.287

Table 6.12 : FEA calculations of $\bar{B}_{Net}$ and the self-field correction for the four models at B_{App}= 0 T from Figure 6.23 and Figure 6.25.

The I_C vs $\bar{B}_{Net}$ data for models 1 to 4 are reported in Figure 6.25. The ITER data is shown in Figure 6.25 (a) and MST in Figure 6.25 (b). The value of $\bar{B}_{Net}$ in the ITER and MST geometry at B_{App}= 0 T, are summarised in Table 6.12. The self-field corrections calculated by these models are smaller than both the literature values and the comparison with the magnetisation data, section 6.4.1. The self-field correction results for models 2-4 are similar to the results of model 1. In Figure 6.24 (b), the MST results are of a similar magnitude to the ITER. This is similar to Figure 6.24 which highlighted the inaccuracy of the analysis. The results of the different FEA calculations of self-field Figure 6.25 demonstrate serious difficulties in using this approach to analyse the experimental data. The effect of self-field on the measured I_C was not accounted for properly with the analysis used here a $J_C(B)$ that explains the four data sets was not produced. When considering the B_{App}= 0 T data, it is possible that by calculating the average of B_{Net} rather than a component of B the magnitude of the self-field correction is increased, due to $B_{Net} > 0$ T. The calculation of the magnitude of a vector could skews how the data is interpreted.

The distribution of the B_{Net} was investigated further. The probability distribution data for $J_C(B)$ in model 2, ITER geometry, is shown in Figure 6.26 (a). The experimental transport ITER data are replotted in Figure 6.26 (b). The resultant $J_C(B_{Net})$ where B_{Net} is defined by the average or the peak produces two equivalent $J_C(B)$ relationships, which can be described by a simple relationship. The differences in resultant B correction between the two data sets is 0.67 T.

(a)   (b)
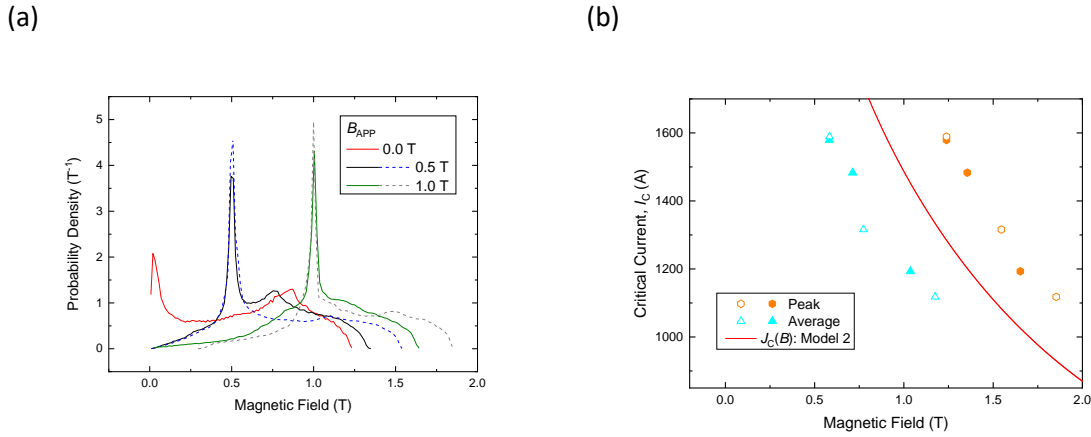
Figure 6.26 : Model [2] (a) The probability distribution as a function B_{App} and Lorentz force orientation for the ITER geometry calculated using the $J_C(B)$ model 2, see Table 6.11. Dashed line is the outward F_L data and sold line the inward F_L data (b) Comparison of the methods of self-field analysis, calculated peak and average of the distribution for both F_L orientations.

6.5.2.1.   Resistivity Definition

The final annular cross-section FEA model discussed is referred to as model 5. Model 5 is a development on model 4, using the same numerical parameters in the definition of $J_C(B)$, outlined in Table 6.11. The difference is in the implementation of the FEA, the definition of ρ_{SC}. The magnetic field term in the exponents of Eq. (6.15) was modified by replacing the magnitude of the local field, $|\boldsymbol{B}|$ with the maximum value of the magnetic field, $(|B|_{max})$ in the superconducting domain. The I_C vs $\bar{B}_{Net}$ for model 5 is compared with model 4 and the experimental transport data for the ITER geometry, shown in Figure 6.27 (a) and MST geometry shown in Figure 6.27 (b). The $\bar{B}_{Net}$ of model 4 and 5 in the ITER and MST geometry are compared for the inward F_L in Table 6.13.

It was expected that by taking $|B|_{max}$ would result in a larger $\bar{B}_{Net}$ which is essential to understand the low B_{App} data. The results in Figure 6.27 show the larger $\bar{B}_{Net}$ for the data except the B_{App} = 1 T in the ITER geometry. Using model 5 again results in a multivalued $J_C(B)$.

B_{App} [T]	ITER		MST	
	$\bar{B}_{Net}$ [ρ ($|\boldsymbol{B}|$)] [T]	$\bar{B}_{Net}$ [ρ ($|B|_{max}$)] [T]	$\bar{B}_{Net}$ [ρ ($|\boldsymbol{B}|$)] [T]	$\bar{B}_{Net}$ [ρ ($|B|_{max}$)] [T]
	Model 4	*Model 5*	*Model 4*	*Model 5* [T]
0.0	0.495	0.647	0.354	0.504
0.5	0.653	0.673	0.658	0.657
1.0	1.029	0.962	1.020	1.144

Table 6.13 : Comparison of the calculated $\bar{B}_{Net}$ for models 4 and 5, with the ρ_{SC} defined using local $|\boldsymbol{B}|$ and maximum $|B|_{max}$ magnetic field value.
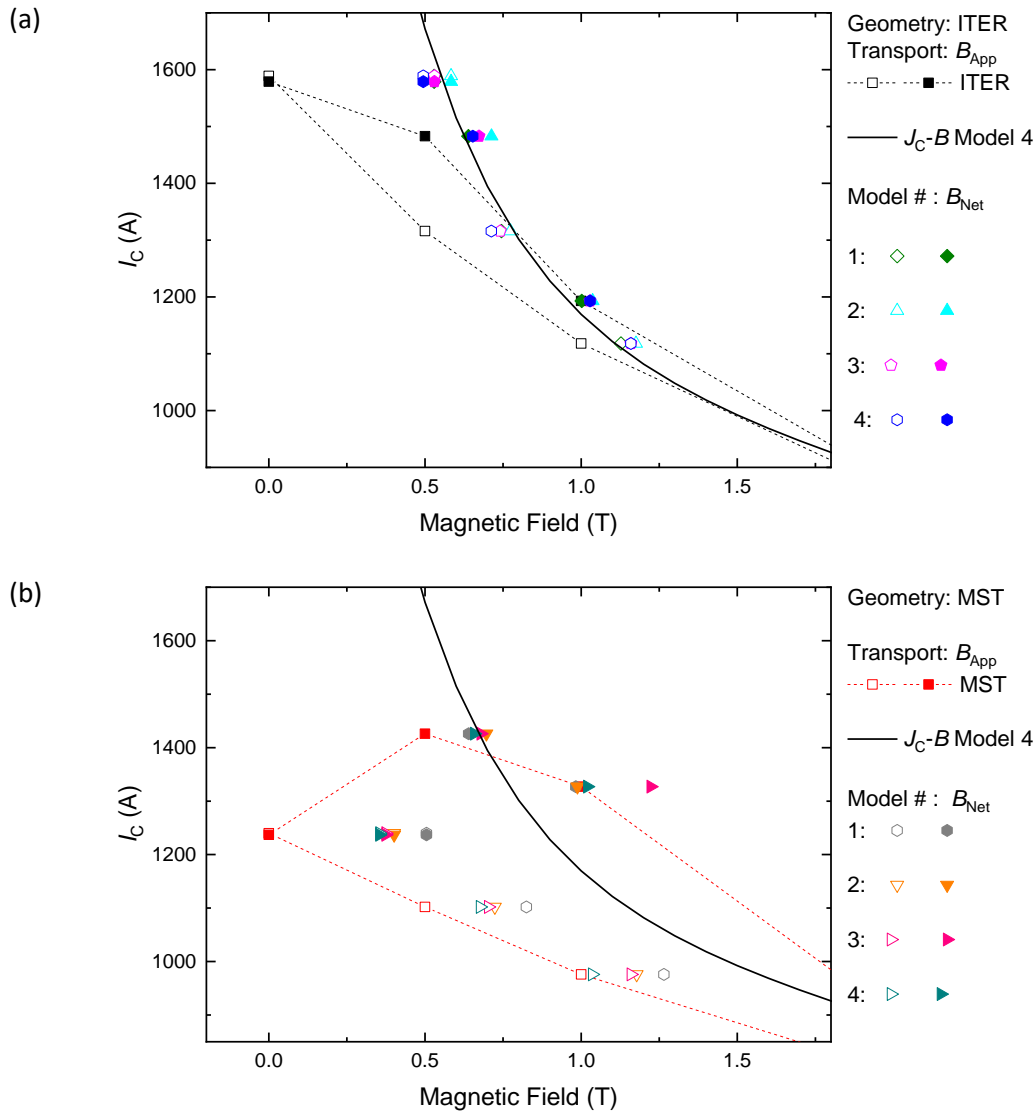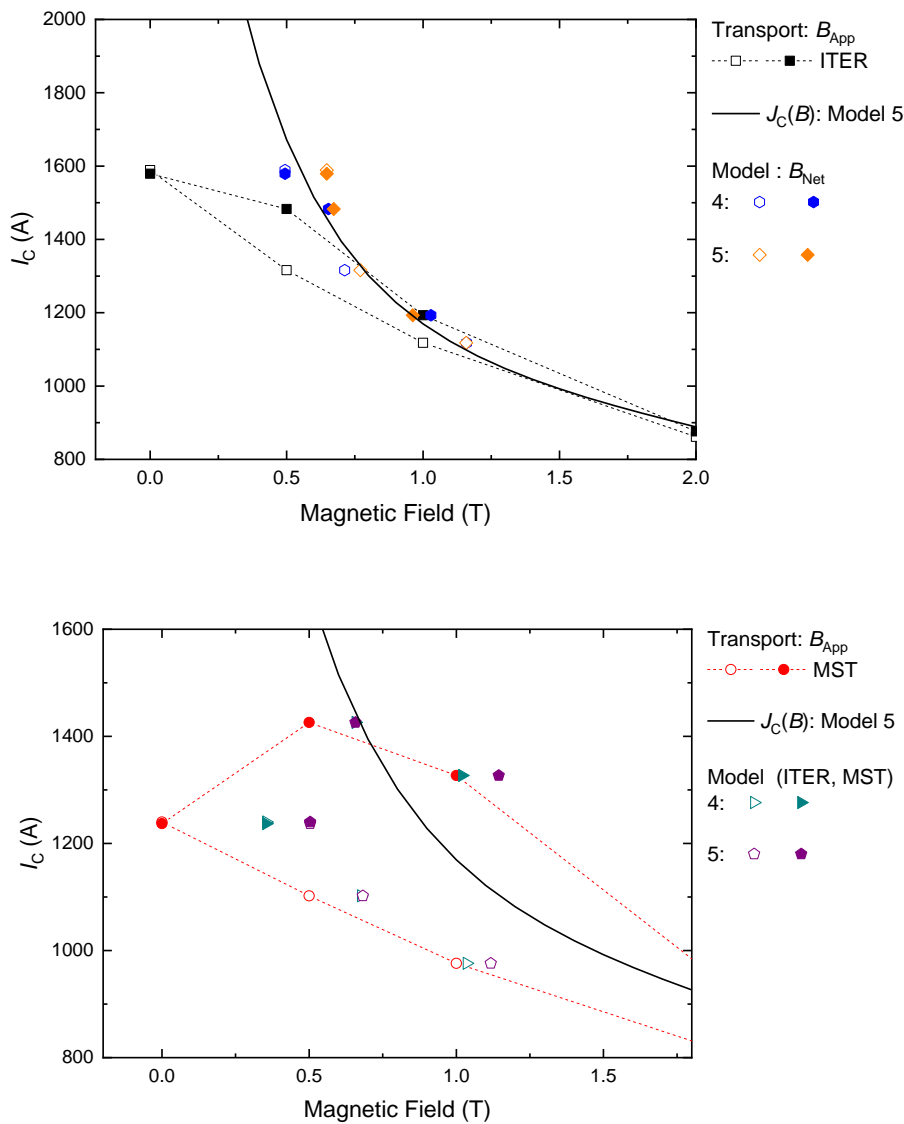
Figure 6.27 : Model [4,5] Comparison of the experimental data (I_C-B_{App}) and helical models with varied $J_C(B)$ relationship (I_C-$\bar{B}_{Net}$). (a) ITER measurement geometry (b) MST measurement geometry. Dashed lines are a guide for the eye, open symbols: outward F_L, closed symbols: inward F_L orientation.

6.5.3. Self-field Calculation: Tubes-within-tubes Cross-section

Unlike sections 6.5.1 and 6.5.2, the geometry modelled in this section is a 13 turn ITER helix, and 51 turn MST helix. To implement the three tubes, the definition of resistivity in the superconducting domain is defined separately for each of the three domains. Model 6 was calculated using the $J_C(B)$ relationship implemented in model 1, detailed in Table 6.10. The self-field was calculated for $B_{App} <$ 0.5 T. The analysis considers the value of I_C for the various B_{App} values when the E-field reached the E_C criteria. The resultant I_C (B_{App} = 0 T) is 2180 A, 38% larger than the experimental transport measurement, but 364 % smaller than the magnetisation measurement. The I_C vs $\bar{B}_{Net}$ is compared with the experimental data (I_C vs B_{App}) shown in Figure 6.28. It was again not possible to find a $J_C(B)$ relationship which describes the four data sets.
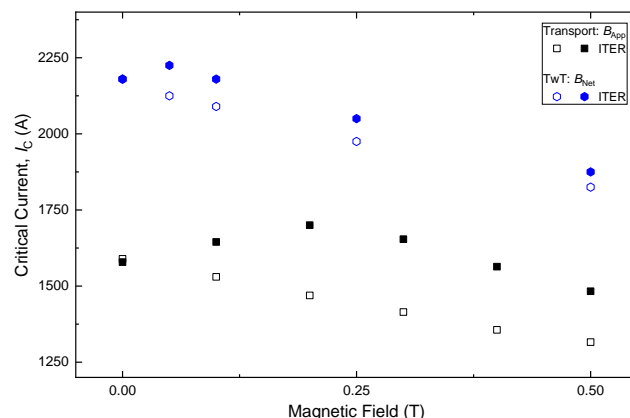
Figure 6.28 : Model [6] Comparison of the experimental I_C-B_{App} and the I_C-$\bar{B}_{Net}$ for a 13 turn ITER helix with a Tubes-within-tubes cross-section.

6.5.4. Conclusion

Several approaches have been considered to calculate the effect of self-field using FEA methods. Throughout, the analysis has relied upon the accuracy and absolute values of the transport measurement data. The $J_C(B)$ data has two distinct field ranges, the high and low B_{App}. The analysis of the self-field at high B_{App} result in effect of self-field being small and confidence with this data enables the low field data to be investigated further. The resultant $J_C(B_{Net})$ is compared with the average of the measured inward and outward J_C. in section 6.5.1 the difference in the average of the magnetic field with F_L varies by ~60 mT at B_{App}= 7 T, is inconsistent with experimental I_C. The simplification of the FEA model, both the measurement geometry, and the $J_C(B)$ input, were considered to be limiting the models ability to resolve the differences in J_C due to F_L.

The FEA model in section 6.5.2 resulted in a self-field corrected ITER data set that reduced the variance between the inward and outward F_L, J_C value. Additionally, the $J_C(\bar{B}_{Net})$ at low B_{App} range converged on to a single curve. It was clear that the more complex magnetic field due to the MST geometry was not accounted for with the FEA analysis. The modification of the definition of the relevant magnetic field in defining J_C did not produce consistent results, and more research is needed.

6.6.   Semi-Analytic Method

As the focus of this thesis was the architecture of the strand, and as the distribution of the magnetic field and the transposition of the filaments were not properly accounted for in the FEA model, a semi-analytic method was developed. Using the spatial distribution of the magnetic field inside the TwT from the FEA analysis the current distribution inside the strand was calculated. The semi-analytic method was used to generate a universal $J_C(B)$ for the Nb-Ti strands.

The critical current density as a function of magnetic field was derived by calculating the spatial distribution of the current in the tubes for a TwT model for the cross-section of the Nb-Ti strand. A linear $J_C(B)$ relationship,

$$J_C = X_0 + X_1 (B_{Max}) \tag{6.16}$$

is assumed as a first-order approximation. The numerical values of the parameters X_0, X_1 and B_{Max} are unknown but considered to be universal, i.e, describe the $J_C(B)$ of the strand without errors associated due to effect of self-field. The form of Eq. (6.16) defines a positive X_0, intercept and a negative X_1 gradient. The field matrices in the axial direction and the experimental J_C transport measurements of strand DR 4810 were used to calculate the numerical values of the unknown parameters in Eq. (6.16).

6.6.1.   Problem Specification

The cross-section of the Nb-Ti strand was modelled as three TwT, with an unknown current distribution. The notation for current flow in each tube is I_{Ti} for current flow in tube i. The areas of the tubes (A_{Ti}) are known, Table 5.11. The total current (I_T) in the strand is the summation of the current in each of the tubes:

$$I_T = I_{T1} + I_{T2} + I_{T3}. \tag{6.17}$$

The current that flows in each tube is calculated assuming the same functional form of the $J_C(B)$ relationship Eq. (6.16), with the unknown parameters X_0 and X_1. The current in each tube is defined by,

$$\begin{aligned}
I_{T1} &= A_{T1}[X_0 + X_1 B_{T1Max}] \\
I_{T2} &= A_{T2}[X_0 + X_1 B_{T2Max}]. \\
I_{T3} &= A_{T3}[X_0 + X_1 B_{T3Max}]
\end{aligned} \tag{6.18}$$

The current in the tube is a function of the tube dependent maximum self-field i.e., B_{T1Max}. The maximum self-field in each tube is the product of the product of the current flowing in each tube e.g., I_{T1}, and the spatially dependent magnetic-field parameter in the tube, e.g., F_{12}. In addition to the magnetic field associated with the current flow, there is the applied field, B_{App} with direction defined by sign of B_{App}. The maximum magnetic fields in the tubes are given by:

$$
\begin{aligned}
B_{T1Max} &= F_{11}I_{T1} + F_{12}I_{T2} + F_{13}I_{T3} + B_{App} \\
B_{T2Max} &= F_{21}I_{T1} + F_{22}I_{T2} + F_{23}I_{T3} + B_{App} \\
B_{T3Max} &= F_{31}I_{T1} + F_{32}I_{T2} + F_{33}I_{T3} + B_{App}
\end{aligned}
\tag{6.19}
$$

It is possible to solve Eq. (6.16) by substituting the RHS of Eq. (6.19) into Eq. (6.18). Rearranging Eq. (6.18) it is written using a matrix of equations:

$$
\begin{pmatrix}
(A_1F_{11}X_1 - 1) & A_1F_{12}X_1 & A_1F_{13}X_1 \\
A_2F_{21}X_1 & (A_2F_{22}X_1 - 1) & A_2F_{23}X_1 \\
A_3F_{31}X_1 & A_3F_{32}X_1 & (A_3F_{33}X_1 - 1) \\
1 & 1 & 1
\end{pmatrix}
\begin{pmatrix}
I_1 \\ I_2 \\ I_3
\end{pmatrix}
$$
$$
=
\begin{pmatrix}
-A_1X_0 - A_1X_1B_{App} \\
-A_2X_0 - A_1X_1B_{App} \\
-A_3X_0 - A_1X_1B_{App} \\
I_T
\end{pmatrix}.
\tag{6.20}
$$

Using Mathematica's [83] linear solver function, the unknowns in the matrix (I_1, I_2, I_3) are eliminated; i.e., I_1 is a function of the spatially dependent magnetic field parameters, tube areas and the magnitude of B_{App}. The spatially dependent magnetic field parameters are input from Table A.12. The transport measurement I_C data of strand DR 4810 is used to define the total current (I_T). The equation is solved using 'NSolve' with values of X_0 and X_1 parameters calculated. Depending on the orientation of the F_L, the magnetic field parameters on the inner side of the strand wound on the barrel ($r < R_{Maj}$) or outer side ($r > R_{Maj}$) are input to calculate the numerical solutions of Eq. (6.20). The Mathematica function 'Reals' calculates the solutions in the real number domain (x∈Reals).

The definition of B_{Max} in Eq. (6.16) is an average value: the product of the maximum magnetic field in each tube and the area of the tube, divided by the total area of the superconducting region:

$$
B_{Max} = (A_1B_{T1Max} + A_2B_{T2Max} + A_3B_{T3Max})/(A_1 + A_2 + A_3).
\tag{6.21}
$$

There are three methods available to solve Eq. (6.20). One method is to fix the geometry (ITER or MST) and the orientation of F_L and vary B_{App}. This method has the advantage of negating any error with the calculation of the matrix element. A second method is to fix the B_{App} and orientation of F_L and vary the geometry. The third method is to fix the geometry and B_{App} and vary the orientation of F_L. Using the number of magnetic-field parameter matrices, several $J_C(B)$ relationships were calculated. The $J_C(B)$ was calculated for the matrices for the different geometries in Table 5.13. The $J_C(B)$ was calculated piecewise, with values of X_0 and X_1 at each B_{App}, F_L and geometry.

6.6.2. Derived $J_C(B)$ Relationships

The value of X_0 = 1.926 and X_1 = -1.1435 for varying the geometry at fixed B_{App}= 0 T results in the distribution of current in the three tubes, for the ITER and MST geometry outlined in Table 6.14. The consistency checks used in the analysis ensure that each of the tube current terms is less than the total current, each current is in the same direction (> 0 A), and the sum of the currents $\equiv I_T$. The highest current is in the central tube, Table 6.14 and is expected due to the lowest $\bar{B}_{Net}$.

The derived $J_C(\bar{B}_{Net})$ values for B_{App}= 0 to 8 T are summarised in Figure 6.29. The straight wire, ring array, and helical geometry matrices have been used as inputs. Initially, a single method was used to solve Eq. (6.20), using the matrix elements calculated for the straight wire array, shown in Figure 6.29 (a). The B_{App} and ITER geometry were fixed, and the only variables were the experimental J_C data for inward and outward F_L. The data does not collapse on to a single curve, with $B < 1.5$ T data oscillating. At B_{App}= 7 T the resultant change in $\bar{B}_{Net}$ results in a smaller difference than the experimental J_C measurement, a change of 38 mT and 3×10^6 A·m^{-2}. For the inward orientation, the self-field correction term varies between 0.433 and 0.491 T·kA^{-1}, and in the outward between 0.573 and 0.628 T·kA^{-1}.

The second data set used in the analysis was the matrix elements for the array of rings. The self-field correction was calculated for both the ITER and MST experimental data. The $J_C(\bar{B}_{Net})$ relationship is plotted in Figure 6.29 (b). Two methods of calculating the parameters in Eq. (6.16) are compared, with the variable being either the orientation of F_L or B_{App}.

Geometry	I_{T1} [kA]	I_{T2} [kA]	I_{T3} [kA]	I_T [kA]
ITER	0.583	0.523	0.478	1.584
MST	0.484	0.408	0.346	1.238

Table 6.14 : Distribution of the current in the three TwT model. B_{App}= 0 T

These two methods of solving Eq. (6.20) produce very similar results for the ITER and MST data. It was not possible to calculate the values for X_0 and X_1 for the outward F_L MST data, as did not converge to a physical solution. The ITER and MST FEA helix matrices were used to calculate the $J_C(\bar{B}_{Net})$ relationship plotted in Figure 6.29 (c). It was not possible to calculate the varied B_{App} curve for the outward F_L MST data, because the results did not converge to a physical solution.

The three self-field corrected ITER inwards F_L data are compared, shown in Figure 6.29 (d). The resultant $J_C(\bar{B}_{Net})$ using the ring array and the helix field values are similar, with the helix J_C slightly higher. The straight wire array is the highest of the three data sets. The $\bar{B}_{Net}$ calculated using the three geometries matrix elements, and two methods of solving for the ITER geometry are similar as shown in Table 6.15.

The $J_C(B)$ calculated using the helix matrix element are compared with the experimental data, shown in Figure 6.30. The experimental data are replotted at the calculated $\bar{B}_{Net}$. In the comparison with the transport measurements, shown in Figure 6.30 (a), it is clear that the measurements in the two geometries are well approximated by a single universal curve. Extrapolation of the $J_C(\bar{B}_{Net})$ data suggest the J_C at $B = 0$ T is actually a factor of five higher than the transport measurement at $B_{App} = 0$ T. These results have not been seen before and therefore are important results. The I_C data for $B = 7$ T is summarised in Table 6.16.

Geometry	Method: Varied	$\bar{B}_{Net}$ [T]	B_{SF} [T·kA^{-1}]
Straight wire	F_L	1.023	0.646
Ring Array	F_L	0.812	0.513
	B_{App}	0.838	0.529
Helix	F_L	0.860	0.543
	B_{App}	0.853	0.539

Table 6.15 : Comparison of analytic method calculation of $\bar{B}_{Net}$ at $B_{App} = 0.0$ T, ITER geometry, inward F_L. Figure 6.29 (d)
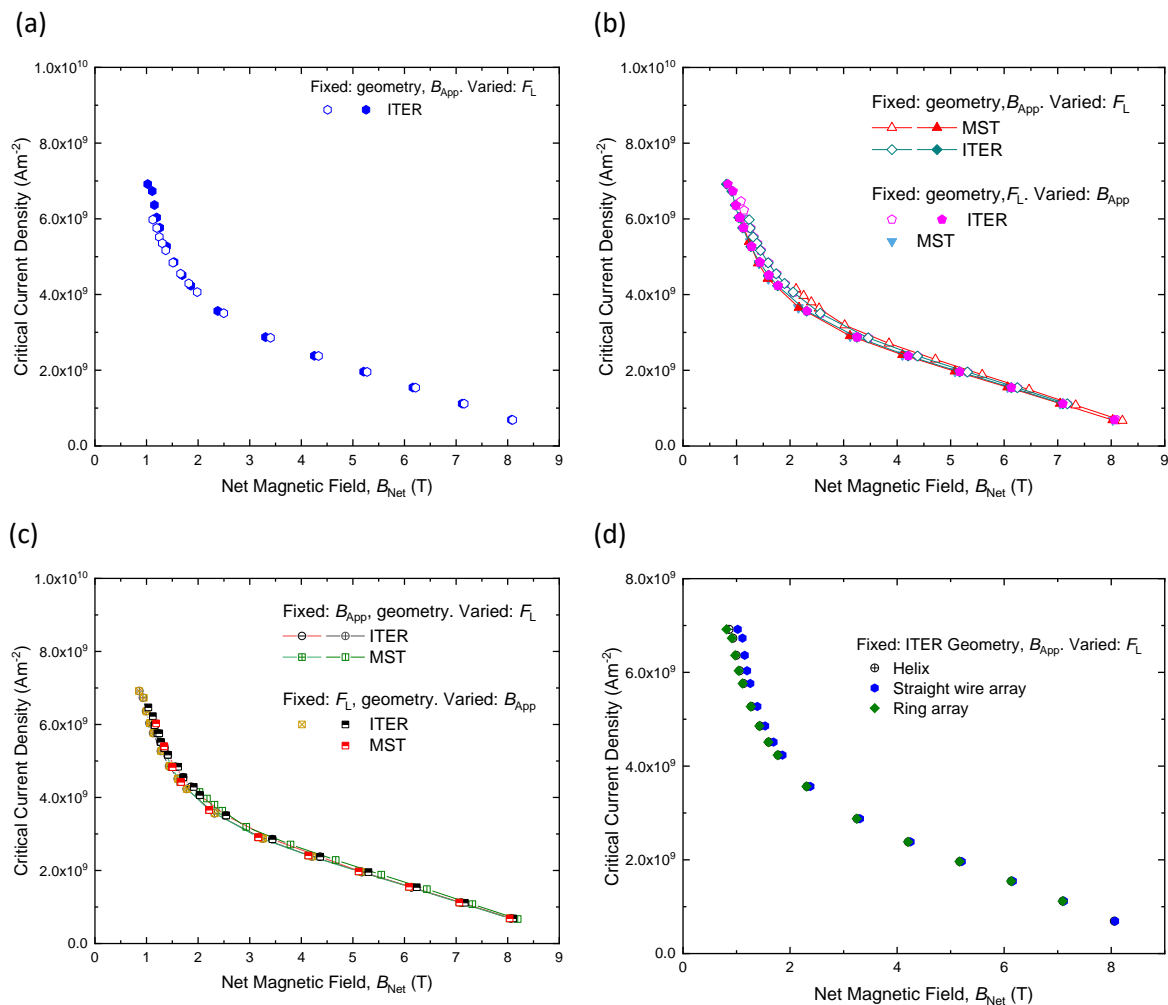
Figure 6.29 : Piecewise $J_C(\bar{B}_{Net})$ relationship calculated using the position-dependent field matrix elements for the approximation of the helical geometry both the ITER and MST data (a) Straight wire array. (b) Ring array (c) 13 turn and 51 turn helix. The $J_C(\bar{B}_{Net})$ are calculated by fixing two parameters and varying the third (ITER or MST geometry, Lorentz fore orientation, Applied magnetic fields). (d) Comparison of three different approaches for the inward Lorentz force ITER geometry J_C data, where the varied F_L method has been used to solve. The ring array data are very similar to the helix data.

Geometry	Method: Varied	I_C [A]	Increase in I_C [%]
Straight wire	F_L	287.9	4.7
Ring Array	F_L	285.5	3.8
	B_{App}	285.6	3.8
Helix	F_L	285.9	4.0
	B_{App}	293.5	6.7

Table 6.16 : Interpolated I_C at B = 7.0T and percentage increase from I_C (B_{App}= 7.0 T) = 275 A ITER geometry, inward F_L. Figure 6.30 (b)
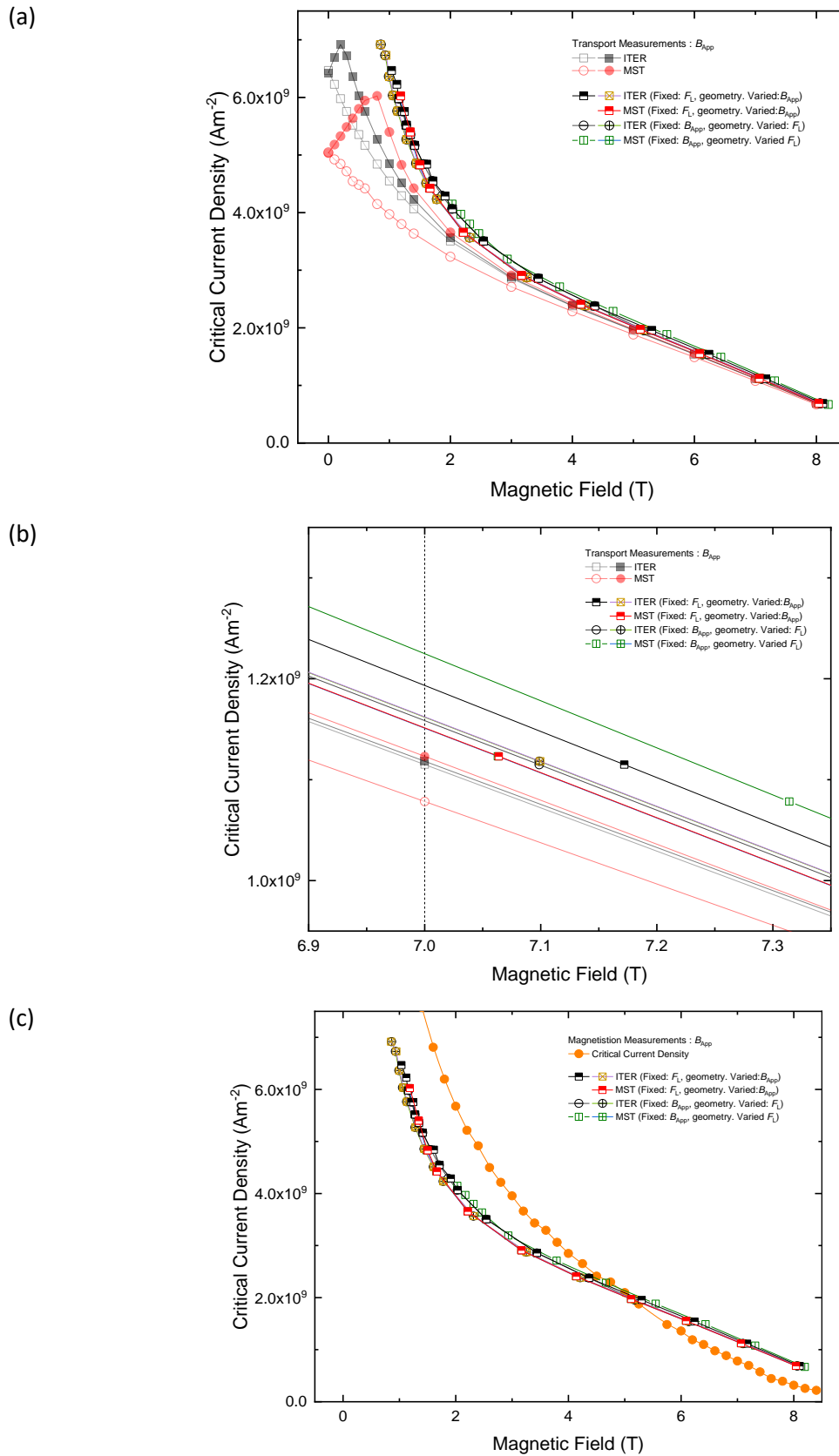
Figure 6.30 : Comparison of the semi-analytic $J_C(\bar{B}_{Net})$ and the experimental data. (a) Transport measurements data for 0 to 8 T (b) Transport measurements data around B = 7 T (c) Magnetisation measurement.

6.7.   Discussion

There are several novel results presented in this chapter. The extensive transport and magnetisation J_C measurements, of the Nb-Ti strands over a range of B_{App} and the two Lorentz force orientations is new information about the strands performance. Due to self-field instabilities at low B_{App}, and the high current requirements, high-quality transport measurements of Nb-Ti strand are unusual at low B_{App}, but have been achieved.

The compilation of the literature self-field corrections highlights the number of self-field corrections that have been attempted. The literature self-field calculations generally consider a fixed current and investigate the relationship between the radius of the strand and the self-field correction. A different approach has been adopted in this work, using two measurement barrels with the same major radius R_{Maj} and a different separation of turns. As the same probe was used and values of B_{App} were fixed, this has the advantage that the variation of the critical current density is only due to the different geometries. At each B_{App} the transport measurement of the same strands in the four configurations results in different J_C values.

In the standard inward F_L measurements the strand is supported by the barrel. Although there was concerns about measuring the strand in the outward Lorentz force measurements, complimentary data was obtained. The data shows a systematically lower J_C for strands measured in the ourward F_L. As the hysteresis measurements demonstrate the strand was not affected by the cycling of the Lorentz force, the differences in J_C can be characterised using the direction of the Lorentz force.

The measurement data demonstrates that the value of J_C at high B_{App} cannot be used to understand the low B_{App} data. At low B_{App}, the peaks in $J_C(B)$ highlight the current densities at which the self-field changes the orientation of the net magnetic field.

When comparing the magnetisation to the transport data, the J_C data at low B_{App} data was higher. The transport critical current measured at B_{App} = 0 T, was 1 600 A, while fits to the magnetisation data suggest at B = 0 T the I_C is between 7 and 12 kA.

The simple method of evaluating the self-field correction by comparison of transport with the magnetisation measurement provides a useful result. The method in section 6.1.4 provides an estimate for the difference in self-field that is due to the geometry. The self-field correction of the two geometries, ITER: 0.63 T·kA^{-1}, and MST: 1.87 T·kA^{-1} is a ratio 1: 2.9.   In work comparing the magnetisation method with transport, the ratio between the magnetisation J_C at low fields

(B_{App}= 0.3 T) and transport J_C (B_{App}=5.0 T) is expected to be about 5 [84]. For the Nb-Ti strands characterised, the ratio is between 6.0 and 6.3.

The work presented in this chapter demonstrates the use of FEA and semi-analytic methods that were implemented to try and understand the effect of self-field. The FEA was unsuccessful in accurately recreating the experimental E-J behaviour because the model was not precise enough to describe the behaviour of a transposed multifilamentary superconductor. Using the FEA method, a $J_C(B_{\text{Net}})$ was not found that could be used to explain the four data sets. The problem of characterising the self-field correction in transport measurement has not been solved. This result is useful, as FEA analysis, or similar (Fortran) has been used to characterise the self-field effect by others previously. Agreement between the different methods does not establish the accuracy or applicability. The ITER geometry was easier to describe with simple analytic methods.

Using the semi-analytic methods, it was possible to account for the two geometries and Lorentz force orientations and generate a piecewise universal $J_C(B)$ curve that converges. The method could be extended to consider an increased number of tubes-within-tubes, and other components of the magnetic field within the cross-section.

The FEA and semi-analytic methods of calculating $J_C(B)$ produce several self-field correction terms that vary both in magnitude and orientation relative to literature values and relationships defined. The analysis in this chapter presents the evidence that the average of the distribution of the magnetic field can be used to calculate a self-field correction that leads to a universal curve for $J_C(B)$. While the analysis focussed on strand DR 4810, the successful method which generates a universal curve should be equally applicable to the other strands.

In the literature, it has been suggested that the only objective statement is that the strand is exposed to a field range [34]. The self-field corrections presented in this chapter suggest that the average value provides a better understanding of the universal $J_C(B)$.

References for chapter 6:

[1]   A. Sanchez and C. Navau, "Critical-current density from magnetization loops of finite high-Tc superconductors," *Superconductor Science and Technology,* vol. 14, p. 4, 2001.

[2]   P. Sunwong, J. S. Higgins, Y. Tsui, M. J. Raine, and D. P. Hampshire, "The critical current density of grain boundary channels in polycrystalline HTS and LTS superconductors in magnetic fields," *Superconductor Science and Technology,* vol. 26, p. 095006, 2013, Art. no. 095006.

[3]   M. Garber, A. K. Ghosh, and W. B. Sampson, "The effect of self field on the critical current determination of multifilamentary superconductors," *IEEE Transactions on Magnetics,* vol. 25, no. 2, pp. 1940-1944, 1989.

[4]   P. Fabbricatore, M. Greco, R. Musenich, S. Farinon, F. Kircher, and B. Cure, "Electrical characterization of S/C conductor for the CMS solenoid," *IEEE Transactions on Applied Superconductivity,* vol. 15, no. 2, pp. 1275-1278, 2005.

[5]   L. D. Cooley, P. S. Chang, and A. K. Ghosh, "Magnetization, RRR and Stability of Nb$_3$Sn Strands With High Sub-Element Number," *IEEE Transactions on Applied Superconductivity,* vol. 17, no. 2, pp. 2706-2709, 2007.

[6]   T. Baumgartner *et al.,* "Evaluation of the Critical Current Density of Multifilamentary Nb$_3$Sn Wires From Magnetization Measurements," *IEEE Transactions on Applied Superconductivity,* vol. 22, no. 3, p. 6000604, 2012, Art. no. 6000604.

[7]   M. Greco, P. Fabbricatore, and R. Musenich, "Critical current measurements on the CMS stabilized conductor," *IEEE Transactions on Applied Superconductivity,* vol. 12, no. 1, pp. 381-384, 2002.

[8]   W. M. de Rapper, "Thermal Stability of Nb$_3$Sn Rutherford Cables for Accelerator Magnets," PhD, Physics, University of Twente, Enschede, the Netherlands, 2014.

[9]   W. M. de Rapper, B. Bordini, S. le Naour, L. Bottura, and H. H. J. ten Kate, "Critical Current in High-J_c Nb$_3$Sn Rutherford Cables Affected Substantially by the Direction of the Applied Magnetic Field," *IEEE Transactions on Applied Superconductivity,* Article; Proceedings Paper vol. 22, no. 3, p. 4, 2012, Art. no. 6001704.

[10]   A. Godeke *et al.,* "A Review of Conductor Performance for the LARP High-Gradient Quadrupole Magnets," *Superconductor Science and Technology,* Article vol. 26, no. 9, p. 15, Sep 2013, Art. no. 095015.

[11]   B. Bordini, "Self-Field Correction in Critical Current Measurements of Superconducting Wires Tested on ITER VAMAS Barrels," in "CERN-ITER Collaboration Report," ITEREDMS Nr: 1105765, 2010.

[12]   A. K. Ghosh, "Effect of Copper Resistivity and Filament Size on the Self-Field Instability of High-J(c) Nb$_3$Sn Strands," *IEEE Transactions on Applied Superconductivity,* vol. 23, no. 3, p. 7, 2013, Art. no. 7100407.

[13]   R. Soika, "Fixture for Short Sample Testing of Modern High Energy Physics Nb3Sn Strands," *AIP Conference Proceedings,* vol. 711, pp. 67-74, 2004.

[14]   A. K. Ghosh, "Effect of Barrel Material on Critical Current Measurements of High-J(c) RRP Nb$_3$Sn Wires," *IEEE Transactions on Applied Superconductivity,* Article vol. 21, no. 3, pp. 2327-2330, Jun 2011.

[15]   T. Boutboul, S. Le Naour, D. Leroy, L. Oberli, and V. Previtali, "Critical current density in superconducting Nb-Tistrands in the 100 mT to 11 T applied field range," *IEEE Transactions on Applied Superconductivity,* Article; Proceedings Paper vol. 16, no. 2, pp. 1184-1187, Jun 2006, Art. no. 1643060.

[16]   L. F. Goodrich and A. N. Srivastava, "II-3: Critical current measurement methods: quantitative evaluation," *Cryogenics,* vol. 35, pp. S19-S23, 1995, Art. no. pp. S19-S23.

[17]   A. Torre, D. Ciazynski, G. Gros, H. Cloez, M. Tena, and R. Goncalves, "A New Experimental Setup to Measure Critical Current in Superconducting Strands Under Periodic Bending," *IEEE Transactions on Applied Superconductivity,* vol. 25, no. 3, pp. 1-5, 2015.

[18]   I. Pong *et al.*, "Current sharing temperature of NbTi SULTAN samples compared to prediction using a single pinning mechanism parametrization for NbTi strand," *Superconductor Science and Technology,* vol. 25, no. 5, p. 054011, 2012, Art. no. 054011.

[19]   M. Lyly, A. Stenvall, and R. Mikkonen, "Validation of Homogenized Filament Bundle Model in AC Loss Computations," *IEEE Transactions on Applied Superconductivity,* vol. 22, no. 3, p. 5, 2012, Art. no. 4705505.

[20]   K. Osamura, *Composite Superconductors* (Applied Physics). New York: M. Dekker, 1994, p. 440.

[21]   M. N. Wilson, *Superconducting Magnets*. Oxford, UK: Oxford University Press, 1986.

[22]   A. Stenvall, M. Siahrang, F. Grilli, and F. Sirois, "Computation of self-field hysteresis losses in conductors with helicoidal structure using a 2D finite element method," *Superconductor Science and Technology,* vol. 26, no. 4, p. 045011, Apr 2013.

[23]   D. Liu, H. Yong, and Y. Zhou, "A 3-D Numerical Model to Estimate the Critical Current in MgB2 Wire and Cable with Twisted Structure," *Journal of Superconductivity and Novel Magnetism,* journal article vol. 30, no. 7, pp. 1757-1765, July 01 2017.

[24]   M. Lyly, A. Stenvall, and R. Mikkonen, "Validation of Homogenized Filament Bundle Model in AC Loss Computations," *IEEE Transactions on Applied Superconductivity,* vol. 22, no. 3, p. 4705505, 2012.

[25]   M. Lyly, V. Zermeno, A. Stenvall, V. Lahtinen, and R. Mikkonen, "Finite Element Simulations of Twisted NbTi Conductors," *IEEE Transactions on Applied Superconductivity,* vol. 23, no. 3, 2013.

[26]   J. L. Duchateau, "New Considerations About Stability Margins of NbTi Cable in Conduit Conductors," *IEEE Transactions on Applied Superconductivity,* vol. 19, no. 2, pp. 55-62, 2009.

[27]   M. Nannini *et al.*, "Characterization of industrial NbTi strands at variable field for JT-60SA toroidal field coils," *Fusion Engineering and Design,* vol. 84, no. 7, pp. 1404-1407, 2009/06/01/ 2009.

[28]   P. Fabbricatore and R. Musenich, B. Seeber, Ed. *Critical current measurements of superconducting cables by the transformer method* (Handbook of Applied Superconductivity). Bristol, UK: IOP Publishing Ltd, 1998.

[29]   P. Fabbricatore, R. Musenich, R. Parodi, S. Pepe, and R. Vaccarone, "Self field effects in the critical current measurements of superconducting wires and cables," *Cryogenics,* vol. 29, no. 9, pp. 920-925, 1989/09/01 1989, Art. no. pp. 920-925.

[30]   M. Greco, P. Fabbricatore, R. Musenich, C. Priano, and F. Kircher, "Self-field effects on critical current measurements of large multi-strand conductors," *IEEE Transactions on Applied Superconductivity,* Article; Proceedings Paper vol. 13, no. 2, pp. 3374-3377, Jun 2003, Art. no. 1212351.

[31]   R. Wesche *et al.*, "Self-field effects in NbTi subsize cable-in-conduit conductors," *Physica C: Superconductivity and its Applications,* vol. 401, no. 1–4, pp. 113-117, 1/15/ 2004.

[32]   A. Nijhuis, H. G. Knoopers, Y. Ilyin, A. Godeke, B. ten Haken, and H. H. J. ten Kate, "Effect of self-field and current non-uniformity on the voltage–temperature characteristic of the ITER central solenoid insert coil by numerical calculations," *Cryogenics,* vol. 42, no. 8, pp. 469-483, 2002/08/01/ 2002.

[33]   T. Boutboul, P. Lezza, and R. Wolf, "Low-current Resistance of Multifilamentary Superconducting Cu/NbTi Strands," in "Accelerators and Storage Rings," CERN2003.

[34]   M. Greco, P. Fabbricatore, S. Farinon, and R. Musenich, "Critical current and n-value modifications from superconducting strands to Rutherford cables," *Physica C: Superconductivity,* vol. 401, no. 1, pp. 124-128, 2004/01/15/ 2004.

[35]   V. Zermeno, F. Sirois, M. Takayasu, M. Vojenciak, A. Kario, and F. Grilli, "A self-consistent model for estimating the critical current of superconducting devices," *Superconductor Science and Technology,* Article vol. 28, no. 8, p. 12, Aug 2015, Art. no. 085004.

[36]   R. Wesche, A. Anghel, B. Stepanov, and P. Bruzzone, "DC performance of subsize NbTi cable-in-conduit conductors," *IEEE Transactions on Applied Superconductivity,* vol. 14, no. 2, pp. 1499-1502, 2004.

[37]   D. M. J. Taylor and D. P. Hampshire, "Properties of helical springs used to measure the axial strain dependence of the critical current density in superconducting wires," *Superconductor Science and Technology,* vol. 18, pp. 356-368, 2005.

[38]   M. C. Jewell *et al.*, "World-Wide Benchmarking of ITER Nb$_3$Sn Strand Test Facilities," *IEEE Transactions on Applied Superconductivity,* vol. 20, no. 3, pp. 1500-1503, Jun 2010.

[39]   A. Godeke *et al.*, "Interlaboratory Comparisons of NbTi Critical Current Measurements," *IEEE Transactions on Applied Superconductivity,* vol. 19, no. 3, pp. 2633-2636, 2009.

[40]   I. Pong *et al.*, "Worldwide Benchmarking of ITER Internal Tin Nb$_3$Sn and NbTi Strands Test Facilities," *IEEE Transactions on Applied Superconductivity,* Article; Proceedings Paper vol. 22, no. 3, p. 4802606, Jun 2012, Art. no. 4802606.

[41]   C. R. Walters, I. M. Davidson, and G. E. Tuck, "Long sample high sensitivity critical current measurements under strain," *Cryogenics,* vol. 26, pp. 406-412, 1986.

[42]   H. Wada, L. F. Goodrich, C. Walters, and K. Tachikawa, "Second intercomparison of critical current measurements," *Cryogenics,* vol. 35, pp. S65-S80, 1995.

[43]   M. T. Naus, R. W. Heussner, A. A. Squitieri, and D. C. Larbalestier, "High field flux pinning and the upper critical field of Nb-Ti superconductors," *IEEE Transactions on Applied Superconductivity,* vol. 7, no. 2, pp. 1122-1125, 1997.

[44]   D. P. Hampshire and D. C. Larbalestier, "The critical current of NbTi multifilamentary wire: a comparison between critical current densities using AC magnetization techniques (JCM) and DC transport measurement (JCT) throughout the superconducting phase," *IEEE Transactions on Magnetics,* vol. 25, no. 2, pp. 1956-1959, 1989.

[45]   Y. V. Karasev *et al.*, "J$_C$(B,T) Characterization of Commercial NbTi Strands for the ITER Poloidal Field Coils by Transport and Magnetization Methods," *IEEE Transactions on Applied Superconductivity,* vol. 23, no. 3, June 2013, Art. no. 6001304.

[46]   L. Muzzi *et al.*, "Test Results of a NbTi Wire for the ITER Poloidal Field Magnets: A Validation of the 2-Pinning Components Model," *IEEE Transactions on Applied Superconductivity,* Article vol. 21, no. 3, pp. 3132-3137, Jun 2011.

[47]   M. A. Green, "Calculating the Jc, B, T Surface for Commercial Niobium Tin Conductors Using a Reduced State Model," in *Advances in Cryogenic Engineering Materials*, vol. 40(An International Cryogenic Materials Conference Publication Springer, 1994, pp. 733-739.

[48]   M. N. Wilson, "Practical Superconducting Materials," in *Superconductor Materials Science: Metallurgy, Fabrication, and Applications*, S. Foner and B. B. Schwartz, Eds. (NATO Advanced Study Institutes, Boston, MA: Springer US, 1981, pp. 63-130.

[49]   J. W. Ekin *et al.*, "Evidence for weak link and anisotropy limitations on the transport critical current in bulk polycrystalline Y$_1$Ba$_2$Cu$_3$O$_x$," *Journal of Applied Physics,* vol. 62, no. 12, pp. 4821-4828, 1987.

[50]   S. Le Naour *et al.*, "Magnetization measurements on LHC superconducting strands," *IEEE Transactions on Applied Superconductivity,* vol. 9, no. 2, pp. 1763-1766, 1999.

[51]   T. Baumgartner, S. Pfeiffer, J. Bernardi, A. Ballarino, and M. Eisterer, "Effects of inhomogeneities on pinning force scaling in Nb$_3$Sn wires," *Superconductor Science and Technology,* 2018.

[52]   A. V. Pan, I. A. Golovchanskiy, and S. A. Fedoseev, "Critical current density: Measurements vs. reality," *Epl,* Article vol. 103, no. 1, p. 5, Jul 2013, Art. no. 17006.

[53]   E. F. Talantsev and J. L. Tallon, "Universal self-field critical current for thin-film superconductors," *Nature,* Article vol. 6, p. 7820, 08/04/online 2015.

[54]   J. W. Ekin, "Relationships between critical current and stress in NbTi," *IEEE Transactions on Magnetics,* vol. 23, no. 2, pp. 1634-1637, 1987, Art. no. 1064844.

[55]   J. W. Ekin, "Strain scaling law for flux pinning in NbTi, Nb_3Sn, Nb-Hf/Cu-Sn-Ga, V_3Ga and Nb_3Ge," *IEEE Transactions on Magnetics,* vol. 17, pp. 658-661, 1981.

[56]   A. Nijhuis *et al.*, "Impact of spatial periodic bending and load cycling on the critical current of a Nb3Sn strand," *Superconductor Science and Technology,* vol. 18, no. 12, pp. S273-S283, 2005/11/04 2005.

[57]   K. P. Jungst, "Anisotropy of pinning forces in NbTi," *IEEE Transactions on Magnetics,* vol. 11, no. 2, pp. 340-343, 1975.

[58]   K. P. Jungst, "Orientation effects on the magnetization of NbTi superconductors," *IEEE Transactions on Magnetics,* vol. 13, no. 1, p. 209, 1977.

[59]   A. Godeke, A. Nijhuis, H. G. Knoopers, B. ten Haken, H. H. J. ten Kate, and P. Bruzzone, "Angular dependence of critical current versus magnetic field in Nb3Sn wires at 9-15T," in *Applied Superconductivity 1997, Vols 1 and 2: Vol 1: Small Scale and Electronic Applications; Vol 2: Large Scale and Power Applications*, H. Rogalla and D. H. A. Blank, Eds. (Institute of Physics Conference Series, no. 158) Bristol: Iop Publishing Ltd, 1997, pp. 917-920.

[60]   L. F. Goodrich and F. R. Fickett, "Critical current measurements: a compendium of experimental results," *Cryogenics,* vol. 22, no. 5, pp. 225-241, 1982.

[61]   M. J. Raine, S. A. Keys, and D. P. Hampshire, *Characterisation of the Transport Critical Current Density for Conductor Applications*. Accepted by Taylor and Francis, 2017.

[62]   M. I. D7177. (2018, 11/07/2018). *Weather Station ID: ICODURHA5*. Available: https://www.wunderground.com/personal-weather-station/dashboard?ID=ICODURHA5#history

[63]   R. D. McCarty and V. D. Arp, "A New Wide Range Equation of State for Helium," in *Advances in Cryogenic Engineering: Part A & B*, R. W. Fast, Ed. Boston, MA: Springer US, 1990, pp. 1465-1475.

[64]   M. S. Lubell, "Empirical scaling formulas for critical current and critical field for commercial NbTi," *IEEE Transactions on Magnetics,* vol. 19, pp. 754-757, 1983.

[65]   L. F. Goodrich, L. T. Medina, and T. C. Stauffer, "Repeatability of critical-current measurements on Nb_3Sn and Nb-Ti wires," *IEEE Transactions on Applied Superconductivity,* Article; Proceedings Paper vol. 7, no. 2, pp. 1508-1511, Jun 1997.

[66]   J. W. Ekin, *Experimental Techniques for Low-Temperature Measurements*. New York: Oxford University Press, 2007.

[67]   L. F. Goodrich and T. C. Stauffer, "Variable-Temperature Critical-Current Measurements on a Nb-Ti Wire," *AIP Conference Proceedings,* vol. 711, no. 1, pp. 338-348, 2004/06/28 2004.

[68]   F. J. Ridgeon, M. J. Raine, M. Lakrimi, A. Thomas, T. Boutboul, and D. P. Hampshire, "Self-field Effects on $J_C(B,T)$ Measurements of Nb-Ti Strands in High Magnetic Fields," *IEEE Transactions on Applied Superconductivity,* 2018.

[69]   L. Bottura, "A practical fit for the critical surface of NbTi," *IEEE Transactions on Applied Superconductivity,* vol. 10, no. 1, pp. 1054-1057, 2000, Art. no. 828413.

[70]   B. Bordini *et al.*, "Extensive Characterization of the 1 mm PIT Nb3Sn Strand for the 13-T FRESCA2 Magnet," *IEEE Transactions on Applied Superconductivity,* Article; Proceedings Paper vol. 22, no. 3, p. 4, Jun 2012, Art. no. 6000304.

[71]   J. W. Ekin, N. Cheggour, L. Goodrich, J. Splett, B. Bordini, and D. Richter, "Unified Scaling Law for flux pinning in practical superconductors: II. Parameter testing, scaling constants, and the Extrapolative Scaling Expression," *Superconductor Science and Technology,* Review vol. 29, no. 12, p. 38, Dec 2016, Art. no. 123002.

[72]   D. M. J. Taylor and D. P. Hampshire, "Relationship between the *n*-value and critical current in Nb_3Sn superconducting wires exhibiting intrinsic and extrinsic behaviour," *Superconductor Science and Technology,* vol. 18, pp. S297-S302, 2005, Art. no. p. S297-S302.

[73]   B. Bordini and L. Rossi, "Self Field Instability in High-J_C Nb_3Sn Strands With High Copper Residual Resistivity Ratio," *IEEE Transactions on Applied Superconductivity,* vol. 19, no. 3, pp. 2470-2476, 2009.

[74] B. Bordini, L. Bottura, L. Oberli, L. Rossi, and E. Takala, "Impact of the Residual Resistivity Ratio on the Stability of Nb₃Sn Magnets," *IEEE Transactions on Applied Superconductivity,* vol. 22, no. 3, p. 4, 2012, Art. no. 4705804.

[75] Q. D. Inc. (2019, 23/11/2096). *Physical Property Measurement System, Quantum Design PPMS®.*

[76] M. J. Raine, "High Field Superconductors for Fusion Energy Applications," Physics, Durham University, 2015.

[77] J. W. Ekin, "Irregularity in Nb-Ti filament area and electric field versus current characteristics," *Cryogenics,* vol. 27, no. 11, pp. 603-607, 1987.

[78] M. Breschi and P. L. Ribani, "Electromagnetic Modeling of the Jacket in Cable-in-Conduit Conductors," *IEEE Transactions on Applied Superconductivity,* vol. 18, no. 1, pp. 18-28, 2008.

[79] P. Gislon, L. Muzzi, S. Chiarelli, A. Di Zenobio, M. V. Ricci, and M. Spadoni, "Electrical characterization of the NbTi strand for the ENEA stability SEx-up experiment," *IEEE Transactions on Applied Superconductivity,* vol. 13, no. 2, pp. 1429-1432, 2003, Art. no. 1211867.

[80] V. M. R. Zermeno, S. Quaiyum, and F. Grilli, "Open-Source Codes for Computing the Critical Current of Superconducting Devices," *IEEE Transactions on Applied Superconductivity,* Article vol. 26, no. 3, p. 7, Apr 2016, Art. no. 4901607.

[81] V. Zermeno, K. Habelok, M. Stepien, and F. Grilli, "A parameter-free method to extract the superconductor's J_c (B , ϑ) field-dependence from in-field current–voltage characteristics of high temperature superconductor tapes," *Superconductor Science and Technology,* vol. 30, no. 3, p. 034001, 2017.

[82] W. A. Fietz, M. R. Beasley, J. Silcox, and W. W. Webb, "Magnetization of Superconducting Nb-25%Zr Wire," *Physical Review,* vol. 136, no. 2A, pp. A335-A345, 10/19/ 1964.

[83] "Mathematica," 11.0.0.0 ed. Champaign, Illinois: Wolfram Research, Inc., 2018.

[84] W. B. Sampson, "Procedures for measuring the electrical properties of superconductors for accelerator magnets," presented at the ICFA Workshop on Superconducting Magnets and Cryogenics, Brookhaven National Laboratory, 1986.

CHAPTER 7

7.   Conclusions and Future Work

7.1.   Conclusions

In the transport measurements and in operation in a superconducting system such as MRI or fusion confinement magnets, current flow generates a magnetic self-field. In order to assess how the magnet system will perform, it is crucial to characterise the strand's critical current density as a function of the net magnetic field, and this requires a quantification of the self-field. The main contributions of this thesis are highlighted below.

An existing transport measurement experimental set-up was modified to increase the current capacity; high currents up to 1 600 A were measured. The hybrid material current lead and the current terminal interfaces design ensured that current transfer to the strand was efficient. The clamping mechanisms ensured that the current contact was reliable. Consistency checks of the $J_C(B)$ data, acquired using the new high-current probe, demonstrated agreement between the new probe and the Durham reference laboratory measurements of the strands.

The superconducting properties of the titanium alloy Ti-6Al-4V (Ti-64) used for standard ITER measurement barrels were characterised. As Ti-64 superconducts an alternative titanium alloy (Ti-6242) with similar physical properties was identified and characterised. The Nb_3Sn strand for the ITER magnet systems is heat-treated on the Ti-64 measurement barrel. To investigate the effect of heat treatment on Ti-64, the alloy was characterised following the bronze route and internal tin heating schedules. Both measurement barrels (in the ITER and MST geometries) were manufactured from Ti-6242 alloys, which remains in the normal state at 4.22 K.

A custom minimum separation of turns (MST) measurement barrel was designed, to investigate how the helical geometry affects the self-field. With an increased density of turns, for the MST barrel, the effect of self-field is larger than in the standard ITER geometry. The barrel was designed to ensure that there were no other differences in the position of the strand when measured.

Transport and magnetisation measurements of three Nb-Ti strands were performed. The dependency of the magnitudes and orientation of self-fields with measurement geometry and current orientation relative to the applied magnetic field was highlighted. The differences in J_C for the variable-temperature measurements, at the benchmarking range of magnetic fields and temperature for strand characterisation, was less than 1% for the opposite orientations of the Lorentz force. Extensive measurements at 4.22 K, over the complete range of magnetic fields, highlighted the large effect of self-field at low B_{App}. Transport measurements were compared with magnetisation measurements of the three strands over the same applied field range and temperatures. The low field magnetisation J_C data demonstrates that the self-field suppresses J_C of the strand and reveal the large uncertainty in the magnetic field measured at with transport measurements.

To calculate the magnetic field distribution in the volume of the strand during the transport measurements, a 3D finite element analysis model using the *H*-formulation in Comsol Multiphysics was developed. The modelling methodology was verified using simpler geometries and analytic solutions. The radial distribution in the self-field was calculated for the experimental helical geometries and analysed. How accurately a straight wire array and a stack of rings described the radial distribution of the magnetic field due to the current flowing helically, was compared with the FEA results for both experimental measurement geometries.

Using experimental data, and literature methods for self-field corrections calculated using simple geometries, it was not possible to generate a universal $J_C(B)$ for the experimental data. It was not possible to describe the experimental data with a helical geometry, with a circular cross-section, where the peak in the z-component of the net magnetic field defines the self-field correction. For the experimental geometry modelled with a helix with a strand with an annular cross-section, magnetic field distributions were calculated. Inputting the experimental $J_C(B)$ data a universal $J_C(B)$ was explored. The superconducting domain resistivity was defined by the maximum value of the magnetic field in the domain, rather than the local value. Partial transposition was modelled by considering the cross-section as tubes-within-tubes, with suitable accuracy and in limited computational time.

With the experimental critical current density data and spatial distribution of the magnetic field from the FEA calculations a semi-analytic, piecewise, linear $J_C(B)$ relationship was derived. Using the matrix elements for the varied geometries, considering the strands cross-section as three tubes-within-tubes, a number of $J_C(B)$ were calculated using the semi-analytic method. The resultant data when replotted resulted in a single curve that described the $J_C(B)$ of the Nb-Ti strand.

7.2.   Future Work

The results of this investigation are promising, with improvements to the FEA model required to converge upon a robust self-field correction. Possible future work, focussing on an improved FEA model, is outlined below.

The properties of the strand were defined with a number of $J_C(B)$ relationships which were simplistic. Several of the bulk room temperature and cryogenic characteristics of the strand were measured, but not incorporated into the FEA models. A higher CnC ratio results in a more stable wire, which was observed experimentally; the transport $J_C(B)$ was only measured at high currents for the strand with the largest CnC ratio. The relationship between self-field instabilities and *RRR* is well documented [1-3] and was not considered as an independent parameter in the model. The field-dependency of the index of transition $n(B)$ was measured and it would be possible to include the $n(B)$ relationship in the definition of $J_C(B)$.

The simplification of the architecture could be addressed with further development of the cross-section. The FEA model is composed of circular components but experimentally the copper can be deformed when wound, resulting in a non-circular cross-section. For the helical FEA models, the number of tubes considered was limited to three. For the helical FEA geometries, three tubes were the limit with the computing resources available. With the radius of the annulus of filament and the filament diameter, it is possible that 26 tubes are required to accurately model the architecture. For the straight wire and ring array, it is possible to use the analytic equations to calculate the field and defining matrices.

The twisted helical geometry was modelled using a mathematical parametrisation in 3D cartesian coordinates. The discretisation of the structure resulted in impractical simulation times. As the models considered do not consider the transposition directly, if it is possible to generate self-field distributions with transposed filaments it would be useful to quantify the effect. In the literature, the helical geometry has been parameterised using the Frenet frame to investigate transposed filaments. Although non-cartesian geometry [4] have been considered in the literature, it was not attempted in this research.

The speed of the solving of the FEA model could be improved. It is typical to define material properties as look-up functions [5], which could reduce computation time, which was investigated but not

implemented. With the complexity of the $J_C(B)$ increased, a linearised power-law could improve the solver speed.

The self-field was not considered in the analysis of the magnetisation $J_C(B)$ data. The measurement geometry is known, and the current flow can be assumed, it is possible to use FEA to calculate the magnetic field distribution. The field distribution in the strand for the magnetisation would be different from the transport measurements, which could verify the argument for the average of the magnitude of the magnetic field. Field distributions and hysteresis behaviour have been modelled for superconducting strips using H-formulation [6].

The analysis of the experimental data assumes an isothermal system, for transport measurements, the heat generated in the transition could affect both the measured n-value and the J_C. The FEA model does not consider $J_C(T)$, which could be added into the definition of resistivity, $\rho(B, T)$. The variable-temperature data could be used to verify the self-field correction. For an accurate self-field correction, the method should be valid for the extended temperature and Lorentz force data set.

The magnetic field in the magnet bore used for the transport measurement is inhomogeneous. The field profile within the magnet is accounted for experimentally, with a smaller correction applied for the MST measurement, due to the reduced z-dimension the strand is measured over. Defining a spatially dependent B_{App} in the FEA calculations could provide useful information.

There are several interesting results presented in this thesis, in addition to the high-quality experimental transport and magnetisation data, a consideration of the experimental set-up and sources of uncertainty. However, the uncertainty due to the effect of self-field was not accurately quantified using the FEA methods.

Since the discovery of the superconductor Nb-Ti, a significant effort by the superconductivity research community has resulted in an increased critical current density of this material. The stable, and cost-effective material has been widely and successfully utilised. In addition to the technology it currently underpins, recent research has outlined the possibility of commercial use of Nb-Ti in H_{98} - factor tokamaks [7]. The data shown in Figure 6.1 outlines the distribution in the size of the effect that is assumed. The possibility of increasing the operational currents of these materials with a thorough understanding of self-field and the understanding of the behaviour of these materials at low applied fields is of interest to magnet designers.

References for chapter 7:

[1]   B. Bordini and L. Rossi, "Self Field Instability in High-J_C Nb$_3$Sn Strands With High Copper Residual Resistivity Ratio," *IEEE Transactions on Applied Superconductivity,* vol. 19, no. 3, pp. 2470-2476, 2009.

[2]   B. Bordini, L. Bottura, L. Oberli, L. Rossi, and E. Takala, "Impact of the Residual Resistivity Ratio on the Stability of Nb$_3$Sn Magnets," *IEEE Transactions on Applied Superconductivity,* vol. 22, no. 3, p. 4, 2012, Art. no. 4705804.

[3]   A. K. Ghosh, "Effect of Copper Resistivity and Filament Size on the Self-Field Instability of High-J(c) Nb$_3$Sn Strands," *IEEE Transactions on Applied Superconductivity,* vol. 23, no. 3, p. 7, 2013, Art. no. 7100407.

[4]   M. Lyly *et al.*, "Suitability of Bundle Approximation in AC Loss Analysis of NbTi Wires: Simulations and Experiment," *IEEE Transactions on Applied Superconductivity,* vol. 25, no. 3, pp. 1-5, 2015.

[5]   *Comsol Multiphysics Reference Guide* (Comsol Ltd). Cambridge, 2015.

[6]   G. Iannone, S. Farinon, G. D. Marzi, P. Fabbricatore, and U. Gambardella, "Modeling Experimental Magnetization Cycles of Thin Superconducting Strips by Finite-Element Simulations," *IEEE Transactions on Applied Superconductivity,* vol. 25, no. 1, pp. 1-7, 2015.

[7]   S. B. L. Chislett-McDonald, E. Surrey, and D. P. Hampshire, "Could High H98-Factor Commercial Tokamak Power Plants Use Nb–Ti Toroidal Field Coils?," *IEEE Transactions on Applied Superconductivity,* vol. 29, no. 5, pp. 1-5, 2019.

A.   Appendix

A.1.   Nb-Ti strands Properties

The material and physical properties of the strands characterised in this work are outlined in this section. The data was provided by Dr Mark J Raine [1].

The diameter of the strand is required to be 0.730 ± 0.005 mm. The strand is measured using a Scantron dual-axis laser micrometre, with an uncertainty of 0.1 µm. The values for the strand are summarised in Table A.1. The twist pitch of the strand is required to be 15 ± 2 mm. The twist pitch is obtained by measuring the angle of the filaments and the diameter using visual inspection under a microscope [2]. The strands characterised are within requirements, reported in Table A.1.

The Cu to non-Cu Ratio (CnC) of the strand is required to between 1.55 to 1.75. The CnC was calculated using the change in the mass of the strand before and after the copper matrix was etched, a volumetric ratio and the density of copper [2]. The CnC of the strands characterised in this work are outlined in Table A.1. All three strands are within the required specifications for ITER. The nickel plating of the strand is required to between 1 to 2 mm. The nickel plating is measured using a Couloscope®, a commercially available machine produced by Fischer that use electrochemical analysis method to determine the thickness of metal coatings. The strands characterised are within requirements, reported in Table A.1.

The residual resistivity ratio (RRR) of the strands is required to be >100. The *RRR* is measured using the standard *V-I* measurements using the Quantum Design Physical Properties Measurement System (PPMS). The values measured are within requirements, reported in Table A.1.

Strand ID	Diameter [mm]	Twist Direction	Twist pitch [mm]	CnC Ratio	Ni-plating thickness [µm]	*RRR* ($\rho_{273\,K} / \rho_{10\,K}$)
DR 4810	0.736 ± 0.001	RH	14	1.68 ± 0.03 : 1	1.8	123
DR 5049	0.733 ± 0.001	RH	14	1.58 ± 0.03: 1	1.5	127
DR 5534	0.732 ± 0.001	RH	16	1.67± 0.03 : 1	1.6	112

Table A.1 : Properties of the Nb-Ti strands measured in this work. Data provided by Dr Mark J Raine. RH: Right hand

A.2.   Experimental Set-up

The details in this section are additional information not included in chapter 3, and provide a useful reference if interested in repeating the experiment in the Durham magnet system.

To enable machining of the different twist pitches, an outer diameter of 32 mm on the ITER barrel shown in Figure A.1(a), and 31 mm on the MST barrel [Figure A.1(b)].

The probe head and tubing are manufactured from 316 L stainless steel. The top half of the internal current leads have a rectangular cross-section that is 15 × 6 mm The Tufnol reinforcing structures (25 × 16 mm) are attached along the length of the current leads and separate the two leads to prevent electrical shorting shown in Figure A.2 (a). The current leads are insulated using Kapton tape along the length. The tubing, shown in Figure A.2 (b) is shortened from the original JLab design to the length of 500 mm to attach the newly designed bottom of the probe. The tubing has an internal diameter of 36 mm and an outer diameter of 38 mm to fit through the Dewar opening.

The depth of the probe into the magnet can be adjusted by raising or lowering the adjustable platform which it rests on ensuring that the strand is measured in the most homogenous region of the magnet. The centre of the barrel is positioned in the diameter sphere volume (DSV) to ensure, the homogeneity of the magnetic field. To fix the barrel vertically, the length of the probe is specified, for details see Table A.2. When the probe is in the magnet, the vertical position is fixed by clamping the probe to the adjustable platform.

Component	Description	Dimension [mm]
Wooden support	Total length	150.0
Platform	Height from top of magnet Dewar	217.1
Barrel	Half of total height	25.5
Magnet	Dewar to the centre of the magnetic field	1197.4
Internal current leads	Bottom of the probe can to bottom	1590.0

Table A.2 : Components, relationship with respect to the probe in the magnet, and relevant dimensions.

(a)   (b)
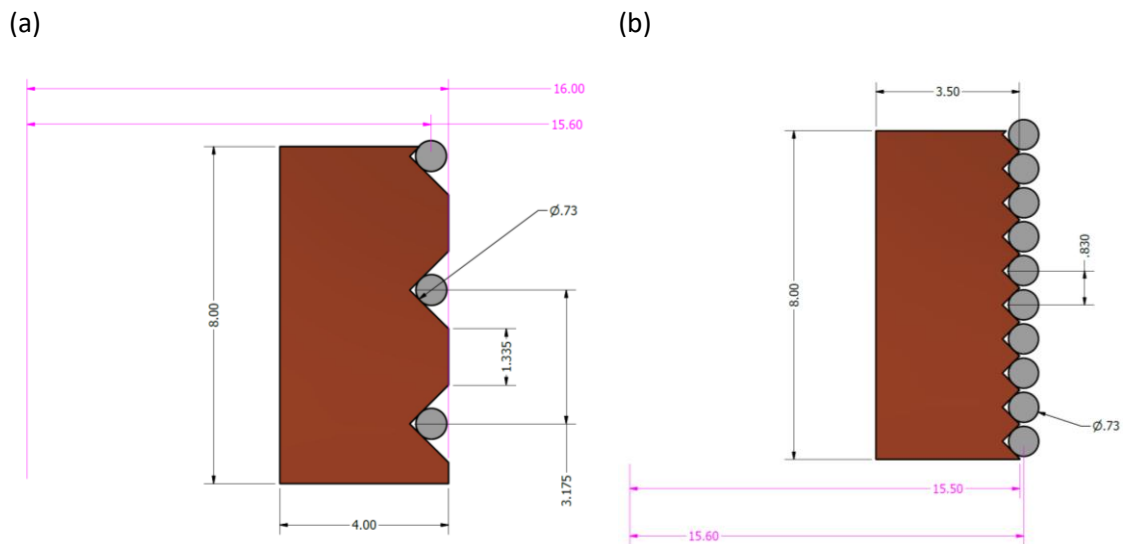
Figure A.1 : Comparison of the strand's position in the OFHC copper rings groove for the two barrel designs. (a) ITER (b) minimum separation of turns (MST). The vertical dashed line is the centre of the helix. [mm].

(a)   (b)

Tufnol reinforcing structure (25 × 16)
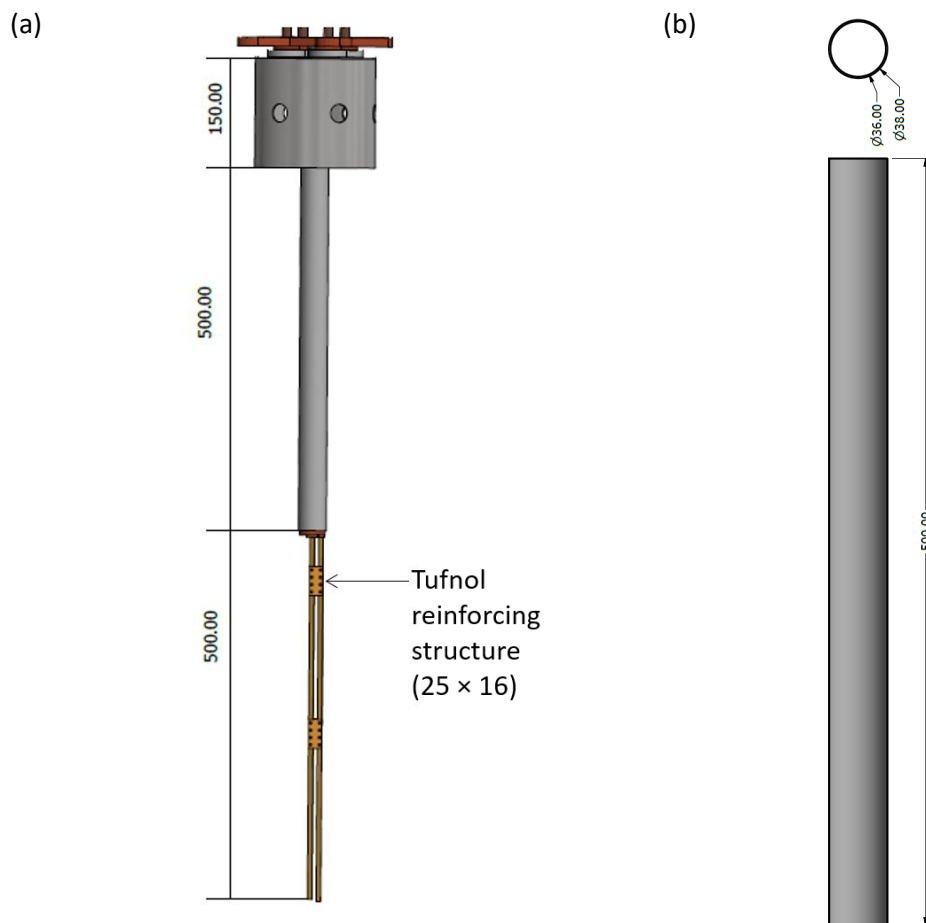
Figure A.2 : (a) Technical drawing of the top part of the probe assembly head and the top half of the internal current leads. (b) Stainless steel tubing which is hard-soldered to the bottom of the probe head can.

The technical drawing of the probe head and internal components is shown in Figure A.3. The internal structure, Figure A.3 (a) shows the four external current contacts. The individual external current contact, Figure A.3 (b), are manufactured with both insulating and conducting components. The probe head current terminals to the external transport current source, Figure A.3 (c), is attached to the internal current contacts. The assembly is fitted inside of the probe can, Figure A.3 (d). The insulating components in the assembly are manufactured from Macor – a machineable glass-ceramic – which provides thermal insulation and performs well at high temperatures [3].

To ensure reliable current transfer from the current leads to the strand, a clamping mechanism was developed. The clamping mechanism was manufactured from 316 L stainless steel. Technical drawings for the four components, shown in Figure A.4 (a-d). Figure A.4 (a) is the bottom stainless steel part, which is hard-soldered {using Silver-flo^{TM} 55 [$Ag_{55}Cu_{21}Zn_{22}Sn_2$ (wt %)]} to the bottom current terminal to the barrel. The large hole allows for helium flow. The top clamping mechanism, Figure A.4 (b), is a 5 mm thick stainless steel component has 8 tapped holes for M2.5 screws. The screws are tightened to distribute the pressure on the top copper terminal to the barrel. The brace, Figure A.4 (c) is hard soldered to part (a). The titanium spacer, Figure A.4 (d), is insulated with Kapton polyimide tape. The stainless-steel clamp is pushed against the stainless-steel brace and screwed into the titanium alloy spacer. The clamping mechanism assembly, Figure A.4 (e), without the measurement barrel and the current terminals to aid interpretation.

Differences in the position of the strand in the magnet with respect to the field calibration position can cause systematic errors [4]. To ensure the centralisation of the probe radially, a cotton textile-phenolic resin (Tufnol) centring guide was designed and used (Figure A.5). A 5 mm hole is incorporated for helium flow and aligns with a hole in the bottom current terminal to the barrel. The maximum diameter of the guide is 38 mm; this ensures that the probe cannot move laterally. The large opening in the structure ensures helium can flow through the probe. The M2 clearance holes are for attaching a guide to the bottom of the probe.

(a)

(b)

Ø165,00

Ø105,00

Ø44,00

Ø38,00

50.80

35.00

5.00

10.00

2.00

18.00

5.00

12.00

30.00

34.00

Copper Connector

Stainless Steel Fitting Top

Macor

Stainless Steel Spacer

Macor Washer

Copper Connector

(c)

(d)

Ø32.00

61.25

38.26

M10 Clearance

M6 Clearance

Ø32.00

12.00

Ø165,00

Ø141,00

Ports for
(i) Bubblers
(ii) Blanking

150,00
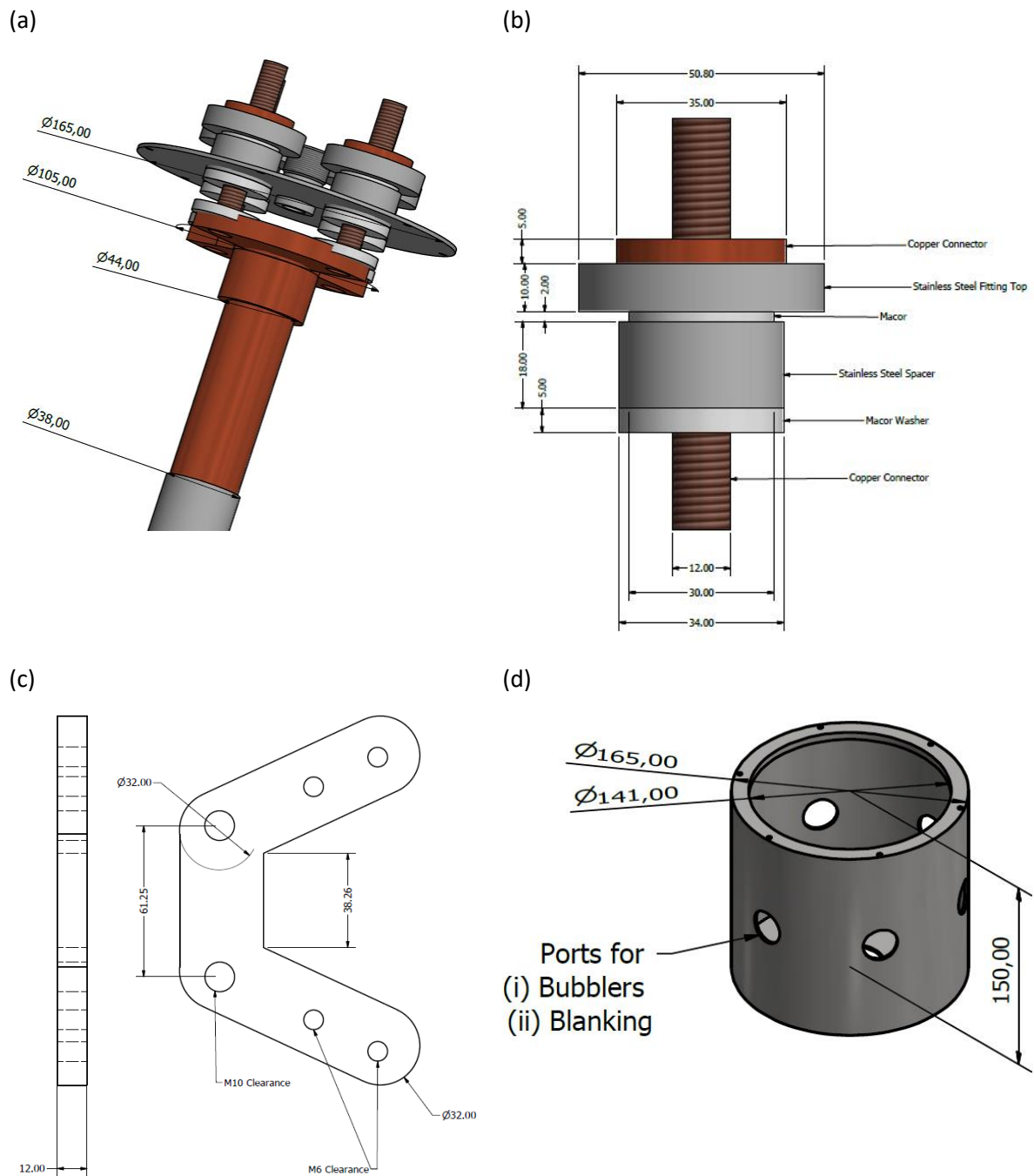
Figure A.3 :Probe head assembly drawings: (a) Internal components of the probe head and the top plate. (b) One of the four current connectors inside the probe head. (c) The probe head current contacts manufactured from OFHC copper. [mm] (d) The stainless steel can of the probe which is soldered to the stainless-steel tube. Bubblers and blanking plates are connected to the ports.

(a)

(b)

(c)   (d)   (e)
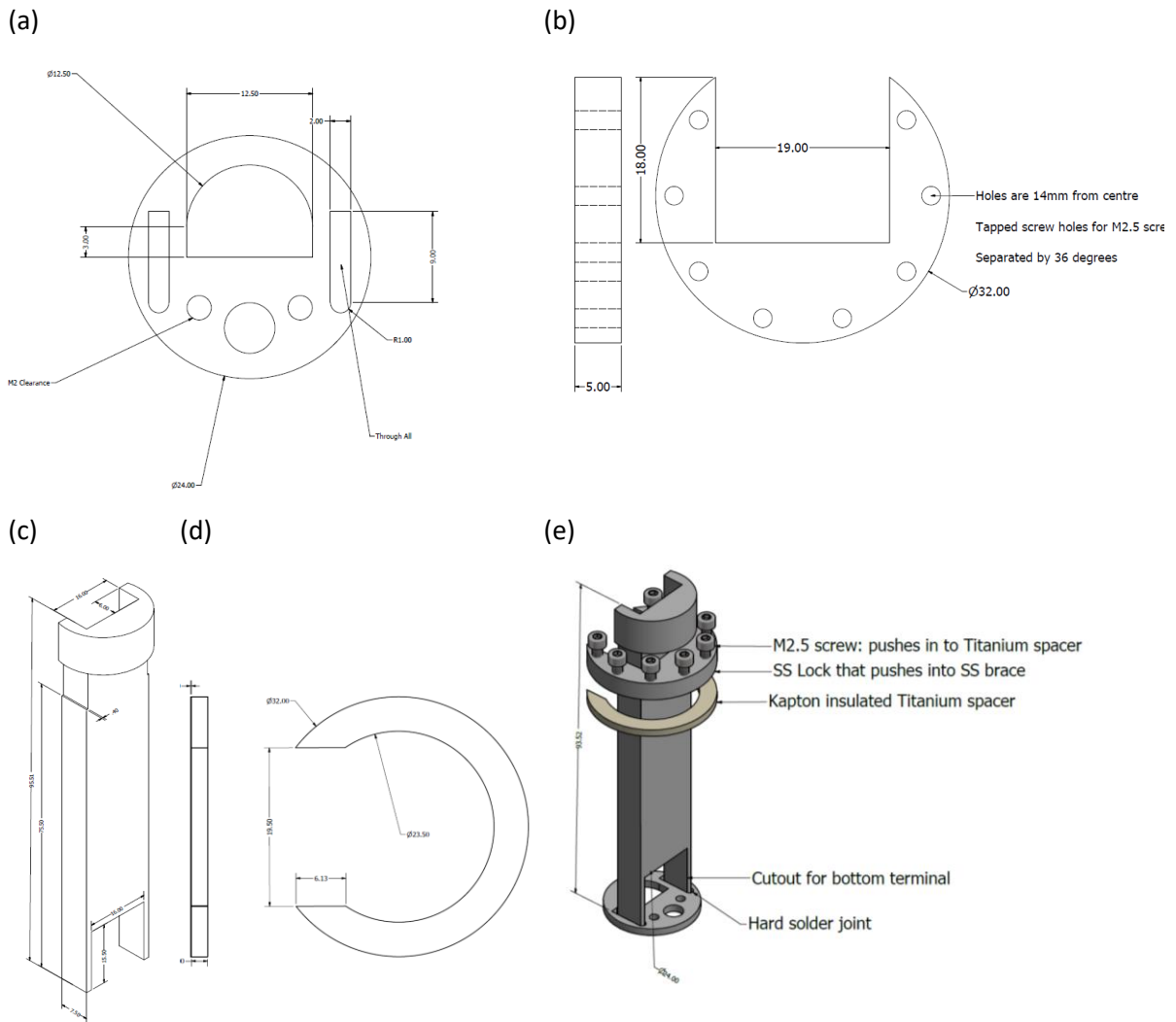
Figure A.4 : Drawings of the components in the measurement barrel clamping mechanism (a) Stainless steel plate (b) Stainless steel clamping mechanism (c) Stainless steel brace (d) Kapton insulated titanium spacer (e) Assembled clamping mechanism. [mm]
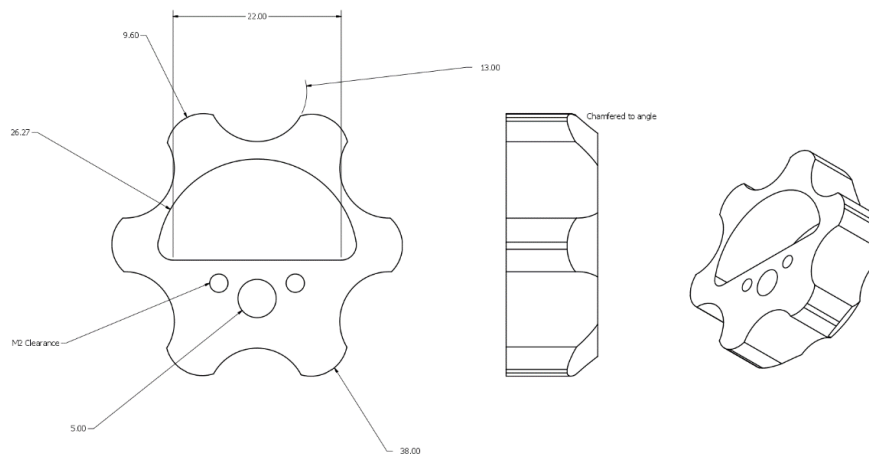
Figure A.5 : Drawing of the Tufnol centring guide. The M2 clearance is for screwing to the bottom terminal. The large gaps are to enable maximum helium flow. [mm]

A.3.   Finite Element Analysis

In this section the broad approach to calculating magnetic field distributions using a commercial finite element analysis (FEA) package is outlined. In this thesis, Comsol Multiphysics [5] has been used. The approach detailed is specific to the modelling of high-field application Nb-Ti strands [6] which consist of thousands of superconducting filaments embedded in a copper matrix. The strand is wound helically for transport measurements. One conclusion of this thesis is that it is simply not possible to model the exact structure and architectural details of the strand of the transport measurement. It is necessary to use a simplified structure, that captures the essential science, which can be solved using state of the art computers in a reasonable timeframe.

In the applied superconductivity literature, numerical models have typically been performed at two length scales. *Macroscopic* models use Ginzburg-Landau theory, where the wave function defines the superconducting properties. Time-dependent Ginzburg-Landau models can be implemented using finite difference methods [7, 8]. *Bulk* models use experimentally measured superconducting properties and are implemented with FEA, and/or boundary element methods. Using FEA, it is possible to calculate magnetic fields due to current flow in complex geometries. FEA models of superconducting systems are used to calculate magnetic and electric fields, AC losses, and thermal loads. Significant research is being undertaken to design and optimise high-temperature superconductor (HTS) devices, where electromagnetic modelling is key [9].

FEA is a numerical modelling technique that takes a complex object and discretises the object into small elements. The partial differential equations (PDE) used are reduced to linear algebraic equations, with solutions approximating the unknown potentials. The modelling of superconductors is difficult due to their complex thermal and electromagnetic behaviour. There can be rapid variations in the superconducting state, with quickly changing dynamics. In the region around the sharp transition [10], the non-linearity between superconducting and normal state is computationally heavy. When discretising large geometries (or geometries with high aspect ratios), investigating an extensive number of parameters, or calculating fine details, computation time can be extremely long. Simple models are built to investigate the method of implementation, (e.g., a parameter, or an aspect of the pre-processing) and ideally a rapid solution provides feedback for model development. One difficulty when using the *H*-formulation in Comsol was that these simple models can take days to converge on a solution.

To calculate the magnetic field distribution using FEA, there is a standard workflow that has been followed. The first step is pre-processing, where the problem is specified, and meshes are generated.

The formulation of equations is implemented in the constructed geometry and the bulk properties (electrical, magnetic) in each domain are defined. On the surfaces, internal and external, boundary conditions are defined. The next step is processing, where the problem is solved, the final step is post-processing, where the solutions are visualised, and the data analysed.

A.3.1. Partial Differential Equations (PDEs)

Superconductor models are implemented using Maxwell's equations in PDE form. The general form of PDE for a single dependent variable u is defined,

$$e_a \frac{\partial^2 u}{\partial t^2} + d_a \frac{\partial u}{\partial t} + \nabla \cdot \mathbf{\Gamma} = f.$$

(A.1)

The first step involves defining both the number of dependent variables (u) and the dimension (0D - 4D). For the *H*-formulation, the dependent variable is the magnetic field *H* (A·m⁻¹), the conservative flux vector Γ is the electric field term (V·m⁻¹). For the 3D *H*-formulation calculations, the source term f (scalar) is defined as zero.

A.3.1.1.   Governing Equations
The equations used to model electromagnetic behaviour are Maxwell's four equations. The first two Gauss's law Eq. (A.2) and Gauss's divergence law Eq. (A.3) written in the differential form:

$$\nabla \cdot \mathbf{E} = \rho/\epsilon_0,$$

(A.2)

$$\nabla \cdot \mathbf{B} = 0.$$

(A.3)

Where ϵ_0 is the vacuum permittivity. The third is the Maxwell-Faraday equation Eq. (A.4) that states the curl of the electric field is related to a change in the magnetic field with time. The fourth is Ampère's Maxwell law Eq. (A.5) that states the curl of the magnetic field is proportional to the electric current plus a displacement current density.

$$\nabla \times \mathbf{E} = -\frac{\partial \mathbf{B}}{\partial t}.$$

(A.4)

$$\nabla \times \mathbf{B} = \mu_0 \mathbf{J} + \mu_0 \epsilon_0 \frac{\partial \mathbf{E}}{\partial t}.$$

(A.5)

When implementing the FEA model, the displacement current term in Eq. (A.5) is neglected i.e., $(\partial \boldsymbol{E})/\partial t = 0$ [11]. The assumption of relatively low excitation frequencies leads to the quasi-static situation. Like other models of bulk superconducting systems, the electromagnetic radiation is neglected.

The constitutive relationship between the magnetic flux density, $\boldsymbol{B}$ and the magnetic field strength $\boldsymbol{H}$ is defined using the relative permeability μ_r as follows:

$$\boldsymbol{B} = \mu_0 \mu_r \, \boldsymbol{H}. \tag{A.6}$$

When modelling low-temperature superconductor (LTS) materials, with non-magnetic materials in the composite, $\mu_r = 1$ is used. In the literature, when modelling composites with magnetic materials, e.g., second-generation HTS tapes with magnetic coatings, $\mu_r \neq 1$ is used and hysteresis effects are included to accurately describe the material [12].

The other constitutive relationship, central to this thesis, is the generalised Ohm's law. The relationship between the electric field $\boldsymbol{E}$ and the current density $\boldsymbol{J}$:

$$\boldsymbol{E} = \rho \, \boldsymbol{J}. \tag{A.7}$$

The normal conducting domains in the models are implemented using resistivity $\rho = \rho_N$. To account for the non-linear resistivity of the superconducting domains, $\rho_{\mathbf{sc}}$ is defined,

$$\rho_{\mathbf{sc}}(B, n) = \frac{E_{\mathrm{C}}}{J_{\mathrm{C}}(B)} \left(\frac{J}{J_{\mathrm{C}}(B)} \right)^{(n-1)} \tag{A.8}$$

where Eq. (A.8) is a modified version of the often used power-law model [13], a form of Eq. (2.16) written in terms of Ohm's law.

A.3.1.2.   Formulations of Maxwell's Equations

The formulations of Maxwell's equations are summarised in Table A.3. The four formulations can be grouped into two pairs. *A-V* and *E* define conductivity in terms of the electric field [14] while T-Ω and *H* use the resistivity as a function of the current density. The *A-V* formulation is widely used to solve steady-state problems [15-20]. The A-V formulation is only useful for constant conductivity. For the superconducting domains with a magnetic-field-dependent resistivity, using *A-V* formulation means the current is circularly defined, it is, therefore, necessary to use the *H*-formulation.

Formulation	Constitutive equations	Definitions
Vector and Scalar potential *A-V*	$$\nabla^2 \boldsymbol{A} = \mu\sigma\left(\frac{\partial \boldsymbol{A}}{\partial t} + \nabla V\right)$$ $$\nabla \cdot \left(\frac{\partial \boldsymbol{A}}{\partial t} + \sigma\nabla V\right) = 0$$	$$\mathbf{B} = \nabla \times \mathbf{A}$$ $$\boldsymbol{E} = -\frac{\partial \boldsymbol{A}}{\partial t} - \nabla V$$ $$\sigma = \sigma(E)$$
E-Field	$$\nabla \times \nabla \times \mathbf{E} = -\mu\frac{\partial(\sigma\mathbf{E})}{\partial t}$$	$$\sigma = \sigma(E)$$ $$\nabla \times \mathbf{E} = -\frac{\partial \boldsymbol{B}}{\partial t}$$
Current Potential **T**-Ω	$$\nabla \times (\rho\nabla \times \mathbf{T}) = -\mu(\dot{\mathbf{T}} - \nabla\dot{\Omega})$$ $$\nabla^2\Omega = 0$$	$$\boldsymbol{J} = \nabla \times \mathbf{T}$$ $$\boldsymbol{H} = T - \nabla\Omega$$ $$\rho = \rho(J)$$
H-field	$$\nabla \times \rho\nabla \times \mathbf{H} = -\mu\frac{\partial \boldsymbol{H}}{\partial t}$$	$$\boldsymbol{J} = \nabla \times \mathbf{H}$$ $$\rho = \rho(J)$$

Table A.3 : Summary of formulations for modelling superconductors. Modified from Ref. [21]

The **T**-Ω formulation uses a vector potential $\boldsymbol{T}$ which is defined to satisfy the equation $\boldsymbol{J} = \nabla \times \boldsymbol{T}$. The scalar magnetic potential Ω is defined as $\boldsymbol{H} = \boldsymbol{T} - \nabla\Omega$ [22-24]. The initial condition $\nabla \cdot [\mu(\mathbf{T} - \nabla\Omega)] = 0$ is required to impose Gauss' law. There are three unknowns per node. For systems without ferromagnetic materials, the **T**-Ω formulation is reduced to *H*-formulation, as Ω is zero throughout the domain. The state variable in the *H*-formulation is the magnetic field, and it is solved for directly. When implemented using the finite difference methods the *E*-field formulation is numerically more efficient than the *H*-formulation [25]. One problem associated with using the *E*-field formulation is the calculation of the current density [26]. Another problem with the *E*-Field method is the numerical inaccuracies when taking the curl of the magnetisation function.

A.3.1.3.   Boundary Conditions and Constraints

Boundary conditions (BC) are essential to construct a model, specifying the solutions the dependent variable can take on that boundary. Whole functions are used as boundary conditions. There are two types of BC. The Dirichlet BC [19] is usually a mathematical constraint on a dependent variable whereas the Neumann BC which is usually a constraint on the flux through a boundary.

The generalised form of the Neumann domain boundary is defined

$$-\boldsymbol{n} \cdot \boldsymbol{\Gamma} = g - qu + h^T \mu \tag{A.9}$$

where $\boldsymbol{n}$ is the outward unit normal vector on the surface $d\Omega$. The variables g, q, are user-defined coefficients. An essential boundary condition is used if the boundary is insulated or has a fixed value r. The dependent variable is fixed as:

$$u = r. \tag{A.10}$$

The default zero-flux boundary condition prescribes zero-flux insulation across the boundary, the divergence of the dependent variable is u zero

$$\boldsymbol{n} \cdot \boldsymbol{\Gamma} = 0. \tag{A.11}$$

In this thesis, zero flux boundary conditions are often used on the boundaries of the air domain and non-zero boundary conditions are used to define the current into the superconducting system. With an applied magnetic field it is important to ensure that the correct components are continuous across a boundary. If the magnetic field at internal boundaries, in the tubes-within-tubes cross-section, is fixed the assembly of equations is ill-defined, and the FEA calculation does not converge on a solution.

A.3.2. Methodology

Comsol was the FEA software used during this thesis. Comsol is known for being easy to understand and has a user-friendly graphic interface [27]. Researchers at various institutes have established a superconductivity model workgroup [28] which is used as a reference and resource. For a complete description of the Comsol see the reference guide [5].

A.3.2.1.   Problem Specification

The experimental geometry, the Nb-Ti strand's dimensions, the measurement barrel, and the design of the transport measurements, specify the problem. The other dimensions of the computational model are reported in Table A.4. The system modelled contains a conducting domain, Ω_C where current flows and a non-conducting air domain Ω_N. Figure A.6 is a schematic of the modelling system. A common standard that is implemented is that the air domain is ten times the volume of the superconducting domain, allowing numerical errors to dissipate [29].
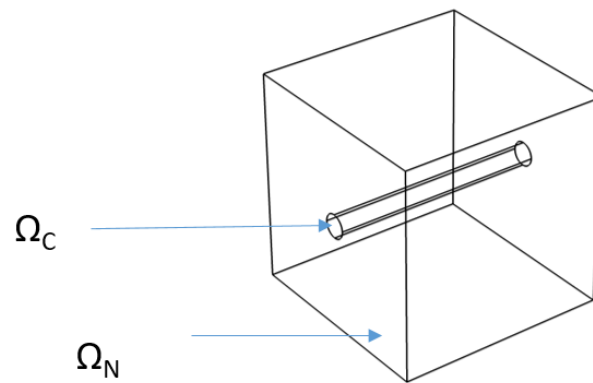
Figure A.6 : FEA modelling domain structure. The conducting region Ω_C extends to the ends of the insulating air region Ω_N.

Variable	Dimension	Volume [mm^3]	Mesh Elements
Extrude length	0.30 x 80 [mm]	36.5	6,045
Large air domain	160 x 160 x 160 [mm^3]	4.096 x10^6	12,194
Small air domain (around central helix volume)	ITER: 3 x 3 x 3 [mm^3] MST: 1 x 1 x 0.830 [mm^3]	ITER: 27 MST: 0.83	174,151

Table A.4 : Geometry of the modelling domains implemented in meshing the ITER and MST helices. The mesh is subdivided, with the small air domain having the highest density mesh.

The air domain has been defined with a finite, non-zero value of resistivity, which is typical in the community. Finite values are used to avoid singularities in the system of equations. FEA models where ρ_{Air} = 0 Ωm have been presented [30]. The current flow should not occur in the air, a robust standard for the non-finite conductivity of air has not yet been defined. The leakage of currents can be minimised by increasing the resistivity of the air [31]. A range of values has been used in the literature for the air's resistivity, with very low 1 x 10^{-8} [31], 1 x 10^{-6} Ωm [11], to very high 2 x 10^{14} Ωm [23]. In the models used in this thesis, ρ_{Air} = 1 Ωm.

A.3.2.2.   *A-V* formulation in Comsol

Magnetic field calculations using the *A-V* formulation with an applied magnetic field can be performed using the Comsol AC-DC magnetic field module. The steady-state solutions are generated quickly, depending on the meshes and error tolerances. Using the pre-defined algorithms, it was possible to generate highly efficient meshes. Implementing magnetic-field dependent parameters, using the *A-V* formulation was unsuccessful, as it resulted in a circular dependency. It is not possible to implement the field-dependency of the resistivity or investigate time-dependent using the *A-V* formulation, and so was of limited use in the analysis .
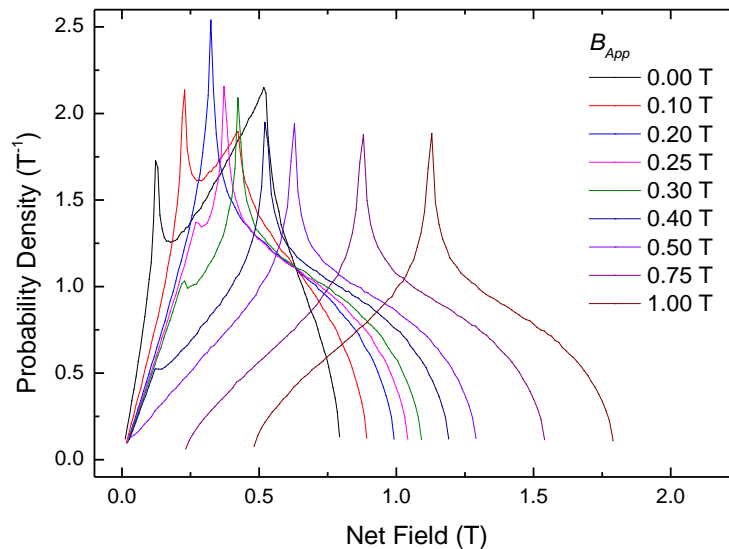
Figure A.7 : Probability density distribution with a varied applied magnetic field. The *A-V* formulation ITER geometry (11 turns, solid cross-section).

The results of the *A-V* calculations were of limited use to modelling the experiment as the redistribution of current whilst it is being ramped was the focus for analysis. Calculations of the field distributions as a function of the net magnetic field, for a helix with the circular cross-section, is shown in Figure A.7.

A.3.2.3.   *H*-formulation in Comsol

Using the *H*-formulation is time-intensive, both in computational time and when implementing and verifying new features [32]. The *H*-formulation enables the superconductors' non-linear resistivity relationship, to be modelled. At each instance, the magnetic field due to the current flow from the entire system is used in calculating the resistivity of each part of the superconducting domain. Using Ohm's law, the electric field can be calculated and *E-J* traces that can be compared to experimental results are produced.

For a 3D model, the state variable (u) in the PDE is the three Cartesian independent magnetic field components:

$$u = \begin{bmatrix} H_x \\ H_y \\ H_z \end{bmatrix} \tag{A.12}$$

For calculations in an applied magnetic field, the variable H_z is modified.

Assuming an isotropic magnetic field in the z-direction, the z-component of the magnetic field is rewritten as:

$$H_z{}^* = H_z + H_{\mathrm{App,z}}. \tag{A.13}$$

By substituting Ohms law, and the simplified Maxwell-Ampère's law (relating $\boldsymbol{H}$ and $\boldsymbol{J}$), the Maxwell-Faraday equation law is defined:

$$\left(\boldsymbol{\nabla} \times (\rho \boldsymbol{\nabla} \times H)\right) = \left(-\frac{\partial(\mu_0 H)}{\partial t}\right). \tag{A.14}$$

As this equation is over-constrained, the divergence is taken

$$\boldsymbol{\nabla} \cdot \left(\boldsymbol{\nabla} \times (\rho \boldsymbol{\nabla} \times H)\right) = \nabla \cdot \left(-\frac{\partial(\mu_0 H)}{\partial t}\right). \tag{A.15}$$

The second-order differential operator $(\boldsymbol{\nabla} \times \boldsymbol{\nabla} \times)$ can result in ill-conditioned matrices. When the divergence of the curl is set equal to zero, Eq. (A.15) is rewritten as

$$\mu_0 \frac{\partial \mathbf{H}}{\partial t} + \boldsymbol{\nabla} \times \mathbf{E} = 0. \tag{A.16}$$

The three components of the current density [$\boldsymbol{\nabla} \times H$ in Eq. (A.15)], are calculated by taking the derivates of the three components of H:

$$\boldsymbol{J} = \begin{matrix} J_x \\ J_y \\ J_z \end{matrix} = \begin{bmatrix} \dfrac{dH_z}{dy} - \dfrac{dH_y}{dz} \\ \dfrac{dH_x}{dz} - \dfrac{dH_z}{dx} \\ \dfrac{dH_y}{dx} - \dfrac{dH_x}{dy} \end{bmatrix}. \tag{A.17}$$

The conservative flux vector in Eq. (A.1) is modified, the cross product in Eq. (A.16) is defined as a dot product, this is implemented using the matrix:

$$\Gamma = \begin{pmatrix} 0 & E_z & -E_y \\ -E_z & 0 & E_x \\ E_y & -E_x & 0 \end{pmatrix}. \tag{A.18}$$

The other terms in the PDE Eq. (A.1) are the damping coefficient d_a which is set to the μ_0, and the mass and source coefficient defined $e_a = f = 0$. The initial conditions in the model are the field components and its time derivative, defined as 0 A·m^{-1} and A·m^{-1}·s^{-1} respectively.

The variables H and J have an additional term in their definition, a very small number (10^{-15}), defined in Comsol as 'eps', to avoid division by zero.

To model superconductors in the Comsol general form PDE interface, it is necessary to use the curl operation. It is typical to use the curl operation when calculating electromagnetic vector fields, as it reduces the number of dependent variables to *H* with field components mod1.H.

A.3.2.4.   Element Order and Nodes

The simulation domain is discretised into a number of elements, defined by a set of points called nodes. The adjacent elements share the degree of freedom at connected nodes. The elements have a finite size and the subsequent description of the problem uses a finite number of degrees of freedom. Each node has a set of shape functions or basis functions. The default in Comsol, for a single degree of freedom at each node, are first-order elements. First-order elements have a node with a value of unity and at each other node zero, Figure A.8 (a). A second-order has a node at the midpoint of the vertex, with nine shape-functions, Figure A.8 (b). The node orders that are available to approximate a function increase in complexity from linear to quintic. Well-posed problems converge toward the same answer, regardless of the element order, but converge on the solution at different rates. The first-order element approximates all sides of the domain as straight lines. A curved domain Figure A.8 (c-i) is approximated with straight lines (c-ii), or curved lines (c-iii). Depending on the shape between nodes, the mesh generated can result in geometric discretisation error.

In the Comsol AC-DC magnetic field module, the default element order for the magnetic vector potential *A* is quadratic. The effect of element order for a straight wire (radius 10 mm, length 100 mm), with identical meshing (540 boundary elements), is shown in Figure A.9. The degrees of freedom and computation times are defined in Table A.5. It is possible to change the element order in *H*-formulation, but only *linear* elements are possible in 3D models. The approach employed to generate accurate results is to increase the mesh density until results converge.
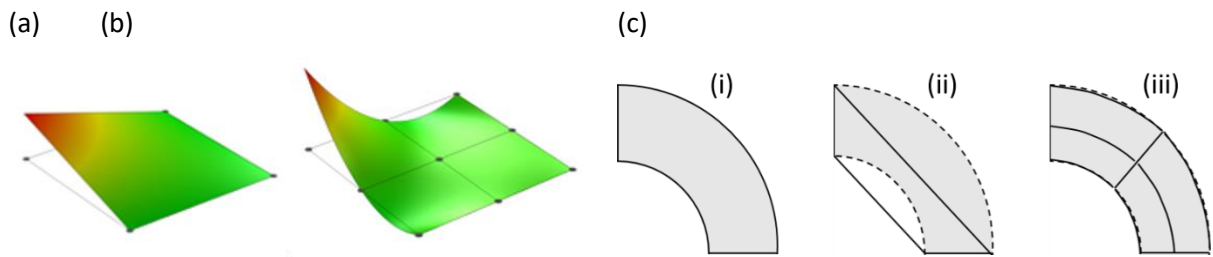
Figure A.8 : (a) First-order node (b) Second-order node (c) curved domain (i) being approximated with first-order (ii) and second-order (iii) quadrilateral elements.
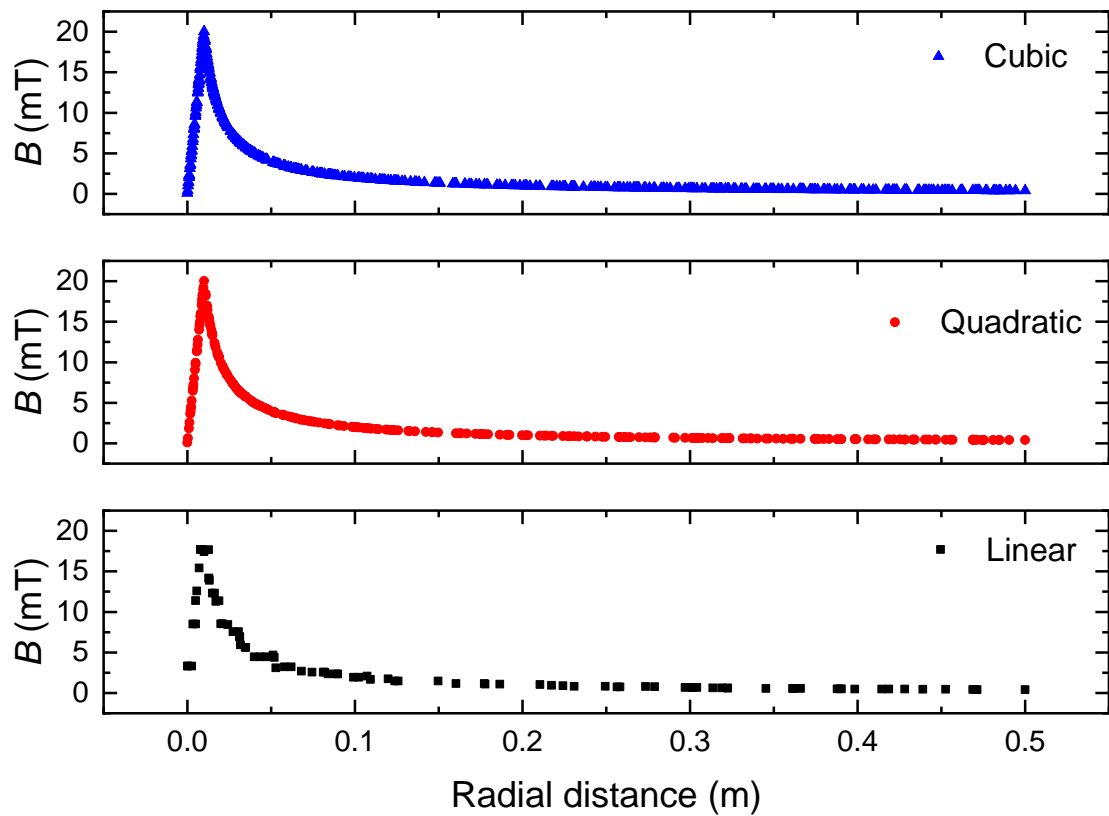
Figure A.9 : Radial distribution of the magnetic field with varied element order. *A-V* formulation for an infinite straight wire.

Element order	Degrees of Freedom	Calculation time [s]
Linear	35,930	4
Quadratic	201,401	24
Cubic	597,432	249

Table A.5 : Element order and calculation time using the *A-V* formulation for an infinite straight wire.

Domain	Mesh Type	Minimum element size [mm]	Maximum element size [mm]	Maximum element growth rate	Curvature factor	Resolution of Narrow regions:
Small air domain	Extra fine	0.12	2.8	1.35	0.3	0.85
Helix	Finer	0.32	4.4	1.40	0.4	0.7
Extrude	Normal	2.24	8	1.50	0.6	0.5
Large air domain	Coarser	3.2	15.2	1.70	0.8	0.3

Table A.6 : Structure of the helix mesh and element sizes.

A.3.2.5.   Pre-processing

The geometry in the model was constructed using standard computer-aided design (CAD) tools. The properties of the domains were defined using the definitions of resistivity. The current injection was implemented across surfaces where the flux integrals were specified.

A.3.2.6.   Meshing

A challenge of FEA is generating an efficient mesh for complex systems. The mesh density was increased in regions of interest, where the mesh elements size was as small as the smallest detail resolved. The mesh elements maximum and minimum sizes were varied, along with the element growth rate, the curvature factor and the resolution of narrow regions. The compromise between a sufficiently accurate mesh and reasonable computational time was a continuous challenge throughout the work.

The geometry of the transport measurements has the inherent challenge that the strand has a small minor radius and the helix a relatively large major radius. In addition to the aspect ratio, the curved boundaries of the helix can result in discretisation errors. The mesh size feature was used, with a sequence of different densities used. The default meshes used are listed in Table A.6 for the 3D calculations. The hierarchy and structure of the mesh were varied to achieve a suitably high-density mesh. With a strand diameter of 0.730 mm, extra-fine meshing is necessary to understand the redistribution of current on the scale of the strand's architecture.

A.3.2.7.   Processing

FEA problems in Comsol are calculated using a non-linear solver. The solver approximates a continuous equation with a set of discrete polynomial equations, written as the matrix M. The form of the assembled equation is,

$$\mathrm{M}\dot{\boldsymbol{X}} = \boldsymbol{f}(t, \boldsymbol{X}),$$

(A.19)

where $\boldsymbol{f}(t, \boldsymbol{X})$ is the formulation of unknown variables in time t and space $\boldsymbol{X}$. The discretised form of the linear model is solved using by taking Newton steps, δU. The iteration at $U_1 = U_0 + \lambda\ \delta U$ is calculated and the error in U_1 is estimated. When a successful step is taken, the algorithm proceeds with the next Newton iteration. When the estimated error is less than the relative tolerance, the calculations stop. Numerical errors may accumulate over time, resulting in the solution diverging. For linear problems, the relative tolerance is typically 1 x 10^{-1}, for the non-linear superconducting system 1 x 10^{-5} was used [33]. Table A.7 summarises the solver configuration.

Comsol uses the multifrontal massively parallel sparse direct solver (MUMPS) in the calculations. The advantage of using MUMPS is both the speed and that all the processor cores on a single machine are used. MUMPS uses fifth element-order backward differentiation formulation (BDF). Table A.8 summarises the time-dependent solver settings.

Variable	Value
Global method	*Scaled*
Tolerance Method	*Manual*
Relative tolerance	1 x 10^{-5}
Absolute tolerance	1 x 10^{-7}, 1 x 10^{-3}
MUMPS: memory allocation factor	*1.2* (4.0)

Table A.7 : Solver configuration, the options that are default are italicised.

Variable	Value
Steps taken by solver	*Free*
Initial step	*No*
Maximum step	*No*
Maximum BDF order	*5*
Minimum BDF order	*1*
Event tolerance	*0.01*
Nonlinear controller	*No*

Table A.8 : Time-dependent solver settings,
the default choices are italicised.

A.3.2.8.   Batch Calculation

As the complexity of the model increased, the runtime also increased. FEA models that were stable could be calculated using batch mode. Batch calculation reduces user input time if a calculation fails the next model in the batch script runs automatically [5].

A.3.2.9.   Post-processing

Once the solution has been calculated, the data was analysed. Plots were produced in 1, 2, and 3D, with examples in Figure A.10. An example of the type of 3D plot is shown in Figure A.10 (a) showing the magnetic field profiles, current direction and the geometry of the ITER measurement barrel. Colour plots of the cross-section of the strand, Figure A.10 (b, c) are used in visualising the magnetic field and current distribution. A normalised histogram of the volume of the central turn of the helix is presented in Figure A.10 (d) which is used to calculate field distribution statistics.

To calculate the average value of the field distribution, the volume of interest is exported using Comsol's results export function. The data is output as separate .txt files where the value of the desired variable is evaluated at x, y, z position with a constant step size. From the histogram, the average value magnetic flux density is calculated,

$$\bar{B} = Mn/N, \tag{A.20}$$

where M is the midpoint of the box, n the frequency in the box, and N the total number of data points. Fixed bin width was used in the analysis. The python script used to generate Figure A.10 (d) is reported in Table A.9. The domain file and magnetic field files are loaded. The magnetic field data that is in the domain of interest is selected. The spatial information is not required for the histogram. The histogram is plotted, and statistics output, maximum, minimum, and the average is calculated from the midpoint.

```
dom=loadtxt("dom.txt")
mag=loadtxt("magB.txt")
wirem=mag[:,3][dom[:,3]==5]
plt.hist(wirem,100, normed=True, histtype='step',stacked=True)
print max(wirem)
print min(wirem)
FreqB,BWB,l=plt.hist(wirem,100,normed=True,histtype='step', stacked =True)
FieldB=(BWB[1:]+BWB[:-1])/2
averB=FieldB*FreqB
BavB=sum(averB)/sum(FreqB)
print (BavB)
```

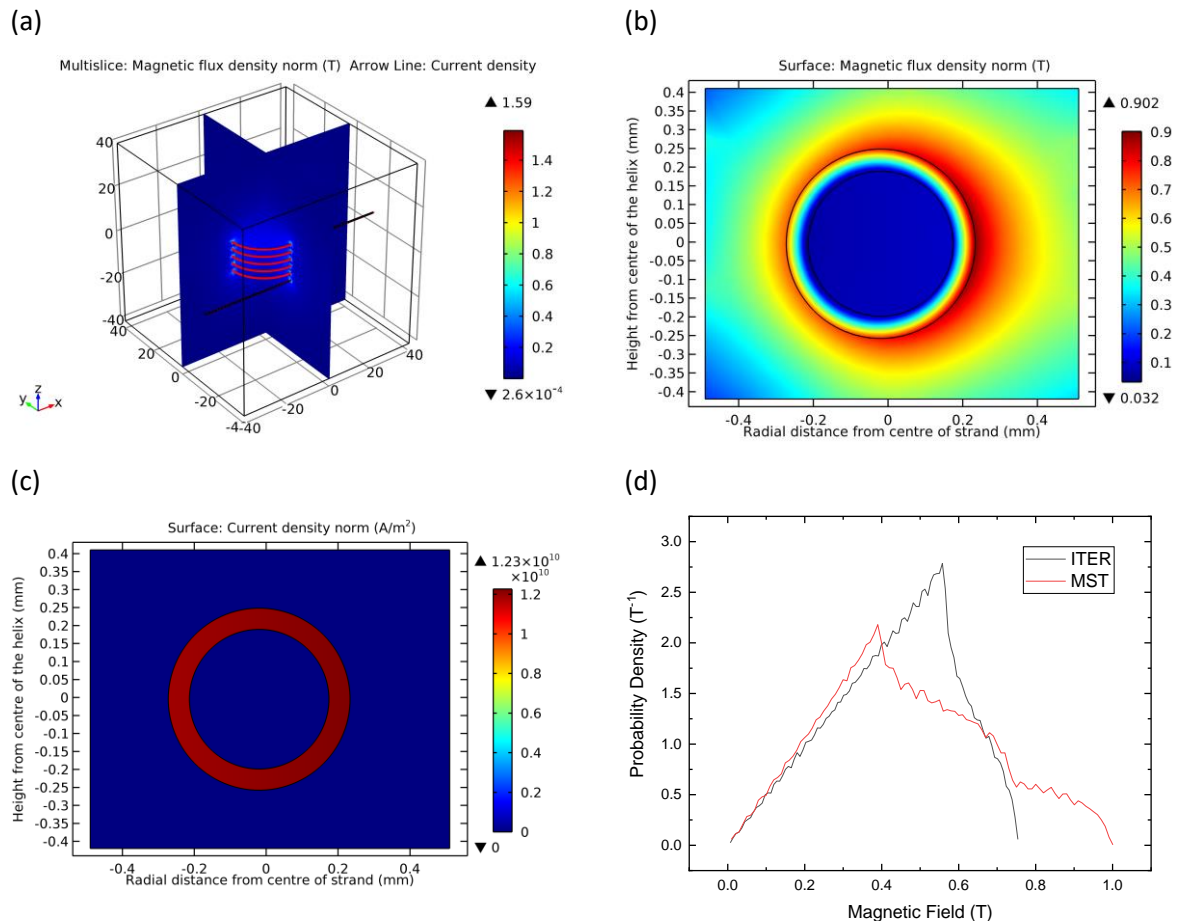Table A.9 : Typical python script for field calculations.

(a)

(b)

(c)

(d)

Figure A.10 : Typical FEA post-processing of the ITER helix geometry (a) 3D plot of the magnetic field distribution, with arrow vector field of the current direction (b) 2D profile of magnetic field in the volume of the strand in the centre of the helix (c) 2D profile of the current distribution in the strands cross-section (d) 1D plot – comparison of the probability density for ITER and MST geometries (zero applied magnetic field, current of 1 kA).

A.3.3. Computation

A.3.3.1. Software

Several commercial FEA software packages were considered for this PhD. FlexPDE was initially used as Durham have experience studying electromagnetic behaviour in 3D planar geometries [34]. *H*-formulation has been implemented using FlexPDE in the literature [35]. However early work using FlexPDE was limited by the complexity of modelling the helix geometry, a necessary component of the thesis.

In the community, there are several commercial software being used to study superconductors [36]. An alternative commercial FEA software is Flux [15, 37] which used the *A-V* formulation as the basis for simulations and has been used to define self-field AC losses [38]. The commercial FEA software Opera [39] is a specialist package used for very precise MRI field calculations and is too specialised for this work. Opera uses the Biot-Savart integral to calculate magnetic field profiles for

superconductors [40]. An expensive software for electromagnetic calculations is Ansys [41], which has been used by the ITER and fusion for energy (F4E) team [42]. An open-source FEA software investigated was ParaFEM [43] as it is used widely in teaching and research, but has not yet been used for modelling superconductors. Although it is possible to use and develop open-source software, the lack of documentation and insufficient user support is a drawback. It is common to validate the results from an open-source FEA software with equivalent results from Comsol. Comsol was chosen as it is a well-documented software package, with a broad community of users working on the *H*-formulation.

A.3.3.2.   Hardware

The FEA models were solved using three computers, their properties are summarised in Table A.10. The two workstations have the same: amount of random-access memory (RAM), number of cores, and processor architecture. The computational time for an *H*-formulation ITER geometry with a five-turns model is recorded in Table A.11. The model has 7314 degrees of freedom, and 1887 timesteps in the calculation. The shortest calculation time was the AN workstation, with the newest generations of RAM and processors this is expected. The server has the most RAM, enabling systems with more degree of freedom to be studied, but this was significantly slower.

Machine ID	Processor	Cores	Processor speed [GHz]	RAM [GB]
FJR: Workstation	Intel i7-4790	4	3.60	32
AN: Workstation	Intel i7-6700	4	3.40	32
Server	Intel Xeon E5620	8	2.40	144

Table A.10 : Properties of the three computers used in calculations.

Machine ID	Total Time [s]	Time per step [s]
AN: Workstation	3622	1.92
FJR: Workstation	4515	2.39
Server	7650	4.05

Table A.11 : Computational times for helix calculation.

A.3.4. Results

The matrix elements for the geometries reported in, Table A.12 and Table A.13. were calculated using the experimental number of turns, i.e., 13 turns on the ITER barrel and 51 turns on the MST barrel. The FEA results and analytic solutions are compared with the matrix elements (Table A.12) for the arrays and a single ring. The radial distribution of the magnetic field around the volume of the strand at the centre of the helix (z = 0 mm), with the centre of the strand defined as 0 mm. The structure of the annulus cross-section is demarcated with dashed lines (R_i = 0.136 mm, R_O = 0.194 mm).

Geometry	Field Term	$B_z(r > R_\text{Maj})$ [·kA^{-1}]	$B_z(r < R_\text{Maj})$ [T·kA^{-1}]
An Array of Straight wires: TwT	Central tube: B_Annulus	$\begin{pmatrix} -1.023 & 0.000 & 0.000 \\ -0.785 & -0.791 & 0.000 \\ -0.643 & -0.643 & -0.643 \end{pmatrix}$	$\begin{pmatrix} 1.031 & 0.000 & 0.000 \\ 0.791 & 0.791 & 0.000 \\ 0.643 & 0.643 & 0.643 \end{pmatrix}$
	ITER: 13 B_Net	$\begin{pmatrix} 0.967 & -0.055 & -0.055 \\ 0.734 & 0.734 & -0.051 \\ 0.589 & 0.589 & 0.589 \end{pmatrix}$	$\begin{pmatrix} 1.114 & 0.078 & 0.078 \\ 0.880 & 0.890 & 0.082 \\ 0.735 & 0.735 & 0.735 \end{pmatrix}$
	MST: 51 B_Net	$\begin{pmatrix} 0.921 & -0.101 & -0.101 \\ 0.731 & 0.731 & -0.054 \\ 0.627 & 0.627 & 0.627 \end{pmatrix}$	$\begin{pmatrix} 1.489 & 0.454 & 0.454 \\ 1.299 & 1.299 & 0.501 \\ 1.195 & 1.195 & 1.195 \end{pmatrix}$
An Array of Rings: TwT	Central ring: $B_{z,ring}$	$\begin{pmatrix} 0.988 & -0.030 & -0.029 \\ 0.750 & 0.749 & -0.029 \\ 0.605 & 0.604 & 0.603 \end{pmatrix}$	$\begin{pmatrix} 1.075 & 0.031 & 0.030 \\ 0.832 & 0.833 & 0.030 \\ 0.683 & 0.684 & 0.685 \end{pmatrix}$
	ITER: 13 B_Net	$\begin{pmatrix} 0.885 & -0.133 & -0.132 \\ 0.651 & 0.650 & -0.128 \\ 0.509 & 0.508 & 0.507 \end{pmatrix}$	$\begin{pmatrix} 1.201 & 0.157 & 0.156 \\ 0.962 & 0.963 & 0.159 \\ 0.816 & 0.817 & 0.818 \end{pmatrix}$
	MST: 51 B_Net	$\begin{pmatrix} 0.649 & -0.37 & -0.368 \\ 0.459 & 0.458 & -0.320 \\ 0.357 & 0.356 & 0.355 \end{pmatrix}$	$\begin{pmatrix} 1.768 & 0.724 & 0.722 \\ 1.573 & 1.574 & 0.771 \\ 1.469 & 1.469 & 1.47 \end{pmatrix}$
FEA: Helix	ITER: 13 B_Net	$\begin{pmatrix} -0.862 & 0.106 & 0.115 \\ -0.675 & -0.658 & 0.109 \\ -0.521 & -0.525 & -0.489 \end{pmatrix}$	$\begin{pmatrix} 1.141 & 0.1403 & 0.139 \\ 0.956 & 0.928 & 0.143 \\ 0.808 & 0.798 & 0.769 \end{pmatrix}$
	MST: 51 B_Net	$\begin{pmatrix} 0.672 & -0.309 & -0.293 \\ 0.542 & 0.492 & -0.246 \\ 0.457 & 0.429 & 0.395 \end{pmatrix}$	$\begin{pmatrix} 1.656 & 0.651 & 0.646 \\ 1.512 & 1.452 & 0.6924 \\ 1.400 & 1.400 & 1.354 \end{pmatrix}$

Table A.12 : Summary table of matrices for tubes-within-tube (TwT) cross-section in the radial direction for an array of straight wires, an array of rings, and helix.

Geometry	Field Term	$\lvert B \rvert\ (z>0)$ [T·kA^{-1}]			$\theta(degree)$		
An Array of Straight wires: TwT	Central wire: B_{Annulus}	$\begin{pmatrix} 1.031 & 0.000 & 0.000 \\ 0.791 & 0.791 & 0.000 \\ 0.643 & 0.643 & 0.643 \end{pmatrix}$					
	ITER: 13 B_{Net}	$\begin{pmatrix} 1.020 & 0.074 & 0.074 \\ 0.780 & 0.780 & 0.074 \\ 0.628 & 0.628 & 0.628 \end{pmatrix}$			$\begin{pmatrix} 4.09 & -80.73 & -80.73 \\ 5.36 & 5.36 & -77.99 \\ 6.66 & 6.66 & 6.66 \end{pmatrix}$		
	MST: 51 B_{Net}	$\begin{pmatrix} 0.886 & 0.342 & 0.342 \\ 0.608 & 0.608 & 0.381 \\ 0.427 & 0.427 & 0.427 \end{pmatrix}$			$\begin{pmatrix} 18.69 & -56.27 & -56.27 \\ 27.82 & 27.82 & -48.25 \\ 41.65 & 41.65 & 41.65 \end{pmatrix}$		
An Array of Rings: TwT	Central ring: $B_{z,ring}$	$\begin{pmatrix} 1.031 & 0.000 & 0.000 \\ 0.790 & 0.790 & 0.000 \\ 0.643 & 0.643 & 0.643 \end{pmatrix}$					
	ITER: 13 B_{Net}	$\begin{pmatrix} 1.029 & 0.147 & 0.145 \\ 0.788 & 0.788 & 0.146 \\ 0.640 & 0.640 & 0.640 \end{pmatrix}$			$\begin{pmatrix} 8.27 & -85.21 & -85.13 \\ 10.77 & 10.69 & -83.65 \\ 13.23 & 13.16 & 13.07 \end{pmatrix}$		
	MST: 51 B_{Net}	$\begin{pmatrix} 1.006 & 0.583 & 0.581 \\ 0.769 & 0.768 & 0.606 \\ 0.317 & 0.636 & 0.635 \end{pmatrix}$			$\begin{pmatrix} 33.32 & -70.92 & -70.87 \\ 45.90 & 45.87 & -65.07 \\ 60.10 & 60.07 & 60.03 \end{pmatrix}$		

Table A.13 : Summary table of matrices for tubes-within-tube (TwT) cross-section in the z-direction for straight wire arrays, ring arrays, and helix.

A.3.5. Conclusions

If the geometry and superconducting properties of a system are known, numerical models are a useful and flexible tool to predict behaviour. Finite element analysis can provide useful information about the distribution in the magnetic field profile and the redistribution of current in a helical strand. In this thesis, Comsol has been used and the *H*-formulation implemented to solve the necessary field equations directly.

References for Appendix:

[1]   M. J. Raine, T. Boutboul, and D. P. Hampshire, "Verification of Nb$_3$Sn and Nb-Ti strands for the ITER toroidal and poloidal field magnets," *Private Communication*, 2018.

[2]   D. R. McGuire *et al.*, "Verification Testing of ITER Nb$_3$Sn Strand at the NHMFL," *IEEE Transactions on Applied Superconductivity,* vol. 25, no. 3, pp. 1-4, 2015.

[3]   (19/03/2020). *MACOR Data sheet*. Available: https://www.corning.com/media/worldwide/csm/documents/71759a443535431395eb34ebead091cb.pdf

[4]   A. Godeke *et al.*, "Interlaboratory Comparisons of NbTi Critical Current Measurements," *IEEE Transactions on Applied Superconductivity,* vol. 19, no. 3, pp. 2633-2636, 2009.

[5]   *Comsol Multiphysics Reference Guide* (Comsol Ltd). Cambridge, 2015.

[6]   M. Sborchia *et al.*, "Overview of ITER Magnet System and European Contribution," *IEEE/NPSS 24th Symposium on Fusion Engineering,* pp. 1-8, 2011.

[7]   G. J. Carty and D. P. Hampshire, "Visualising the mechanism that determines the critical current density in polycrystalline superconductors using time-dependent Ginzburg-Landau theory," *Physical Review B,* vol. 77, p. 172501, 2008.

[8]   A. I. Blair and D. P. Hampshire, "Time-Dependent Ginzburg-Landau Simulations of the Critical Current in Superconducting Films and Junctions in Magnetic Fields," *IEEE Transactions on Applied Superconductivity,* vol. 28, no. 4, pp. 1-5, 2018.

[9]   F. Sirois and F. Grilli, "Potential and limits of numerical modelling for supporting the development of HTS devices," *Superconductor Science and Technology,* vol. 28, no. 4, p. 043002, 2015.

[10]   A. Stenvall, M. Siahrang, F. Grilli, and F. Sirois, "Computation of self-field hysteresis losses in conductors with helicoidal structure using a 2D finite element method," *Superconductor Science and Technology,* vol. 26, no. 4, p. 045011, Apr 2013.

[11]   K. Kajikawa, T. Hayashi, R. Yoshida, M. Iwakuma, and K. Funaki, "Numerical evaluation of AC losses in HTS wires with 2D FEM formulated by self magnetic field," *IEEE Transactions on Applied Superconductivity,* vol. 13, no. 2, pp. 3630-3633, 2003.

[12]   P. Kruger, F. Grilli, M. Vojenciak, V. M. R. Zermeno, E. Demencik, and S. Farinon, "Superconductor/ferromagnet heterostructures exhibit potential for significant reduction of hysteretic losses," *Applied Physics Letters,* Article vol. 102, no. 20, p. 4, May 2013, Art. no. 202601.

[13]   J. Rhyner, "Magnetic properties and AC-losses of superconductors with power law current—voltage characteristics," *Physica C: Superconductivity and its Applications,* vol. 212, no. 3-4, pp. 292-300, 1993.

[14]   J. K. Sykulski, M. Rotaru, and R. L. Stoll, "2D modeling of field diffusion and AC losses in high temperature superconducting tapes," *IEEE Transactions on Magnetics,* vol. 36, no. 4, pp. 1178-1182, 2000.

[15]   S. Stavrev *et al.*, "Comparison of Numerical Methods for Modeling of Superconductors," *IEEE Transactions on Applied Superconductivity,* vol. 38, no. 2, pp. 849-852, 2002.

[16]   G. Barnes, M. McCulloch, and D. Dew-Hughes, "Computer modelling of type II superconductors in applications," *Superconductor Science and Technology,* vol. 12, no. 8, p. 518, 1999.

[17]   L. Prigozhin, "Analysis of critical-state problems in type-II superconductivity," *IEEE Transactions on Applied Superconductivity,* vol. 7, no. 4, pp. 3866-3873, 1997.

[18]   A. M. Campbell, "A direct method for obtaining the critical state in two and three dimensions," *Superconductor Science and Technology,* vol. 22, no. 3, p. 034005, 2009.

[19]   Z. Hong, A. M. Campbell, and T. A. Coombs, "Numerical solution of critical state in superconductivity by finite element software," *Superconductor Science and Technology,* vol. 19, no. 12, pp. 1246-1252, 2006/10/23 2006.

[20]   A. Morandi, "2D electromagnetic modelling of superconductors," *Superconductor Science and Technology,* vol. 25, no. 10, p. 104003, 2012.

[21]   R. Brambilla, F. Grilli, and L. Martini, "Development of an edge-element model for AC loss computation of high-temperature superconductors," *Superconductor Science and Technology,* vol. 20, no. 1, p. 16, 2007.

[22]   N. Amemiya, S. Murasawa, N. Banno, and K. Miyamoto, "Numerical modelings of superconducting wires for AC loss calculations," *Physica C: Superconductivity and its Applications,* vol. 310, no. 1, pp. 16-29, 1998.

[23]   V. Lahtinen, M. Lyly, A. Stenvall, and T. Tarhasaari, "Comparison of three eddy current formulations for superconductor hysteresis loss modelling," *Superconductor Science and Technology,* vol. 25, no. 11, p. 115001, 2012, Art. no. 115001.

[24]   A. Stenvall and T. Tarhasaari, "Programming finite element method based hysteresis loss computation software using non-linear superconductor resistivity and T-ϕ formulation," *Superconductor Science and Technology,* vol. 23, no. 7, p. 075010, 2010.

[25]   J. K. Sykulski, R. L. Stoll, A. E. Mahdi, and C. P. Please, "Modelling HTc superconductors for AC power loss estimation," *IEEE Transactions on Magnetics,* vol. 33, no. 2, pp. 1568-1571, 1997.

[26]   J. Barrett, W. and L. Prigozhin, "Electric field formulation for thin film magnetization problems," *Superconductor Science and Technology,* vol. 25, no. 10, p. 104002, 2012.

[27]   F. Sass, D. H. N. Dias, G. G. Sotelo, and R. de Andrade, "Superconducting magnetic bearings with bulks and 2G HTS stacks: comparison between simulations using H and A-V formulations with measurements," *Superconductor Science & Technology,* Article vol. 31, no. 2, p. 16, Feb 2018, Art. no. 025006.

[28]   (22/01/2018). *HTS Modelling Workgroup* [Website]. Available: http://www.htsmodelling.com/

[29]   F. Gomory and B. Klincok, "Self-field critical current of a conductor with an elliptical cross-section," *Superconductor Science and Technology,* Article vol. 19, no. 8, pp. 732-737, Aug 2006.

[30]   A. Stenvall, V. Lahtinen, and M. Lyly, "An H-formulation-based three-dimensional hysteresis loss modelling tool in a simulation including time varying applied field and transport current: the fundamental problem and its solution," *Superconductor Science and Technology,* vol. 27, no. 10, p. 104004, 2014.

[31]   K. Kajikawa, T. Hayashi, R. Yoshida, M. Iwakuma, and K. Funaki, "Influence of vacuum region on AC losses in superconducting wires with 2D FEM formulated by self-magnetic field," *Physica C: Superconductivity and its Applications,* vol. 392-396, pp. 1113-1117, 2003/10/01/ 2003.

[32]   F. Sirois, M. Dione, F. Roy, F. Grilli, and B. Dutoit, "Evaluation of two commercial finite element packages for calculating AC losses in 2-D high temperature superconducting strips," *Journal of Physics: Conference Series,* vol. 97, no. 1, p. 012030, 2008.

[33]   M. Zhang and T. A. Coombs, "3D modeling of high-T_c superconductors by finite element software," *Supercond. Sci. Technol.,* vol. 25, no. 1, p. 015009, 2012, Art. no. 015009.

[34]   Y. Tsui, E. Surrey, and D. P. Hampshire, "Soldered Joints - an essential component of demountable high temperature superconducting fusion magnets," *Superconductor Science and Technology,* vol. 290, p. 075005, 2016.

[35]   S. Grieco, Y. D. Nyanteh, and P. J. Masson, "Monte Carlo Design Space Exploration of Superconducting Wind Generator Using MgB2 and YBCO Conductors," *IEEE Transactions on Applied Superconductivity,* vol. 26, no. 3, pp. 1-5, 2016.

[36]   V. M. R. Zermeno, S. Quaiyum, and F. Grilli, "Open-Source Codes for Computing the Critical Current of Superconducting Devices," *IEEE Transactions on Applied Superconductivity,* Article vol. 26, no. 3, p. 7, Apr 2016, Art. no. 4901607.

[37]   "Flux," vol. 12.3, Altair, Ed., ed, 2018.

[38]   S. Stavrev, B. Dutoit, and F. Grilli, "Self-field and geometry effects in transport current applications of multifilamentary Bi-2223/Ag conductors," *IEEE Transactions on Applied Superconductivity,* vol. 13, no. 3, pp. 3807-3813, 2003.

[39]   "Opera FEA Simulation Software," 18 ed, 2018.

[40]   M. Greco, P. Fabbricatore, R. Musenich, C. Priano, and F. Kircher, "Self-field effects on critical current measurements of large multi-strand conductors," *IEEE Transactions on Applied Superconductivity,* Article; Proceedings Paper vol. 13, no. 2, pp. 3374-3377, Jun 2003, Art. no. 1212351.

[41]   "Ansys: Maxwell," Ansys, Ed., ed, 2018.

[42]   I. Pong *et al.*, "Current sharing temperature of NbTi SULTAN samples compared to prediction using a single pinning mechanism parametrization for NbTi strand," *Superconductor Science and Technology,* vol. 25, no. 5, p. 054011, 2012, Art. no. 054011.

[43]   "ParaFEM," 5.0.3 ed, 2015.